Assessing the systematic uncertainties influencing radio continuum weak gravitational lensing surveys

by

Alexander D. Hill

A thesis submitted in partial fulfillment of the requirements of
Liverpool John Moores University
for the degree of
Doctor of Philosophy

April 2022

Declaration

The work presented in this thesis was carried out at the Astrophysics Research Institute, Liverpool John Moores University. Unless otherwise stated, it is the original work of the author.

While registered as a candidate for the degree of Doctor of Philosophy, for which submission is now made, the author has not been registered as a candidate for any other award. This thesis has not been submitted in whole, or in part, for any other degree.

Alexander Hill
Astrophysics Research Institute
Liverpool John Moores University
146 Brownlow Hill
Liverpool
L3 5RF
UK

April 2022

Abstract

Astronomy is a field uniquely afflicted by a limited ability to design and run controlled experiments. Hydrodynamical simulations of galaxy formation and evolution are used to alleviate this problem and are widely used in contemporary astronomy. They help interpret observations, validate methodologies, and make new predictions. This thesis concerns the use of simulations in addressing two outstanding questions at the frontier of the field. What are the systematic uncertainties influencing radio continuum weak gravitational lensing surveys such as those conducted with the upcoming Square Kilometer Array (SKA) telescope? What is the predicted dependence of galaxy clustering on various properties at fixed halo mass?

I first measure the morphology and orientation of the radio continuum emitting component of central and satellite galaxies in the EAGLE simulation suite, a good proxy for which is the star-forming gas. Approximating the 3-dimensional morphology as an ellipsoid whose axis ratios are specified by the eigenvalues of the moment of inertia tensor, I show that the star-forming gas characteristically takes the form of a flattened disc at $z = 0$. This is in contrast to the morphology of the stars, which is typically more extended along the minor axis. There exists, however, a significant correlation between the morphology of the two components in individual galaxies, with flatter stellar distributions generally being associated with flatter star-forming gas distributions. The difference in 3-dimensional morphology between the two components results in differences in their projected ellipticities, with the star-forming gas exhibiting a broader spread. The consequence of this for weak lensing surveys is that there will likely be a larger shape noise for galaxies as characterised by radio continuum emission than is the case for the optical. Assessing the redshift dependence, I show that the morphology of the star-forming gas comprising the progenitors of present day $\sim M_\star$ galaxies (i.e. those

with stellar mass similar to that which defines the knee of the galaxy stellar mass function) shows significant evolution, with flattening increasing with time. I show that this is also the case in projection for all galaxies regardless of mass, which indicates that a redshift-dependent shape-fitting algorithm is likely necessary to measure the shapes of real galaxies in SKA-based surveys.

Characterising orientation in terms of the minor axis direction, I present results showing that the star-forming gas is preferentially aligned with its host dark matter halo, however the degree of this alignment is found to be weaker than is the case between stars and dark matter. I provide fitting functions to the distribution of star-forming gas-dark matter alignment angles, which may be applied to semi-analytic models to more realistically model the intrinsic alignment (IA) effect in far larger volumes than can be followed by the current generation of state of the art hydrodynamical simulations. The morphological minor axis of the star-forming gas is found to align strongly with its kinematic axis, affording a route to observational identification of the unsheared morphological axis.

The internal alignment between a galaxy and its host halo has significant implications for the IA of galaxy pairs, a key source of systematic bias in cosmic shear measurements. Using EAGLE, I measure the IA of galaxies as characterised by their star-forming gas. I find that in 3-dimensions and in projection the same qualitative results hold: the star-forming gas IA is weaker at all galaxy pair separations than is seen for the stars, however it is non-negligible when one considers orientation-direction alignment. IA strength as characterised by this measure increases with decreasing galaxy pair separation, following the same general trend as the stars. I find that the strong IAs seen at short pair separation are driven primarily by the one-halo term associated with central-satellite pairs in the haloes that host $M_\star$ central galaxies. At fixed comoving separation, the radial alignment is stronger at higher redshift. My findings imply that the systematic uncertainty due to IA may be less severe in radio continuum weak lensing surveys than in optical counterparts, and that this stems from former's tendency to be less well aligned with the dark matter structure of galaxies than the latter. Alignment models equating the orientation of star-forming gas discs to that of stellar discs or the DM structure of host subhaloes will therefore overestimate the impact of IAs on radio continuum cosmic shear measurements.

I next address the topic of galaxy assembly bias. This is a consequence of the well-known prediction of halo assembly bias from simulations of the ΛCDM concordance model of cosmology, however it has yet to be conclusively observed in galaxy surveys. I first measure the galaxy assembly bias effect in EAGLE, and then assess the degree of correlation between various galaxy/halo properties with halo assembly time at fixed halo mass. Most properties which correlate with assembly time are found to be generally associated with galaxy clustering strength, however some properties which are not correlated with assembly time also exhibit secondary biases in galaxy clustering. This indicates that in EAGLE, not all of the secondary biases in galaxy clustering can be attributed to halo assembly time.

While contemporary hydrodynamical simulations appear to agree in the existence of galaxy assembly bias and secondary bias, the exact nature of the signal varies, seemingly due to differences in the implementation of baryonic processes. I find that the EAGLE, BAHAMAS, and IllustrisTNG simulations agree in the prediction that galaxies with higher stellar mass cluster more strongly at fixed halo mass, EAGLE and IllustrisTNG predict a larger effect than is seen in BAHAMAS. The halo mass scale at which the secondary bias signal exhibits an inflection point is lower in EAGLE than is seen in IllustrisTNG.

I next explore the possibility of using measures of environmental density to probe the dependence of clustering on properties at fixed halo mass. For such probes to be unbiased, it is required that measures of environmental density are uncorrelated with halo mass. I confirm this is the case with ρ_N for $M_{200} < 10^{12}$ $\mathrm{M}_\odot$. After confirming that ρ_N correlates strongly with clustering, I demonstrate that galaxies residing in more dense regions exhibit higher stellar masses at fixed halo mass.

I finally explore the feasibility of conducting a similar study using a 2-dimensional environmental measure more readily accessible in observation. Σ_N is the 2-dimensional equivalent of ρ_N, and the two measures are closely linked. I minimise the scatter in Σ_N-ρ_N by optimising the selection of the recessional velocity cut used to reduce the influence of projection effects. I confirm that Σ_N correlates strongly with clustering, and demonstrate that higher Σ_N values are correlated with higher stellar masses at fixed halo mass.

Contents

List of Figures

Publications

During the course of the preparation of this thesis, the contents of Chapters 3 and 4 have been submitted and accepted for publication in a refereed journal:

- *The morphology of star-forming gas and its alignment with galaxies and dark matter haloes in the EAGLE simulations*
  Hill, A. D., Crain, R. A., Kwan, J., and McCarthy, I. G., 2021, MNRAS, 505, 65.

- *Intrinsic alignments of the extended radio continuum emission of galaxies in the EAGLE simulations*
  Hill, A. D., Crain, R. A., Kwan, J., and Brown, S. T., 2022, MNRAS, 511, 3844.

The contents of Chapter 5 correspond to a third study currently in preparation for eventual submission to MNRAS.

Acknowledgements

Firstly I would like to thank Rob Crain, who throughout our time together has managed to balance being an exceptionally supportive supervisor, a new father, and a fan of Manchester United. I'll leave it to him to decide which of these he's found the most challenging. I would also like to thank the rest of my supervisory team, Ian McCarthy and Ivan Baldry, whose scientific insights and generosity of time are a great help and inspiration. I owe a great deal to the members of the High Performance Computing group, past and present. In all the journal clubs and group meetings, I have been consistently impressed with their professionalism, amiability, and love of what they do. Directly through collaborations and their advice, and indirectly through sharing their work, they have made me a better researcher. In no particular order they are Andreea Font, Adrien Thob, Simon Pfeifer, Egidijus Kukstas, Juliana Kwan, Alberto Acuto, Shaun Brown, Rob Poole-McKenzie, Sam Stafford, Amol Upadhye, Jon Davies, Jemima Briggs, Vika Yankelevich and Violeta Gonzalez-Perez.

Throughout my life I have benefited from a host of dedicated teachers, lecturers and supervisors, who have enabled me to get to this stage. They encouraged me to always push myself to reach new heights and take on new challenges. From Durham University, I particularly thank Mark Swinbank and Chris Done for giving me my first taste of life as an astrophysicist. My high school, St. Wilfrid's, not only provided me with the education to achieve my goals, it welcomed me back as a teacher after I graduated from Durham, while giving me the time and opportunity to apply and interview for Ph.D. schemes. I am grateful to everyone from my time here. Here I will mention just a few, mainly from the Mathematics and Science departments: Brian O'Rourke, Marie Rafferty, Helen Murphy, Penny Doig, Tom Hanks, Kevin Field, Phil Turnbull, John Lee, John Murphy, Laura Murphy, Angela Perea, Ian Storey, Ray Rowett, Simon Hall, Ed Larrington, and Rebecca Cunningham-Rose.

The Astrophysics Research Institute is a truly exceptional place filled with exceptional people. It was a pleasure to join as part of a bumper cohort and go through this journey together - to Joaquín, Tom, Meghan, Charlotte, Tricia, Brandon, Joe, Mike, Alex, Danny, Conor, Sarah, Fiona, and everyone else, thank you! I must also thank Phil James and Marie Martig for their help in challenging moments. Finally I would like to thank Anna Hodgkinson, Danielle Coogan, Daniel Harman, and Ben Clark for keeping the machine working.

I was lucky to be part of the LIV.DAT programme, a joint venture between the astronomers of LJMU and the physicists of the University of Liverpool. I have enjoyed many hours at home and abroad in the company of Julia, Selina, Phil, Fraser, Aravinda, Ron, Joe, Tom and Thomas. Finally, a huge thanks to the climbers, hikers, and rugby players of Liverpool, for helping me keep the cheese on the cracker.

I owe everything to my parents, who put their children first in everything they do. Without their encouragement, stability, and sacrifice, I couldn't have hoped to reach this point. I know that my sister Katherine feels the same. Finally I thank Eloise, with whom I have been lucky enough to share my life throughout this process. For all the times you comforted me, supported me, and listened to me blither on about 'space and stuff', thank you. I would not be the man that I am without you.

The author of this thesis is supported by an STFC doctoral studentship within the Liverpool Big Data Science Centre for Doctoral Training, hosted by Liverpool John Moores University and the University of Liverpool [ST/P006752/1]. The EAGLE, BAHAMAS and IllustrisTNG teams are acknowledged for making their simulation data available. The study made use of high performance computing facilities at Liverpool John Moores University, partly funded by the Royal Society and LJMU's Faculty of Engineering and Technology, and the DiRAC Data Centric system at Durham University, operated by the Institute for Computational Cosmology on behalf of the STFC DiRACHPCFacility (www.dirac.ac.uk). This equipment was funded by BIS National E-infrastructure capital grant ST/K00042X/1, STFC capital grants ST/H008519/1 and ST/K00087X/1, STFC DiRAC Operations grant ST/K003267/1 and Durham University. DiRAC is part of the National E-Infrastructure. This thesis has benefited from funding from the European Research Council (ERC) under the European Union's Horizon 2020 research

and innovation programme (grant agreement No 769130). All analyses and plots presented in this thesis were produced using `Python`, most notably its packages `numpy`, `scipy`, `matplotlib`, `h5py`, `astropy`, `py-sphviewer` and `read_eagle`. Many of the figures in this thesis make use of the colourblind friendly palettes created by Paul Tol (`personal.sron.nl/~pault`).

Images of broken light which dance before me like a million eyes,

They call me on and on across the universe.

Thoughts meander like a restless wind inside a letterbox

They tumble blindly as they make their way across the universe.

Lennon–McCartney

For Andrew and Carol
and don't forget Eloise Winona

Chapter 1

Introduction: Scientific Background

The highest object that human beings can set before themselves is not the pursuit of any such chimera as the annihilation of the unknown: it is simply the unwearied endeavour to remove its boundaries a little further from our sphere of action.

Huxley

On the largest scales, the luminous Universe appears as a collection of *galaxies*. Billions of galaxies have been discovered, each containing a multitude of stars. They are distributed throughout our Universe not randomly, but with structure. Galaxies themselves exhibit a wide range of shapes, sizes, colours and ages. Astronomers are then faced with a number of questions. How did galaxies come to be? Why are they located where they are? How do they evolve over time? Why do they have their particular characteristics?

1.1 Galaxies and dark matter

Yet humanity has been privy to this perspective for little over a century. For most of our history our view of the Universe was limited to that which was visible to the naked eye. Planets and stars are both visible as points of light on the sky, however planets (from the Greek 'planete', meaning wanderer) meander across the sky, while stars remain distant, fixed and eternal. Occasional transitory phenomena such as comets and supernovae ('guest stars' in Chinese astronomy) were seen as a herald of change. Interspersed within the stars are nebulae, so named for the Latin word for mist, diffuse and extended sources of light. The band of light spanning the sky known as the Milky Way (MW) was variously theorised by ancient Greek, Persian and Islamic scholars to be comprised of distant stars, a fact later proven by Galileo in 1610 with his telescope. Thus it was thought that the MW contained all the stars in the Universe. Wright (1750) postulated (later expounded by Kant, 1755) that the appearance of the MW on the sky was caused by "an optical effect due to our immersion in what locally approximates to a flat layer of stars". They further suggested that many of the faint celestial nebulae were in fact their own 'island universes', analogous to the MW and containing their own collection of stars. Support for this claim arose more than a century later, when astronomers utilised new techniques combining equatorial mounts and cameras to obtain long-exposure images of 'The Great Nebula in Andromeda' (Fig. 1.1). For the first time, the spiral structure of a distant nebula was observed in clarity. At the time, Andromeda was misidentified as a star-forming region within the MW.

The island universe hypothesis found support from Slipher (1913, 1915, 1917), whose measurements of the radial velocities of 'spiral nebulae' were found to be notably large. The later 'Great Debate' between Harlow Shapley and Herber Curtis in 1920 (Shapley & Curtis, 1921) centred on these 'spiral nebulae' and the true size of the Universe. Shapley (1919) argued against the island universe hypothesis, stating that Andromeda had similar velocities to objects in the MW, while Curtis (1917) argued in favour following detections of nova in Andromeda many times fainter than those observed in the MW, and the great distance that this implied. This debate was settled by Hubble

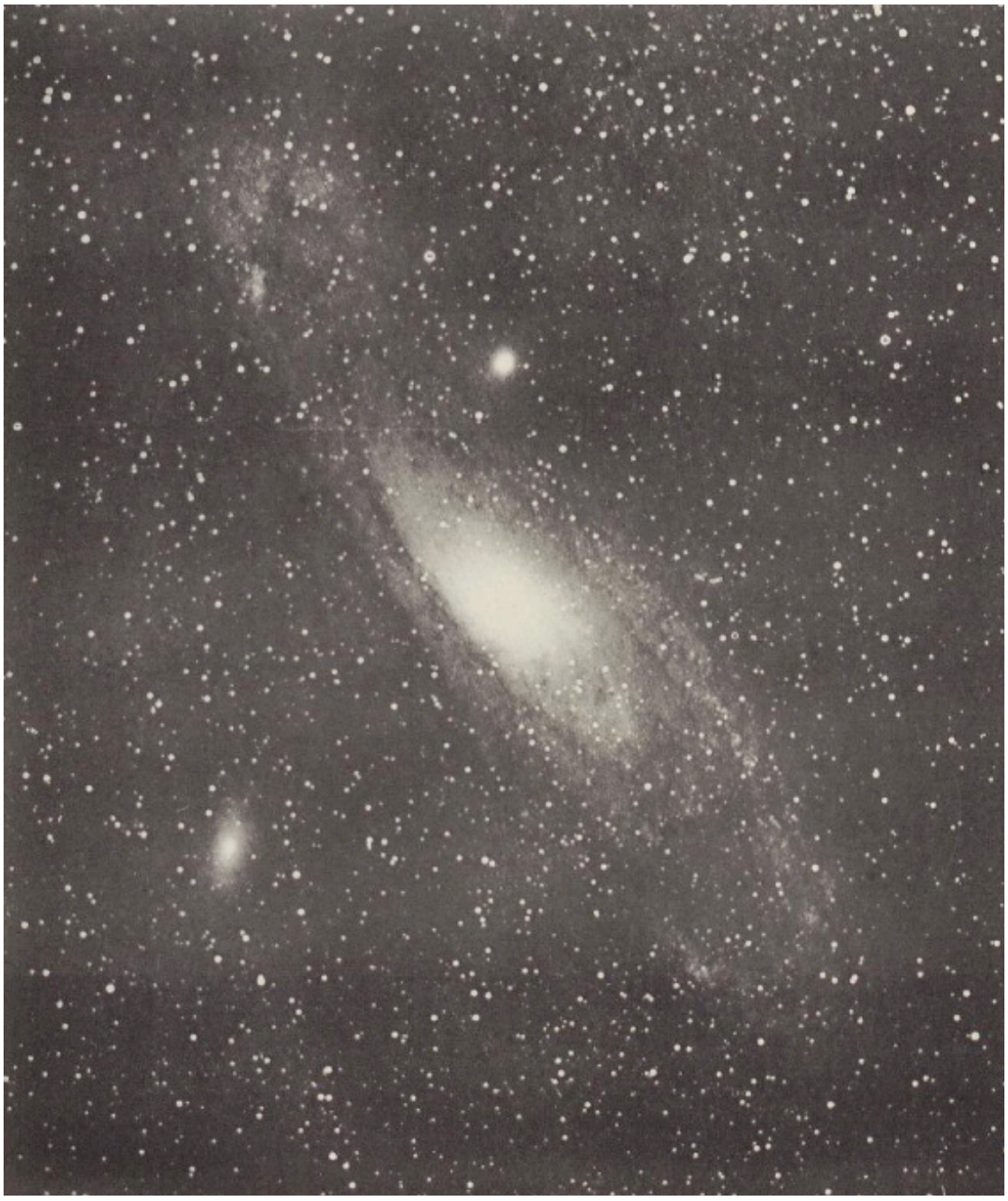

FIGURE 1.1: 'The Great Nebula in Andromeda', a candidate for the earliest identifiable image of a galaxy. Captured by Isaac Roberts in Maghull, Liverpool (1888). Novel combinations of equatorial mounted telescopes and long exposure photography allowed the spiral structure of nebula to be observable for the first time. This later led to the Great Debate (Shapley-Curtis Debate) in astronomy, and the emerging view that the Universe is composed of galaxies, rather than a single extended structure.

(1929b), who used the 2.5-metre Hooker telescope to observe Cepheid variable stars in Andromeda in order to obtain distance measurements of 275 kpc, far beyond the distance to other observed stars now known to belong to the MW and Small Magellanic Cloud, and indicating that Andromeda is a galaxy in its own right. Hubble (1929a) prompted a revolution in cosmology, the study of the origin and evolution of the Universe, when he presented the a study into the relationship between the distances and recessional velocities of extra-galactic nebulae (galaxies). By finding that recessional velocity increases with distance, he proposed that the Universe, rather than being static, is expanding. This ran contrary to the popular steady-state theory of cosmology, which posited that on large scales the Universe is largely unchanging with time.

Following the publication of the general theory of relativity (Einstein, 1916), Einstein successfully reproduced Newton's equations in the limit of a weak gravitational fields, and surpassed them in providing a theoretical description for the observed precession of the perihelion of Mercury. Einstein's field equations relate mass and energy to the curvature of spacetime. He applied the field equations to the Universe as a whole, incorrectly positing that the average density does not change with time, $\frac{\partial \rho}{\partial t} = 0$. This led to the unphysical solution $\rho = 0$. Einstein, as a proponent of the steady-state theory, introduced a 'cosmological constant', Λ, to the field equations. This inclusion had no effect on the prior successes of relativity, and resulted in the solution $\rho \propto \Lambda$. Alexander Friedmann proposed an alternative solution which omitted the assumption the Universe is static and unchanging with time (Friedmann, 1922). He found that the Einstein's field equations reduced to two. One links the change in scale factor of the Universe (a) with the density (ρ), following

$$H^2 = \frac{\dot{a}^2}{a^2} = \frac{8\pi G}{3}\rho - \frac{kc^2}{a^2} + \frac{\Lambda c^2}{3}, \tag{1.1}$$

where H is the Hubble constant, and G is the gravitational constant. The speed of light, c, is typically set to unity for convenience. The curvature of space, k, is equal to zero for a spatially flat universe. Λ was included by Friedmann with the knowledge that it could be set to zero if it were eventually found to be unnecessary. The second equation considers the change in velocity in the expansion of the Universe over time, and is given by

$$\frac{\ddot{a}}{a} = -\frac{4\pi G}{3}\left(\rho + \frac{3p}{c^2}\right) - \frac{\Lambda c^2}{3}, \tag{1.2}$$

p is pressure. This equation shows that the gravitational influence of the matter in Universe should result in a deceleration in any expansion, and indeed possibly an eventual

contraction, unless Λ exists and takes a value to counteract this effect. The findings of Hubble (1929a) appeared to remove the need for Λ to be included. Einstein later described this as his 'biggest blunder', however Λ would later be revived in contemporary cosmological models, which I shall discuss in Section 1.2.

The observational work of Edwin Hubble pointing to an expanding Universe was preceded by theorists, who independently provided solutions to Einstein's field equations (Friedmann, 1922; Lemaître, 1927). These solutions led to the Friedmann-Lemaître-Robertson-Walker (FLRW) metric, which describes a homogeneous, isotropic and expanding Universe. The Friedmann equations are the solution to Einstein's field equations in this metric. Lemaître (1931) proposed that Hubble's observed expansion implied that at earlier times the Universe would be smaller. Reversing the expansion, one would eventually find that all the matter and energy would be concentrated at a single point in space and time, termed by Lemaître as the 'primeval atom'. This provided the foundation for the Big Bang theory of cosmology, support for which arose from agreement between the predicted and observed elemental abundances (Big Bang Nucleosynthesis, Alpher et al., 1948).

The steady-state model was latterly adapted to accommodate Hubble's observations by continually having matter be created within an expanding universe in order to maintain the present day density (Bondi & Gold, 1948; Hoyle, 1948), however as the 20th century progressed it was increasingly disfavoured by the vast majority of the astronomical community. The steady-state theory was finally discounted with the discovery of the Cosmic Microwave Background (CMB, Penzias & Wilson, 1965), relic radiation from the epoch of recombination. It exhibited a thermal, black-body spectrum, which could be explained by the Big Bang theory but not with a steady-state model (Peebles et al., 1991).

The epoch known as recombination is the time when the expanding Universe had cooled sufficiently to allow for the union of electrons and nucleons into atoms. This process quickly turned the Universe from opaque to transparent as photons were able to freely propagate, now unimpeded by the sea of free electrons via Thompson scattering. The CMB originates from the 'last-scattering surface', at a time ($t = 370,000$ yr) when the average temperature was 3000 K and the Universe was 1/1000 times its present comoving scale length (see e.g. Tanabashi et al., 2018, pg. 358). The CMB displays minute variations ($\sim$1 in 10^5) in the temperature of the last scattering surface known as anisotropies. These temperature variations correspond to small differences in the density of the primordial matter distribution, and are evidence for the predicted inflated quantum fluctuations, which are the seeds for all structure in the Universe. The anisotropies may be decomposed into an angular power spectrum, the form of which

may be predicted from cosmological models. In comparing theory with observation, one finds evidence that there is for there being more to the Universe than first meets the eye (e.g. Planck Collaboration et al., 2020). In our paradigm we have galaxy formation and evolution taking place within the context of primordial density fluctuations collapsing within an expanding Universe. To this we are required to add another element: dark matter.

One of the earliest suggestions of an invisible contributor to the cosmic matter budget was given by the mathematician Lord Kelvin, who utilised measurements of the velocity dispersion in the central regions of the MW to infer that the dynamical mass differed from that the of visible stars. He hypothesised the existence of an unseen majority population of known as dark bodies (Kelvin, 1904). This was further discussed by Poincare (1906), who referred to 'matière obscure'. Kapteyn (1922) first proposed the measuring stellar velocities as a means of determining the mass of dark matter in the Universe. Oort (1932) found that the motion of stars suggested a total mass in the galactic plane greater than the apparent contribution of luminous matter. Zwicky (1933) studied the Coma Cluster and estimated the dynamical mass based on the motions of galaxies at the cluster's outer edge. He found that the inferred mass was far greater than that which would be suggested by the luminous material alone, pointing towards the presence of some 'dunkle Materie'. Further observational evidence for the existence of dark matter came later in the century with Rubin & Ford (1970) and Rubin et al. (1980), who found that the velocity curves of spiral galaxies beyond a certain radii did not behave as expected. Individual stars orbit their host galaxy according to Kepler's law. For a star at radius R, balancing the centripetal acceleration with the incident gravitational force resulting from the enclosed galaxy mass within the radius, $M(< R)$, one obtains

$$v = \sqrt{\frac{GM(< R)}{R}}. \tag{1.3}$$

This implies that beyond the radius within which the majority of the galaxy's mass is contained ($M_{\rm gal} \sim M_{\rm gal}(< r)$), the circular velocity of individual stars should decrease according to the square root of the distance. This is not observed, instead the circular velocity is roughly constant with increasing radii, implying the presence of unseen mass. Further observational (Ostriker et al., 1974; Einasto et al., 1974; Mathews, 1978; Faber & Gallagher, 1979) and simulation-based studies (Ostriker & Peebles, 1973) supported the case for the existence of some missing matter within galaxies and clusters. Cosmologists were simultaneously developing a galaxy formation model that involved the gravitational collapse of the initial density perturbations into the structures seen in the local Universe. Models assuming that baryons were the only contributors to the cosmic mass budget were found to be incompatible with the then upper limits of the amplitude

of anisotropies (Sachs & Wolfe, 1967; Silk, 1967, 1968; Peebles & Yu, 1970; Doroshkevich et al., 1978; Wilson & Silk, 1981; Uson & Wilkinson, 1984). Other models partitioned the mass between baryons and a dominant, unobserved component termed dark matter. Predictions that took dark matter to be 'cold', that is non-relativisitic at recombination, were successful in linking the fluctuations signalled by the CMB anisotropies with the large scale structure (LSS) of the evolved Universe (White & Rees, 1978; Peebles, 1982; White et al., 1983; Blumenthal et al., 1984; Davis et al., 1985; Frenk et al., 1990). This research provided the basis for CDM, currently the model of dark matter with the most widespread acceptance.

1.2 The ΛCDM model of cosmology

The expression 'ΛCDM' itself indicates a universe with: 'dark energy' described by a positive cosmological constant (Λ); dark matter described as 'cold' (CDM), that is non-relativistic, collisionless, and interacting only through gravity. In this paradigm, the Universe experiences a rapid expansion from an initial singularity in spacetime through a process known as inflation. Following this, its evolution follows the Friedmann equations within a FLRW metric. The Universe is geometrically flat[1], expanding, and contains matter comprising of baryons and cold dark matter. At late times, the positive Λ drives an acceleration in expansion. The energy density content of the Universe can be expressed via the density parameter $\Omega_0 = \rho/\rho_{\rm crit}$, where $\rho_{\rm crit}$ is the 'critical density' that would be required for the Universe to expand forever. Ω_0 may be decomposed into its contributing components as

$$\Omega_0 = \Omega_{\rm m} + \Omega_{\rm rel} + \Omega_\Lambda \tag{1.4}$$

where these are the mass density, the energy density of relativistic particles (i.e. electromagnetic radiation and neutrinos), and the energy density of dark energy. $\Omega_{\rm m}$ is further decomposed into baryonic and dark matter components as $\Omega_{\rm m} = \Omega_{\rm b} + \Omega_{\rm DM}$. The values of these parameters may be computed from measurements of the angular fluctuations in the CMB temperature (see e.g. Roos & Harun-or-Rashid, 2002; Mo et al., 2010, for a more complete description). The fluctuations can be expressed as the weighted sum of spherical harmonics, $\sum_{l,m} a_{lm} Y_{l,m}(\theta\phi)$. The angular power spectrum is given as $C_l(l) =< |a_{lm}|^2 >^{1/2}$, where this is averaged over m, and takes the appearance of a series of peaks and troughs thought to be the result of acoustic waves in the Universe at the decoupling time. It is rich with cosmological information, dependent as the various

[1] i.e. Euclidean geometry is satisfied; the internal angles of three connecting points sum to 180°.

features are on the physical properties of the Universe. The ratio of the amplitude of the first two peaks is sensitive to $\Omega_{\rm b}$, the position of the first peak in l-space is sensitive to Ω_0, and Ω_Λ affects both the peak heights and their positions in l-space. Planck Collaboration et al. (2020) finds the following best fitting values for the present-day: $\Omega_{0,\rm b} \sim 0.049$, $\Omega_{0,\rm DM} \sim 0.265$ and $\Omega_{0,\Lambda} \sim 0.684$ (Planck Collaboration et al., 2020). The energy density of radiation and neutrinos are negligible at $z = 0$.

ΛCDM posits that structure in the Universe has its roots in adiabatic fluctuations in the primordial density field, themselves seeded by quantum fluctuations made macroscopic by inflation. Overdense regions grew via gravitational instability within an expanding background. The initial distribution of matter is described by the primordial power spectrum, $P(k)$, which details the amplitude of overdensities as a function of spatial scale. This is the Fourier transform of the two-point correlation function, $\xi(r)$, which measures the likelihood of two instances of the same matter tracer being separated by some distance r. At early times the Universe was in a radiation-dominated state. Radiation pressure retarded the gravitational collapse of structures on scales within the cosmological horizon. As the Universe expanded, the energy densities of radiation and matter reduced according to the increase in volume. Radiation, however, is subject to the additional factor that photon wavelength (energy) increases (decreases) as the Universe expands, which results in $\rho_{\rm m} \propto a^{-3}$ and $\rho_{\rm r} \propto a^{-4}$. This led to matter-radiation equality, after which structures were able form more rapidly. There is then a suppression in the primordial power spectrum at scales that re-entered the horizon during the radiation dominated era (see Mo et al., 2010, for a more complete discussion of density fluctuations in the early Universe).

The ΛCDM model arose through the efforts of astrophysicists, particle physicists and mathematicians throughout the $20^{\rm th}$ and $21^{\rm st}$ centuries, who worked to combine the study of structure formation with that of general relativity. It is remarkably successful at predicting the geometry of the Universe's LSS, as well as some properties of galaxies that reside within dark matter haloes. The remarkable complexity of the predictions belie the relative simplicity of the model. It is often said that only six independent values are needed to parameterise the model, however I caution that this is based on a number of simplifying assumptions. These are ($A_{\rm s}$, $n_{\rm s}$, H_0, $\Omega_{\rm b}$, $\Omega_{\rm m}$, τ): the amplitude of the primordial power spectrum, the scalar spectral index, the present-day Hubble constant, the optical depth of reionisation, the dimensionless density parameters of baryons, and that of the total matter. From the latter two parameters the corresponding density of dark matter may be computed via $\Omega_{\rm m} - \Omega_{\rm b}$, and that of dark energy via $1 - \Omega_{\rm m}$ for a flat Universe. In the following subsections I shall discuss the key tenets of ΛCDM and their implications, as well as challenges facing the model.

1.2.1 Cold dark matter

The fundamental nature of an indivisible unit of dark matter, be this a particle or other, remains unknown. An open objective of particle physics is the direct detection of a dark matter particle via nucleon scattering. Numerous studies have posited tentative positive findings (e.g. DAMA/LIBRA (Bernabei et al., 2013) and CDMS (CDMS Collaboration et al., 2013)), however various null results have also been reported from other experiments (e.g. Aprile et al., 2017).

Indirect detection experiments aim to infer the presence of dark matter through electromagnetic radiation observed by ground- or space-based telescopes. Various dark matter candidates are thought to produce a theoretically observable electromagnetic radiation signal through processes such as decay or self-annihilation, which may be present in such areas of high dark matter density as the Galaxy centre (e.g. Weakly Interacting Massive Particles (WIMPs), see Arcadi et al., 2018, for a review). The expected signals from both direct and indirect detection studies rely on an understanding of the expected distribution of dark matter at a given region of space. This is informed by the prevailing cosmological model, specifically the quantity and velocity distribution of dark matter at a given location in space predicted by the standard halo model (SHM). Simulations constructed on this basis may be used in providing detection limits for dark matter (e.g. Bozorgnia et al., 2016; Calore et al., 2016; Poole-McKenzie et al., 2020), in the case of direct detection the expected differential scattering rate of dark matter-nucleon interactions depends on the nature of individual particles and the astronomical macroproperties of dark matter. See Feng (2010) for a review of dark matter candidates and methods of direct detection.

The macroscopic properties of dark matter are significantly better understood than its microscopic nature. Despite the current lack of robust detection, dark matter provides the means of explaining numerous and apparently independent otherwise confusing phenomena. As discussed previously, dark matter can provide an explanation for the observed dynamics of cluster galaxies (Zwicky, 1933, 1937), as well as the rotation curves of galaxies (Rubin & Ford, 1970; Rubin et al., 1980). The presence of dark matter additionally explains the observed degree of gravitational lensing for background galaxies by massive foreground objects (Tyson et al., 1990), provides the theoretical means for the collapse of the initial distribution of baryons as observed by the CMB into the diversity of galaxies in the local Universe (Ma & Bertschinger, 1995), as well as being needed to predict the power spectrum of the CMB (e.g. Planck Collaboration et al., 2020) and the observed clustering of galaxies (e.g. Blumenthal et al., 1984). Alternative explanations for these diverse phenomena usually take the form of modified gravity models (e.g. Milgrom, 1983), however challenges to these relate to structures seemingly without dark

matter (and therefore no need for a gravity modification, e.g. van Dokkum et al. (2018)), the apparent dark matter displacement with respect to the luminous component (Clowe et al., 2006), and the need for ad hoc scale-based screening methods due to the success of general relativity in describing interaction in the solar system.

The apparent need for dark matter to be 'cold' arose from studies which seemingly rule out other possibilities. Initially, neutrinos were proposed as dark matter candidates due to their lack of interaction with luminous matter. Their relativistic speeds led to their categorisation with other similar candidates as 'hot' dark matter (HDM). HDM candidates remain relativistic until relatively late in the Universe's evolution and therefore exhibit a long free streaming length, which smooths out primordial density perturbations on super-galaxy scales and results in the dissolution of small structures. The chief consequence of this is that galaxies and dark matter structures form in a top-down fashion. Structure forms slowly, as the surviving large perturbations are required to undergo fragmentation into small clumps (Bond et al., 1996; Doroshkevich et al., 1981; Zeldovich et al., 1982; Bond & Szalay, 1983), which results in the late formation of galaxies. Other models posit non-baryonic candidates with behaviour termed 'warm' (WDM Blumenthal et al., 1982; Bond et al., 1982) and 'cold' (CDM Peebles, 1982), which relates to their velocity dispersion and the time in the Universe's evolution when the particles became non-relativistic. In these schemes, the free-streaming length of dark matter is shorter, smaller scale perturbations survive, and galaxy and structure formation occur bottom-up. In WDM models, the growth (gravitational collapse) of galaxy-scale perturbations in the primordial density fluctuations are suppressed due to the free-streaming length of the particles. HDM was ruled-out by White et al. (1983), whose $N-$body simulations included a population of massive neutrinos. The clustering scale of the neutrinos was found to be larger than that of observed galaxies for reasonable cosmological parameters. Blumenthal et al. (1984) conversely found that a universe with $\sim$10 times as much CDM as baryons agreed well with reality in a number of key areas, for example predicting the approximate observed mass range and clustering of galaxies.

1.2.2 Large scale structure

Following the growth of the initial density perturbations, the dark matter takes the form of a complex system of nodes, filaments and voids, known as the 'cosmic web' (Zel'Dovich, 1970; Bond et al., 1996). These perturbations continue to grow linearly until a critical density is reached, after which point they 'turn around' from the general expansion of the Universe and collapse to form virialised dark matter haloes (e.g. Mo et al., 2010). While halo mass, $M_{\rm h}$ is a challenging property to precisely define, it is often given in terms of the virial mass, $M_{\rm vir}$. This is usually defined as the mass enclosed

within some radius defining the halo's outer edge, $R_{\rm vir}$, within which the matter density is some multiple of average cosmic background density:

$$M_{\rm vir} = \frac{4\pi}{3} R_{\rm vir}^3 \Delta \rho_{\rm m}, \tag{1.5}$$

where Δ is the virial overdensity parameter, chosen to approximate the predicted overdensity for a virialised region of dark matter that has undergone an idealised spherical collapse (Bryan & Norman, 1998). The virial velocity of a dark matter halo is defined as

$$V_{\rm vir} = \sqrt{\frac{GM_{\rm vir}}{R_{\rm vir}}}. \tag{1.6}$$

Following equations 1.5 and 1.6 for a given overdensity parameter, knowledge of one of the virial properties allows the calculation of the other two. $V_{\rm vir}$, $M_{\rm vir}$ and $R_{\rm vir}$ are then effectively equivalent mass labels. As an example, a large galaxy cluster with halo mass $M_{\rm vir}{\sim}10^{15}{\rm M}_\odot$ will have a virial velocity $V_{\rm vir} \sim 1000$ kms^{-1}. MW-mass galaxies are typically hosted by haloes with $M_{\rm vir}{\sim}10^{12}{\rm M}_\odot$ have $V_{\rm vir} \sim 100$ kms^{-1}, and small dwarf galaxies have $M_{\rm vir}{\sim}10^{9}{\rm M}_\odot$ and $V_{\rm vir} \sim 10$ kms^{-1} (e.g. Bullock & Boylan-Kolchin, 2017).

Simulations have shown that dark matter haloes exhibit radially dependent densities which can be approximated by a Navarro-Frenk-White (NFW) profile (Navarro et al., 1997),

$$\rho(r) = \frac{\rho_{\rm s}}{\frac{r}{r_{\rm s}}\left(1+\frac{r}{r_{\rm s}}\right)^2}, \tag{1.7}$$

where the free parameters are the scale density and scale radius, $\rho_{\rm s}$ and $r_{\rm s}$. A final halo property which I shall detail here is the concentration parameter c, defined as $c = R_{\rm vir}/r_{\rm s}$.

A prediction of ΛCDM is that smaller haloes will collapse earlier, and then go on to merge and form larger objects. $N-$body simulations indicate that the dense cores of the small, merging haloes survive the process (e.g. Ghigna et al., 1998; Klypin et al., 1999). They thus provide substructure to large dark matter haloes, termed 'subhaloes'. The galaxies residing in these subhaloes are referred to as 'satellites', while those associated with the main halo as a whole are named 'centrals'. ΛCDM predicts that dark matter haloes contain subhaloes with a mass function ${\rm d}n/{\rm M} \propto M^\alpha$, with $\alpha \simeq -1.8$ (Bullock & Boylan-Kolchin, 2017). While the cosmic web and dark matter haloes are inherently invisible, their structure and distribution can be traced by luminous galaxies, which

reside in the most massive haloes, acting like the summits of underwater mountain ranges that crest just above the ocean to hint at what lies beneath. As dark matter is the most abundant form of matter in the Universe, it largely dictates the Universe's LSS. Primordial gas generally follows the gravitational pull of the dark matter as it collapses from its initial nebulous structure to take the form of the cosmic web. Stars are born from a fraction of this gas and galaxies subsequently form, growing hierarchically as small galaxies residing in small dark matter haloes combine to form large galaxies. The most luminous galaxies are preferentially found in the densest regions of the cosmic web, the nodes at the intersections of filaments. While galaxies trace underlying dark matter distribution to a degree, they are thought to do so in a *biased* fashion, a concept I shall return to later (see Desjacques et al., 2018, for a recent review).

1.2.3 Dark energy

The inclusion of Λ in cosmological models was omitted for much of the 20th century after it was discovered that the Universe was expanding. As Λ's purpose was originally to enable a steady-state Universe solution to Einstein's field equations, it was deemed unnecessary. Early physical motivation for a positive Λ came as a means of explaining the observed brightness-redshift relation of quasars (e.g. Petrosian et al., 1967; Shklovsky, 1967; Kardashev, 1967). These observational results led Zel'dovich (1968) to propose that a quantum vacuum state, the lowest energy quantum state, could manifest with a non-zero energy density, which would result in cosmological constant-like behaviour. Cosmological simulations provided a novel tool, allowing researchers to test which models matched best with observations. Efstathiou et al. (1990) found that a spatially flat Universe with a dominant contribution to the energy density coming from CDM ($\Omega_0 \approx \Omega_{\rm CDM} = 1$) underestimated the level of structure on large scales ($\leq 10\ h^{-1}$Mpc). A low-density $\Omega_{\rm CDM} = 0.2$ model, however, agreed well with galaxy survey data on large scales, motivating an addition to the standard CDM model. Efstathiou et al. (1985) argued that a non-zero cosmological constant allows the retention of such successful aspects of the CDM model as a spatially flat Universe, while providing changes to the Universe's geometry useful in addressing separate phenomena, such as the large abundance of classes of high-redshift galaxies. White et al. (1993) presented further evidence for a $\Omega_{\rm m} < 1$ universe, finding the baryon content of the Coma cluster to be at least three times the value predicted by cosmic nucleosynthesis in a $\Omega_{\rm m} = 1$ universe. White et al. (1993) suggested that a lower matter density would resolve this discrepency, while the inclusion of a non-zero cosmological constant would 'rescue' the spatially flat universe required by the inflationary model.

Higher-resolution imaging of CMB anisotropies with the Cosmic Microwave Background Explorer (COBE) satellite appeared to allow for a CDM model with a non-zero Λ value (Smoot et al., 1992; Wright et al., 1992; Efstathiou et al., 1992; Kofman et al., 1993; Ostriker & Steinhardt, 1995). Riess et al. (1998b) and Perlmutter et al. (1999) provided evidence of a positive Λ by demonstrating that the expansion of the Universe is accelerating, rather than decelerating as would be expected purely as a result of gravitational attraction. This was achieved by using Type Ia supernovae (SNe Ia) as standard candles to provide robust measurements of distance to distant galaxies independent of their redshift. The distances were found to be farther than expected for a universe solely subject to the influence of gravitational attraction. Thus Λ became a founding principle of modern cosmology. ΛCDM posits that the acceleration of the Universe's expansion began ∼5 Gyr ago, before which time the expansion was decelerating due to the gravitationally attractive influence of matter. The transition between the two states occurred as the variation in the energy densities of matter and dark energy depend differently on the scale factor of the Universe. As the volume of the Universe doubles the density of matter is halved, while the energy density of dark energy is unchanged when described by a cosmological constant. An open area of research explores alternative formulations of the dark energy, introducing a time dependence to the equation of state (e.g. Chevallier & Polarski, 2001; Linder, 2003).

1.2.4 Challenges to ΛCDM

The current consensus model of cosmology is remarkably successful at predicting the structure of the Universe. Space-based telescopes have validated this model to a high degree of precision at high redshift (see e.g. Planck Collaboration et al., 2016), while the low redshift distribution of galaxies observed with large surveys such as SDSS have been found to match mock observations from simulations, as seen in Fig. 1.2 (Springel et al., 2006; Bower et al., 2006; Croton et al., 2006; De Lucia & Blaizot, 2007; Guo et al., 2011). The obvious pressing challenge facing ΛCDM is the lack of a direct detection of a dark matter particle within the CDM framework. Additionally, in the 'cosmological constant problem' there is a enormous disagreement (120 orders of magnitude) between the observationaly inferred value of the cosmological constant and the value of zero-point energy as posited by quantum field theory. In the 'small scale crisis', on length scales below ∼1 Mpc and masses smaller than $\sim 10^{11}$ $M_{\odot}$, ΛCDM faces a number of open challenges (see Bullock & Boylan-Kolchin, 2017, for a review). Possible solutions to these have been proposed within the theory, however extensions may be required. I briefly detail the most well-documented challenges in this section.

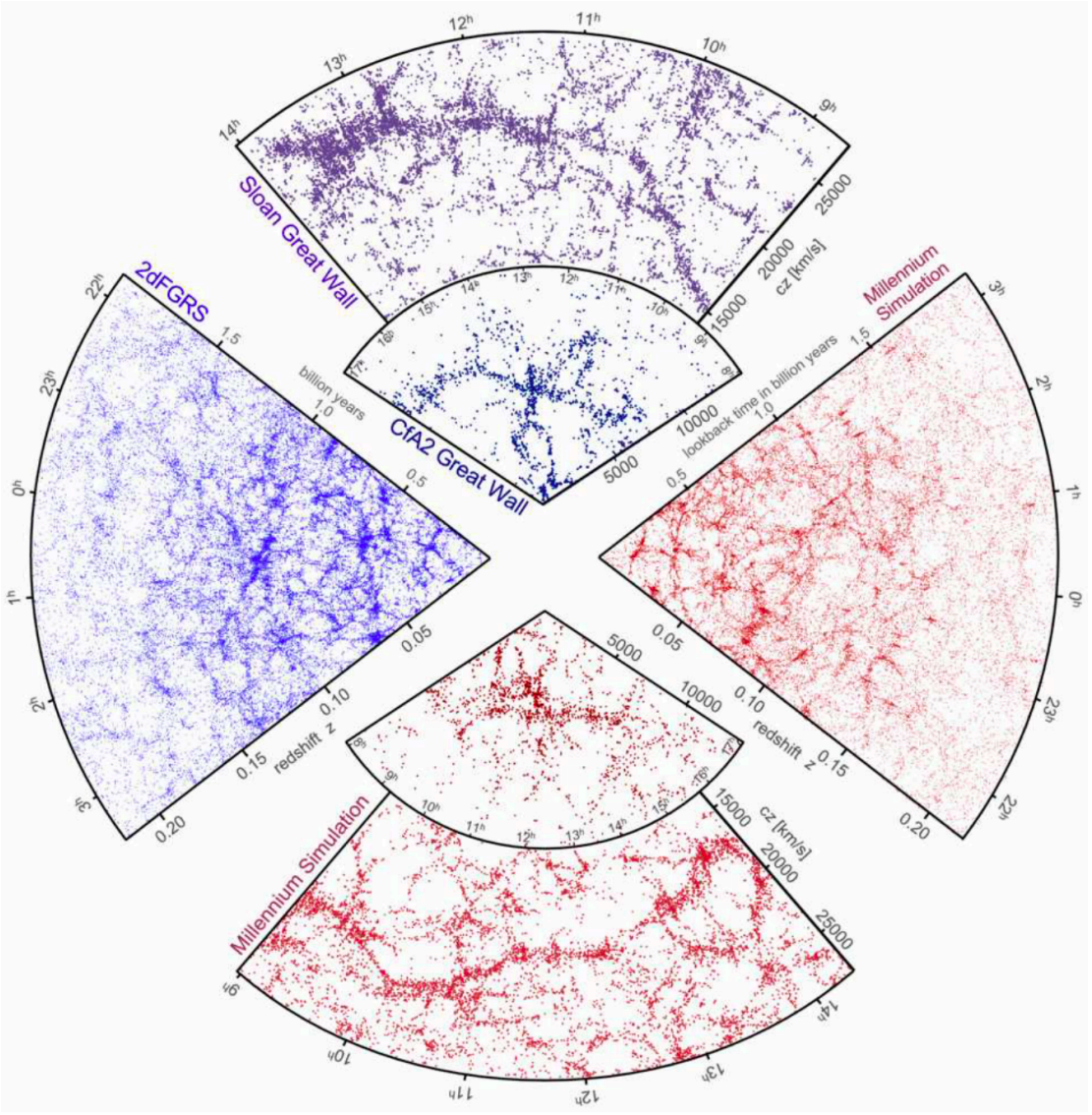

FIGURE 1.2: The similarity in the spatial distribution of galaxies in simulations (red points) and observations (blue points). Observed galaxies are taken from the spectroscopic redshift surveys SDSS, CfA2 and 2dFGRS. Mock galaxy surveys are created by running semi-analytic galaxy formation models in conjunction with the dark matter distribution of the MILLENIUM simulation. Figure reproduced from Springel et al. (2006)

- The Missing Satellites Problem (Boylan-Kolchin et al., 2012): Simulations predict that MW-mass haloes should contain thousands of subhaloes with masses that are theoretically large enough to allow molecular cooling, and thus contain galaxies. To date, this has not been supported in observation. The MW halo has been found to contain only ∼50 galaxies with stellar mass greater than ∼300 $M_\odot$ within the virial radius (Drlica-Wagner et al., 2015). It is hoped that future surveys will increase the number of known ultra-faint dwarf galaxies (e.g. Tollerud et al., 2008; Hargis et al., 2014), however it seems unlikely that this alone will resolve the tension. A possible resolution to this within ΛCDM relates to the efficiency of dark matter haloes in forming galaxies, with smaller mass haloes becoming increasingly unable to form stars, and below some threshold being unable to form galaxies entirely. For instance, it is possible that the UV background radiation relating to reionisation suppresses gas accretion for $M_{\rm vir} < 10^9$ $M_\odot$ (e.g. Efstathiou et al., 1992; Bullock et al., 2000; Benson et al., 2002a,b; Bovill & Ricotti, 2009; Sawala et al., 2016).

- The Cusp-Core Problem (Flores & Primack, 1994; Moore, 1994): Once N-body simulations were able to resolve the inner structure of CDM haloes, it was noted that there was a discrepancy between the density profiles within simulations and those inferred from observed rotation curves in low-mass galaxies. Simulations display 'cuspy' distributions, where the dark matter density continually increases with decreasing radius, while observed dwarf galaxies display flat central profiles. Full hydrodynamical simulations, which self-consistently include baryonic physics, have displayed that it is possible for baryonic feedback to flatten previously cuspy profiles and produce rotation curves similar to those observed (Mashchenko et al., 2008; Pontzen & Governato, 2012; Madau et al., 2014; Oñorbe et al., 2015; Read et al., 2016). Other possible solutions appeal to WDM (e.g. Lovell et al., 2012) and self-interacting dark matter (SIDM, e.g. Elbert et al., 2015) models, while some posit that the mass profiles inferred from kinematic data may be incorrect (Oman et al., 2015).

- Too-Big-To-Fail: A solution to the missing satellites problem is to assume that the observed MW satellite galaxies reside in the most massive subhaloes, and that smaller subhaloes contain either faint or no stars due to baryonic physics. Boylan-Kolchin et al. (2012) suggested a testable prediction, that the inferred masses of the MW satellite galaxies should be comparable with the most massive subhaloes of MW-mass haloes in ΛCDM-based simulations. It was found that while simulations contained subhaloes with mass comparable to Milky Way satellites, these weren't the most massive (e.g. Springel et al., 2008; Diemand et al., 2008). 'Too-big-to-fail' refers to the fact that these apparently dark subhaloes should be incapable of *not* hosting a galaxy. Another way of viewing this is that central densities of

the most massive subhaloes in simulated MW-mass haloes are higher than those observed in reality. This has also been observed for M31 and its satellites (Tollerud et al., 2014). The suggested baryonic alleviation of the cusp-core problem would in part simultaneously resolve too-big-to-fail by reducing the predicted density of simulated subhalo centres. Environmental influences such as tidal stripping (e.g. Zolotov et al., 2012) are often also proposed as means of resolving too-big-to-fail within $1-2\ R_{\rm vir}$ of the MW, while Benítez-Llambay et al. (2013) notes that ram pressure stripping from the cosmic web may also be significant.

One of the chief purposes of a cosmological simulation is that it enables the user to 'observe' the unobservable. Simulated dark matter is just as visible to an astronomer as simulated stars. A key technique for understanding the macro-behaviour of dark matter is to compare observations of the real, luminous Universe with stars and gas within simulations, and see what formulations of simulated dark matter provide the best match. Simulations also provide the means of testing degeneracies between the uncertain formulation of dark matter and the equally ill-constrained baryonic physics.

1.3 Galaxy formation in ΛCDM

ΛCDM provides the framework within which galaxy formation and evolution may be understood, stating that the energy density is partitioned between dark energy, dark matter and baryonic matter; from best-fit measurements of the CMB by Planck Collaboration et al. (2020), each contributes ∼4.96%, ∼26.5% and ∼68.5% respectively. Many physical processes are thought to influence galaxies over their lifetimes; a key challenge in astronomy is in determining their relative importance, and how they interlink, from the epoch recombination to produce the multitude of types that we can observe in the Universe today. I will briefly summarise the processes currently thought to be the most important in the initial creation and later regulation in the growth of galaxies.

1.3.1 Gas accretion and stellar mass assembly

The earliest galaxy formation models (Binney, 1977; Rees & Ostriker, 1977; Silk, 1977) posited that galaxies cannot form through gravitational collapse alone. The non-linear collapse of baryonic gas caused strong shocks, which heats the material and renders it incapable of forming stars without subsequent means for the hot gas to lose mechanical energy through such dissipative processes as radiative cooling. In this framework, regions of higher-density diffuse gas collapse under gravity and are subsequently shock-heated.

Radiative cooling follows, enabling the formation of cool molecular gas clouds, which further fragment and form stars in the centre of overdense regions.

In the bottom-up formulation, galaxies form hierarchically, with smaller galaxies merging over time to form larger galaxies. This takes place as follows: initial overdensities in the primordial density distribution of matter in the Universe survive only if they are of sufficient amplitude to survive the free-streaming of dark matter particles and the Hubble expansion. Prior to recombination, baryons are coupled to the radiation, preventing their collapse. Dark matter on the other hand is decoupled and therefore able to collapse. Following recombination, baryons and radiation decouple and the cosmic 'dark ages' begin, so named for the lack of luminous objects and the opacity of the now-neutral baryons. The already-collapsing dark matter regions are able to gravitationally attract baryons, which eventually form the first stars and protogalaxies after cooling in the potential wells of the dark matter halo. The intense UV light emitted from these nascent stars acts to re-ionise the neutral gas of the Universe. As stated previously, more massive galaxies arise over time as smaller galaxies (and their host haloes) merge, however low-mass haloes are far more numerous. This is reflected in the halo mass function (HMF), which describes the relative abundance of haloes as a function of their mass. The stellar mass of galaxies is positively correlated with the host halo mass, however haloes have a mass-dependent varying efficiency in forming stars. This results in the galaxy stellar mass function (GSMF) not sharing the same profile as the HMF, nor evolving in the same fashion.

The clustering of galaxies is set by a combination of the initial density perturbations, the process of galaxy-merging (Press & Schechter, 1974), as well as baryonic processes. The inclusion of a gravity-only dark matter component enabled an improvement in the realism of models. White & Rees (1978) employed a 4:1 ratio of dark matter to gas. Their model demonstrated the simultaneous virialisation of dark matter into a halo, the cooling of gas via radiative processes within a halo's gravitational potential well, and the subsequent formation of stars in the central regions. A reasonable approximation of the galaxy luminosity function was produced. This model was developed over years to predict varied properties of haloes and galaxies (White & Frenk, 1991), such as the mass- and time-dependent star formation rates (SFR) of galaxies, as well as the abundance and structure of their host dark matter haloes. Dark matter has hence become an requisite component in subsequent galaxy formation models.

The gas fuelling star formation in galaxies resides in a region known as the interstellar medium (ISM). This gas is continually accreted from the intergalactic medium (IGM) via 'cold' and 'hot' modes. The former relates to the filamentary accretion of cold gas directly onto a galaxy. Star formation from such gas is efficient as the cooling time is

short relative to the dynamical time, and the growth of the baryonic component closely tracks that of the dark matter halo (e.g. Katz et al., 2003; Kereš et al., 2005). The latter mode relates to accreted gas which has been shock heated to the virial temperature of the halo and cannot cool quickly. Regions of sufficiently dense hot gas are able to cool via radiative processes and form stars. While the cold mode dominates gas accretion across cosmic time, the hot mode becomes significant for high mass systems at late times (e.g. Birnboim & Dekel, 2003; Kereš et al., 2009; van de Voort et al., 2011).

Within the ISM, the molecular gas fuelling star formation is arranged in giant molecular clouds (GMCs). GMCs display an inhomogeneous substructure of sheets, filaments, cores and bubbles (Williams et al., 2000). Stars form within the dense cores when the pressure of gas is no longer sufficient to balance gravity, a phenomenon known as a Jeans instability (Jeans, 1902). The stellar population that forms this collapse can be described by an initial mass function (IMF), which quantifies the relative abundances of stars of given mass (Salpeter, 1955; Chabrier, 2003). Few massive ($\sim$100 $M_\odot$) and many low mass ($\sim$1 $M_\odot$) stars form. The more massive a star, the shorter its lifespan. The massive stars evolve rapidly over the order of a few million years, forming elements heavier than hydrogen through nuclear fusion and dispersing them through stellar winds and core-collapse (Type II) supernova, a process known as 'enrichment'. The primary pollutant arising from this stellar population are α-elements. Lower-mass stars survive on the main sequence for billions of years, eventually reaching the the asymptotic giant branch (AGB) phase, whereupon they drive stellar winds which chemically enrich the ISM (Wiersma et al., 2009b, their Fig. 2). The degenerate remnants of massive stars, white dwarfs, can contribute to the iron enrichment of the ISM following SNe Ia, as well as other elements such as carbon, nitrogen and silicon. Comparing the ratio of α-elements to iron ([α/Fe]) with the iron abundance ([Fe/H]) is a popular diagnostic in studies investigating the origin of stars in the Galaxy (e.g. Fuhrmann, 1998; Bensby et al., 2003; Anders et al., 2014; Mackereth et al., 2018).

The SFR of a galaxy is directly related to the surface density of gas in the interstellar medium through the empirical Kennicutt-Schmidt relation (Kennicutt, 1998). While the SFR of an individual galaxy may be highly variable with time, the SFR density of the Universe as a whole is observed to have peaked at $z \sim 2$ (Madau et al., 1998). Star formation reduces, or ceases, through a process known as quenching. Actively star forming galaxies in the local Universe are characterised by an instrinsically blue colour, resulting from presence of young, massive stars. Quenched galaxies are redder, as the young stars have long since been removed from the stellar population. The observed population of galaxies displays strong bimodality when regarded by their colour, roughly separating into the 'blue cloud' and 'red sequence'. This is most commonly presented in terms of their $u - r$ colour as a function of stellar mass (e.g. Baldry et al., 2004,

2012; Schawinski et al., 2014). The bimodal populations are separated by an apparently transitory population of galaxies residing in a region of the parameter space termed the 'green valley'.

The means by which star formation is quenched is thought to result from a number of phenomena which act to physically remove the gas reservoir fuelling the process, or otherwise render it unsuitable. The most simple of these is the conversion of a finite quantity of molecular gas into stars; unless the gas is re-supplied the star formation will eventually cease (Larson et al., 1980). The environment surrounding a galaxy may also act to remove the reservoir through a process known as ram pressure stripping (Gunn & Gott, 1972; Poggianti et al., 2017). This is particularly evident in the dense regions of galaxy clusters, which are permeated by a hot, X-ray emitting gas termed the intracluster medium. The cold ISM of a star-forming galaxy falling into a cluster will in effect experience the hot gas as a wind, which if sufficiently strong can drive a complete evacuation. The integrated SFR history of a galaxy has an impact on its observed galaxy properties, such as the metallicity and colour, as such many studies have found a link between these properties with environmental density (e.g. Hashimoto et al., 1998; Lewis et al., 2002; Blanton et al., 2003; Weinmann et al., 2006; Burton et al., 2013). Environment-dependent quenching processes are particularly evident in dense regions of the cosmos, such as galaxy clusters, however they have also been theorised to act in less dense regions of the LSS, such as the walls and filaments thought to frame voids (e.g. Winkel et al., 2021). While it is true that environment appears to play a role in quenching galaxies, massive galaxies ($M_\star > 2 \times 10^{10}$ $M_\odot$) are found to quench regardless of their environment, as is seemingly necessary from the point of view of the GSMF (Wetzel et al., 2012, 2013; Peng et al., 2015; Davies et al., 2019a). This suggests an internal mechanism by which a galaxy becomes less efficient at forming stars with increased mass. These are known as feedback processes, energetic events which can expel the gas reservoir by driving strong galaxy-scale winds. In the following subsection I will briefly relate the two most important of these: stellar and active galactic nuclei (AGN) feedback. Other mechanisms are thought to also play a role in producing the observed quenched-fraction of galaxies, including either gas-stripping or rapid gas consumption following galaxy-galaxy mergers (Mihos & Hernquist, 1996), and background ionising UV radiation.

1.3.2 Galaxy feedback

Figure 1.3 displays the stellar mass - halo mass relation constructed from subhalo abundance matching (SHAM) at $z = 0.1$, reproduced from Behroozi et al. (2019). Here we

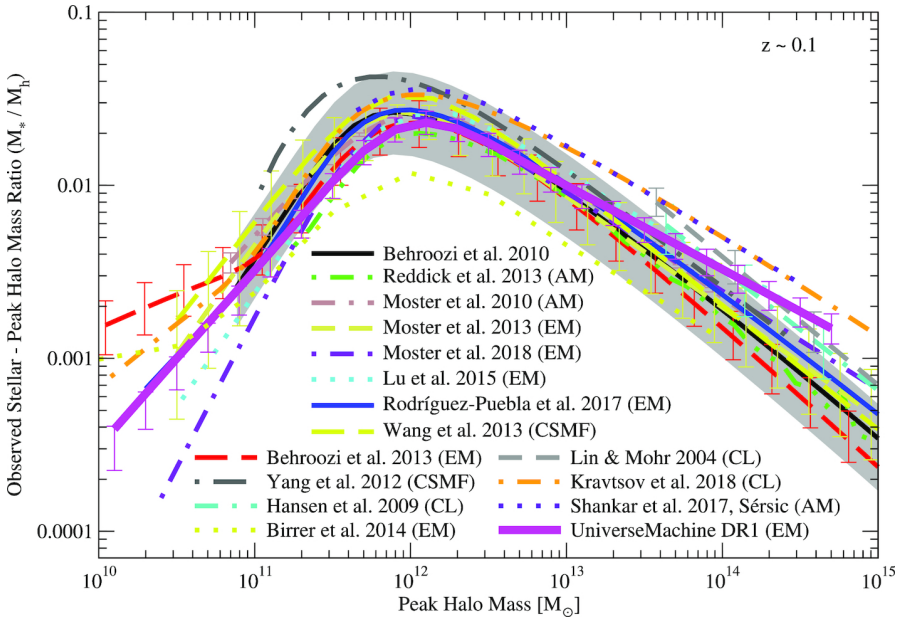

FIGURE 1.3: The median observed stellar mass - halo mass relation at $z \sim 0.1$. The figure displays the stellar-halo mass ratio as a function of halo mass. Star formation efficiency peaks within haloes of mass $\sim 10^{12}$ $M_\odot$. Several results from different labelled studies are presented, applying such techniques based on abundance matching (AM), empirical modelling (EM), conditional stellar mass function (CSMF) modelling, and X-ray measurements of cluster mass (CL). Figure reproduced from Behroozi et al. (2019).

see that galaxies residing in haloes of 10^{12} $M_\odot$ are the most efficient at forming stellar mass, while both below and above the point galaxies grow increasingly inefficient. It is thought that stellar feedback is the dominant process regulating galaxy growth $M_\mathrm{h} < 10^{12}$ $M_\odot$ haloes, while AGN feedback dominates for $M_\mathrm{h} > 10^{12}$ $M_\odot$ haloes. In the early Universe star formation was regulated by the ionising UV radiation emitted by the first stars, which in ionising gas clouds may have acted to prevent small, nascent haloes from retaining their gas (Bullock et al., 2000).

Stellar feedback relates to the energetic Type II supernovae occurring within regions containing young stellar populations. These highly energetic events ($\sim 10^{51}$ erg per event) deposit energy into the surrounding molecular gas clouds, heating them and driving winds. Enough of these supernovae events acting in unison acts to remove the gas reservoir fuelling star formation, thereby lowering the SFR. As the rate of supernovae is itself directly proportional to the SFR, stellar feedback is described as a self-regulating process. As M_h increases, the gravitational potential well of the halo deepens, impeding the removal of the gas. In part by this mechanism, stellar mass assembly efficiency increases with halo mass for $M_\mathrm{h} < 10^{12}$ $M_\odot$. Stellar feedback additionally decreases in efficiency as halo mass increases, up to approximately Milky Way-mass haloes. This is due to an increase in the characteristic gas density and gas metallicty. The former occurs as the ram pressure experienced by feedback-driven winds is proportional to the density

of the medium ($P_{\rm ram} \sim \rho v_{\rm wind}^2$), which results in the retardation of outflows for gas-rich systems. The latter factor relates to radiative cooling losses, which is proportional to the metallicity ($T_{\rm cool} \sim n_{\rm H}^2 Z$), thus heated gas is able to efficiently cool and become capable of star formation. Stellar feedback plays a key role in producing the correct number of low-mass ($< M_\star$) galaxies in simulations (e.g. Dekel & Silk, 1986; Katz et al., 1996; Springel & Hernquist, 2003; Oppenheimer & Davé, 2008; Oppenheimer et al., 2010; Schaye et al., 2010, 2015). Physical evidence for stellar feedback comes includes observations of high-velocity gas outflows (>100 kms^{-1}) produced by star forming galaxies (e.g. Martin et al., 2012; Rubin et al., 2014; Nielsen et al., 2020).

AGN feedback is thought to regulate star formation in high mass galaxies. Supermassive black holes (SMBH) reside in the centres of most, if not all, galaxies (e.g. Genzel et al. (1997); Kormendy & Ho (2013); Event Horizon Telescope Collaboration et al. (2019)). Nearby gas falls towards the SMBH and a disc of accreting material forms. These are regions of high friction, capable of efficient conversion of mass into energy. This energy is radiated out into the galaxy, capable of driving large gas outflows and quenching star formation (Silk & Rees, 1998; Kauffmann & Haehnelt, 2000; Di Matteo et al., 2005). AGN-induced outflows are observed at both high and low redshifts (e.g. Rupke & Veilleux, 2011; Maiolino et al., 2012; Harrison et al., 2014; Cicone et al., 2015, 2016). AGN feedback is thought to become important due to the growing inefficiency of stellar feedback in quenching star formation as $M_{\rm h}$ increases; cold gas accumulates in the central regions of galaxies and SMBHs are able to form/grow rapidly (e.g. Bower et al., 2006; Croton et al., 2006). There is therefore naturally a transitional halo mass at which point stellar mass assembly is most efficient, where stellar feedback is increasingly poor at driving outflows but before AGN feedback becomes the dominant regulation mechanism. AGN feedback is an important component in contemporary cosmological simulations, playing an important role in shaping the high mass end of the GSMF, driving cosmic 'downsizing' (e.g. Cowie et al., 1996), and governing the structure of the intragroup and intracluster media.

1.3.3 Morphology

Investigation into the observed diversity in morphology of galaxy types has a rich history, most famously represented in the 'tuning fork' classification which partitions galaxies roughly into quasi-spherical 'elliptical' (or early-type) galaxies, and flattened 'spirals' (late-type) (Hubble, 1926; de Vaucouleurs, 1959). Ellipticals populate one half of the classical tuning fork, while spirals are partitioned into two subgroups depending on whether they exhibit a central bar feature. Galaxies not consistent with an elliptical or spiral appearance are classified as 'irregular', their shapes possibly derived from ongoing

merger events or tidal torques. The early- and late-type naming convention persists to this day, however it is based on the outdated belief that ellipticals, being morphologically simple, would form earlier while spirals, as a more complex and apparently further evolved form of structure, would form later. It is now thought the opposite is true, with a typical elliptical galaxy forming from the merger of two spiral galaxies of similar mass, while spiral galaxies are thought to form and assemble stellar mass primarily through the gradual accretion of gas and angular momentum, while experiencing merging events with comparably smaller galaxies. Distinct satellite accretion events in the Milky Way's history have been suggested by various studies through the identification of distinct populations of stars in phase space, such as the Gaia-Enceladus/Sausage system (Belokurov et al., 2018; Haywood et al., 2018; Helmi et al., 2018; Mackereth et al., 2019), Sequoia (Myeong et al., 2019), the Kraken (Kruijssen et al., 2019), Thamnos 1 and 2 (Koppelman et al., 2019), and Heracles (Horta et al., 2021). It is believed that in four-to-five billion years, the Milky Way and Andromeda will collide in a major-merger event, producing an elliptical galaxy often named *Milkdromeda* (Nagamine & Loeb, 2003; Loeb & Cox, 2008; Darling, 2011; van der Marel et al., 2012; Sohn et al., 2012).

Separating galaxies into spirals and ellipticals, one finds that the two populations display drastically different properties. Spirals tend to be of low and intermediate mass, while the high-mass end of the GSMF is predominantly populated by ellipticals. Spirals are generally blue in appearance, indicative of ongoing star formation. This is fuelled by the continuous supply of gas via accretion, or the stripping of gas from local satellite galaxies during interaction or merger events (Sancisi et al., 2008). Spiral galaxies are characterised by a flattened, disc-like morphology. Star formation occurs predominantly in the spiral 'arms', gravitationally unstable regions capable of initiating the collapse of cold gas into star-forming clumps. Observing a spiral galaxy in some wavelength that traces the star-forming gas (e.g. the Hα emission line), one finds the ISM is flatter in morphology than the stellar disc as a whole. Young blue stars are born in the ISM, giving spirals their characteristic blue, armed appearance. Older stars are found throughout the disc and the central bulge.

Spiral galaxies also contain a stellar halo, where exclusively old stars are found. The orbits of these stars are more irregular than those found in the disc, and are hypothesised to be the wreckage of previous minor mergers or tidal interactions with dwarf galaxies. Coherent streams of stars from individual disrupted satellites are observed in the Milky Way's stellar halo (e.g. Saggitarius Stream Lynden-Bell & Lynden-Bell, 1995; Newberg et al., 2002; Majewski et al., 2003; Belokurov et al., 2006). Simulations have suggested a dual stellar halo, comprised of inner and outer regions primarily containing stars formed in and ex situ respectively (McCarthy et al., 2012). In this framework, in situ halo stars are removed from the thin disc through dynamical heating, likely associated with

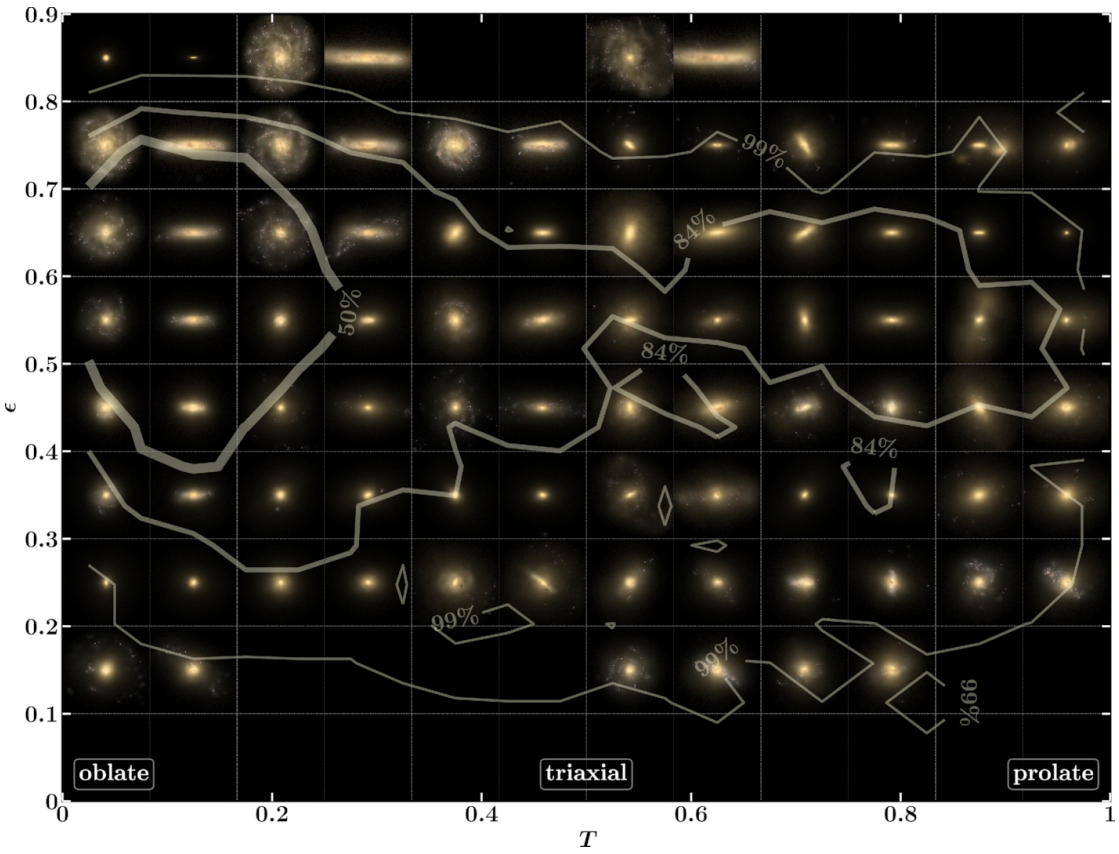

FIGURE 1.4: The appearance of galaxies with a given morphology in the EAGLE suite of simulations, as measured by the triaxiality, T, and flattening, ϵ shape parameters. Images are presented as a face- and edge-on pair for a representative galaxy. The overlaid contours indicate the relative frequency of occurrence for a given $T-\epsilon$ combination. Galaxies are most commonly high-ϵ and low-T. Figure reproduced from Thob et al. (2019).

the accretion of satellites. Observational evidence of the dual stellar halo has yet to be confirmed (Beers et al., 2012; Schönrich et al., 2014).

As most stars in spirals are seen to be orbiting the galactic centre in coherent motions, they are considered 'rotation-supported'. Elliptical galaxies are red in appearance as they do not contain the young and hot blue stars associated ongoing star formation, for which reason they are termed 'red-and-dead'. Star formation in these galaxies ceases following the depletion of their gas reservoirs during the post-merger stage of their formation. In contrast to the heterogeneity of spirals, they display a homogeneous quasi-spherical (ellipsoidal) morphology. The orbits of stars in elliptical galaxies do not take place in a common plane, as is mostly the case in spirals, rather their orientations are seemingly random. This has led to ellipticals being termed 'dispersion-supported'.

In Thob et al. (2019) and other hydrodynamical simulation-based studies of galaxy morphology (e.g. Bett, 2012; Tenneti et al., 2014; Velliscig et al., 2015a; Pillepich et al., 2019), shape is determined by finding the best-fitting 3D ellipsoid to the stars (or another

matter choice) within some aperture. This ellipsoid is described by three orthogonal axes, named in order of increasing lengh as the minor, intermediate and major. Morphology can be quantified in terms of various ratios of the lengths of these axes. Thob et al. (2019) defines the flattening parameter ϵ as the ratio of the minor and major axis lengths subtracted from one. For perfectly spherical galaxies $\epsilon = 0$, and for increasingly flattened galaxies $\epsilon \to 1$. The triaxiality parameter, T, combines the three axis lengths into a single measure, where low (high) values correspond to an oblate (prolate) structure. Figure 1.4 displays the typical morphologies of central galaxies in the EAGLE simulation suite, reproduced from Thob et al. (2019). For bins in $\epsilon - T$ parameter space, images of representative galaxies are presented in face- and edge-on orientations. Overlaid contours represent the frequency of occurrence of galaxies in terms of their morphology. Blue, star forming spiral galaxies are preferentially described by low ϵ and high T, indicative of a disc-like structure. Quiescent and red elliptical galaxies are found in the low-ϵ region, indicating an increasingly spherical structure. As noted by Thob et al. (2019), asymmetric galaxies in the prolate regime occasionally exhibit a blue colour. Trayford et al. (2016) states that interactions between a quiescent galaxy and a neighbouring galaxy can induce a prolate morphology and trigger star formation in the former ('rejuvenation', see Robertson et al., 2006).

Mass is the main predictor of galaxy morphology, however a secondary dependence on environment has been found. Dressler (1980) demonstrated that galaxy morphology is a function of projected galaxy density, with ellipticals (spirals) located in more (less) dense environments. As mentioned previously, dense environments such as galaxy clusters are capable of quenching star formation in infalling galaxies through ram pressure stripping. Nuza et al. (2014) demonstrated in N-body simulations that elliptical galaxies preferentially reside in the clusters over less-dense regions of the cosmic web, while the reverse is true for spirals. Some research suggests that other features of the cosmic web (e.g. filaments) are capable of directly influencing galaxy morphology (e.g. Pichon et al., 2016).

1.4 Weak lensing as a study of large scale structure

Various observational probes exist that enable the investigation of the Universe's properties, as well as the constraining of parameters that describe various cosmological models. In this section I will predominantly discuss weak gravitational lensing, however first for context I will mention other complementary probes.

- **Cosmic Microwave Background (CMB)**: As discussed in Section 1.1, the CMB originates from the last scattering surface, when photons were first able to

propagate freely through the newly transparent Universe at $z \sim 1100$. As these photons have travelled through the expanding cosmos, they have been redshifted to microwave wavelengths with a characteristic temperature of $T_{\rm CMB} = 2.725$ K. The discovery that the CMB behaves as a black body ran counter to the steady-state theory (Penzias & Wilson, 1965; Peebles et al., 1991). Subsequent measurements of the CMB found anisotropies in the temperature of the last scattering surface on the order of $\Delta T/T \sim 10^{-5}$, indicating the existence of perturbations in the plasma (COsmic Background Explorer satellite (COBE), (Smoot et al., 1992); Wilkinson Microwave Anisotropy Probe (WMAP), (Hinshaw et al., 2013); Planck (Planck Collaboration et al., 2014a)). These perturbations are the source of the observed distribution of matter in the present-day Universe. Measurements of CMB anisotropies provide constraints on cosmological parameters, as the wavelength and amplitude of the acoustic peaks in the CMB power spectrum may be compared with expected values from models such as ΛCDM. As an example, $\Omega_{\rm b}h^2$ is determined via the ratio of the first and second acoustic peaks.

- **Type Ia Supernovae (SNe Ia)**: White dwarfs are the remnants of stellar cores from stars with insufficient mass to form neutron stars or black holes at the end of their life cycle. Fusion reactions no longer occur within white dwarfs, and it is only the electron degeneracy pressure that prevents further gravitational collapse. The Chandrasekhar limit ($\sim$1.44 $M_\odot$) sets the maximum mass for which a white dwarf remains supported by this pressure. SNe Ia occur when a white dwarf in a stellar binary pair is able to accrete mass from its partner and so exceed the Chandrasekhar limit, initiating carbon fusion and triggering a runaway reaction. Due to this fixed critical mass limit, these supernovae produce predictable peak luminosities. They are therefore used as standard candles, as the distance to them may be accurately calculated via their known intrinsic luminosity and the observed flux. As mentioned previously, evidence for dark energy arose from measurements of SNe Ia. Riess et al. (1998a) and Perlmutter et al. (1999) computed the luminosity distances for SNe Ia at $0.18 \leq z \leq 0.83$, which were found to differ from those expected for a Universe without dark energy. The next generation of surveys aim to increase the depth (DES Bernstein et al., 2012) and quantity (LSST Science Collaboration et al., 2009) of SNe Ia observations, enabling cosmologists to further constrain the expansion history of the Universe. Another possible mechanism for triggering a SNe Ia is the merger of two white dwarfs, in which case the Chandrasekhar limit is instantaneously exceeded. This has raised questions as to the use of SNe Ia as standard candles.

- **Baryon Acoustic Oscillations (BAOs)**: As SNe Ia are used as standard candles, BAOs are used as standard rulers. Prior to decoupling, the Universe was

comprised of a primordial plasma through which acoustic density waves were able to propagate. Overdense regions in this plasma attracted surrounding material through gravity, which was counteracted by the outward pressure resulting from photon-matter interactions. This caused oscillations in the density field, resulting in spherical sound waves of the coupled baryons and photons propagating outwards, away from the overdensity. Dark matter interacts only gravitationally, and so remains at the site of the overdensity. Following decoupling, the outward pressure ceased and the shell radius became frozen at a fixed comoving length. While the radiation diffused, the baryonic remnant of the shell persisted, representing an overdensity which influences the eventual clustering of galaxies. Specifically, one finds an excess of galaxy pairs separated by the 'sound horizon' (Eisenstein et al., 2005; Percival et al., 2007), the fixed co-moving distance between the location of the initial density peak and the crest of the first oscillation. As standard rulers, measuring BAOs at different redshifts provides a measure of the Hubble parameter and the angular diameter distance.

- **Redshift Space Distortion (RSD)**: The observed redshift of galaxies is a sum of their recessional velocity due to the Hubble expansion and their peculiar velocity due to gravitational instabilities in their local environment. An example of this is within collapsing galaxy clusters, where all galaxies are falling towards the cluster centre. Galaxies closer to us along the line-of-sight will be travelling away from us in comoving coordinates, while galaxies at the far side will be travelling towards us. This causes a compression of the galaxies in redshift space, a phenomenon known as the Kaiser effect, and occurs in large-scale overdensities whose growth occurs in the linear regime. The 'Fingers-of-God' effect see galaxies elongated in redshift space due to their high peculiar velocities in highly non-linear overdensities. Information relating to the peculiar velocities of galaxies within clusters is extractable through RSD measurements, and as these are caused by gravitational instabilities, general relativity is able to provide testable predictions (e.g. Peacock et al., 2001; Hawkins et al., 2003; Tegmark et al., 2006; Reid et al., 2012; Beutler et al., 2014).

- **Galaxy Clusters**: Galaxy clusters are the most massive gravitationally bound objects in the Universe, with highest baryon fraction of all haloes (Kravtsov & Borgani, 2012). They result from the largest fluctuations in the primordial density field and therefore represent sensitive tracers of the underlying matter distribution and cosmology (Allen et al., 2011). As an example, the number of clusters observed as a function of mass and redshift is sensitive to $\Omega_{\rm m}$ and σ_8.

1.4.1 Gravitational lensing introduction

Photons emitted from distant galaxies propagate through the Universe along a null geodesic, following the shortest route through spacetime from source to observer. A homogeneous topology of spacetime is not predicted by general relativity, rather it is curved in the presence of massive bodies (Einstein, 1916). The mass-induced curvature of spacetime results in the deflection of photons in the presence of massive objects, as was first seen for photons passing close to the surface of the Sun (Dyson et al., 1920). This phenomenon is called gravitational lensing, as it has obvious analogues with optical physics. The massive object distorting spacetime and altering the path of the photons is termed the *lens*. In the scenario described, where the extent of the lens' mass distribution is small compared to the distances between source, lens and observer, the thin lens approximation may be applied. This treats the mass distribution as residing within a plane, and the deflection of a photon taking place only within this plane. The deflection angle, α, is then determined by two parameters, the mass M of the lens and the impact parameter (the perpendicular separation of the photon and the centre of the potential well) b, as

$$\alpha = \frac{4GM}{bc^2}. \tag{1.8}$$

In practice, when observing a *lensed* galaxy we capture many photons. The summation of the deflections experienced by individual photons results in the galaxy's image being distorted from its true appearance, much as an object will appear distorted when held underneath a disturbed body of water. Evidence of non-solar gravitational lensing occurred with the observation of a quasar whose light had been gravitationally lensed by a foreground galaxy cluster, resulting in two images of the same quasar being visible (Walsh et al., 1979; Young et al., 1980).

We will briefly describe the strong regime of gravitational lensing, before discussing in more depth weak gravitational lensing as a probe of LSS.

1.4.2 Strong gravitational lensing

As might be inferred from equation 1.8, larger distortions of a galaxy's image result from situations where the source, lens and observer are well aligned (resulting in small b), and where the lens is a massive object. This is revealed most dramatically in the regime of *strong gravitational lensing*, where distant galaxies appear as great arcs, or even complete rings, around a lensing galaxy clusters in the foreground. An illustration

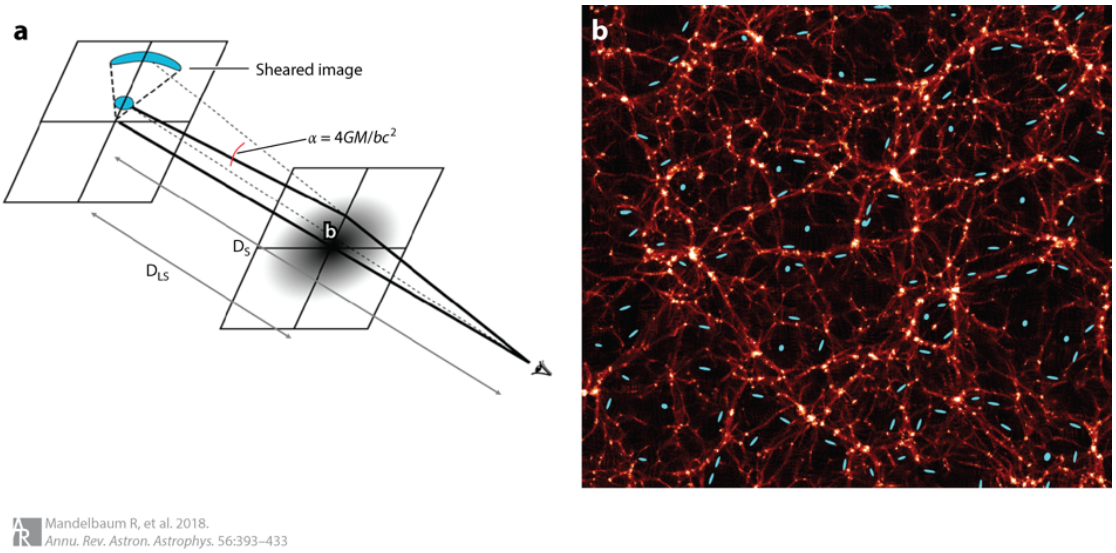

FIGURE 1.5: An illustrative depiction of the weak gravitational lensing effect. The diagram in the left panel shows the impact of shear distortion on the apparent image of a distant galaxy at position **a**, caused by a lens at position **b**. The right panel displays the cosmic web in a simulation, which induces a correlation in the observed ellipticites of background galaxies (blue ellipses). Figure reproduced from Mandelbaum (2018), which in turn credits LSST Science Collaboration et al. (2009) for the left panel and Canada-France-Hawaii Telescope for the right.

of this effect can be seen in the left panel of Fig 1.5. Predictions of the gravitational distortion of light arose as a consequence of the theory of general relativity, however the first detection of 'Einstein rings', the distortion of background galaxies into a near-complete ring around a lens, only took place much later in the century (e.g. Hewitt et al., 1988; King et al., 1998; Sluse et al., 2003). Strong gravitational lensing increases the quantity of photons from a distant galaxy that reach the Earth, enabling the study of objects that would otherwise be too dim to be observed. Strong gravitational lensing can also inform on the halo substructure of the lensing system. An example of this is the lensing system B1938+666, first discovered by King et al. (1998). The lens in this case is an elliptical galaxy at redshift $z = 0.881$, while the source is a bright infrared galaxy at $z = 2.059$. The brightness of the Einstein ring enabled precise measurements of the fluctuations in surface density, which led to the construction of an accurate gravitational model of the lens system. This revealed the presence of a dark satellite galaxy of mass $(1.9 \pm 0.1) \times 10^8$ $M_\odot$ (Vegetti et al., 2012), consistent with predictions from ΛCDM simulations (e.g. Springel et al., 2008).

1.4.3 Weak gravitational lensing

The *weak* regime of gravitational lensing occurs when the lensing effect results not in the striking arcs detailed above, but rather in minute changes to a galaxy's image, such

as in the position, shape, size and brightness. As a photon propagates throughout the Universe, it is continually deflected by the continuous matter distribution. Weak gravitational lensing can only be detected statistically, as the distortion in the shape of individual galaxies is much less than the dispersion in intrinsic sizes and shapes. In practice, weak gravitational lensing is measured as the coherent distortion in the observed shapes of distant galaxies in a given patch of sky. Modern galaxy surveys attempt to measure the weak lensing effect caused by the integrated matter distribution across the sky. Weak lensing caused by the LSS (i.e. the cosmic web) is known as the *cosmic shear*. As weak lensing measurements are sensitive to the geometry and evolution of the cosmic web, they offer a powerful means of testing many facets of cosmology, including the nature of dark matter and the growth of structure in the Universe (for a review of the use of weak lensing in cosmology see Kilbinger, 2015). The structure of the cosmic web is also sensitive to dark energy, which increasingly acts to suppress clustering as the Universe's expansion accelerates. Weak lensing is then a natural means of placing constraints on this enigmatic aspect of cosmology (e.g. Hu, 2002; Huterer, 2002; Peacock et al., 2006; Albrecht et al., 2006).

For cosmic shear, lensing occurs along the path of the photon due to the continuous mass distribution, rather than occurring once in a single plane. The total deflection angle is treated as the sum of deflections caused by individual point masses along the photon's trajectory. Weak lensing can be described as a linear mapping of coordinates between unlensed and lensed planes by the (inverse) amplification matrix, as:

$$\begin{bmatrix} x_u \\ y_u \end{bmatrix} = \begin{bmatrix} 1-\gamma_1-\kappa & -\gamma_2 \\ -\gamma_2 & 1-\gamma_1 \end{bmatrix} \begin{bmatrix} x_l \\ y_l \end{bmatrix}, \tag{1.9}$$

where the convergence, κ, controls the apparent size and brightness of the observed object, and the complex shear term, $\boldsymbol{\gamma} \equiv \gamma_1 + i\gamma_2 = \gamma \exp[2i\alpha_p]$, describes the stretching of a galaxy image at an angle α_p (see e.g. Bartelmann & Schneider, 2001). In the limit of weak gravitational lensing, $\kappa << 1$. Both the convergence and the complex shear are related to the local lensing potential.

As the intrinsic shapes of individual galaxies are not known, weak lensing studies proceed by measuring the shapes of many galaxies in a given match of sky and performing a statistical analysis of the ensemble. While galaxies are complex structures with radially varying morphology and surface brightness, their shapes in the field of weak lensing are treated as simple ellipses as illustrated in the right panel of Fig. 1.5. Galaxy shapes are characterised by the two-term *ellipticity*, a complex number containing information regarding the orientation and of the galaxy ellipse. The definition of galaxy ellipticity vector is given by

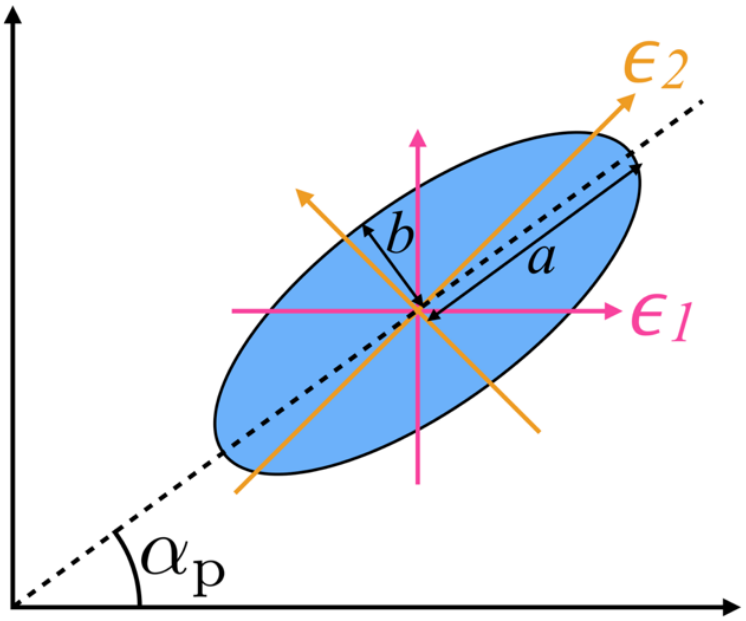

FIGURE 1.6: Schematic of the galaxy ellipticity measure given in equation 1.10. The shape of a galaxy at position angle α_p is approximated with an ellipse, whose axis lengths are given by a and b. The components of the complex ellipticity, ϵ_1 and ϵ_2, give the elongation relative to an arbitrary Cartesian reference frame, and at $\pm 45°$. Figure reproduced from Hillier (2020).

$$\epsilon = (\epsilon_1, \epsilon_2) = \frac{a-b}{a+b}(\cos 2\alpha_p, \sin 2\alpha_p), \tag{1.10}$$

where $a > b$ are the axis lengths, α_p is the position angle, ϵ_1 describes elongation and compression in the direction of the reference axis, and ϵ_2 describes the same but at $\pm 45°$ relative to the reference frame. The precise definition of ϵ varies in the literature, commonly differing from that given in equation 1.10 by replacing $(a-b)/(a+b)$ with $(a^2-b^2)/(a^2+b^2)$. This definition has also been called the polarisation (e.g. Blandford et al., 1991). Fig. 1.6 displays a schematic depicting the meaning of the parameters of equation 1.10.

In practice there are a number of approaches to measuring the ellipticity of a galaxy. These are broadly separable into moment-based methods and shape fitting algorithms, which aim to maximise the cosmological information by minimising induced biases from shape dispersion and measurement systematics. An example of the former is the Kaiser, Squires and Broadhurst method (KSB), which was popular in previous generation weak lensing surveys. Here the ellipticity is measured by calculating the quadrupole moments of the projected light distribution, which can be related to the ellipticity (Kaiser et al., 1995). A drawback of KSB is that it initially assumes a cirular point spread function (PSF), which requires a statistical correction (e.g. Narayan & Bartelmann, 1996). Shape

fitting methods take advantage of the fact that most galaxies are reasonably well described by a Sérsic profile (Trujillo et al., 2001), enabling the construction of a model based on morphology, orientation and surface brightness from which a best fit galaxy ellipticity may be extracted. Various means of finding the optimal parameters are in use, including IM3SHAPE (Zuntz et al., 2013) and LENSFIT (Miller et al., 2007), which employ maximum likelihood estimators and Bayesian methods respectively. Also in use is the 'shapelet' method (Refregier, 2003; Refregier & Bacon, 2003), which linearly decomposes the images of galaxies into basis functions describing shape.

For a set of measurements centred on a small patch of sky, galaxies are assumed to have been lensed to the same degree, i.e. have a constant amplification matrix. An approximation of the observed ellipticity of a given galaxy, $\boldsymbol{\epsilon}^{\mathrm{I}}$, can be given as

$$\boldsymbol{\epsilon}^{\mathrm{I}} \simeq \boldsymbol{\epsilon}^{\mathrm{S}} + \frac{\gamma}{1-\kappa}, \tag{1.11}$$

where $\boldsymbol{\epsilon}^{\mathrm{S}}$ is the intrinsic, source-plane ellipticity (Blandford et al., 1991). It is assumed that for a sufficiently large ensemble of galaxies the average source-plane ellipticity is zero (see Section 1.4.4 for further discussion). Recalling that $\kappa << 1$ in weak gravitational lensing, measuring the average ellipticity of galaxies is a direct measure of the cosmic shear, as the above equation reduces to

$$< \boldsymbol{\epsilon}^{\mathrm{I}} > \simeq \gamma. \tag{1.12}$$

This may be understood as the cosmic shear inducing an apparent alignment in the images of galaxies.

Cosmic shear measurements are a competitive cosmological probe, as being sensitive to the geometry of the LSS of the Universe they are able to inform on the form of the matter power spectrum. It measures the clustering of the LSS on the non-linear small scales ($<$ 1 Mpc), out to large, linear scales (100s of Mpc). Furthermore, by binning source galaxies by redshift, one is able to measure the evolution of the projected mass distribution with time (see e.g. Bartelmann & Schneider, 2001; Hoekstra & Jain, 2008; Kilbinger, 2015, for reviews). The first detection of cosmic shear took place in the year 2000 (Bacon et al., 2000; Kaiser et al., 2000; Van Waerbeke et al., 2000; Wittman et al., 2000), and the following decades have seen a considerable advancements in field, with dedicated ground- and space-based surveys coming online and providing an ever increasing quality and quantity of source galaxy images. The first workhorse weak lensing survey was the Canada France Hawaii Telescope Lensing Survey (CFHTLenS) (Benjamin et al., 2013; Erben et al., 2013; Heymans et al., 2013; Kilbinger et al., 2013; Kitching et al., 2014;

Miller et al., 2013), a deep survey with a relatively small sky coverage of 154 $\deg^2$. In current usage are the following 'Stage III' surveys: the Hyper Supreme-Cam survey (HSC; Aihara et al., 2018a); the Kilo-Degree Survey (KiDS; Kuijken et al., 2015); and the Dark Energy Survey (DES; e.g. Troxel et al., 2018; Amon et al., 2022). Cosmic shear measurements have proved competitive in constraining cosmological parameters (e.g. Hikage et al., 2019; Asgari et al., 2021), and are also well-suited to joint analyses with other measures based on galaxy positions and/or lensing, such as galaxy-galaxy lensing and galaxy clustering (e.g. Abbott et al., 2018; DES Collaboration et al., 2021). Joint analyses combining multiple independent probes enables the breaking of degeneracies in cosmological parameters, as well as the decreasing the influence of observational and astrophysical uncertainties. 'Stage IV' surveys such as the Vera C. Rubin Observatory's Legacy Survey of Space and Time (LSST; LSST Dark Energy Science Collaboration, 2012), *Euclid* (Laureijs et al., 2011), and the Nancy Grace Roman Space Telescope (Spergel et al., 2015), are set to further develop the field of optical weak lensing with full-sky coverage at increased depths. A key benefit of weak lensing as a cosmological tool is that it is a low-redshift measure, which can be compared with high-redshift probes such as the CMB to provide a robust test of ΛCDM.

Having introduced weak gravitational lensing as a cosmological probe, I will now describe the main observational and astrophysical systematic uncertainties involved.

1.4.4 Systematic uncertainties of weak gravitational lensing

Systematic uncertainties in cosmic shear measurements may be broadly separated into two classes: observational and theoretical. Observational systematics relate to uncertainties incurred in the measurement process, as the images of galaxies that are obtained are subject to pixelation and atmospheric blurring. As weak lensing analysis is conducted for many galaxies at a time, uncertainties also arise from measurements of their redshift distribution and shape. Theoretical systematics concern our uncertainty in the predictions of ΛCDM in the non-linear regime. In order to constrain cosmological parameters and distinguish between different cosmologies, predictions with ∼1% accuracy are required (e.g. Huterer & Takada, 2005). The main challenges arise from the uncertain impact of baryons on the matter power spectrum at small scales, and the intrinsic alignment of galaxies. In this section I will briefly describe a selection of significant systematic uncertainties in contemporary weak lensing measurements and means of mitigating them, with a particular focus on the intrinsic alignment of galaxies. For a more complete discussion see Mandelbaum (2018).

The point spread function: The PSF is caused by a combination of atmospheric, telescopic and equipment effects, and imposes a blurring effect on galaxy images. The significance for weak lensing is that the PSF will act to change the observed shape of a galaxy, which imposes a bias on measurements of the cosmic shear. The PSF is a challenge for all astronomical observations, however it is particularly relevant for weak lensing measurements as PSF sizes are comparable to the angular size of source galaxies. Additional complication arises from the fact that the PSF is anisotropic and non-deterministic, changing with the variation in atmospheric seeing conditions (e.g. Heymans et al., 2012). In optical studies stars provide the means of ascertaining the impact of the PSF on a point source at different positions across the sky. Interpolation is then required to estimate the PSF at a galaxy's position (Jain et al., 2006).

Redshift distribution errors: In weak lensing measurements, galaxies are observed as 2D images projected on the sky. A third dimension, the distance to the galaxy, may additionally be convolved if the galaxy's redshift is known. This enables tomographic cosmic shear analysis, namely the measurement of the cosmic shear signal as a function of redshift. The strength of this analysis is that the evolution of the matter power spectrum is sensitive to a potentially time-varying dark energy parameter, $w(t)$. Due to the faintness and number of source galaxies in weak lensing studies, obtaining spectroscopic measurements for individual galaxies is infeasible. As a result, redshifts are typically obtained photometrically. Any errors in the measurement of redshift will propagate through into the final cosmological parameter inference. This effect is compounded as uncertainty in galaxy redshift is also significant in attempts to mitigate the influence of galaxy intrinsic alignments (see below). Photometric redshift (photo-z) error is treated statistically, as the true redshift distribution of galaxies coarsely binned in photo-z is the primary measure of concern. The true galaxy redshift distribution is estimated by summing over the redshift probability distribution function, obtained with spectroscopic measurements (e.g. Benjamin et al., 2013). A lack of spectroscopic redshift measurements for a representative sample of galaxies at higher redshift places a limit on the depth of weak lensing surveys (e.g. Shirasaki & Yoshida, 2014).

The impact of baryons on the matter power spectrum: As the cosmic shear is used as a means of measuring the matter power spectrum, $P(k)$, it is potentially able to distinguish between various extensions to ΛCDM, each of which make different predictions for the form and amplitude of $P(k)$. On linear scales dominated by the physics of collisionless dark matter, precise predictions of $P(k)$ are possible. The non-linear baryonic physics of galaxy formation and evolution is thought to impact $P(k)$ on scale of dark matter haloes, which may lead to biases in cosmological parameter inference (e.g. Semboloni et al., 2011). Dark matter-only (DMO) N-body simulations are therefore ill-suited for making predictions of $P(k)$ on small scales. Hydrodynamical

simulations which sufficiently resolve the processes of galaxy formation and evolution, while being large enough so as to measure $P(k)$ on large scales, are required. The current generation of such simulations (e.g. EAGLE (Schaye et al., 2015; Crain et al., 2015) and IllustrisTNG (Springel et al., 2018)) meet these criteria, however predictions for the baryonic-induced suppression of $P(k)$ remain varied due to uncertainty in the physics of galaxy formation (van Daalen et al., 2020). One means of removing the uncertainty induced by baryonic physics is to only probe the power spectrum on linear scales, however this comes at the cost of losing information on the scales where cosmological models are at their most differentiable. Eifler et al. (2015) presented a principal component analysis (PCA) of the impact of baryons of $P(k)$ in hydrodynamical simulations. By excluding the four largest principal components, it was found that baryonic effects could be mitigated without having to resort to scale-dependent cuts. An alternative approach involves using the halo model to predict the mass-dependent 'halo-bloating' parameter and changes in halo concentration (Mead et al., 2015; Hildebrandt et al., 2017). This has been found to be reasonably successful in characterising $P(k)$ on small scales.

Intrinsic alignments: The elimination of $\boldsymbol{\epsilon}^{\mathrm{I}}$ between equations 1.11 and 1.12 is predicated on the cosmological principal, which manifests in this case as galaxies having no preferred orientation (i.e. $< \boldsymbol{\epsilon}^{\mathrm{I}} >= 0$). In practice this is not true, the shapes of galaxy images may be correlated for reasons other than coherent shearing (Croft & Metzler, 2000; Heavens et al., 2000; Lee & Pen, 2000, 2001; Catelan et al., 2001). The alignment of galaxies by astrophysical (rather than cosmological) means is known as intrinsic alignment. If not properly accounted for, the intrinsic alignment of galaxies can masquerade as a cosmic shear signal and thereby bias inferred cosmological parameters. The observed ellipticity of a galaxy can be defined as the sum of its true, source-plane ellipticity, and the induced cosmic shear as $\epsilon_i^{\mathrm{obs}} = \epsilon_i^{\mathrm{s}} + \gamma_i$. Following Kirk et al. (2015), the observed ellipticity correlation between galaxy pairs is given by

$$< \epsilon_i^{\mathrm{obs}} \epsilon_j^{\mathrm{obs}} >=< \gamma_i \gamma_j > + < \epsilon_i^{\mathrm{s}} \epsilon_j^{\mathrm{s}} > + < \gamma_i \epsilon_j^{\mathrm{s}} > + < \epsilon_i^{\mathrm{s}} \gamma_j >, \tag{1.13}$$

which may also be written as

$$< \epsilon_i^{\mathrm{obs}} \epsilon_j^{\mathrm{obs}} >= \mathrm{GG} + \mathrm{II} + \mathrm{GI} + \mathrm{IG}. \tag{1.14}$$

The term of interest in weak lensing is GG (Gravitational-Gravitational, $< \gamma_i \gamma_j >$), which measures the correlation between the shears incident on source galaxies i and j. The remaining terms are nuisance parameters when attempting to measure the cosmic shear, however they are of astrophysical interest. II (Intrinsic-Intrinsic, $< \epsilon_i^{\mathrm{s}} \epsilon_j^{\mathrm{s}} >$) relates to the correlation in the intrinsic shapes of a galaxy pair. Source galaxies experiencing

a common tidal gravitational field caused by the LSS are likely to be preferentially aligned. This scenario is depicted in the lower-left panels of Fig. 1.7. Satellite galaxies are found to be preferentially located along the major axis of their host halo in both observation (Brainerd, 2005; Yang et al., 2006; Wang & Kang, 2018) and in simulations (Libeskind et al., 2005; Kang et al., 2005, 2007; Agustsson & Brainerd, 2006b; Wang et al., 2014), possibly due to the anisotropic accretion of galaxies along cosmic web filaments (Libeskind et al., 2011; Kang & Wang, 2015; Wang & Kang, 2018). Satellites are also observed to be oriented in the direction of their host central (Agustsson & Brainerd, 2006a). Applying a filament finding algorithm to SDSS DR12, Wang et al. (2020) discovered that the major axes of satellites are significantly correlated with the direction of the spine of their closest cosmic filament. Intrinsic alignment is not merely a small scale effect; massive galaxy clusters have been found to be correlated on scales of $\sim 100h^{-1}$Mpc (Smargon et al., 2012; van Uitert & Joachimi, 2017; Xia et al., 2017). For a review of galaxy alignments in general, see Joachimi et al. (2015) and Kiessling et al. (2015). For a review on the impact of intrinsic galaxy alignments on weak gravitional lensing see (Troxel & Ishak, 2015).

The GI term in equation 1.14 (Gravitational-Intrinsic, $< \gamma_i \epsilon_j^{\rm s} >$), occurs when the two correlating galaxies are at different redshifts, and the lower redshift of the two is gravitationally influenced by some object that is simultaneously lensing the distant, high-redshift galaxy. This effect is illustrated in the upper-right panels of Fig. 1.7. The IG term (Intrinsic-Gravitational, $< \epsilon_i \gamma_j^{\rm s} >$) has the gravitationally attractive structure coincident with the high-redshift galaxy, however as it is then impossible for it to lens the lower redshift galaxy, the IG correlation is in practice nil.

The GG and II terms both produce positive correlations, as lensing produces a tangential shear, while gravitational attraction results in radial alignments. The GI terms produces a negative correlation, as a tangentially sheared galaxy is correlated with a radially aligned galaxy. Mitigation of the intrinsic alignment systematic is then an important consideration for cosmic shear studies (e.g. Singh & Mandelbaum, 2016). Dark matter haloes within the ΛCDM model are known to demonstrate intrinsic alignments (e.g. Schneider et al., 2012). Predicting the intrinsic alignment of the baryonic component is active area of research. Hydrodynamical simulations which self-consistently model the evolution of the baryonic and dark matter components of the Universe have been used to measure the intrinsic alignment of galaxies (e.g. Velliscig et al., 2015b; Tenneti et al., 2016; Chisari et al., 2017; Hilbert et al., 2017). Using the EAGLE and cosmo-Owls simulations, Velliscig et al. (2015b) finds a non-vanishing 3D alignment between both flattened and spherical galaxies, as well as for those residing within high- and low-mass subhaloes. Observational confirmation for the II correlation has been found at low redshift (e.g. Pen et al., 2000; Bernstein & Norberg, 2002; Brown et al., 2002; Hirata

et al., 2004) and for luminous red galaxies within large galaxy surveys (e.g. Okumura et al., 2009). This effect has been found to be smaller than has been found in N-body DMO simulations, indicating that galaxies are not perfectly aligned with their host haloes (e.g. Heymans et al., 2004; Mandelbaum et al., 2006). Alignments of blue, star-forming galaxies has yet to be robustly detected in observations, leading to these objects being the preferred targets of cosmic shear studies. Mitigation of the II term initially involved down-weighting or entirely removing galaxy pairs at low 3D separation (King & Schneider, 2002; Heymans & Heavens, 2003). The GI term has likewise been found in observation (Mandelbaum et al., 2006; Hirata et al., 2007), however its mitigation is a challenging, as two galaxies well-separated in redshift can display a significant anti-correlation (e.g. Hui & Zhang, 2008; Joachimi & Schneider, 2008).

Contemporary efforts to excise the intrinsic alignment signal typically involve parameterised models (e.g. Bridle & King, 2007) or self-calibration. The latter of these jointly analyses galaxy-galaxy, galaxy-shear and shear-shear correlations (Abbott et al., 2018; Joudaki et al., 2018; Yao et al., 2017), taking advantage of the fact that these have different redshift dependencies, allowing the marginalisation of the alignments. As an example of modelling, the Dark Energy Survey (DES) makes use of the Tidal Alignment and Tidal Torquing model (TATT, Blazek et al., 2019), which succeeded the non-linear alignment model (NLA) (e.g. Troxel et al., 2018; Asgari et al., 2021; Hildebrandt et al., 2020; Hamana et al., 2020). TATT is a non-linear perturbative prescription, modelling linear tidal alignments and quadratic tidal torquing, as well as source density weighting. Cosmological analysis marginalises over the five floating parameters of this model (Amon et al., 2022), which are given broad priors. More work is needed to provide informative priors to these models. For tests of intrinsic alignment mitigation for current and furture surveys, see Krause et al. (2016).

Amon et al. (2022) presented DES Year 3 cosmic shear measurements, using over 100 million source galaxies covering $4,143$ deg^2. The cosmic shear measurement obtained was the most statistically significant to date with a signal-to-noise ratio of 40. The primary cosmological parameter measured, $S_8 = \sigma_8/(\Omega/0.3)^{0.5} = 0.772^{+0.018}_{-0.017}$, was found to be statistically consistent with results from Planck, albeit with a 2.1σ offset. Amon et al. (2022) performed an analyses of the 19 systematic parameters that could limit cosmological constraining power (their Fig. 12). These were separated into observational and theoretical systematics, where the former relates to the calibration of redshift and shear measurements, and the latter concerns the gaps in the theoretical modelling, particularly understanding of non-linear processes, such as the impact of baryonic physics on the matter power spectrum and intrinsic alignments.

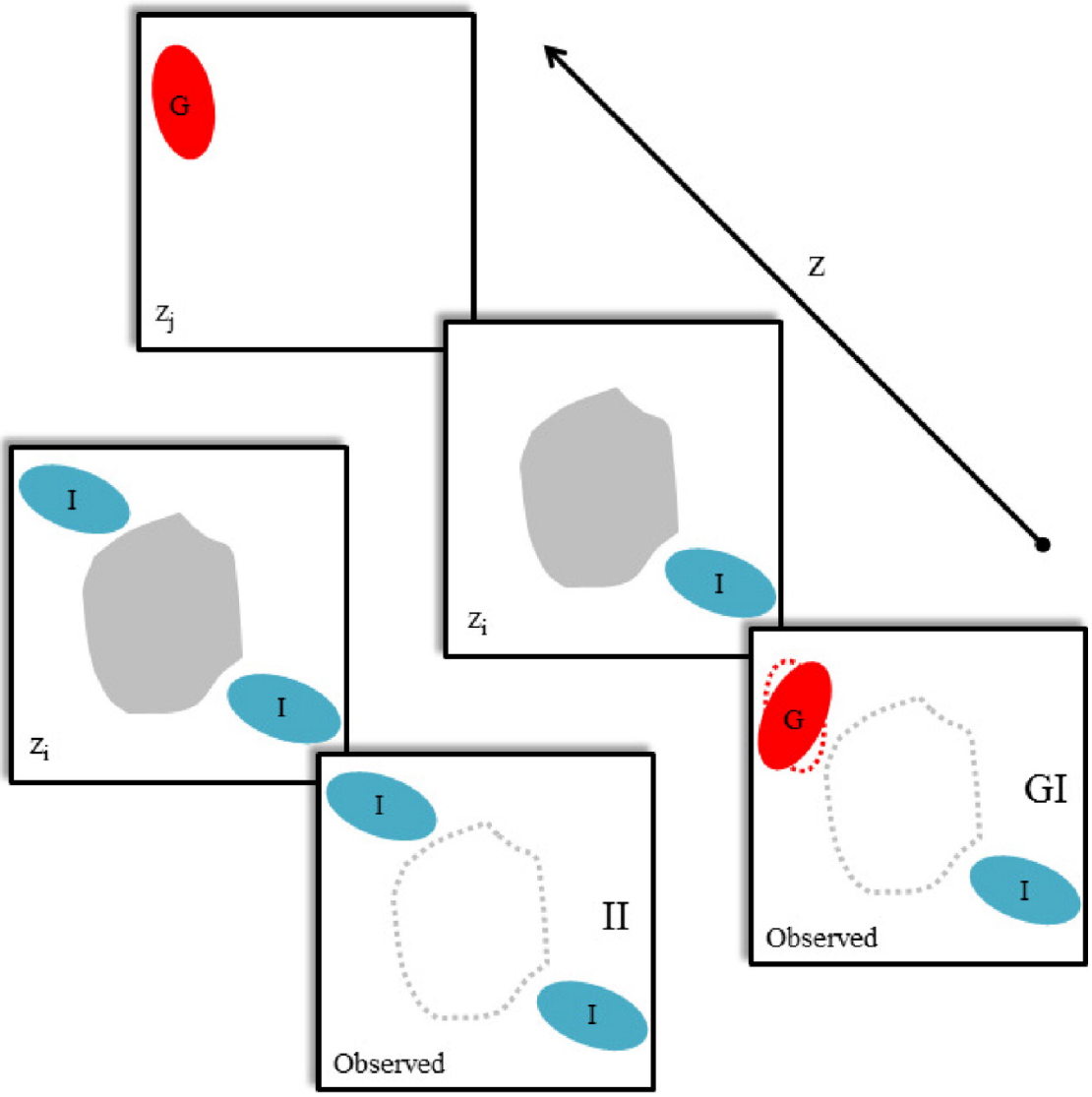

FIGURE 1.7: A schematic illustrating the II and GI intrinsic alignment correlations. Overlapping panels belong to the same scenario. The lower-right panels of both series represent the observer's view at low redshift, while each of the other panels connected in a chain are at sequentially higher redshift. The red, 'G' labelled galaxies are sheared, while the blue, 'I' marked galaxies are subject to tidal gravitational forces. The grey shape at intermediate redshift represents some mass which acts to gravitationally torque nearby galaxies, while possibly also acting as a lens for another galaxy at higher redshift. The grey dotted image in the observer plane represents the 2D location on the sky of the massive object, while the red dotted shape highlights the galaxy shape prior to shearing. For the II case, the two galaxies are both aligned with the massive object dominating their local space, and so their shapes are correlated. For the GI case, the galaxy at $z_{\rm i}$ is aligned with a massive structure due to gravitational forces, while this same structure is lensing the image of a galaxy at $z_{\rm j}$. As the direction of the shearing tends to be at right angles to the intrinsic alignment, this produces an anti-correlation in the observed galaxy shapes. Figure reproduced from Troxel & Ishak (2015).

It was found that theoretical systematics were dominant in limiting the constraining power of the DES Y3 cosmic shear measurement, imposing a 2/3 reduction in power. Amon et al. (2022) comments that this indicates that an improvement in the quality of observations will not necessarily cause a commensurate improvement in constraining power, and that more work needs to be done in the fields of galaxy formation and cosmological simulations to better improve our understanding of non-linear processes.

1.5 Cosmic shear measurement in the radio continuum

Current weak lensing measurements are the preserve of optical/near-IR facilities, as only these have been able to provide the large number of faint sources required for robust signal extraction. As an example, the KiDS survey boasts a source count of $\sim$10 galaxies arcmin^{-2} over 450 deg^2 (Hildebrandt et al., 2017), and DES Y3 data set contains 5.59 galaxies arcmin^{-2} over $4,143$ deg^2, while deep radio surveys such as COSMOS (Smolčić et al., 2017) and the SuperCLuster Assisted Shear Survey (SuperCLASS, Battye et al., 2020; Manning et al., 2020; Harrison et al., 2020) provide just $\lesssim 1$ galaxies arcmin^{-2} over a few square degrees. The next generation Square Kilometer Array (SKA[2]) radio interferometer telescope has the potential to break this optical hegemony, with the first phase (SKA1) forecasted to provide cosmological constraining power on the level of Stage III optical surveys, while the second (SKA2) will be comparable with Stage IV surveys such as *Euclid* and LSST (Harrison et al., 2016). Radio weak lensing measures have a number of benefits which make their study attractive, which I will detail below. I refer the interested reader to Tunbridge et al. (2016), Harrison et al. (2016), Camera et al. (2017), Tunbridge (2018) and Hillier (2020) for further details.

- As discussed previously, the PSF is a significant systematic in weak lensing measurements. Unlike their optical counterparts, radio observations suffer negligible blurring from the atmosphere. The radio PSF is then deterministic and diffraction limited, enabling its precise removal.
- The distribution of source redshifts accessible to the SKA will be characteristically higher than is the case for current Stage III and upcoming Stage IV optical surveys. This will push weak lensing measurements to higher redshifts, enabling tomographic analysis of the growth of structure at a novel intermediate epoch, between the quality data sets provided by the CMB and low redshift optical surveys

[2] `www.skatelescope.org/`

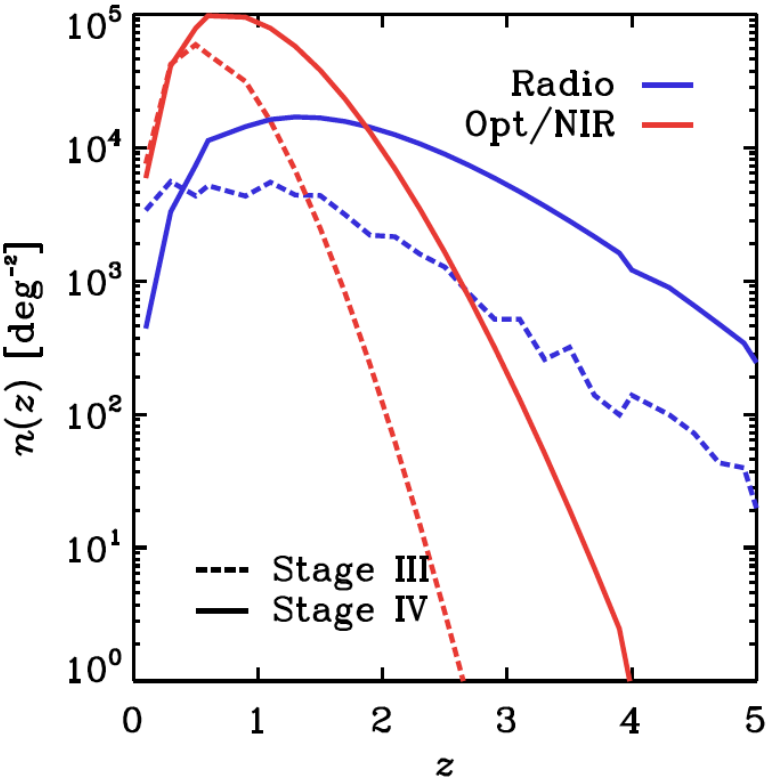

FIGURE 1.8: Comparison of the predicted redshift distribution of sources for Stage III and IV weak lensing surveys. SKA1 and SKA2 are the example radio Stage III and IV experiments, while DES and a *Euclid*-like survey are the corresponding optical/near-IR surveys. Figure reproduced from Camera et al. (2017)

(Brown et al., 2015; Camera et al., 2017; Square Kilometre Array Cosmology Science Working Group et al., 2020). See Fig. 1.8 for a comparison of the estimated redshift distribution of sources for Stage III and Stage IV-like radio and optical surveys. An additional advantage of higher redshift observations is that the shear signal will be stronger, due to the increased column density of the cosmic web photons will traverse.

- Radio surveys are capable of obtaining observations of the polarisation of light from source galaxies. Polarised light is unaffected by lensing (Dyer & Shaver, 1992; Brown & Battye, 2011), and so is a strong tracer of intrinsic alignment. Polarisation therefore provides a promising means of mitigating the intrinsic alignment systematic from radio weak lensing measurements (Whittaker et al., 2015).

- Studies have suggested that by obtaining a (lensed) velocity map of a galaxy, one may be able to estimate the shear by determining the transformation necessary to return the map to symmetry (Blain, 2002; Morales, 2006; Huff et al., 2013). With the SKA, velocity maps could be obtained with the HI 21 cm emission line. This same line could provide spectroscopic redshifts, however the number of galaxies for which this information will be limited to ∼10% of low redshift SKA1 sources.

While the above highlights the benefit of radio weak lensing as an isolated endeavour, the greatest boon comes from its synergies with optical studies. Conducting cosmological measurements in multiple wavelengths and subsequently cross-correlating the results leads to improved cosmological constraints. This can be seen for the case of the following optical ('O') and radio ('R') survey. For measured shears $\tilde{\gamma}_{\rm R}$ and $\tilde{\gamma}_{\rm O}$ (with $\tilde{\gamma} = \gamma + \gamma^{\rm int} + \gamma^{\rm sys}$), the cross-correlation is given as

$$< \tilde{\gamma}_{\rm R}\tilde{\gamma}_{\rm O} >=< \gamma\gamma > + < \gamma_{\rm R}^{\rm int}\gamma > + < \gamma_{\rm O}^{\rm int}\gamma > + < \gamma_{\rm R}^{\rm int}\gamma_{\rm O}^{\rm int} > + < \gamma_{\rm R}^{\rm sys}\gamma_{\rm O}^{\rm sys} >, \quad (1.15)$$

where γ is the true shear, 'int' relates to the intrinsic alignment of galaxies, and 'sys' indicates a fake shear signal arising from systematic effects relating to hardware or incorrect removal of the PSF. The final term is suppressed for cross-correlations, as a number of the systematic uncertainties afflicting each wavelength will be unique to that wavelength. For auto-correlations this term can be challenging to mitigate. For forecasts of future SKA weak lensing surveys, see Square Kilometre Array Cosmology Science Working Group et al. (2020).

1.6 The prediction of assembly bias

As discussed, cosmic shear measurements involve a convolution of clustering statistics and an assessment of galaxy shapes. Galaxy clustering itself, however, is the subject of interest in part due to the assembly bias prediction of simulations. The primary predictor of halo clustering as predicted by simulations is halo mass, with more massive haloes clustering most strongly (Kaiser, 1984; Sheth & Tormen, 1999). Simulations based on the ΛCDM paradigm predict that clustering exhibits dependencies on other properties even after the dominating affect of halo mass has been controlled for, the most discussed being the assembly time of the halo. This *halo assembly bias* predicts that early-forming haloes cluster more strongly than is seen for late-forming haloes (e.g. Sheth & Tormen, 2004; Gao et al., 2005; Wechsler et al., 2006; Angulo et al., 2008; Li et al., 2008; Lazeyras et al., 2017; Salcedo et al., 2018; Mao et al., 2018; Johnson et al., 2019). Other halo properties have been found to be closely linked with clustering, for example halo concentration (e.g. Salcedo et al., 2018; Sato-Polito et al., 2019; Paranjape et al., 2018).

Galaxy assembly bias is the secondary dependence in the clustering of galaxies on halo assembly time once the primary influence of halo mass has been accounted for (e.g. Croton et al., 2006; Zhu et al., 2006; Zentner et al., 2014; Xu & Zheng, 2020; McCarthy et al., 2022). This raises the prospect of observational detection of assembly bias in

large-sky galaxy surveys, as certain galaxy properties are thought to correlate with assembly time (e.g. Matthee et al., 2017; Davies et al., 2019b, 2020). In this thesis I refer to the general dependence of clustering on galaxy/halo properties other than halo mass as 'secondary biases'. While certain studies have announced a tentative prediction of the effect, consensus has yet to be reached. For example while Miyatake et al. (2016) and More et al. (2016) claimed the detection of a secondary bias in SDSS galaxy clustering based on concentration, subsequent works refuted this, raising concerns as to the handling of projection effects (Zu et al., 2017; Sunayama & More, 2019). With the prospect of the next generation of galaxy surveys achieving unprecedented precision and sample sizes, a measurement of galaxy assembly bias may be achieved in the short to medium term.

Simulation-based studies have attempted to determine how halo assembly time correlates with various observable galaxy properties, and thence investigate the secondary bias of clustering based on these galaxy properties (e.g. Montero-Dorta et al., 2020). Simulations vary in their implementation of baryonic processes, which will naturally impact the correlation between galaxy and halo properties, and therefore the relative strengths of secondary biases. Ahead of observational detection, we require a determination of the expected variance in the galaxy assembly bias prediction of hydrodynamical simulations with varied (but feasible) cosmology and baryonic implementation.

Galaxy environmental density measures which are based on counts of neighbours within a certain aperture are closely related to two-point clustering statistics. The topic of the correlation between galaxy environment and galaxy properties are well-studied (e.g. see Tanaka et al., 2004; Wang et al., 2018, for observations and simulations, respectively). As assembly time also correlates with environment and certain galaxy properties at fixed halo mass (Matthee et al., 2017; Davies et al., 2019b, 2020), the question raised is whether at least part of the environmental dependence of galaxy properties can be explained by the halo assembly time. The 'occupancy variation' of galaxies within a halo relates to the dependence of galaxy properties on halo properties beyond halo mass, and in the context of halo occupation distribution (HOD) models is used in combination with halo assembly bias to characterise galaxy assembly bias (Artale et al., 2018; Zehavi et al., 2018; Bose et al., 2019).

1.7 This thesis

This thesis explores some of the concepts introduced in this chapter. The three main areas of focus are broadly summarised in the following questions:

1. What is the expected morphology of the radio continuum-emitting regions of galaxies, and how does it relate to the stellar and dark matter components?

2. What is the expected intrinsic alignment of the radio continuum regions, and how will it affect future radio weak lensing surveys?

3. What is the connection between galaxy properties and their clustering, and how does this manifest for different properties and different simulations?

These topics can be addressed using state-of-the-art hydrodynamical, cosmological simulations of galaxy formation and evolution. Such simulations model the baryonic physics underpinning galaxy formation directly, including the back-reaction of these processes onto the dark matter distribution. I introduce these simulations in **Chapter 2**, with specific reference to the Evolution and Assembly of GaLaxies and their Environments (EAGLE) suite (Schaye et al., 2015; Crain et al., 2015) which is the primary source of data employed in this work.

Question 1 is addressed in **Chapter 3**, where I explore the 3- and 2-dimensional morphology of the star-forming ISM, the target of radio weak lensing surveys. The morphology of such regions has relevance to weak lensing measurements, which convolve the shapes of galaxies with their clustering. Particular focus is given to the 'shape noise' of such objects in projection, which is of particular consequence to cosmological forecasting (Harrison et al., 2016). I probe the redshift evolution of morphology, determining that the star-forming ISM becomes more disc-like with advancing cosmic time. I also measure the orientation of the star-forming ISM and make comparison with respect to the stellar and dark matter distributions. I show that the radio continuum emission is more poorly aligned with dark matter haloes than is found for optical emission (traced by stars). As introduced in Section 1.5, simultaneous observation of the 21-cm emission line of galaxies introduces the possibility of using kinematic information to mitigate the intrinsic alignment effect. This holds true only if galaxy kinematics and morphology are well aligned, which I demonstrate is the case in EAGLE.

Chapter 4 explores the consequences of galaxy morphology and orientation on the expected intrinsic alignment of radio continuum-emitting galaxies, thereby addressing Question 2. I show that the GI contaminant of weak lensing measurements (Section 1.4.4) is non-negligible and increases with decreasing galaxy pair separation, however the II contribution appears consistent with zero in projection and in 3-dimensions. In all cases the intrinsic alignment associated with radio continuum emission is lower in amplitude than the is seen for the stars. Exploring the mass dependence of intrinsic alignment signal, I show that the strong signal at low separations is driven by the one-halo term in $\sim M_\star$ haloes. Positing that the intrinsic alignment of the baryonic component of galaxies

relates directly to the internal alignment between the baryons and dark matter within a halo, I demonstrate that binning galaxies by their internal alignments is a strong predictor of intrinsic alignments. The apparent consequence of these findings is that radio weak lensing surveys will be less afflicted by intrinsic alignments than is the case for surveys conducted in the optical regime.

Chapter 5 focuses on Question 3, making use of several simulation suites to compare predictions of secondary biases in galaxy clustering. I also compare the correlation between assembly time and several galaxy and halo properties in EAGLE, and then measure the secondary bias associated with these properties. I demonstrate that there is a link between clustering and galaxy properties which correlate with assembly time (e.g. stellar and black hole mass), and also for properties which do not correlate with assembly time (star formation rate). I then introduce the 3-dimensional environmental density measure ρ_N as a possible alternative means of characterising galaxy clustering and subsequently measuring assembly bias. Such a measure is required to be uncorrelated with halo mass in order to probe differences in clustering at fixed halo mass, which I demonstrate is the case for centrals with $M_{200} < 10^{12}$ $\mathrm{M}_{\odot}$. I go on to link ρ_N with its 2-dimensional equivalent, Σ_N, and discuss means of limiting projection effects such that Σ_N is as closely correlated with ρ_N as possible. I finally demonstrate that galaxy assembly bias measurements are possible with 2-dimensional environmental density measures.

Finally, **Chapter 6** summarises the findings of this thesis and discusses avenues for future research.

Chapter 2

Introduction: Computational Cosmology

We can only see a short distance ahead, but we can see plenty there that needs to be done.

Turing

2.1 Introduction

In this chapter I will surmise computational cosmology, the main tool employed in my research. After introducing cosmological simulations generally, I will in Section 2.2 contrast two popular means of constructing mock-galaxy catalogues: semi-analytic models and hydrodynamical simulations. I go on to describe hydrodynamical simulations in more detail, summarising the setting of initial conditions in Section 2.3, the techniques and codes used to solve equations of gravity and hydrodynamics in Section 2.4 and Section 2.5. I then outline the the prescriptions used to model sub-resolution physics in Section 2.6, and finally the methods for identifying structure, namely (sub)haloes and galaxies, in Section 2.7.

2.2 General comments

Most of the relevant physical processes involved in the evolution of galaxies and the Universe occur over too long a timescale to be observed by an astronomer over the course of their lifetime. Astronomers are similarly unable to directly observe dark matter, the dominant contributor to the cosmic matter budget, however it is possible to infer its presence. For example peculiar velocity surveys (e.g. Adams & Blake, 2017) attempt to dissociate the motions of galaxies from the Hubble flow, and link the velocity field to the underlying density through Euler's equation. The phenomena of weak and strong gravitational lensing also enables the mapping of large-scale structure (e.g. Van Waerbeke et al., 2013), as well as the structure of dark matter haloes (e.g. Koopmans, 2005; Vegetti et al., 2010, 2012; Massey et al., 2015; Hezaveh et al., 2016). Additionally, the methods by which astronomers interpret observations often lack an obvious means of validation. All of this motivates the construction of theoretical models which predict the growth of cosmic structure and the concurrent formation and evolution of galaxies over time. There exist methods for mapping the observed properties of galaxies with the predicted properties of dark matter haloes, including models based on halo occupation distribution (e.g. Berlind & Weinberg, 2002; Zheng et al., 2005), conditional luminosity functions (e.g. Yang et al., 2003; van den Bosch et al., 2007), and subhalo abundance matching (e.g. Tasitsiomi et al., 2004; Conroy et al., 2006; Behroozi et al., 2010; Moster et al., 2010). These models while useful in studying the expected links between galaxies and haloes do not, however, track the temporal evolution of a *given* galaxy over time. The complex, three-dimensional and highly non-linear physics that underpins theories of structure formation and galaxy evolution cannot be fully solved analytically. Numerical approaches circumvent this problem by repeatedly solving the relevant equations over

discretised timescales for which they remain tractable. These simulations thus represent approximations of a full-analytic description, and can be applied to a variety of topics and span a range of length scales, from high-resolution simulations of the Local Group (e.g. APOSTLE Sawala et al., 2016), to gargantuan volumes on scales similar to that of the observable Universe (e.g. EuclidFlagship Potter et al., 2017). Despite this diversity, simulations aimed at constructing realistic galaxy populations within a cosmological framework largely fall into one of two categories: semi-analytic models and hydrodynamical simulations.

Semi-analytic models are able to construct mock galaxy catalogues relatively cheaply in terms of time and computational expense. They typically first obtain merger trees from $N-$body dark matter-only (DMO) simulations of large-scale structure formation to produce an evolving population of dark matter haloes with realistic clustering and properties, however analytic means of constructing merger trees based of extended Press-Schechter theory are also in use (e.g. Parkinson et al., 2008). Merger trees from these simulations are then combined with an analytic prescription for baryonic physics in order to populate these haloes with galaxies (e.g. Kauffmann et al., 1993; Somerville & Primack, 1999; Croton et al., 2006; Bower et al., 2006). $N-$body simulations (e.g. Trenti & Hut, 2008) are widely used in astronomy to solve equations of motion for N objects interacting gravitationally, for instance the orbital dynamics of objects in the solar system. In the ΛCDM paradigm, dark matter is thought to interact only through gravitational forces. $N-$body simulations are therefore an appropriate tool to use in computing the evolution of the large-scale dark matter distribution from a cosmogony-dependent selection of initial conditions. The semi-analytical models themselves assume that each halo hosts a galaxy, and track the ongoing baryonic physics within the context of the merger history of dark matter haloes provided by the $N-$body simulations. They calculate, for example, the accretion of gas onto a halo, the heating and cooling of gas, the formation of stars, the growth of black holes, and AGN and stellar feedback processes. The prescriptions for baryonic physics are based on theoretical laws or analytic approximation. This process results in a simulated galaxy catalogue. For each galaxy there exists information relating to its physical properties and temporal evolution. These can be compared with real galaxies in order to reach new insights into the physical mechanisms that underpin observed properties, and to improve our understanding of the processes that drive galaxy formation and evolution. The advantages of semi-analytic models relate to their computational efficiency, which enables the quick computation of a range of models and the construction of large mock galaxy catalogues. They suffer, however, from a lack of self-consistency in their treatment of baryons and dark matter. In ΛCDM, prior to recombination dark matter collapses into non-linear

structures (haloes) following the gravitational collapse of the primordial density fluctuations, while baryons and radiation remain tightly coupled. Following recombination, the now-neutral gas falls into the local gravitational potentials of dark matter haloes, where it cools and forms galaxies (e.g. Blumenthal et al., 1984). The location of galaxies then is strongly dependent on the dark matter distribution, however it is thought that there exists a significant back-reaction of baryons on dark matter (e.g. dark matter halo contraction in Blumenthal et al., 1986), which is not explicitly modelled in semi-analytic models.

Pure hydrodynamical simulations evolve dark matter and baryons simultaneously and self-consistently. In practice, however, these simulations include phenomenological routines which break self-consistency. These routines are included to model phenomena which are either too computationally expensive or occur on too-small a scale to be explicitly included. Individual resolution elements representing 10^4-10^7 solar masses-worth of material in these simulations are often referred to as 'particles', and should not be confused with individual protons, neutrons, electrons, or any other objects from particle physics. These simulations typically employ a numerical scheme in common with semi-analytic models, modelling the progression of baryonic and dark matter particles from one timestep to the next, starting at some high-redshift just before the growth of structure ('growth' here meaning enhancement in overdensity) within the volume transitions from the linear to non-linear regime, with an set of initial particle positions and velocities known as the initial conditions (see Section 2.3). These are determined according to chosen cosmogony. The discretisation of timesteps in the simulation are chosen according to precision requirements. Hydrodynamical simulations generally advance according to three processes, which consider the conditions at timestep t_i to compute the locations and properties of particles at t_{i+1}. These are:

- Computation of the gravitational potential field, and the resulting particle accelerations (Section 2.4).
- Computation of the hydrodynamical forces experienced by baryons (Section 2.5).
- The sequential execution of an ensemble of analytic routines which control the processes underpinning galaxy formation and evolution, for example: star formation; the heating and radiative cooling of gas; stellar and AGN feedback; enrichment of gas following supernovae etc (Section 2.6).

These steps all occur within a 3-dimensional Cartesian space, a cube of side-length L, with an imposed periodic boundary. This is known as a three-torus topology. Periodicity is included to mimic the assumed homogenity and isotropy of the Universe on large scales

and induce large-scale tidal fields. The use of the efficient Fast Fourier Transform (FFT) technique in computing the gravitational potential (see Section 2.4) also necessitates the use of periodicity.

Compared with $N-$body simulations of dark matter, the complex hydrodynamical physics underpinning baryonic processes require more calculations and shorter timesteps, therefore incurring a greater computational cost. As such hydrodynamical simulations are characteristically of lower volume. Their advantages over semi-analytic models, however, are numerous. They are able to make detailed predictions of the distribution and properties of the multi-phase gas in different regions, such as the circumgalactic medium (CGM) (e.g. recently Peeples et al., 2019; van de Voort et al., 2019; Suresh et al., 2019; Hummels et al., 2019) and the intergalactic medium (IGM) (e.g. Hernquist et al., 1996). They are additionally able to make predictions for the impact of baryons on dark matter, both in terms of the profile and distribution of haloes (e.g. Debattista et al., 2008). Blumenthal et al. (1986) found that baryons fall into dark matter haloes during galaxy formation and cause the adiabatic contraction of the dark matter distribution, creating smaller and denser cores than would have evolved in the absence of dissipative baryons. Duffy et al. (2010) demonstrated that dark matter haloes can be significantly impacted by baryonic physics; in one prescription with efficient radiative cooling and relatively weak feedback processes, the halo concentration of Milky Way-like objects was found to increase by as much as 30%. Baryonic physics is also known to affect the clustering of the total distribution of dark matter, which is most commonly seen through a suppression in the matter power spectrum (e.g. van Daalen et al., 2011). Hydrodynamical simulations retain a semi-analytic aspect, due to the finite resolution in mass and spatial scales (e.g. particle masses of $\sim 10^{6-7}$ $M_{\odot}$ for the flagship EAGLE simulation, Schaye et al., 2015), certain baryonic processes are modelled in a semi-analytic manner alongside the and gravity and hydrodynamics that are modelled explicitly. These 'subgrid models' typically include the treatment of star formation and stellar feedback. The scales upon which subgrid models are utilised are much smaller than is the case for semi-analytic models, which typically occurs on the scales of haloes. I will discuss the treatment of subgrid prescriptions in Section 2.6.

Advances in computational resources, techniques and an increased understanding of the processes governing galaxy formation and evolution in the past decade have led to a proliferation in the quantity and fidelity of hydrodynamical simulations. Among these are a class of simulations which aim to track the formation and evolution of galaxies within a cosmological context. This requires a large dynamic range of scales to be simulated, a large box size to minimise cosmic variance, and a sufficiently large galaxy population to quantify scatter in properties. Simulations of this class were first presented in the 2000s (e.g. Oppenheimer & Davé, 2008; Crain et al., 2009), proliferated in the 2010s and are in

widespread use within the astronomical community. The simulation volumes are typically on the order of $(25-100\ \mathrm{cMpc})^3$, with particle masses of approximately $10^{6-7}\ \mathrm{M}_\odot$. They include: EAGLE (Evolution and Assembly of GaLaxies and their Environments Schaye et al., 2015; Crain et al., 2015), FIRE (Feedback In Realistic Environments Hopkins et al., 2014, 2018), Horizon-AGN (Dubois et al., 2014), Illustris (Vogelsberger et al., 2014), IllustrisTNG (Springel et al., 2018; Marinacci et al., 2018; Pillepich et al., 2018b; Naiman et al., 2018; Nelson et al., 2018), Magneticum (Bocquet et al., 2016), MassiveBlack-2 (Khandai et al., 2015), MUFASA (Davé et al., 2016), OWLs (Schaye et al., 2010) and SIMBA (Davé et al., 2019).

That these simulations converge on similar box-sizes and particle masses is a combined consequence of the capability of the current generation of high-performance computating facilities, the complexity of the physical processes that require inclusion, and the need to simulate a broadly representative volume of the Universe while resolving the Jeans scale. This latter point relates to the fact that in self-gravitating systems, the density varies on the scale of the Jeans length. It therefore represents a useful resolution target.

To illustrate this issue, consider the following representative example. If a single fluid element employed in the computation of hydrodynamics tracks 32 distinct variables (particle ID, 3-vector position and velocity, density, etc.), in single precision at 4 bytes per variable this results in a requirement of 128 bytes per element. Modern compute nodes typically contain a few gigabytes of memory per compute core, which then enables for $\sim 10^7$ elements to be handled per core. For a cluster of $\sim$1000 cores, the number of fluid elements that can be handled is then $\sim 10^{10}$ (or $\sim 2000^3$). A volume of $(L = 100\ \mathrm{Mpc})^3$ is typically targeted as it allows sampling beyond the knee of the galaxy stellar mass function (GSMF). For this box-size and particle number, one obtains a spatial resolution at average density of $100\ \mathrm{Mpc}/2000 = 50$ kpc, though this can be improved at higher densities with adaptive techniques to $\sim$1 kpc. The associated baryonic particle mass is $\sim 10^6 \mathrm{M}_\odot$. For simulations to have any hope of convergence (return broadly similar results at differing resolution), it is required that the Jeans scale be resolved. For a Jeans mass and length defined as

$$M_\mathrm{J} \simeq 1.5 \times 10^7 \mathrm{M}_\odot f_\mathrm{g}^{3/2} \left(\frac{n_\mathrm{H}}{10^{-1}\mathrm{cm}^{-3}}\right)^{-1/2} \left(\frac{T}{10^4\mathrm{K}}\right)^{3/2} \tag{2.1}$$

$$L_\mathrm{J} \simeq 2.2\mathrm{kpc} f_\mathrm{g}^{1/2} \left(\frac{n_\mathrm{H}}{10^{-1}\mathrm{cm}^{-3}}\right)^{-1/2} \left(\frac{T}{10^4\mathrm{K}}\right)^{1/2}, \tag{2.2}$$

where n_H and f_g are the volume density of Hydrogen and the mass fraction in gas respectively, a resolution of 1kpc and $10^6 \mathrm{M}_\odot$ is sufficient to resolve the warm, photoionised interstellar gas phase ($n_\mathrm{H} \sim 0.1\mathrm{cm}^{-3}$ and $T \sim 10^4\mathrm{K}$). Conversely the molecular phase

of the ISM is characterised by densities of $n_{\rm H} > 10^2 {\rm cm}^{-3}$ and temperatures $T < 10^2 {\rm K}$, and is therefore much more computationally challenging for large-scale simulations to resolve. The convergence of computational limitations and the need to model explicitly Jeans scales for warm, photoioinised gas has caused several simulation families to target the ($\sim$1kpc, $\sim 10^6$ M$_\odot$) regime. Simulations more focussed on large-scale structure cosmology necessarily follow a larger volume, and offset the increased computational cost with a reduced particle resolution. This of course necessitates an expansion of the spatial scale over which subgrid routines operate. Notable among these is BAHAMAS (BAryons and HAloes of MAssive Systems McCarthy et al., 2017), with a box-size 400 Mpc/h and particle masses $\sim 10^9 {\rm M}_\odot$.

These hydrodynamical simulations then combine techniques for solving gravity and hydrodynamics with subgrid routines. 'Successful' simulations reproduce key statistics of the observed galaxy population. The subgrid routines are parameterised by certain tunable values, the appropriate selection of which requires careful calibration. Observed relationships such as the GSMF are typically employed as measures to which the subgrid parameters are tuned, such that the simulated universe accurately reproduces the true Universe in terms of these observables. The targeting of observed measures in the calibration process is not required as such, however their inclusion can greatly improve the realism of simulations. It should be noted that due to such tuning, simulation results relating to the observed relations used in the calibration process cannot be considered true predictions, as simulations are in effect 'forced' to return accurate measures.

While it would certainly be preferable to design and run simulations which reproduce key observables from first principles, the limited resolution of hydrodynamical simulations and our ignorance of the microphysics relating to feedback processes renders this infeasible. To illustrate this, I explore the case of galaxy stellar mass. The stellar mass of a galaxy depends on its integrated star formation rate (SFR), which in turn initially depends on the inflow of cold gas streams and the efficiency with which this gas is converted into stars. A consequence of star formation is feedback from supernovae, which acts to evacuate the galactic gas reservoir in an 'outflow' and subsequently decreases the galactic SFR. The degree to which this feedback energy couples to the surrounding gas and drives outflows is known as stellar feedback efficiency. The physics of stellar feedback is complex and insufficiently understood to build a robust, physically motivated subgrid model with a foreknown stellar feedback efficiency value. In the self-regulated picture of galaxy evolution (e.g. White & Frenk, 1991), inflow and outflow rates in galaxies will reach a state of quasi-equilibrium. Hence, the outflow rate is determined fundamentally by the inflow rate, which itself is set by cosmology via its tracking of the dark matter accretion rate (excluding such processes as re-accretion), and not the SFR nor the stellar feedback efficiency. As such, at fixed efficiency the SFR will adjust to balance

inflow with outflow. As the correct stellar feedback efficiency is unknown, and the correct subgrid model is uncertain besides, this does not necessarily result in a physically realistic SFR. Hence galaxies can attain an unphysical stellar mass. Hydrodynamical simulations therefore typically elect to calibrate the stellar feedback efficiency such that realistic galaxy stellar masses are produced.

Measures to which the simulations have not been calibrated may be viewed as true predictions and often show strong agreement with a diverse range of observables, for example EAGLE reproduces an analogue of the observed Tully-Fisher relation to better than 0.03 dex, while the passive fraction of galaxies sharply increases with stellar mass, as seen in observation. A reasonable question may be raised as to the utility of hydrodynamical simulations which are unable to reproduce, for example, a realistic GSMF ab initio, and instead are required to calibrate to this observable. While the reproduction of key observables of the galaxy population is a useful target, the utility of hydrodynamical simulations extends to their ability to allow an investigation of the physical processes that result in these measures (as argued by Schaye et al., 2015). They can also be used to make robust, quantitative predictions for next-generation observations targeting diffuse, low-surface brightness emission from regions such as the IGM. Further, as is the case for semi-analytic models, hydrodynamical simulations are useful in the planning and interpretation of observations.

In this thesis I largely analyse the EAGLE suite of simulations, which for the first time accurately reproduced the GSMF, populated by galaxies of realistic sizes. Its large volume and high resolution results in a diverse, well-sampled galaxy population that is appropriate for the study of galaxy and halo morphology, orientation and clustering. Furthermore, the EAGLE subgrid parameters were calibrated using the GSMF, the halo mass-stellar mass relation, galaxy sizes and the stellar mass-black hole mass relation. While the (star-forming) gas fraction of galaxies is involved in the calibration of EAGLE via the imposed star formation law (see Section 2.1 of Schaye et al. (2015) for a discussion), the morphology of the gaseous component of galaxies is not given explicit consideration. As a large part of this thesis concerns this, my findings can be considered true predictions.

In recent years the success of EAGLE has inspired the creation of numerous spin-off simulations that build on the realistic galaxy population produced by the original. A number of these are 'zoom' simulations, that re-simulate at higher resolution certain objects and areas. These include APOSTLE (A Project Of Simulations of the Local Environment Sawala et al., 2015, 2016; Fattahi et al., 2016), which focusses on six Local Group candidates, and Hydragngea/C-EAGLE (Bahé et al., 2017; Barnes et al., 2017), which re-simulates 30 clusters of virial mass between $M_{200} = 10^{14}$ and 2.5×10^{15} $\mathrm{M}_{\odot}$.

Other descendants add additional physics to their zooms, for example Oppenheimer et al. (2016) re-simulates 20 Milky Way-mass haloes at higher resolution, further traces an expanded selection of 136 ions and computes their associated physics. E-MOSAICS (MOdelling Star cluster population Assembly In Cosmological Simulations within EAGLE, Pfeffer et al., 2018) tracks the formation and evolution of star clusters within 25 re-simulated Milky Way mass haloes.

We summarise in the remainder of this chapter the basic elements of hydrodynamical simulations, in particular those relevant to the EAGLE suite of simulations. Section 2.3 details the selection of initial conditions, Section 2.4 the gravity solver, Section 2.5 describes the computation of the hydrodynamical equations underlying gas physics, and Section 2.6 discusses subgrid routines and calibration. For a more thorough discussion of contemporary hydrodynamical simulations, I refer the interested reader to the the reviews by Somerville & Davé (2015) and Vogelsberger et al. (2020). The EAGLE suite of simulations have been described in numerous studies previously (e.g. Velliscig et al., 2015a,b; Crain et al., 2017; Thob et al., 2019; Davies et al., 2019b, 2020; Mitchell et al., 2020), however I refer the reader to the initial release papers for a more complete description (Schaye et al., 2015; Crain et al., 2015, and references therein).

2.3 Setting the initial conditions

The initial fluctuations in the primordial density field grow over time to give rise to diversity of structure seen in the present-day Universe. The growth of fluctuations initially occurs in a linear fashion, which can be tracked analytically. The change in their size, which would otherwise follow the expansion of the Universe as a whole, is impeded by gravity. Overdense regions eventually collapse to form non-linear structures, which later reach dynamical equilibrium following virialisation (Peebles, 1980). It is following the evolution of structure in this complex, non-linear regime that is the raison d'etre of simulations based on numerical schemes. It is then important to accurately specify the initial conditions (ICs) with which simulations should start. The ICs are set by the chosen cosmology, which determines the primordial distribution and abundance of matter, as well as the evolving rate of expansion. Specifically, they are characterised by the energy density of dark energy, dark matter and baryons, as well as the primordial distribution of the latter two components. They effectively determine the perturbations to be applied on top of a homogenous expanding background.

In the case of EAGLE, the cosmological parameters are based on Planck Collaboration et al. (2014b) ($\Omega_0 = 0.307$, $\Omega_\mathrm{b} = 0.04825$, $\Omega_\Lambda = 0.693$, $\sigma_8 = 0.8288$, $n_\mathrm{s} = 0.9611$, $h = 0.6777$ and $Y = 0.248$). Inflationary theory predicts that the phase distribution

of the initial density perturbations is 'Gaussian', their probability distribution being a multidimensional Gaussian described by the primordial matter power spectrum $P_i(k) = Ak^n$, where A is the amplitude of the fluctuations and n is the scalar spectral index. As simulations are typically initialised post-recombination, an additional function is required to capture the impact that the physics relating to radiation-matter coupling has on the density fluctuations. This transfer function, $T(k)$, is linearly convolved with the primordial density fluctuation field to determine the initial power spectrum of a simulation, which generally takes the form $P(k) = P_i(k)|T(k)|^2$ (Seljak & Zaldarriaga, 1996; Peacock, 1997; Eisenstein & Hu, 1998, 1999). In practice, $T(k)$ is generated using software such as CAMB (Lewis et al., 2000), which models anisotropies in the cosmic microwave background. The initial linear power spectrum thus defined, the positions and velocities of mass-tracing particles require setting, along with the density, temperature and velocity of the baryons. For the matter density field, this is achieved by perturbing the mass-tracing particles from some an initial uniform Cartesian lattice or 'glass-like' particle structure (e.g. White, 1994; Baugh et al., 1995) into a configuration consistent with the initial linear power spectrum, using for example linear theory (Zel'Dovich, 1970) or first/second-order Lagrangian perturbation theory (e.g. Jenkins, 2010; Hahn & Abel, 2011). The particle velocities are determined by the gravitational instabilities induced by the particle position perturbation, typically imposed as a linear function of the displacement via the Zel'Dovich approximation (Zel'Dovich, 1970). A similar process is undertaken for the baryonic density and velocity fields (e.g. Jenkins, 2013; Jenkins & Booth, 2013), while the temperature is set according to the microwave background temperature, scaled with redshift according to the conditions at recombination (i.e. $T \sim 3000$ K at $z \sim 1100$).

Following the creation of the initial conditions, the mass-tracing particles are decomposed into a dark matter-baryon pair. The dark matter element is typically a particle, while the baryon can either also be represented by a particle in SPH simulations or instead a cell in mesh-based simulations. Their relative masses are determined according to the ratio of the cosmological density parameters: $\Omega_b/(\Omega_0 - \Omega_b)$. The position of two elements are offset from the IC-defined position of the mass-tracer particle in opposite directions along some random orientation. The offset distances are determined again by the mass ratio, such that the centre of mass coincides with the initial position of the mass-tracer particle. At this point, the simulations represent a universe at high-redshift ($z > 100$) post-recombination, and are further evolved according to steps outlined in the following sections.

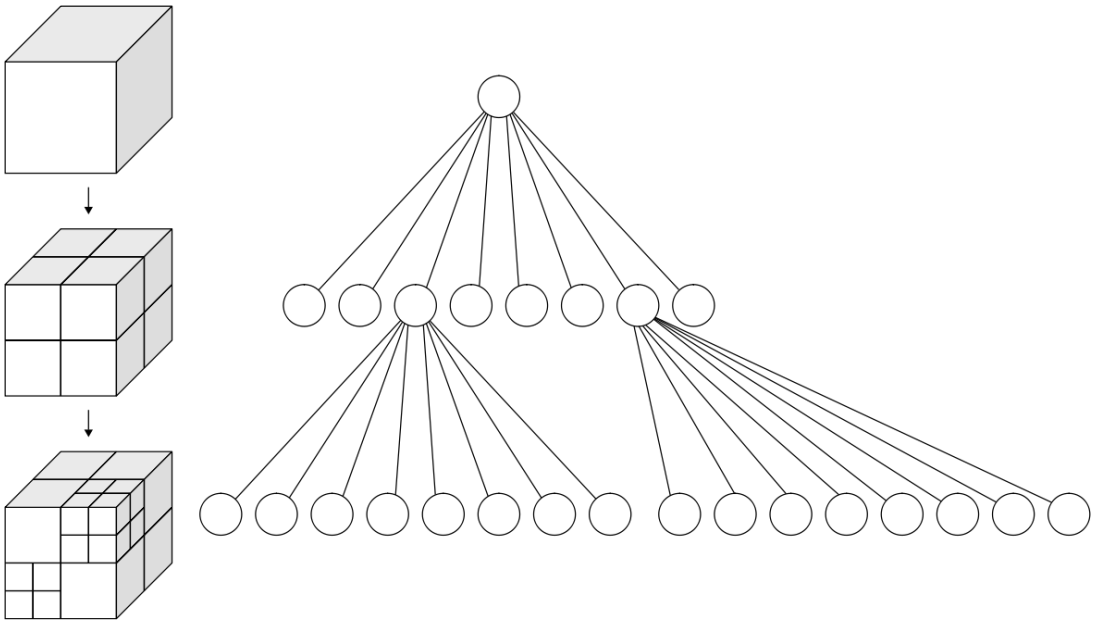

FIGURE 2.1: *Left:* An illustrative depiction of a hierarchical octree recursively segmenting a cube. For each segmentation, a cell is subdivided into eight equal-area volumes. *Right:* A graph representation of the recursive splitting takes the appearance of a tree with a root, branches and leaves.

2.4 Solving the equations of gravity

To advance the particle positions from one timestep to the next, one must consider their velocities and the gravitational forces that they feel at their position within the simulated mass distribution. Constructing the gravitational potential field requires solving Poisson's equation, or at least approximating the solution to some acceptable accuracy and precision. Perhaps the most conceptually simple way to compute the gravitationally induced-acceleration of each particle is to sum the gravitational interaction forces from each of the other elements in the mass distribution. For contemporary simulations of $\sim 10^9$ particles, the $\mathcal{O}(N^2)$ scaling of this approach is rendered impractical.

Means of reducing the computational cost of $N-$body simulations are widely used within the community. As gravitational force is inversely proportional to the square of the distance between masses, the net gravitational potential at a given location is dominated by the closest particles, rather than those at large separations. As a particle has many more neighbours at large separations than close, this motivates treating the gravitational interactions between distant particles less precisely. A class of schemes taking example of this fact employ hierarchical multipole expansion, a popular subset of which are 'tree' methods. These algorithms recursively segment the simulation volume into ever-smaller cells, until each contains no more than a chosen maximum number of particles (e.g. Barnes & Hut, 1986; Dehnen, 2000). This results in a structure resembling a tree,

with a 'root' being the whole simulation volume, a 'branch' representing the next level of recursion, and a 'leaf' cell being the finest possible level of segmentation. For the 'octree' approach employed by GADGET-2/3, each subdivision results in eight new subcells.

This structure allows distant particles to be grouped together and their aggregate gravitational forces to be approximated. The gravitational force experienced by each particle is computed by a process of 'walking the tree', which occurs by starting at the root node and ascertaining whether an 'opening criterion' is met. This criterion determines whether an approximated gravitational force at the current level is acceptably accurate. If this criterion is not reached, the algorithm 'walks' to the next level and repeats the process. A walk is also termed 'opening the cell'. This continues until the criterion has been satisfied, or the leaf cell has been reached. The advantage of this approach is that the opening criterion can control the accuracy of the approximation of the gravitational force calculations. Imposing a distance dependence in the opening criterion enables short-range interactions to be captured by finer nodes within the octree structure. In the GADGET-2/3 code (Springel, 2005), a cell of length l containing a total mass M at a separation r is opened if

$$\frac{GM}{r^2}\left(\frac{l}{r}\right)^2 \leq \alpha|\mathbf{a}|, \tag{2.3}$$

where α and $|\mathbf{a}|$ are the tolerance parameter and acceleration at the previous timestep respectively. The effect of this process is to reduce the quantity of calculations to be made, and so reduce the computational cost to $\mathcal{O}(N\log N)$.

Another class of gravity solvers are particle-mesh (PM) methods (Klypin & Shandarin, 1983), which are considered to provide the quickest computation. A common approach within this class involves creating a continuous 3-dimensional mesh and assigning particles to their closest node, thereby constructing a continuous mass distribution. The gravitational potential is then computed via the Fast Fourier Transform, which through transforming the mesh into spatial frequencies renders Poisson's equation as a linear equation. This is computed, and inversely transformed to obtain the real-space solution. Similarly to the considerations in the octree approach, accurate computation of small-scale interactions requires a fine mesh, whereas a coarse mesh may be desirable for larger-scale. Adaptive meshes aim to increase the number of nodes in locations where higher resolution is desired. The considerable advantage given by rapidity of these PM schemes is offset by their large memory requirements, as these schemes require high-spatial resolution due to the need to mitigate their unfortunate suppression

of gravitational forces on the scale of a mesh cell. There are methdologies that attempt to minimise the effect of this suppression while maintaining a reasonable memory load by combining a PM scheme with another gravity solver, such as direct summation in particle-particle particle-mesh (P^3M) approaches (Hockney & Eastwood, 1981; Efstathiou et al., 1985), and hierarchical trees (as outlined above) in the hybrid 'TreePM' method (Xu, 1995). Simulation codes such as GADGET-2/3 (Springel, 2005) and AREPO (Springel, 2010b) use examples of the latter, where octrees and meshes are used to compute shorter- and longer-scale interactions respectively. A summary of modern simulation codes and their respective treatments of gravity may be found in Table 1 of Vogelsberger et al. (2020).

As the separation between the point particles representing extended mass distributions approaches zero, their mutual gravitational attraction tends towards infinity. In order to remove this numerical effect, a 'softening' factor ϵ is included in calculations. This replaces the $1/r$ factor in computations of gravitational potential with $1/\sqrt{r^2+\epsilon^2}$. The value of ϵ varies between simulations. It generally decreasing with increased resolution, however there are no fixed rules governing the selection of an optimal value. Ludlow et al. (2019b) recently found that cosmological simulations return converged halo properties for a range of softening lengths given two considerations: firstly that $\epsilon < r_{\rm conv}$, where $r_{\rm conv}$ is the 'convergence radius', which depends on two-body relaxation and is determined by the number of particles; and secondly that the orbits of particles with short dynamical times are resolved by sufficient timesteps. There is no consistent ϵ employed in the literature, and it can vary for different matter components within a given simulation. While EAGLE employs a softening length of $\max(\epsilon_{\rm com} = 2.66$ ckpc$, \epsilon_{\rm prop} = 0.7$ pkpc) for all particle types, IllustrisTNG uses $\max(\epsilon_{\rm com} = 1.48$ ckpc$, \epsilon_{\rm prop} = 0.74$ pkpc) for point particles, 2.5 times the effective cell radius for gas cells, and $\epsilon_{\rm BH} = \epsilon_{\rm DM}(m_{\rm BH}/m_{\rm DM})^{1/3}$ for black holes.

2.5 Numerical techniques of hydrodynamics

While dark matter is the dominant matter component, reproducing the observed Universe as accurately as possible requires simulating the luminous baryonic component. These baryons initially take the form of gas (mostly hydrogen and helium), and are converted in part into stars during the growth of structure. It is therefore necessary to accurately simulate gas physics, which involves solving hydrodynamical equations alongside the gravity solver outlined in the previous section. This greatly increases the computational cost involved in running simulations, owing in part to the large dynamic range in spatial scales required to be modelled, as well as the need to impose adaptive

time-stepping in order to capture sudden changes in internal particle energy and the subsequent transmission to neighbours.

The continuous gas distributions within simulations are modelled according to the Euler equations (e.g. Mo et al., 2010, pg. 366). The Euler equations are an inviscid form of the Navier-Stokes equations, which in turn express the conservation of momentum and mass for Newtonian fluids. An artificial viscosity term is often necessary in order to capture shocks and divergent flows. Alternative approaches whereby the Navier-Stokes equations are solved directly are explored in Springel (2010a), which is motivated by the desire to model processes where the inviscid approximation is invalid e.g. black hole accretion discs. Variation within simulations relates to how the Euler equations are discretised, two methods being the Lagrangian and Eulerian specifications. In the Lagrangian approach, simulations track the evolution of individual fluid elements. These parcels are often referred to as particles, similar to the point particles of dark matter. In the Eulerian approach one considers fixed positions in space, often referred to as cells, through which a fluid flows.

The GADGET3 solver employed by EAGLE and other simulations utilises a smoothed particle hydrodynamics (SPH) scheme. In SPH formalism, particles representing fluid elements have their properties 'smoothed' out spatially. In this manner, the fluid properties at any position in the simulation domain may be calculated via a kernel-weighted interpolation of the properties of particles. Simulations employing an SPH scheme interchangeably refer to gas particles as SPH particles. The kernel is set by a smoothing length $h_{\rm sml}$, which is typically chosen to enable the kernel to encompass a fixed number of nearest neighbours or a fixed mass. This imbues the SPH formalism with an adaptive resolution, as the kernel smoothing is naturally finer in higher density regions. This natural adaptive resolution, as well as the relatively straightforward manner by which the Euler equations may be solved, has led to SPH becoming popular within simulations employing a Lagrangian philosophy.

Issues arising from SPH implementation relate to the inclusion of an artificial viscosity parameter (e.g. EAGLE follows Cullen & Dehnen, 2010), necessary to capture shocks, and the pressure gradient found at contact discontinuities. This results in an undesirable and unphysical surface tension, which acts to retard the mixing of gas phases (e.g. cold clumps passing through a hot medium are more resistance to disruption; Agertz et al., 2007) and prevent realistic realisations of Kelvin-Helmholtz instabilities. Another challenge is that low density regions such as the IGM will naturally be poorly resolved as they contain fewer gas particles to act as interpolation points for the reconstruction of macroscopic fluid properties.

Strategies for overcoming these shortcomings include the Hopkins (2013) SPH model employed by EAGLE, which uses a pressure-entropy formalism to infer density rather than tracking and computing it through the kernel-weighted summation directly. This takes advantage of the insight that the problematic presence of density in the equation of motion arose from the chosen manner of SPH volume discretisation, which was typically $\sim m_i/\rho_i$ (Saitoh & Makino, 2013). As this choice is arbitrary, alternate formulations of the volume element enable the derivation of alternate equations of motion. In the method outlined by Hopkins (2013), the SPH equations are derived exactly from the particle Lagrangian and conserve energy, momentum, and angular momentum. Entropy is also conserved in scenarios without sources or sinks. This approach has the advantage of removing the erroneous 'surface tension' term which arises at contact discontinuities in other SPH formulations (e.g. 'density-entropy', Saitoh & Makino, 2013). In addition, the treatment of fluid mixing, such as Kelvin-Helmholtz instabilities, are improved, and differences between SPH and grid-based methods are largely eliminated.

An additional challenge is that 'standard' SPH is non-conductive, which prevents the mixing of gas phases and the transfer of energy. EAGLE navigates this via the inclusion of an artificial conduction switch (Price, 2008). Finally, it is necessary to ensure that sudden changes in particle energy resulting from feedback are properly captured and diffused to neighbouring particles. This requires sufficiently short timesteps, which is achieved in EAGLE by following the timestep limiter outlined in Durier & Dalla Vecchia (2012).

2.6 Subgrid prescriptions

As stated in the introduction to this chapter, many of the baryonic processes that govern galaxy formation and evolution occur on spatial scales that are not resolved by the simulations. They are therefore modelled using subgrid prescriptions. The chief behavioural difference between dark matter and baryons is the ability of baryons to dissipate their potential energy through radiative processes, therefore radiative cooling, photoheating and reionisation are included as subgrid routines in the majority of hydrodynamical simulations. The inclusion of radiative transfer is an active area of research, particularly in simulations relating to the epoch of reionisation, however it is not included in most contemporary simulations owing to its computational cost. Stellar processes relevant galaxy evolution, including star formation, stellar feedback and chemical enrichment of gas via the ejecta of supernovae and asymptotic giant branch (AGB) stars, are also included through subgrid routines. Finally, central black holes have a sizeable impact on their host galaxy, both through their impact on their ability to quench star formation

throughout the disc via active galactic nuclei (AGN) feedback. Black hole seeding, mass accretion, mergers and AGN feedback are therefore commonly included as subgrid routines. I will briefly relate these various processes in more detail in the following sections, specifically within the context of the EAGLE suite of simulations.

2.6.1 Thermal processes in gas

The cooling and heating of gas is a primary driver of galaxy evolution. The important radiative processes that must be considered are the radiative cooling and photoheating of gas, as well as the photoionisation of gas by the CMB and radiation from galaxies and quasars. Radiative cooling and photoheating are dependent on the chemical composition, density and temperature of the gas, as well as the redshift-dependent UVB/X-ray amplitude. While early simulations included radiative cooling only for hydrogen and helium, modern simulations track a number of elemental abundances in gas particles in order to include the efficient cooling process of metal-line emission, which is particularly significant for typical cosmic gases at temperatures $10^5 \leq T \leq 10^7$ K. Simulations such as EAGLE and IllustrisTNG utilise the popular CLOUDY model (Ferland et al., 1998), which models processes relevant to the temperature scales typically followed in simulations ($10^4 \leq T \leq 10^7$ K). Within EAGLE, element-by-element radiative cooling and photoionisation for 11 elements (H, He, C, N, O, Ne, Mg, Si, S, Ca and Fe) are modelled according to the methodology outlined in Wiersma et al. (2009a), within a spatially homogeneous but time-evolving radiation field originating from the CMB and the UVB emitted by galaxies and quasars according to Haardt & Madau (2001). Initially pristine gas particles are subject to chemical enrichment from their neighbouring stellar particles. In EAGLE gas is assumed to be in ionisation equilibrium, which may at times cause an overestimate of the cooling rate (e.g. Oppenheimer & Schaye, 2013).

2.6.2 Star formation

In the real Universe star formation occurs following the collapse of molecular clouds due to the overcoming of radiation pressure and turbulent support by self-gravitation (Jeans instability). Star formation typically takes place within the interstellar medium (ISM), which contains multiple gas phases at strikingly different temperatures and pressures (McKee & Ostriker, 1977). Cosmological simulations lack the resolution to model the cold, dense phase of the ISM where star formation occurs. Additionally, physics such as magnetic fields and turbulence are not generally included, both of which are thought to be significant at the scale of protostars and dense molecular clouds (McKee & Ostriker, 2007). Fortunately, robust observations of scaling relations (for a review, see Kennicutt

& Evans, 2012) allow simulations to appeal to empirical schemes of star formation, which can be imposed on larger scales than the small scales of reality. By this way our ignorance and insufficient resolution are 'smoothed over'.

Generally speaking, simulations model star formation by transforming a fraction of a gas particle/cell into collisionless single-age and single-metallicity stellar particles that represents a population of stars described by an initial mass function. In EAGLE, star formation rate (SFR) follows the Kennicutt-Schmidt law (Kennicutt, 1998),

$$\dot{\Sigma}_\star = A\Big(\frac{\Sigma_\mathrm{g}}{1\mathrm{M}_\odot\mathrm{pc}^{-2}}\Big)^n, \tag{2.4}$$

where $\Sigma_\star$ and Σ_g are the star and gas surface densities, and A and n are free parameters. EAGLE follows Schaye & Dalla Vecchia (2008), who reformulate the Kennicutt-Schmidt relation to be a function of pressure, rather than density (this requires the assumption of a self-gravitating disk). This is expressed as

$$\dot{m}_\star = m_\mathrm{g} A(1\ \mathrm{M}_\odot\mathrm{pc}^{-2})^{-n}\Big(\frac{\gamma}{G}f_\mathrm{g}P\Big)^{(n-1)/2}, \tag{2.5}$$

where m_g is the gas particle mass, the heat capacity ratio $\gamma = 5/3$, G is the gravitational constant, f_g is the gas fraction and P is the pressure. It is assumed that $f_\mathrm{g} = 1$, while A and n are determined from observed scaling relations. As in reality, not all of the gas in simulations is capable of forming stars. Simulations typically follow a model of stochastic star formation where candidacy is based on some criteria, examples of which include density thresholds (e.g. EAGLE & NIHAO Schaye et al., 2015; Wang et al., 2015) and Jeans length-based criteria (e.g. FIRE-2 Hopkins et al., 2018).

EAGLE imposes a density-dependent temperature floor, $T_\mathrm{eos}(\rho_\mathrm{g})$, determined by normalising the equation of state $P_\mathrm{eos} \propto \rho_\mathrm{g}^{4/3}$ to $T_\mathrm{eos} = 8 \times 10^3\mathrm{K}$ at $n_\mathrm{H} = 10^{-1}\mathrm{cm}^{-3}$. This temperature is typical of the warm phase of the ISM. The exponent $\gamma_\mathrm{eos} = 4/3$ is selected to ensure that the Jeans mass and the ratio of the Jeans length and the SPH kernel are density independent. This prevents unphysical fragmentation due to the simulation's finite resolution (Robertson & Kravtsov, 2008; Dalla Vecchia & Schaye, 2008). Gas is deemed eligible to form stars if it has a temperature within 0.5 dex of T_eos and $n_\mathrm{H} > n_\mathrm{H}^*$, where n_H^* is the metallicity-dependent density threshold of Schaye (2004),

$$n_\mathrm{H}^*(Z) = 10^{-1}\mathrm{cm}^{-3}\Big(\frac{Z}{0.002}\Big)^{-0.64}, \tag{2.6}$$

where Z is the gas metallicity, defined as the fraction of gas mass assigned to elements heavier than hydrogen. This enables stars to form from gas particles of lower density if the metallicity is sufficiently high. The imposition of the temperature floor results in the star forming gas having a temperature that is reflective of the effective pressure of the ISM, as opposed to its physical temperature. As the Jeans length at the temperature floor is $\sim$1 pkpc, there is effectively an artificial pressure that prevents the scale heights of star forming gas discs being much shorter than this value. I will return to the implications of this limitation to my work in Section 3.2.1.

Nascent stellar particles inherit the elemental abundances of their parent gas particles. Each star particle is representative of a stellar population characterised with an initial mass function (IMF), $\Phi(M)$. EAGLE assumes an IMF of stars following Chabrier (2003), and production and release of the same nine metals tracked by the cooling routine, from supernovae and AGB. The yields are specified according to Portinari et al. (1998) and Marigo (2001). At each timestep, the fraction of the mass within stellar particles reaching the end of the main sequence is calculated, and the mass and metals are distributed to the surrounding gas particles according to Wiersma et al. (2009b).

2.6.3 Stellar feedback

The realism of hydrodynamical simulations has increased greatly in recent years, following advances in computation and improvement in the treatment in modelling feedback in the form of stellar winds, supernovae and AGN. The requirement to include sources of stellar feedback was first noted by White & Rees (1978), who postulated omission would result in an overabundance of cool, dense gas. This was found in the 'overcooling problem' of early simulations, which formed unphysically massive and compact galaxies (Katz & Gunn, 1991; Navarro & Benz, 1991; White & Frenk, 1991; Navarro & White, 1994; Balogh et al., 2001). Stellar feedback acts as a self-regulating system that mitigates overcooling, at least in relatively low mass galaxies. As gas cools, the star formation increases, which in turn leads to the heating of the surrounding gas, and the subsequent ejection of the gaseous reservoir required for star formation.

Stellar feedback takes to form of supernova-induced galactic-scale winds that act to suppress star formation by depriving a galaxy of the molecular gas 'fuel' required (e.g. Veilleux et al., 2005). The means by which this is imposed in simulations is through the thermal or kinetic injection of energy into the gas surrounding stellar particles following supernovae explosions. The former case can suffer from an inability to drive winds, as too large a fraction 10^{51} erg of energy released by a supernova is radiated away (e.g Katz et al., 1996; Brook et al., 2004). This occurs due to the finite resolution of simulations.

If a simulation does not contain cold and dense clouds, then star formation will not be 'clumpy' and the energy from supernovae will be distributed too smoothly within the surrounding gas. A paucity of gas phases further raises issues, as the lack of a physically realistic cold-ISM results in an overestimation of the warm-ISM mass, which in turn causes an overestimated cooling rate. This can be mitigated by disabling the cooling of heated particles for a certain amount of time (Stinson et al., 2006). In the latter case, radiative cooling does not occur until thermal equilibrium is reached, but additional 'wind particles' may be required to increase the momentum of non-local gas and drive outflows (e.g. Springel & Hernquist, 2003; Pillepich et al., 2018a).

An additional challenge facing the implementation of stellar feedback again relates to the limited mass resolution. A supernova event might be expected to eject 1 $M_\odot$ of material at $\sim 10^4$ kms^{-1}, equating to 10^{51} erg of kinetic energy. This ejecta proceeds to sweep up surrounding gas, and in conjunction with other feedback events drive winds. In cosmological simulations employing a thermal means of injection into the surrounding gas, the gas elements are orders of magnitude more massive than the initial 1 $M_\odot$ ejecta of reality. In order to preserve the correct energy injection, these too-massive gas elements are heated to relatively low temperatures. As the radiative cooling time scales with temperature as $t_c \propto T^{1/2}$, this results in the energy injection dissipating too quickly (Dalla Vecchia & Schaye, 2008). A solution to this is to artificially suppress radiative cooling, which enables the efficient conversion of thermal to kinetic energy (e.g. Gerritsen, 1997; Mori et al., 1997; Thacker & Couchman, 2000; Kay et al., 2002; Sommer-Larsen et al., 2003; Brook et al., 2004; Dubois & Teyssier, 2008; Stinson et al., 2006). Dalla Vecchia & Schaye (2008) argue that this will result in an underestimate of the maximum wind velocity in the mass resolution of a simulation is too coarse. Another means of preventing the rapid loss of energy through radiative cooling is to make the depositing of energy a stochastic process. This removes the need to artificially alter thermodynamic processes in simulations. EAGLE models stellar feedback thermally via the methodology outlined in Dalla Vecchia & Schaye (2012). Feedback occurs stochastically, with newly formed stellar particles heating a number (the average is $\sim$1) of their neighbouring gas particles by $10^{7.5}$K after 30Myr, which corresponds to the minimum expected lifetime of Type-II supernovae (SN II) progenitors. The energy available for heating from a single star particle depends on the fraction of stars within the population ending their life-cycle as SN II, $n_{\mathrm{SN\ II}}$, and $E_{\mathrm{SN\ II}}$, the energy available from a single SN-II. With the total available energy per unit stellar mass given as $\epsilon_{\mathrm{SN\ II}} = n_{\mathrm{SN\ II}} E_{\mathrm{SN\ II}}$, the energy available for distribution from a star particle is $m_\star \epsilon_{\mathrm{SN\ II}}$, where $m_\star$ is the initial stellar mass of the particle. The probability of heating scales the to with the tunable parameter f_{th} (see Section 4.5 of Schaye et al., 2015, for more details), which sets the efficiency of stellar feedback and is used in calibration. It is defined as

$$f_{\rm th} = f_{\rm th,min} + \frac{f_{\rm th,max} - f_{\rm th,min}}{1 + \left(\frac{Z}{0.1Z_{\odot}}\right)^{n_{\rm Z}} \left(\frac{n_{\rm H,birth}}{0.67{\rm cm}^{-3}}\right)^{-n_{\rm n}}}, \tag{2.7}$$

where the independent variables are the metallicity Z and the density of the parent gas particle $n_{\rm H,birth}$, $n_{\rm Z} = n_{\rm n} = 2/\ln 10$, and the values explicitly used in calibration are the asymptotes $f_{\rm th,min} = 0.3$ and $f_{\rm max} = 3$. The stellar feedback was calibrated to reproduce the observed GSMF and galaxy size-mass relation (Crain et al., 2015). This mechanism engenders large temperature, and hence pressure, gradients in the gas and naturally drives galactic-scale outflows.

2.6.4 Black holes and AGN feedback

Initial predictions from the hierarchical model of galaxy formation suggested that the most massive galaxies should form at late times were contradicted by observations that found that the bulk of the Universe's stellar mass was in place at $z \sim 1$. This indicated that the most massive galaxies instead assembled and were quenched of star formation at early times (Cowie et al., 1996; Neistein et al., 2006). While stellar feedback has been found to be essential in reproducing the low mass end of the GSMF, by itself it is unable to effectively prevent the overproduction of high mass galaxies, as following halo growth the gas ejected from the ISM re-cools is able to again fuel star formation at later times (e.g. Benson et al., 2003; Crain et al., 2009).

SMBHs reside at the centres of galaxies spanning a wide range of masses, from dwarfs (e.g. Reines et al., 2011; Moran et al., 2014) to massive ellipticals (e.g. Gehren et al., 1984; Kormendy & Richstone, 1995). There is a remarkably consistment ratio between the mass of the SMBH and the host galaxy (Magorrian et al., 1998; Häring & Rix, 2004), suggesting that the evolution of the two components are closely linked (however Jahnke & Macciò (2011) promote an alternate explanation). Black holes are therefore directly modelled in simulations. A mechanism for the coevolution of SMBHs and their host galaxies is AGN feedback, the energy released following the accretion of mass onto a central black hole. Sufficiently fuelled SMBHs can form high-friction accretion discs where rest-mass is efficiently transformed into energy. This radiated energy can then proceed to drive large outflows (see e.g. Silk & Rees, 1998; Kauffmann & Haehnelt, 2000; Di Matteo et al., 2005). AGN-driven outflows have been observed at a range of epochs (e.g. Rupke & Veilleux, 2011; Maiolino et al., 2012; Harrison et al., 2014; Cicone et al., 2015, 2016), and in simulations are seen to be capable of quenching star formation on galactic scales, and thereby changing galaxy morphology (e.g. Springel et al., 2005a; Hopkins et al., 2005; Sijacki et al., 2007; Booth & Schaye, 2009; Johansson et al., 2009;

Dubois et al., 2013). The semi-analytic models of Croton et al. (2006) and Bower et al. (2006) found that beyond a certain halo mass, star formation becomes inefficient and an excess of gas in the halo centre drives an accelerated SMBH mass accretion and a subsequent increase in AGN feedback. They further found that AGN feedback caused a suppression in the formation of massive galaxies and an agreement with the observed GSMF at the high-mass end.

The importance of accurate treatment of black holes, and the associated AGN feedback, in cosmological simulations is apparent. Black holes are numerically seeded with a initial mass in dark matter haloes of a certain critical mass. In EAGLE a fixed seed mass of 10^5 $\mathrm{M}_\odot h^{-1}$ within 10^{10} $\mathrm{M}_\odot h^{-1}$ haloes that don't already have a black hole is implemented. Black hole growth in simulations happens as in reality: through accretion and mergers. In EAGLE mergers are treated neglecting relativistic effects due to the limited resolution. Black holes merge if they are separated by less than both the black hole softening length, h_{BH}, and three times the gravitational softening length. It is further required that their relative velocities are less than the circular velocity at a distance h_{BH}, such that $v_{\mathrm{rel}} < \sqrt{G m_{\mathrm{BH}} h_{\mathrm{BH}}^{-1}}$. The accretion of stars and dark matter onto black holes is omitted. Gas accretion driven growth follows an Eddington-rate limited Bondi-Hoyle-like model, $\dot{m}_{\mathrm{accr}} = \min(\dot{m}_{\mathrm{Edd.}}, \dot{m}^{'}_{\mathrm{accr}})$, with

$$\dot{m}_{\mathrm{Edd.}} = \frac{4\pi G m_{\mathrm{BH}} m_{\mathrm{p}}}{\epsilon_{\mathrm{r}} \sigma_{\mathrm{T}} c} \tag{2.8}$$

and

$$\dot{m}^{'}_{\mathrm{accr}} = \dot{m}_{\mathrm{Bondi}} \times \min(C_{\mathrm{visc}}^{-1} (c_{\mathrm{s}}/V_\phi)^3, 1), \tag{2.9}$$

where $\dot{m}_{\mathrm{Bondi}}$ is the Bondi & Hoyle (1944) rate for spherically symmetric accretion

$$\dot{m}_{\mathrm{Bondi}} = \frac{4\pi G^2 m_{\mathrm{BH}}^2 \rho}{(c_{\mathrm{s}}^2 + v^2)^{3/2}}. \tag{2.10}$$

For equation 2.8, m_{p} is the proton mass, σ_{T} is the Thompson cross-section, c is the speed of light, ϵ_{r} is the radiative efficiency of the accretion disc (set to 0.1), and v is the relative velocity between the gas and the black hole. For equation 2.9, C_{visc} is a tunable subgrid parameter relating to the viscosity of the accretion disc, c_{s} is the speed of sound, and V_ϕ is is the gas rotation speed around the black hole, computed following Rosas-Guevara et al. (2015) (their equation 16). Finally for equation 2.8, ρ is the density of the gas surrounding the black hole. The increase in black hole mass is related to the accretion rate as $\dot{m}_{\mathrm{BH}} = (1 - \epsilon_{\mathrm{r}}) \dot{m}_{\mathrm{accr}}$. A limitation of this approach is that the accreted

gas is assumed to have no angular momentum, leading to some simulations exploring alternative methods of modelling accretion, for example Hopkins & Quataert (2011) follows the model presented in Shlosman et al. (1989).

Similar to stellar feedback, AGN feedback in EAGLE is treated thermally and stochastically. The energy injection rate is defined as $\epsilon_{\rm f}\epsilon_{\rm r}\dot{m}_{\rm accr}c^2$, where $\epsilon_{\rm f}$ is the fraction of radiative energy that is coupled to the ISM. As with $f_{\rm th}$, $\epsilon_{\rm f}$ is calibrated to an observed measure: the normalisation of the $m_{\rm BH}$-$m_\star$ relation. A value of $\epsilon_{\rm f} = 0.15$ was found to be appropriate in this regard. The energy injection rate is not transferred to SPH neighbours instantaneously. Rather, each black hole holds a 'reservoir' of feedback energy, $E_{\rm BH}$, which increases over each timestep Δt such that $\Delta E_{\rm BH} = \epsilon_{\rm f}\epsilon_{\rm r}\dot{m}_{\rm accr}c^2\Delta t$. Once the black hole has enough energy to heat at least one SPH neighbour by $\Delta T_{\rm AGN} = 10^{8.5}$K, it is assigned a probability of heating each of its SPH neighbours by $\Delta T_{\rm AGN}$ according to

$$P = \frac{E_{\rm BH}}{\Delta\epsilon_{\rm AGN} N_{\rm ngb}\langle m_{\rm g}\rangle}, \tag{2.11}$$

where $\Delta\epsilon_{\rm AGN}$ is the corresponding change in internal energy per unit mass according to a temperature increase $\Delta T_{\rm AGN}$, $N_{\rm ngb}$ is the number of the black hole's SPH neighbours. It has been found that over a large range of values, the chosen value for the efficiency of black hole feedback, $\epsilon_{\rm f}\epsilon_{\rm r}$, impacts only the mass of the black hole (Booth & Schaye, 2010), with star formation and gas inflows largely unaffected. As with stellar feedback, AGN feedback is found to be a self-regulating system that balances outflows and inflows, as $\dot{m}_{\rm accr}$ is dependent on and dependent upon the rate of gas inflow. The most significant factor in the treatment AGN feedback is $\Delta\epsilon_{\rm AGN}$, with larger values increasing the energy of individual feedback events and reducing radiative losses in the ISM, but also decreasing the frequency of individual events. Following equation 18 of Dalla Vecchia & Schaye (2012), the transitional density value above which the energy from feedback is expected to be radiated away increases with ΔT. Therefore as the density of the gas surrounding SMBHs tends increase with resolution, $\Delta T_{\rm AGN} = 10^{8.5}$ K in the reference L0100N1504 simulation, and 10^9 K in higher resolution models such as Recal-L025N0752.

The means by which AGN feedback is implemented varies between simulations. IllustrisTNG, for instance, employs dual thermal and kinetic feedback modes (Pillepich et al., 2018b). These differing feedback mechanisms result in differences in the content of the CGM, which contains the remnants of gas outflows. (Davies et al., 2020).

2.7 Defining haloes, subhaloes and galaxies

Numerous methods exist to identify haloes within simulations. These include usage of the friends-of-friends (FoF) algorithm, the locating of spherical overdensities, and the identifying of structures in 6D phase-space. Knebe et al. (2011) explored differences in halo-finding methodologies and found general agreement in retrieved halo properties and the halo mass function at $z = 0$, however Klypin et al. (2011) found significant disagreement between FoF and spherical overdensity-based finders at high redshift within the Bolshoi simulation. The identification of substructure, such as satellite galaxies and their (sub)haloes, typically occurs in the post-processing of parent haloes and their bound particles. Substructure can be identified either via local peaks in the gravitational potential [e.g. SUBFIND, Springel et al. (2001); Dolag et al. (2009), or within 6D phase-space (e.g. ROCKSTAR, Behroozi et al., 2013).

EAGLE defines galaxies as the cold baryonic component of gravitationally self-bound structures, identified by the application of the SUBFIND algorithm to dark matter haloes first identified with the FoF algorithm, with a linking length of 0.2 times the mean interparticle separation. Subhaloes are identified as overdense regions in the FoF halo bounded by saddle points in the density distribution. Within a given FoF halo, the subhalo comprising the particle (of any type) with the lowest gravitational potential energy is defined as the central subhalo, others are then satellites.

The position of galaxies is defined as the location of the particle in their subhalo with the lowest gravitational potential energy. The position of the central galaxy is used as a centre about which to compute the spherical overdensity mass (see Lacey & Cole, 1993), M_{200}, for the adopted enclosed density contrast of 200 times the critical density, $\rho_{\rm c}$. In general, the properties of galaxies are computed by aggregating the properties of the appropriate particles located within 30 pkpc of the galaxy centre, as this yields stellar masses comparable to those recovered within a projected circular aperture of the Petrosian radius (see Schaye et al., 2015).

Chapter 3

The morphology of star-forming gas and its alignment with galaxies and dark matter haloes in the EAGLE simulations

Ah, but a man's reach should exceed his grasp,

Or what's a Heaven for?

Browning

The content of this chapter was published in the paper Hill et al. (2021) in collaboration with Rob Crain, Ian McCarthy and Juliana Kwan. The simulation data was created by the EAGLE collaboration.

3.1 Introduction

The currently preferred Λ-cold dark matter (ΛCDM) cosmogony posits that the large-scale cosmic matter distribution (spatial scales $\gtrsim 1$ Mpc) is best described as a highly non-uniform system of voids, sheets, filaments and haloes, colloquially termed the 'cosmic web'. This structure forms in response to the gravitational growth of small instabilities in the matter distribution of the early Universe (e.g. Bond et al., 1996; Faucher-Giguère et al., 2008; Shandarin et al., 2010). Spectroscopic redshift surveys have revealed that galaxies are themselves distributed in a cosmic web, as expected if they broadly trace the underlying matter distribution. The non-uniform distribution of galaxies was apparent in early redshift surveys (see e.g. de Lapparent et al., 1986; Geller & Huchra, 1989), but was demonstrated spectacularly by those exploiting the advent of highly multiplexed spectrographs, notably the 2dF Galaxy Redshift Survey (2dFGRS; Colless et al., 2003) and the Sloan Digital Sky Survey (SDSS; Tegmark et al., 2004).

A fundamental tenet of galaxy formation models is that galaxies form within the dark matter (DM) haloes that permeate the cosmic web (e.g. White & Rees, 1978). The broad correspondence between the clustering of galaxies inferred from observational surveys on one hand, and on the other that of the galaxies that form in semi-analytic models of galaxy formation (e.g. Kauffmann et al., 1999; Springel et al., 2005b; Wechsler et al., 2006; Guo et al., 2011) and, more recently, hydrodynamical simulations of large cosmic volumes (e.g. Crain et al., 2017; McCarthy et al., 2017; Springel et al., 2018), can be considered a remarkable corroboration of the ΛCDM paradigm. However, being subject to the rich array of dissipative physical processes that govern their growth, galaxies inevitably represent imperfect tracers of their local environment (e.g. Kaiser, 1984; White et al., 1987), such that their baryonic components do not necessarily trace the shape and orientation of their DM haloes in a simple fashion.

Besides their potential use as a means to place constraints on the ill-understood microphysics of galaxy formation, and to reveal the nature of the environment of galaxies (e.g. Codis et al., 2015; Zhang et al., 2015), differences in the shape and orientation of baryonic components of galaxies with respect to those of their DM haloes are of particular interest because they represent sources of uncertainty in observational inferences of the morphology of DM haloes, and of their orientation with respect to the large-scale matter distribution (e.g. Troxel & Ishak, 2015). This is of consequence for efforts to constrain cosmological parameters via the shape correlation function of galaxies, a key aim of ongoing optical/near-infrared weak lensing surveys such as the Canada-France-Hawaii Telescope Lensing Survey (CFHTLens; Erben et al., 2013), Kilo-Degree Survey (KiDS; de Jong et al., 2015), the Hyper Suprime Cam Subaru Strategic Program (HSC; Aihara

et al., 2018b) and the Dark Energy Survey (DES; The Dark Energy Survey Collaboration, 2005), and ambitious forthcoming surveys with the Vera Rubin Observatory (LSST Science Collaboration et al., 2009), the *Euclid* spacecraft (Laureijs et al., 2012), and the *Nancy Grace Roman Space Telescope* (e.g. Spergel et al., 2015). Moreover, the severity of differences between the shape and alignment of haloes and those of the observable structures used to infer them, has a strong bearing on the accuracy of weak gravitational lensing predictions derived from dark matter-only simulations. At present, such simulations are the only means of modelling the evolution of cosmic volumes comparable to those mapped out by lensing surveys.

Simplified techniques such as halo occupation distribution (HOD) modelling, subhalo abundance matching (SHAM), and semi-analytic models have, in order of increasing sophistication, proven valuable means of understanding the connection between galaxies and the matter distribution (see e.g. Schneider & Bridle, 2010; Joachimi et al., 2013). However, such methods have been shown to exhibit significant systematic differences with respect to the predictions of cosmological hydrodynamical simulations on small-to-intermediate spatial scales (e.g. Chaves-Montero et al., 2016; Springel et al., 2018), in large part because they (by design) do not self-consistently capture the back-reaction of baryon evolution on the structure of DM haloes (Bett et al., 2010; Guo et al., 2016). A comprehensive understanding of the influence of systematic uncertainties stemming from the differences in the shape and orientation of galaxies and their host haloes therefore requires self-consistent and realistic physical models of galaxy formation in a fully cosmological framework.

There is a rich history of the use of numerical simulations to establish the correspondence between the morphology, angular momentum and orientation of galaxies, their satellite systems and their host DM haloes, with particular emphases on the roles played by gas accretion (e.g. Chen et al., 2003; Sharma & Steinmetz, 2005; Sales et al., 2012), mergers (e.g. Dubinski, 1998; Boylan-Kolchin et al., 2006; Naab et al., 2006) and environment (e.g. Croft et al., 2009; Hahn et al., 2010; Shao et al., 2016). However, prior studies have tended to suffer from one or more significant shortcomings, namely relatively poor spatial and mass resolution, relatively small sample sizes, and a poor correspondence between the properties of simulated galaxies with observed counterparts. These shortcomings are significantly ameliorated by the current generation of state-of-the-art hydrodynamical simulations, such as EAGLE (Crain et al., 2015; Schaye et al., 2015), HorizonAGN (Dubois et al., 2014), Illustris/IllustrisTNG (e.g. Vogelsberger et al., 2014; Pillepich et al., 2018b) and MassiveBlack-II (Khandai et al., 2015). Each of these simulations broadly reproduces key observed properties of the present-day galaxy population, thus engendering confidence that they capture (albeit with varying degrees of accuracy) the complexity of the interaction between the baryonic components of galaxies and their

DM haloes. The simulations each follow a cosmological volume sufficient to a yield representative galaxy population ($\sim 100^3\,\mathrm{cMpc}^3$), and do so with a mass resolution ($\sim 10^6\,\mathrm{M}_\odot$) and spatial resolution ($\sim 1\,\mathrm{pkpc}$) that enables examination of the properties and evolution of even sub-$L^\star$ galaxies. Moreover, they capture important second-order effects such as the back-reaction of baryons on the structure and clustering of DM haloes.

The emergence of optical weak lensing surveys as a promising means of constraining the nature of DM and dark energy has intensified the need to assess the severity of systematic uncertainties afflicting cosmic shear measurements (specifically, the galaxy shape correlation function). Cosmological hydrodynamical simulations have proven a valuable tool for this purpose, highlighting that galaxies can be significantly misaligned with respect to their DM haloes (e.g. Faltenbacher et al., 2007; Bett et al., 2010; Hahn et al., 2010; Bett, 2012; Tenneti et al., 2014; Velliscig et al., 2015a; Shao et al., 2016; Chisari et al., 2017) and that the shapes and alignments of galaxies and their haloes are correlated over large distances via tidal forces (Tenneti et al., 2014; Chisari et al., 2015; Codis et al., 2015; Velliscig et al., 2015b). The simulations have also been exploited to examine the morphological and kinematic alignment of galaxies with the cosmic large-scale structure (see e.g. Cuesta et al., 2008; Codis et al., 2018). The current generation of state-of-the-art simulations remains reliant on the use of subgrid treatments of many of the key physical processes governing galaxy evolution and, as noted by Joachimi et al. (2015) the details of their particular implementation can in principle influence the alignment of cosmic structures (see also Velliscig et al., 2015a). However, in key respects the simulations appear to be quantitatively compatible with extant observational constraints, e.g. the $w_{\mathrm{g}+}$ correlation function of luminous red galaxies in SDSS and their analogues in the MassiveBlack-II simulation (Tenneti et al., 2015, their Fig. 21).

A complementary approach to optical/near-IR weak lensing surveys is to measure shear at radio frequencies. The concept has been demonstrated both by exploiting very large area, low source density radio data (Chang et al., 2004), and deep, pointed observations with greater source density (Patel et al., 2010). Ambitious future radio continuum surveys such as those envisaged for the Square Kilometre Array (SKA) may prove to be competitive with the largest optical surveys. An SKA Phase-1 continuum survey of 5000 deg^2 is predicted to observe a source density of resolved star-forming galaxies of 2.7 arcmin^{-2} (Square Kilometre Array Cosmology Science Working Group et al., 2020). Brown et al. (2015) argue that, in the most optimistic case, a full Phase-2 SKA survey over 3π steradians would yield twice the areal coverage of the *Euclid* 'wide survey', with a similar source density of $\simeq$30 galaxies arcmin^{-2}.

The characteristic redshift of sensitive radio continuum surveys may also prove to be significantly greater than that of optical counterparts. By bridging the gap between

traditional shear measurements and those derived from maps of the cosmic microwave background (CMB) radiation, radio weak lensing surveys offer the promise of tomographic mapping of cosmic structure evolution in both the quasi-linear and strongly non-linear regimes. Shear mapping in the radio regime offers advantageous complementarity with optical surveys, in particular to suppress key systematic uncertainties. For example, the use of kinematic and/or polarisation information may enable improved characterisation of the intrinsic (unsheared) ellipticity, and suppress the influence of intrinsic alignment, the deviation from random of the observed ellipticity of a sample (Blain, 2002; Morales, 2006; de Burgh-Day et al., 2015; Whittaker et al., 2015).

Shear measurements in the radio regime are derived from images of the extended radio continuum emission from galaxies, which effectively traces the star-forming component of the interstellar medium (ISM). The morphology and kinematics of this component, and their relationship with those of the underlying DM distribution, can in principle differ markedly from the analogous quantities traced by the stellar component imaged by conventional lensing surveys. However, by design, leading models of the radio continuum sky (e.g. Wilman et al., 2008; Bonaldi et al., 2019) do not account for such differences. This therefore motivates an extension of prior examinations of the relationship between galaxies and the overall matter distribution, and correlation of shapes and alignments of galaxies separated over cosmic distances, focusing on the use of the star-forming ISM to characterise the morphology and orientation of galaxies. The current generation of state-of-the-art cosmological hydrodynamical simulations are well suited to this application since, as for the stellar component, they self-consistently model the evolution of star-forming gas within galaxies, including cosmological accretion from the intergalactic and circumgalactic media (IGM and CGM, respectively), expulsion by feedback processes, and its interaction with a dynamically 'live' DM halo.

In this Chapter, we use the cosmological hydrodynamical simulations of the EAGLE project (Schaye et al., 2015; Crain et al., 2015) to examine the correspondence between the morphology and orientation of the star-forming ISM of galaxies and those of their parent DM haloes. EAGLE is well suited to this application: although the simulations do not explicitly model the balance between molecular, atomic and ionised hydrogen, the use of empirical or theoretical models to partition gas into these phases indicates that the simulations broadly reproduce key properties of the atomic and molecular reservoirs of galaxies (see e.g. Lagos et al., 2015; Bahé et al., 2016; Crain et al., 2017; Davé et al., 2020) including, crucially, the 'fundamental plane of star formation' that relates their stellar mass, star formation rate and neutral hydrogen fraction (Lagos et al., 2016). This study complements prior examinations of the morphology of stars, hot gas and DM in the EAGLE simulations (e.g. Velliscig et al., 2015a,b; Shao et al., 2016). The morphology of the star-forming ISM of galaxies in the IllustrisTNG-50 simulation (hereafter

TNG50) was also examined by Pillepich et al. (2019); whilst the motivation for that study was quite different to that of ours, their findings are of direct relevance and offer an opportunity to assess the degree of consensus between different simulations.

This Chapter is structured as follows. We discuss our numerical methods in Section 3.2, as well as summarising briefly details of the EAGLE simulation and galaxy finding algorithms, and our sample selection criteria. In Section 3.3 we examine the morphology of star-forming gas and its dependence on subhalo mass and redshift. In Section 3.4 we examine the internal alignment of star-forming gas with DM and stars, and its mutual alignment with its kinematic axis, again as a function of subhalo mass and redshift. In Section 3.5 we investigate the shapes and alignments of the various matter components in 2D. In Section 3.6 we discuss and summarise our findings. We then examine the influence of a series of numerical and modelling factors on our findings.

3.2 Methods

In this section we briefly introduce the EAGLE simulation (Section 3.2.1) and key numerical techniques for identifying haloes and subhaloes (Section 3.2.2), and for characterising their morphology with shape parameters (Section 3.2.3). Our sample selection criteria are discussed in Section 3.2.4. Detailed descriptions of the simulations are provided by many other studies using them, so we present only a concise summary of the most relevant aspects and refer the interested reader to the project's reference articles (Crain et al., 2015; Schaye et al., 2015).

3.2.1 Simulations

The EAGLE project (the Evolution and Assembly of GaLaxies and their Environments) comprises a suite of hydrodynamical simulations that model the formation and evolution of galaxies and the cosmic large-scale structure in a ΛCDM cosmogony (Crain et al., 2015; Schaye et al., 2015). Particle data, and derived data products, from the simulations have been released to the community as detailed by McAlpine et al. (2016). The simulations were evolved with a modified version of the Tree-Particle-Mesh (TreePM) smoothed particle hydrodynamics (SPH) solver GADGET-3 (last described by Springel, 2005). The main modifications include the implementation of the pressure-entropy formulation of SPH introduced by Hopkins (2013), a time-step limiter as proposed by Durier & Dalla Vecchia (2012), switches for artificial viscosity and artificial conduction, as per Cullen & Dehnen (2010) and Price (2008), respectively, and the use of the Wendland

Identifier	L (cMpc)	N	m_g ($\mathrm{M}_\odot$)	ϵ_com (ckpc)	ϵ_phys (pkpc)
L025N0376	25	376^3	1.81×10^6	2.66	0.70
L025N0752	25	752^3	2.26×10^5	1.33	0.35
L100N1504	100	1504^3	1.81×10^6	2.66	0.70

TABLE 3.1: The box sizes and resolution details of the EAGLE simulations used in this study. The columns are: comoving box side length, L; number of DM particles (there is initially an equal number of baryon particles); the initial baryon particle mass; the Plummer-equivalent gravitational softening length in comoving units; the maximum proper softening length.

(1995) C^2 smoothing kernel. The influence of these developments on the properties of the galaxy population yielded by the simulations is explored by Schaller et al. (2015b).

EAGLE includes subgrid treatments of several physical processes that are unresolved by the simulations. These include element-by-element radiative heating and cooling of 11 species (Wiersma et al., 2009a) in the presence of a spatially uniform, temporally evolving UV/X-ray background radiation field (Haardt & Madau, 2001) and the cosmic microwave background (CMB); a model for the treatment of the multiphase ISM as a single-phase fluid with a polytropic pressure floor (Schaye & Dalla Vecchia, 2008); a metallicity-dependent density threshold above which gas becomes eligible for star formation (Schaye, 2004), with a probability of conversion dependent on the gas pressure (Schaye & Dalla Vecchia, 2008); stellar evolution and mass-loss (Wiersma et al., 2009b); the seeding of BHs and their growth via gas accretion and mergers (Springel et al., 2005a; Booth & Schaye, 2009; Rosas-Guevara et al., 2015); and feedback associated with the formation of stars (Dalla Vecchia & Schaye, 2012) and the growth of BHs (Booth & Schaye, 2009; Schaye et al., 2015). The simulations adopt the stellar initial mass function (IMF) of Chabrier (2003). The efficiency of stellar feedback was calibrated to reproduce the stellar mass function of the low-redshift galaxy population and, broadly, the sizes of local disc galaxies. The efficiency of AGN feedback was calibrated to reproduce the present-day scaling relation between the stellar mass and central black hole mass of galaxies. The gaseous properties of galaxies and their haloes were not considered during the calibration.

EAGLE adopts values of the cosmological parameters derived from the initial Planck data release (Planck Collaboration et al., 2014b), namely $\Omega_0 = 0.307$, $\Omega_\mathrm{b} = 0.04825$, $\Omega_\Lambda = 0.693$, $\sigma_8 = 0.8288$, $n_\mathrm{s} = 0.9611$, $h = 0.6777$, $Y = 0.248$. Our analyses focus primarily on the EAGLE simulation of the largest cosmic volume, Ref-L100N1504, which follows a cubic periodic volume of side $L = 100\,\mathrm{cMpc}$, realised with $N = 1504^3$ collision-less DM particles of mass $m_\mathrm{DM} = 9.7 \times 10^6\ \mathrm{M}_\odot$, and an initially equal number of baryonic particles of mass $m_\mathrm{g} = 1.81 \times 10^6\ \mathrm{M}_\odot$. The Plummer-equivalent gravitational softening length is 1/25 of the mean interparticle separation ($\epsilon_\mathrm{com} = 2.66\,\mathrm{ckpc}$),

limited to a maximum proper length of $\epsilon_{\rm com} = 0.7\,{\rm pkpc}$. We explore the numerical convergence of the morphology and orientation of the star-forming gas component of galaxies in Section 3.7.1, using the pair of high-resolution L025N0752 EAGLE simulations introduced by Schaye et al. (2015). These follow a cosmic volume of $L = 25\,{\rm cMpc}$ realised with $N = 752^3$ particles of each species, with masses $m_{\rm DM} = 1.21 \times 10^6\,{\rm M}_\odot$ and $m_{\rm g} = 2.26 \times 10^5\,{\rm M}_\odot$. For these simulations the Plummer-equivalent gravitational softening length is $\epsilon_{\rm com} = 1.33\,{\rm ckpc}$, limited to a maximum proper length of $\epsilon_{\rm com} = 0.35\,{\rm pkpc}$. The first of these simulations, Ref-L025N0752, uses the same 'Reference' subgrid model parameters as the Ref-L100N1504, whilst the second, Recal-L025N0752, uses a model whose parameters were recalibrated to achieve a better match to the calibration diagnostics. A summary of the simulations used in this Chapter are given in Table 3.1.

The standard-resolution simulations marginally resolve the Jeans scales at the density threshold for star formation in the warm and diffuse photoionised ISM. They hence lack the resolution to model the cold, dense phase of the ISM explicitly, and so impose a temperature floor to inhibit the unphysical fragmentation of star-forming gas. This floor takes the form $T_{\rm eos}(\rho)$, corresponding to the equation of state $P_{\rm eos} \propto \rho_{\rm g}^{4/3}$ normalised to $T_{\rm eos} = 8 \times 10^3\,{\rm K}$ at $n_{\rm H} = 10^{-1}\,{\rm cm}^{-3}$. The temperature of star-forming gas thus reflects the effective pressure of the ISM, rather than its actual temperature. A drawback of the use of this floor is the suppression of the formation gas discs with scale heights much less than Jeans length of the gas on the temperature floor ($\sim$1 pkpc). In Section 3.7.2, we explore the sensitivity of the star-forming gas morphology to the slope of the ISM equation of state, and the normalisation of the star formation law.

In a recent study, Ludlow et al. (2019a) demonstrated that the scale height of discs can be artificially increased by 2-body scattering of particles with unequal mass, as is the case here since we use (initially) equal numbers of baryon and DM particles, meaning that $m_{\rm dm}/m_{\rm b} \equiv (\Omega_0 - \Omega_{\rm b})/\Omega_{\rm b} \simeq 5.4$. The vertical support of the disc may also have physical causes, such as turbulence stemming from gas accretion and energy injection from feedback (Benítez-Llambay et al., 2018), although it is likely that the these influences are artificially strong in the simulations. Therefore we caution that both the gas and stellar discs of galaxies in EAGLE are generally thicker than their counterparts in nature (see also Trayford et al., 2017). We note however that these effects are unlikely to influence significantly the mutual alignment of the stellar and gaseous discs, nor their alignment with their parent DM halo.

3.2.2 Identifying and characterising haloes, subhaloes and galaxies

We define galaxies as the cold baryonic component of gravitationally self-bound structures, identified by the application of the SUBFIND algorithm (Springel et al., 2001; Dolag et al., 2009) to DM haloes first identified with the friends-of-friends (FoF) algorithm (with a linking length of 0.2 times the mean interparticle separation). Subhaloes are identified as overdense regions in the FoF halo bounded by saddle points in the density distribution. Within a given FoF halo, the subhalo comprising the particle (of any type) with the lowest gravitational potential energy is defined as the central subhalo, others are then satellites.

The position of galaxies is defined as the location of the particle in their subhalo with the lowest gravitational potential energy. The position of the central galaxy is used as a centre about which to compute the spherical overdensity mass (see Lacey & Cole, 1993), M_{200}, for the adopted enclosed density contrast of 200 times the critical density, $\rho_{\rm c}$. In general, the properties of galaxies are computed by aggregating the properties of the appropriate particles located within 30 pkpc of the galaxy centre, as this yields stellar masses comparable to those recovered within a projected circular aperture of the Petrosian radius (see Schaye et al., 2015).

3.2.3 Characterising the morphology and orientation of galaxy components

Following Thob et al. (2019), we obtain quantitative descriptions of the morphology of galaxies and their subhaloes by modelling the spatial distribution of their constituent particles as ellipsoids, characterised by their sphericity[1], $S = c/a$, and triaxiality, $T = (a^2 - b^2)/(a^2 - c^2)$, parameters, where a, b and c are, respectively, the moduli of the major, intermediate and minor axes of the ellipsoid[2]. Therefore $S = 0$ corresponds to a perfectly flattened (but potentially elongated) disc, and $S = 1$ corresponds to a perfect sphere, whilst low and high values of T correspond, respectively, to oblate and prolate ellipsoids.

Axis lengths are given by the square root of the eigenvalues of a matrix describing the 3D mass distribution of the particles in question. The simplest choice is the mass

[1] Thob et al. (2019) used the flattening, $\epsilon = 1 - S$, rather than the sphericity but, as is clear from their definitions, the two are interchangeable.

[2] Thob et al. (2019) present publicly available Python routines for this procedure at https://github.com/athob/morphokinematics.

distribution tensor (e.g. Davis et al., 1985; Cole & Lacey, 1996), defined as:

$$M_{ij} = \frac{\sum_p m_p r_{p,i} r_{p,j}}{\sum_p m_p}, \tag{3.1}$$

where the sum runs over all particles, p, comprising the structure, $r_{p,i}$ denotes the $i^{\rm th}$ component ($i, j = 0, 1, 2$) of each particle's coordinate vector with respect to the galaxy centre, and $m_{\rm p}$ is the particle's mass. As has been widely noted elsewhere, the mass distribution tensor is often referred to as the moment of inertia tensor, as the two share common eigenvectors.

There are several well-motivated alternative choices to the mass distribution tensor and, as per Thob et al. (2019), we elect here to use an iterative form of the reduced inertia tensor (see also Dubinski & Carlberg, 1991; Bett, 2012; Schneider et al., 2012). The reduced form is advantageous because its suppresses a potentially strong influence on the tensor of structural features in the outskirts of galaxies, by down-weighting the contribution of particles at a large (ellipsoidal) radius. The use of an iterative scheme is further advantageous because it enables the scheme to adapt to particle distributions that deviate significantly from the initial particle selection. Since the latter is usually (quasi-)spherical, this is particularly relevant for strongly flattened or triaxial systems. This form of the tensor is thus:

$$M^R_{ij} = \frac{\sum_p \frac{m_p}{\tilde{r}_p^2} r_{p,i} r_{p,j}}{\sum_p \frac{m_p}{\tilde{r}_p^2}}, \tag{3.2}$$

where $\tilde{r}_p$ is the ellipsoidal radius, and the superscript R denotes that this is the reduced form of the tensor. In the first iteration, all particles of the relevant species within a spherical aperture of a prescribed radius, $r_{\rm sph}$, are considered. This yields a initial estimate of the axis lengths (a, b, c). In the next iteration, particles satisfying the following condition relating to the ellipsoidal distance are considered:

$$\tilde{r}_p^2 \equiv \frac{r_{p,a}^2}{\widetilde{a}^2} + \frac{r_{p,b}^2}{\widetilde{b}^2} + \frac{r_{p,c}^2}{\widetilde{c}^2} \leq 1, \tag{3.3}$$

where $r_{p,a}$, $r_{p,b}$ and $r_{p,c}$ are the particle radii projected along the eigenvectors of the previous iteration, $\widetilde{a}, \widetilde{b}$ and $\widetilde{c}$ are the re-scaled axis lengths calculated as $\widetilde{a} = a \times r_{\rm sph}/(abc)^{1/3}$. This ensures the ellipsoid maintains a constant volume; in this respect, we differ from the scheme used by Thob et al. (2019), who maintained a constant major axis length between iterations. We opt for this scheme to avoid artificial suppression of the major axis in cases of highly flattened geometry, which is more common when examining star-forming gas than is the case for stellar distributions. We note that our definition of $\tilde{r}_p^2$ differs with respect to that of Thob et al. (2019) by a factor $\tilde{a}^2$, and that often the

normalisation factor $\sum_p m_p/\tilde{r}_p^2$ is not explicitly adopted in the definition of this tensor (see e.g. Bett, 2012, their equation 6). The axis lengths (and by extension, the shape parameters) recovered from the use of either form of the tensor are identical.

Iterations continue until the fractional change in the axis ratios c/a and b/a falls below 1 percent. If this criterion is not satisfied after 100 iterations, or if the number of particles enclosed by the ellipsoid falls below 10, the algorithm is deemed to have failed and the object's morphology is declared unclassified. We find a failure to converge only in cases of low particle number (e.g. subhaloes with very few gas or star particles) and, crucially, our selection criteria (Section 3.2.4) ensure that no subhaloes with unclassified morphologies are included in our sample.

For consistency with the aperture generally used when computing galaxy properties by aggregating particle properties (see e.g. Section 5.1.1. of Schaye et al., 2015), we adopt a radius of $r = 30\,\mathrm{pkpc}$ for the initial spherical aperture. We use this aperture for all three matter types, star-forming gas, stars and DM, and note that for the latter, this focuses our morphology measurements towards halo centres, since haloes are in general much more extended than their cold baryons (see Section 3.2.5). We retain the use of this aperture for the DM component in order to focus on the DM structure local to star-forming gas discs, and note that the *global* morphology of DM haloes in EAGLE was presented by Velliscig et al. (2015a). In Section 3.5 we examine the 2D projected morphology and alignment of galaxies. When performing these measurements for star-forming gas and stars, we use an initial circular aperture of $r = \max(30\,\mathrm{pkpc}, 2r_{1/2,\mathrm{SF}})$, where $r_{1/2,\mathrm{SF}}$ is the half-mass radius of star-forming gas bound to the subhalo. This ensures a robust morphological characterisation of the image projected by the most extended gas discs when viewed close to a face-on orientation.

Equation 3.2 can be generalised to be weighted by any particle variable, rather than its mass. To crudely mimic the morphology of continuum-luminous regions, when computing the tensor for star-forming gas, we weight by their star formation rate (SFR) rather than their mass, since it is well-established that the relationship between SFR and radio continuum luminosity is broadly linear (see e.g. Condon, 1992; Schober et al., 2017). We do not consider radio continuum emission due to AGN, since this is not extended. Pillepich et al. (2019) recently employed a similar approach to assess the morphology and alignment of Hα-luminous regions of star-forming galaxies in the TNG50 simulation, via the use of the SFR as a proxy for the Hα luminosity. The recovered shape parameters and orientation are little changed with respect to the use of particle mass as the weighting variable, or indeed a uniform weighting, largely because the SFR of particles scales as $\dot{m}_\star \propto P^{1/5}$ for a Kennicutt-Schmidt law with index $n_\mathrm{s} = 1.4$ (see Schaye & Dalla Vecchia, 2008) and the pressure distribution of star-forming gas particles is relatively

narrow: at $z = 0$, the 10th and 90th percentiles of the pressure of star-forming particles in the Ref-L100N1504 volume spans less than two decades in dynamic range.

We define the orientation of galaxies and subhaloes as the unit vector parallel to the minor axis of the best-fitting ellipsoid, and hence measure the relative alignment of structures as the angle between these unit vectors. We note that it is more typical in the literature to use the unit vector parallel to the major axis; this is arguably the best-motivated choice for describing the alignment of systems that are in general prolate (e.g. DM haloes), since in such systems the major axis is the most 'distinct'. In contrast, it is the minor axis that is the most distinct in systems that are preferentially oblate, as is the case for a flattened disc. In Section 3.4.2 we examine the correspondence between the morphological and kinematic axes of the star-forming gas distribution; we define the latter as the unit vector parallel to the angular momentum vector of all star-forming gas particles located within 30 pkpc of the galaxy centre.

3.2.4 Sample selection

We identify subhaloes comprising a minimum of 100 each of star-forming gas particles, stellar particles and DM particles. This numerical threshold is motivated by tests, presented in Appendix 3.7.3 and 3.7.4, that assess the fractional error on shape parameters induced when performing the measurement on subsamples, randomly selected and of decreasing size, of the particles comprising exemplar subhaloes. These tests indicate that a minimum of 100 particles are needed to recover a measurement error of the flattening of star-forming gas discs of less than 10 percent, when using the iterative reduced inertia tensor. We perform a similar test to determine the effect of sampling on the retrieved orientation, and find that a minimum of 100 particles are sufficient to be offset from the 'true' orientation by $< 2°$. We further find that systems that are more flattened require fewer particles in order to accurately retrieve the orientation of their minor axis. As noted by Thob et al. (2019), the sphericity and triaxiality shape parameters are poor descriptors of systems that deviate strongly from axisymmetry, so we excise subhaloes with strongly non-axisymmetric star-forming gas distributions. We quantify this characteristic by adapting the method of Trayford et al. (2019), binning the mass of star-forming gas into pixels of solid angle about the galaxy centre using HEALPIX (Górski et al., 2005). The asymmetry of the star-forming gas distribution, $A_{\rm 3D}$, is then computed by summing the (absolute) mass difference between diametrically opposed pixels and normalising by the total star-forming gas mass. As per Trayford et al. (2019), we use coarse maps of 12 pixels, and exclude systems with $A_{\rm 3D}^{\rm SFG} > 0.6$. This criterion excises 534 subhaloes, mostly of low mass, and leaves us with a sample of 6,764 subhaloes at $z = 0$.

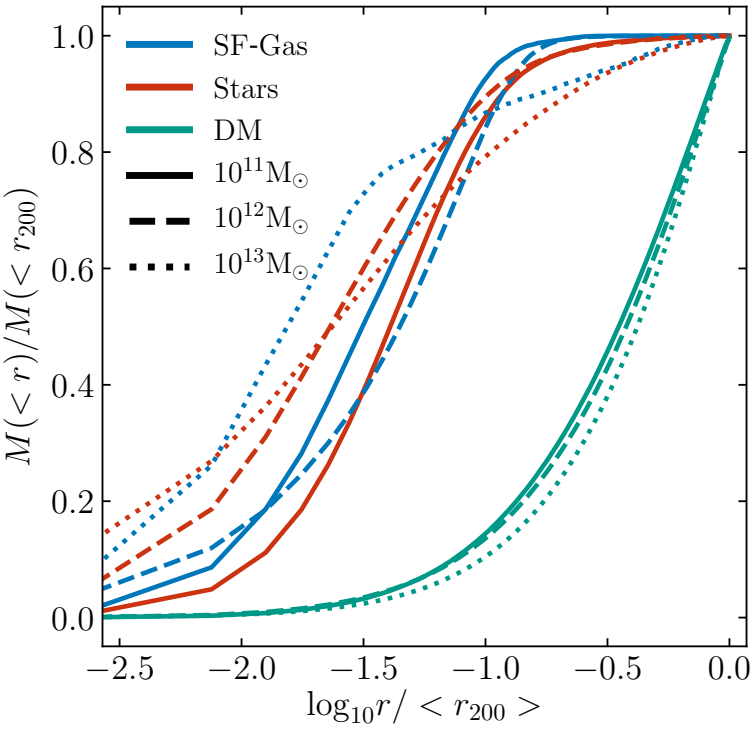

FIGURE 3.1: Mean, spherically averaged cumulative radial mass distribution profiles of the star-forming gas (blue curve), stars (red), and DM (green) of central subhaloes within our sample that have a halo mass $M_{200} \sim 10^{11}$ M$_\odot$ (solid curve), 10^{12} M$_\odot$ (dashed), and 10^{13} M$_\odot$ (dotted). The distributions are normalised relative to the total mass of each component within r_{200}. Star-forming gas is much more centrally concentrated than dark matter at all masses.

Our selection criteria, in particular the requirement for subhaloes to be comprised of at least 100 particles each of stars and star-forming gas, impose a strong selection bias at low halo masses. In practice, for simulations at the resolution of the EAGLE Ref-L100N1504 simulation, the criteria dictate that subhaloes host a galaxy with a minimum stellar of mass of $\sim 10^8$ M$_\odot$ and a minimum SFR of $\simeq 6 \times 10^{-2}$ M$_\odot$yr^{-1}, where the latter assumes the star-forming particles have a density of 0.1 cm^{-3} and pressure corresponding to a temperature of 8000 K. This corresponds to a specific star formation rate (sSFR) of 6×10^{-10} yr^{-1} for the lowest (stellar) mass galaxies, a value that is above the canonical threshold separating the blue cloud of star-forming galaxies and the red sequence of quenched counterparts (e.g. Schawinski et al., 2014). Our selection criteria result in the selection of approximately (0.1, 10, 80) percent of all subhaloes of mass $\log_{10}(M_{\rm sub}/\,{\rm M}_\odot) \sim (10, 11, 12)$, respectively, corresponding to approximately (16, 65, 60) percent of all subhaloes of stellar mass $\log_{10}(M_\star/\,{\rm M}_\odot) \sim (9, 10, 11)$.

3.2.5 Mass distribution profiles

Prior studies have demonstrated that the shape and orientation of stars and DM in haloes can vary significantly as a function of radius (see e.g. Velliscig et al., 2015a). Fig. 3.1 shows the mean, spherically averaged, cumulative radial mass distribution profiles of the star-forming gas (blue curve), stars (red), and DM (green) comprising present-day central subhaloes with halo mass in ranges $M_{200} \sim 10^{11}$ M$_\odot$ (solid curves), 10^{12} M$_\odot$ (dashed), and 10^{13} M$_\odot$ (dotted). As might be naïvely expected, the baryonic components are much more centrally concentrated than the DM, in each of the subhalo mass bins: the median half-mass radius of star-forming gas is $(3, 4.5, 1.5)$ percent of r_{200} for the low, middle and high mass bins respectively, compared with $(35, 37, 42)$ percent of r_{200} for the DM.[3] The standard deviation for the curves is generally highest for the star-forming gas and lowest for the dark matter. The standard deviation also decreases with increased subhalo mass, in part due to the lower sampling of objects in higher mass bins. The standard deviations are typically largest at intermediate radii. At $r \sim 0.1 r_{200}$, $\sigma_{\rm SF-gas} = 0.08,\ 0.12$ and 0.04 for the three mass bins in ascending order, respectively. At the same radius $\sigma_{\rm Stars} = 0.069,\ 0.051$ and 0.051, and $\sigma_{\rm DM} = 0.026,\ 0.020$ and 0.016. Owing to the central concentration of the star-forming gas, we do not consider here how the shape parameters of the star-forming gas distribution change in response to the use of an initial aperture that envelops an ever-greater fraction of the virial radius.

3.3 The morphology of star-forming gas

We begin with an examination of the morphology of star-forming gas associated with subhaloes. To illustrate visually how the method described in Section 3.2.3 yields shape and orientation diagnostics for the simulated galaxies, we show in Fig. 3.2 the star formation rate surface density, $\Sigma_{\rm SFR}$, of star-forming gas (upper row), in face-on and edge-on views, and the mass surface density of stars ($\Sigma\star$, bottom left-hand panel) and DM ($\Sigma_{\rm DM}$, bottom right-hand panel) of a present-day star-forming galaxy from Recal-L025N0752. The galaxy is taken from the high-resolution Recal-L025N0752 run, and its stellar mass is $M_\star = 10^{10.5}\,{\rm M}_\odot$, with a subhalo mass of $M_{\rm sub} = 10^{12.4}\,{\rm M}_\odot$. The galaxy's sSFR is $\dot{M}_\star/M_\star = 10^{-10.5}$ yr^{-1}, and it exhibits reasonably strong rotational support. We quantify rotational support via the $\kappa_{\rm co}$ parameter presented by Correa et al. (2017), which reflects the fraction of kinetic energy invested in ordered rotation, considering only

[3] The figures for the low subhalo mass bin are significantly influenced by our sample selection criteria: removal of the minimum particle number criterion results in the inclusion of systems with less-extended star-forming gas distributions, and further reduces the characteristic half-mass radius of the star-forming gas.

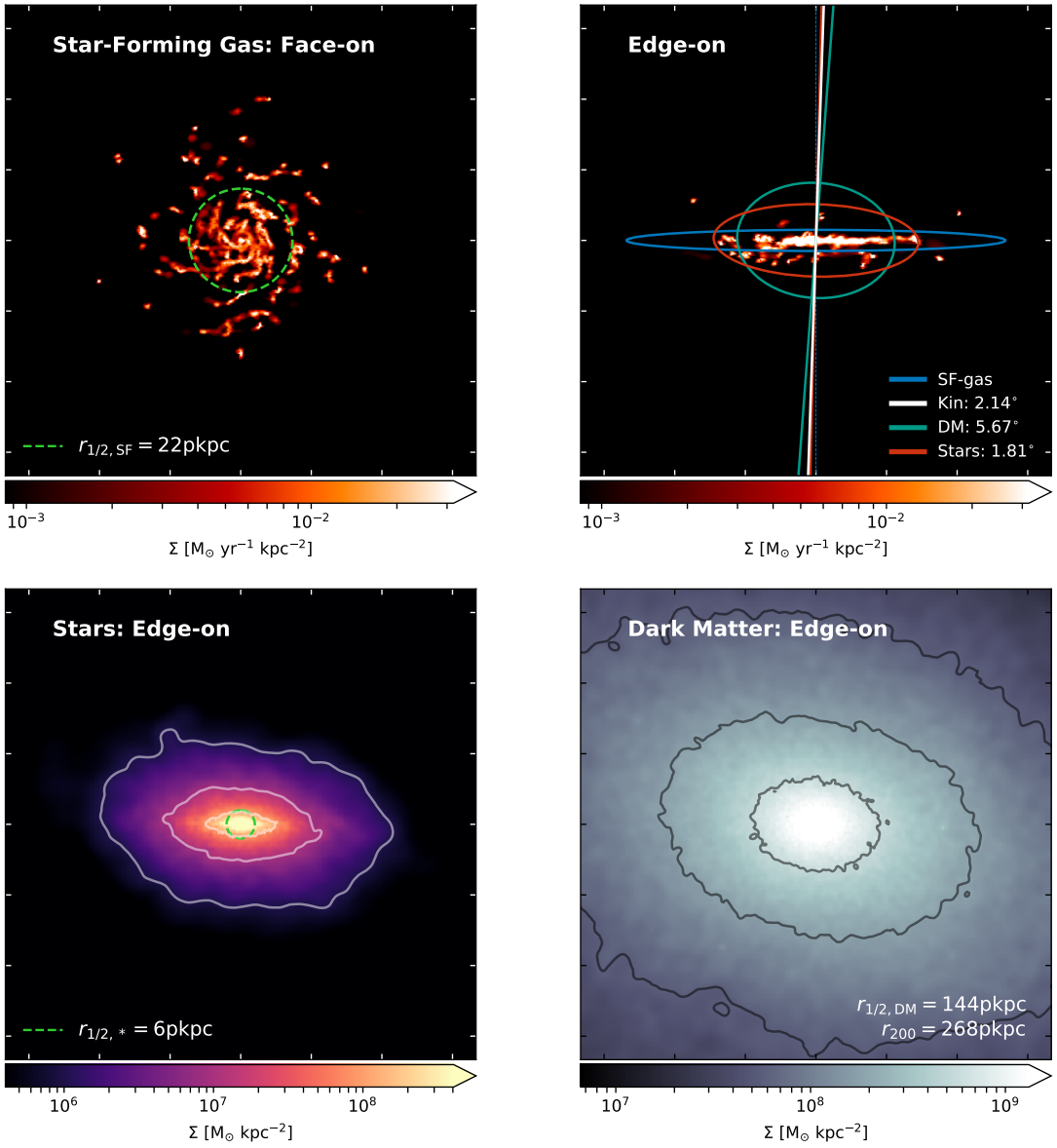

FIGURE 3.2: The star-forming gas, stars and dark matter (DM) comprising a star-forming central galaxy drawn from Recal-L025N0752, with stellar mass $M_\star = 10^{10.5}$ M$_\odot$. Each panel is 200 pkpc on a side. The galaxy's subhalo mass is $M_{\mathrm{sub}} = 10^{12.4}$ M$_\odot$, and its sSFR is $\dot{M}_\star/M_\star = 10^{-10.5}$ yr^{-1}. The upper panels show the star formation rate surface density, a simple proxy for the radio continuum surface brightness, viewed face-on and edge-on. The green circle in the upper left-hand panel denotes the spherical half-mass radius of star-forming gas within 30 pkpc. Ellipsoids in the upper right-hand panel show projections of the best-fitting ellipsoids of the three matter components recovered by the iterative reduced inertia tensor. Overlaid solid lines show the minor axis of the stars (red), and DM (green), whilst the white line corresponds to the rotation axis. The SF-gas is much flatter ($S = 0.06$) than the stars ($S = 0.35$) and DM ($S = 0.73$). The lower panels show the surface densities of stars (left-hand panel) and DM (right-hand panel). Overlaid contours denote surface densities of $\log_{10}(\Sigma_\star) = 6$, 7, 8 M$_\odot$kpc^{-2} and $\log_{10}(\Sigma_{\mathrm{DM}}) = 7.75, 8.25, 8.75$ M$_\odot$kpc^{-2} for the stars and DM respectively. The spherical half-mass radii for the stars and dark matter are 6 pkpc and 144 pkpc respectively. These images have been made using the publicly available code Py-SPHViewer (Benitez-Llambay, 2015)

particles which follow the direction of rotation of the galaxy as a whole. This initially follows Sales et al. (2010), where $\kappa_{\rm rot}$ is defined as

$$\kappa_{\rm rot} = \frac{K_{\rm rot}}{K} = \frac{1}{K} \sum_{i}^{r<30\,{\rm pkpc}} \frac{1}{2} m_i (L_{z,i}/(m_i R_i))^2, \tag{3.4}$$

summing over stellar particles within 30 pkpc of the centre of potential. Here m_i is defined as the mass of stellar particle i, $K = \sum_i^{r<30\,{\rm pkpc}} m_i v_i^2$ is the total kinetic energy, $L_{z,i}$ is the angular momentum of the particle along the direction of the total stellar angular momentum, and R_i is the projected distance between the particle and the axis of rotation. The $\kappa^{\star}_{\rm co}$ parameter of Correa et al. (2017) differs from this by computing $K_{\rm rot}$ only for particles with positive $L_{z,i}$, i.e. following the rotation of the galaxy. Correa et al. (2017) argues that $\kappa^{\star}_{\rm co} > 0.4$ is a useful and simple criterion for identifying star-forming disc galaxies in EAGLE. For the galaxy presented in Fig. 3.2, $\kappa^{\star}_{\rm co} = 0.44$. The star-forming gas exhibits a very high degree of rotation support, $\kappa_{\rm co}^{\rm SF-gas} = 0.97$.

The field of view of each panel is 200 pkpc, and overlaid dashed green circles denote the half-mass radius of the matter type in question. Edge-on images are aligned such that horizontal and vertical image axes are parallel to the major and minor axes, respectively, of the star-forming gas distribution. In the upper right-hand panel, coloured ellipses correspond to projections of the best-fitting ellipsoids describing the respective matter components, whilst the solid coloured lines show the (projected) minor axes of the stellar and DM distributions, and the white line shows the projected rotation axis of the star-forming gas. Contours overlaid on the stellar and DM surface density images correspond to surface densities of $\log_{10}(\Sigma_\star) = 6,\ 7,\ 8\ {\rm M}_\odot{\rm kpc}^{-2}$ and $\log_{10}(\Sigma_{\rm DM}) = 7.75, 8.25, 8.75\ {\rm M}_\odot{\rm kpc}^{-2}$, respectively.

As expected for a galaxy whose gas disc has strong rotational support, the star-forming gas distribution is much more flattened than the corresponding distributions of stars and DM. In this example, the distributions of the three matter components are well aligned: the minor axis of the star-forming gas is misaligned with respect to that of the stars by $\simeq 2$ deg and the DM by $\simeq 6$ deg. As shown in Section 3.7.3, these offsets are comparable to the measurement uncertainty for well-resolved and well-sampled structures. The rotational axis of the star-forming gas is also closely aligned with the minor axis in this example, as naïvely expected for an extended, rotationally supported disc.

3.3.1 Shape parameters as a function of subhalo mass

Fig. 3.3 shows probability distribution functions (PDFs) of the shape parameters of the star-forming gas (blue curves), stellar (red) and DM (green) distributions of the

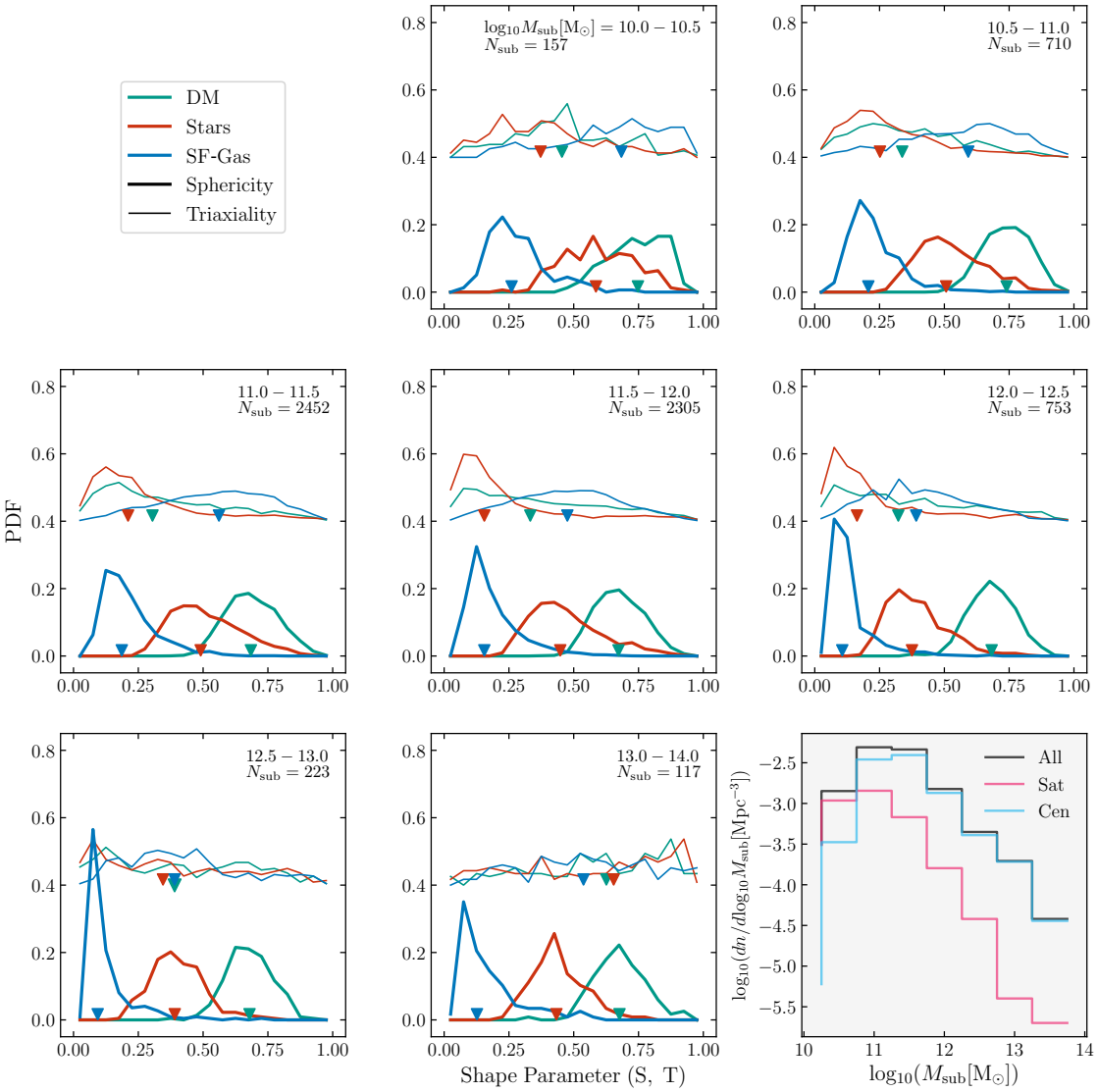

FIGURE 3.3: Probability distribution functions (PDFs) for the sphericity and triaxiality of the star-forming gas (blue), stars (red), and DM (green) comprising sampled subhaloes in Ref-L100N1504 at $z = 0$. Subhaloes are binned by their total mass. The triaxiality PDFs have been raised artificially by 0.4 for clarity. The arrows represent the location of the median for each distribution. The bottom right-hand panel shows volume density function of the satellite and central galaxies. For all subhalo masses, the star-forming gas is significantly more flattened than the stars and DM, and the distribution of the sphericity parameter for star-forming gas is particularly narrow in $\sim L^\star$ galaxies. Star-forming gas does not exhibit a characteristic triaxiality, spanning a wide range of T at all subhalo masses.

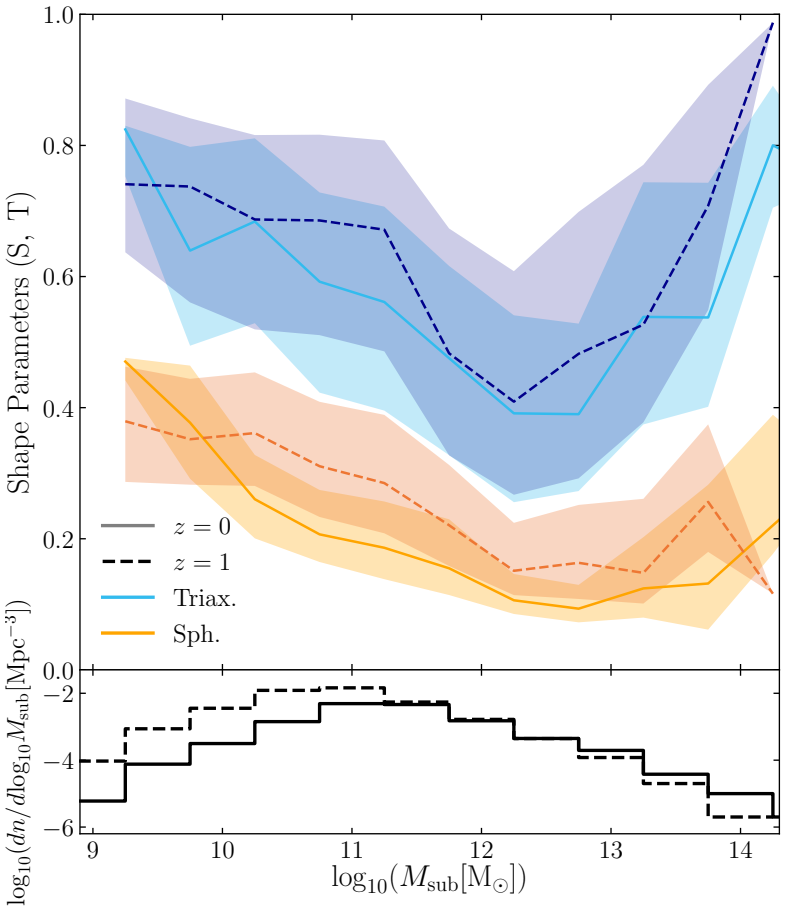

FIGURE 3.4: The median sphericity and triaxiality of the star-forming gas distribution of subhaloes, as a function of subhalo mass, at $z = 0$ and $z = 1$ in bins of 0.5 dex. Shaded regions denote the interquartile range. The orange and blue curves correspond to the sphericity and triaxiality, whilst solid and dashed curves correspond to $z = 0$ and $z = 1$, respectively. The lower panel shows the volumetric mass function of the sampled subhaloes.

subhaloes comprising our sample from Ref-L100N1504 at $z = 0$. We reiterate that measurements of the stellar and DM distributions are included here, despite being previously presented for EAGLE subhaloes by Velliscig et al. (2015a), because we use an alternative form of the mass distribution tensor. Thick and thin lines represent the sphericity and triaxiality parameters respectively. Each panel shows subhaloes split by total mass in bins of 0.5 dex, spanning $M_{\rm sub} = 10^{10} - 10^{14}$ M$_\odot$. For clarity, the PDFs of triaxiality have been artificially elevated in the vertical axis by an increment of 0.4. Down arrows denote the median value of each distribution. The bottom right-hand panel shows the volumetric subhalo mass function, split into central and satellite subhalo populations, highlighting that the sample is dominated by central galaxies at all subhalo masses except for the lowest mass bin. For clarity, we also show the median values of the shape parameters for star-forming gas as a function of subhalo mass in Fig. 3.4. The solid and dashed curves of that plot correspond to the samples, identified as discussed in Section

$\log_{10} M_{\rm sub}$ [$\rm M_\odot$]	Sphericity, S			Triaxiality, T		
	SF-gas	Stars	DM	SF-gas	Stars	DM
10.0-10.5	0.13	0.21	0.16	0.28	0.27	0.26
10.5-11.0	0.11	0.18	0.13	0.31	0.24	0.31
11.0-11.5	0.12	0.19	0.14	0.31	0.23	0.36
11.5-12.0	0.12	0.18	0.13	0.29	0.2	0.41
12.0-12.5	0.06	0.15	0.12	0.29	0.23	0.4
12.5-13.0	0.06	0.14	0.11	0.26	0.48	0.48
13.0-14.0	0.14	0.13	0.13	0.37	0.51	0.38

TABLE 3.2: Interquartile ranges of the distributions of the sphericity (S) and triaxiality (T) shape parameters of the star-forming gas (SF-gas), stars and dark matter (DM) comprising subhaloes in our sample, as a function of subhalo mass.

3.2.4, at $z = 0$ and $z = 1$, respectively. The lower panel of the figure shows the subhalo volumetric mass function at the two epochs.

These figures show that the distribution of sphericities of star-forming gas distributions is peaked at relatively low values for all subhalo masses, but with a long tail towards high S (i.e. quasi-spherical systems). The median value of the distributions, which is qualitatively similar to the peak value of the distribution, declines from $\tilde{S} \simeq 0.25$ for subhaloes of $M_{\rm sub} \sim 10^{10}$ $\rm M_\odot$, to a minimum of $\tilde{S} \simeq 0.1$ at $M_{\rm sub} \sim 10^{12.5}$ $\rm M_\odot$. The sphericity of the star-forming gas is therefore systematically lower than is the case for that of the stars, and much more so than is the case for the DM, consistent with the naïve expectation that this dissipational component is found primarily in flattened discs. Broadly, the peaks of the sphericity PDFs of stars and DM are found at $S \simeq 0.3-0.5$ and $S \simeq 0.7-0.75$, respectively, irrespective of subhalo mass. Thob et al. (2019) noted that present-day galaxies whose stellar component exhibit a sphericity of $S \lesssim 0.6$ generally exhibit stellar corotation kinetic energy fractions of $\kappa^\star_{\rm co} > 0.4$ and so correspond broadly to blue, star-forming disc galaxies (Correa et al., 2017). Despite our use of an initial 30 pkpc aperture for the mass tensor, the median values of the sphericity of the stars and DM are broadly consistent with those recovered by Velliscig et al. (2015a) when applying the standard mass distribution tensor to the entirety of EAGLE subhaloes, and those recovered by Tenneti et al. (2014) for subhaloes in the MassiveBlack-II simulation in the mass range for which our respective selection criteria recover broadly similar samples of galaxies ($M_{\rm sub} \gtrsim 10^{11}$ $\rm M_\odot$). Similarly, the distribution of sphericities of star-forming gas discs are consistent with those recovered by Pillepich et al. (2019) when applying the standard mass distribution tensor to galaxies in the TNG50 simulation. We remark that we have also computed the morphology of star-forming gas structures using an iterative form of the simple mass tensor (equation 3.1), and do not find a significant systematic change.

The sphericity of star-forming gas is most uniform in subhaloes of intermediate mass,

$M_{\rm sub} \sim 10^{11.5-13}\,{\rm M}_\odot$. In such structures, the distribution of S is strongly peaked at low values corresponding to flattened discs, albeit with a long tail to more spherical configurations. Owing to this asymmetry, which is most prominent for the star-forming gas, we quantify the diversity of the shape parameter distributions via the interquartile range (IQR) rather than their variance (see Table 3.2). The IQR of the star-forming gas sphericity decreases from 0.13 for subhaloes of $\log_{10}(M_{\rm sub}/\,{\rm M}_\odot) = 10 - 10.5$ to a minimum of 0.06 for subhaloes of $\log_{10}(M_{\rm sub}/\,{\rm M}_\odot) = 12 - 13$, before increasing again to 0.14 for the most massive haloes in our sample. The greater diversity in low-mass subhaloes is driven largely by stochasticity in the structure of star-forming gas, with star formation in many low-mass galaxies being confined to a small number of gas clumps rather than being distributed throughout a well-defined disc. In massive subhaloes, cold gas discs are readily disturbed by outflows driven by efficient AGN feedback (see e.g. Bower et al., 2017; Oppenheimer et al., 2020), and are less readily replenished with high-angular momentum gas from coherent circumgalactic inflows (see e.g. Davies et al., 2020, 2021).

A potentially surprising finding highlighted by Figs. 3.3 and 3.4 is that the characteristic morphology of present-day star-forming gas distributions can deviate significantly from that of a disc. The characteristic triaxiality of star-forming gas in subhaloes of mass $M_{\rm sub} \sim 10^{12-12.5}\,{\rm M}_\odot$ is $T < 0.5$, consistent with a flattened, oblate spheroid. Subhaloes of all masses exhibit a broad distribution of T, in marked contrast with that of S, and for subhaloes in the lower and higher mass bins, the median value is $T > 0.5$, signifying that the characteristic morphology is prolate, such that even though the structures are flattened, their isodensity contours when viewed face-on deviate significantly from circular. A similar finding from the TNG50 simulation was recently reported by Pillepich et al. (2019). Inspection of face-on projections of the star-forming gas surface density highlights that this behaviour again stems primarily from the stochasticity of star-forming gas structure in low-mass subhaloes. In more massive subhaloes, stochasticity is also relevant, owing to the efficient disruption of well-sampled cold gas discs by AGN feedback. However we note that the stellar and DM components tend towards more prolate configurations in more massive subhaloes (as has been widely reported elsewhere, e.g. Tenneti et al., 2014; Velliscig et al., 2015a), suggesting that the morphology of the gravitational potential may influence that of the cold gas. We examine this further in Section 3.3.3.

As previously noted by Velliscig et al. (2015a), the triaxiality of the stars and DM in EAGLE subhaloes increases as a function of the subhalo mass, such that these components in the most-massive structures are strongly prolate. We note that our quantitative measures are however slightly lower than those reported by Velliscig et al. (2015a), owing to our use of an initial 30 pkpc aperture and the reduced inertia tensor, which ascribes

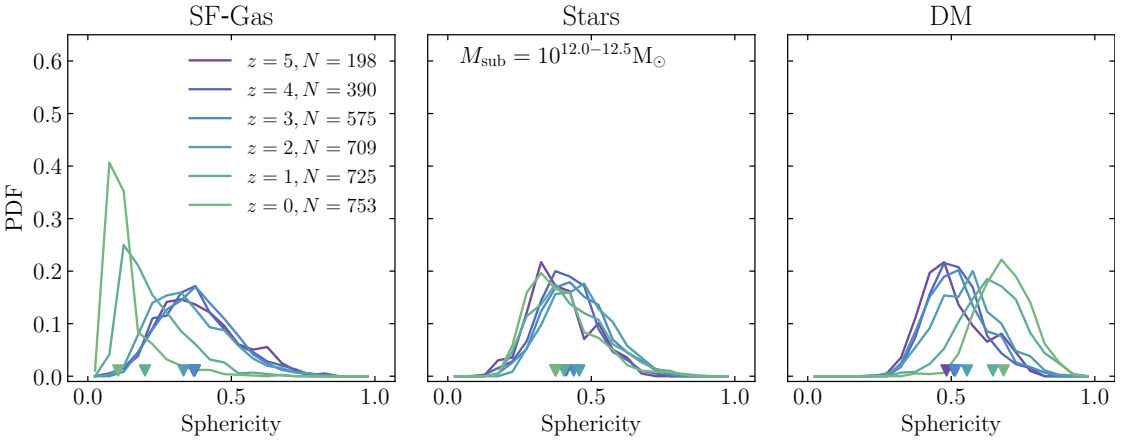

FIGURE 3.5: The sphericities of the three matter components (star-forming gas, stars and DM, from left to right, respectively) comprising subhaloes of present-day mass $\log_{10}(M_{\rm sub}/\,{\rm M}_\odot) = 12 - 12.5$, and their main progenitor subhaloes at $z = (1, 2, 3, 4, 5)$. The latter are included only whilst still satisfying the $z = 0$ selection criteria, so the sample size N, shown in the legend of the left-hand panel, is a monotonically declining function of redshift. The arrows represent the location of the median for each distribution. The characterisation of the matter distributions with the iterative reduced inertia tensor indicates that DM becomes more spherical at late cosmic epochs, the stellar distribution evolves mildly towards a more flattened configuration, and the star-forming gas typically evolves strongly towards a very flattened configuration by the present-day.

less weight to morphology of these structures at large (elliptical) radius. It is well established from prior studies that the condensation of baryons in halo centres drives the morphology towards a more spherical configuration than is realised in dark matter-only simulations (see e.g. Dubinski, 1994; Katz et al., 1994; Kazantzidis et al., 2004; Springel et al., 2004; Zemp et al., 2012).

3.3.2 Shape parameters at $z > 0$

We now turn to the morphology of subhaloes at $z > 0$, for which we take two approaches. First, we identify subhaloes at $z = 1$ (which, for our adopted cosmogony, corresponds to a lookback time of 8.1 Gyr) that satisfy the selection criteria specified in Section 3.2.4, and compare the shape parameters of the samples at these epochs. We subsequently explore the evolution of the shape parameters of the main progenitors of subhaloes that satisfy the selection criteria at $z = 0$. Clearly, these approaches require the examination of increasingly dissimilar subhalo samples as one advances to higher redshift.

The evolution of the characteristic morphology of the star-forming gas for identically selected samples at $z = 0$ and $z = 1$, respectively, can be assessed from comparison of the solid and dashed curves of Fig. 3.4. These curves denote the median values of the shape parameters (sphericity in orange, triaxiality in blue) as a function of subhalo mass,

whilst the shaded regions correspond to the interquartile range. The darker (lighter) shaded areas for each parameter correspond to $z = 1$ ($z = 0$).

It reveals that cold gas structures of fixed subhalo mass, for $\log_{10}(M_{\rm sub}/\,{\rm M}_\odot) \gtrsim 10$, are slightly more spherical (i.e. less flattened) at $z = 1$ than the present-day. However this difference (< 0.1 for all subhalo masses) is smaller than, or comparable to, the interquartile range of S at either epoch, which varies between 0.03 and 0.22 at $z = 0$ and 0.11 and 0.19 at $z = 1$, over the subhalo mass range from $\log_{10}(M_{\rm sub}/\,{\rm M}_\odot) = 9-14$. Similarly, the star-forming gas in subhaloes of the same mass tends to be less oblate / more prolate at $z = 1$ than the present-day, but again the difference is small in comparison to the scatter at fixed subhalo mass. We note that the trend for sphericity is in marked contrast with the qualitative behaviour of the DM, for which there is a consensus that structures become more spherical with advancing cosmic time (see e.g. Bryan et al., 2013; Tenneti et al., 2014; Velliscig et al., 2015a).

Fig. 3.5 shows the sphericity PDFs of the three matter components (star-forming gas, stars and DM from left to right, respectively) of the main progenitor subhalo, at $z = (0, 1, 2, 3, 4, 5)$, of present-day central subhaloes with mass $\log_{10}(M_{\rm sub}/\,{\rm M}_\odot) = 12.0 - 12.5$. Such subhaloes broadly correspond to those that host present-day $\sim L^\star$ galaxies. The progenitors are identified using the D-Trees algorithm (Jiang et al., 2014). The D-Trees algorithm considers the $N_{\rm link}$ most bound particles of any species, and at the next output time identifies the subhalo containing the majority of these particles as a descendent. $N_{\rm link}$ is defined as $N_{\rm link} = \min(100,\ \max(0.1 \times N_{\rm galaxy},\ 10))$, where $N_{\rm galaxy}$ is the number of particles in the parent subhalo. This methodology has the advantage of tracking descendants even in instances when the majority of particles are stripped (Fakhouri & Ma, 2008; Genel et al., 2009). A given galaxy can have only one descendent, but can have multiple progenitors. The main branch progenitor is defined as the progenitor with the largest summed mass *along its branch*, rather than simply the largest instantaneous mass (De Lucia & Blaizot, 2007). This has the advantage of being resilient to main branch swapping in the case of similar mass mergers. A full description of its application to the EAGLE simulations is provided by Qu et al. (2017). The standard 30 pkpc aperture is used at all redshifts[4]. Progenitor subhaloes are included in the $z > 0$ samples only while they still satisfy the selection criteria concerning particle number and asymmetry, to ensure that a robust measurement of their shape parameters can be made. As such, the sample size, N, is a monotonically declining function of redshift, as denoted in the legend of the left-hand panel of the figure.

[4]We have assessed the impact of using an adaptive aperture of initial spherical radius $r = 0.15\, r_{200}(z)$, to account for the decreasing physical size of progenitors at early times, and do not recover significant differences.

We saw from Fig. 3.3 that present-day galaxies hosted by subhaloes in this mass range typically exhibit strongly flattened ($S \simeq 0.1$) star-forming gas discs. The left-hand panel of Fig. 3.5 highlights that, although star-forming gas discs are predominantly flattened[5] even at early epochs, the median sphericity at $z = 5$ is $\tilde{S}_{\rm SF-gas} \simeq 0.37$. The star-forming gas of the main progenitor becomes increasingly flattened with advancing cosmic time, but the emergence of strongly flattened discs ($S \lesssim 0.2$) is generally limited to $z < 2$: the median sphericity evolves from $\tilde{S}_{\rm SF-gas} \simeq 0.33$ at $z = 2$ to $\tilde{S}_{\rm SF-gas} \simeq 0.1$ at $z = 0$. The strong evolution of the star-forming gas sphericity of these progenitors is broadly coincident with the growth of the gas disc's median scale length, which grows only from $\simeq 2\,$pkpc to $\simeq 3\,$pkpc from $z = 5$ to $z = 2$, but by $z = 0$ reaches $\simeq 9\,$pkpc. The decrease in the accretion rate (of all matter types) onto the galaxy+halo ecosystem at later epochs (see e.g. Fakhouri et al., 2010; van de Voort et al., 2011) likely also results in a steady decline of the scale height of the gas disc (e.g. Benítez-Llambay et al., 2018), further contributing to decrease in sphericity. In a later chapter (Section 4.4.2), we present results relating to the redshift evolution of 2 dimensional morphology, considering suhhaloes of all masses and merger histories. We find similar results to those presented here, suggesting that the redshift evolution of $z = 0$ Milky Way-mass systems and their progenitors is broadly representative of the total population.

Strong evolution of the structural parameters of star-forming gas was similarly reported by Pillepich et al. (2019) based on analysis of the TNG50 simulation. Those authors noted that the evolution of the flattening ('disciness' in their terminology, since they also examined kinematic descriptions) of both the star-forming gas and stars increases over time, but that the evolution for the former is much more pronounced than the latter. The same behaviour is evident in EAGLE, as is clear from inspection of the centre panel of Fig. 3.5, which shows that the sphericity of the stellar component of the progenitors of our present-day $\sim L^{\star}$ galaxy sample is largely insensitive to redshift. The majority of the galaxies comprising our sample remain actively star-forming at $z = 0$, and are characterised by flattened discs ($\tilde{S}_{\star} \simeq 0.4 - 0.45$ at all redshifts examined). Such galaxies will therefore have assembled primarily via in-situ star formation (Qu et al., 2017) and will not have experienced the strong morphological evolution that typically follows internal quenching (see e.g. Davies et al., 2020, 2021). Furlong et al. (2017) showed that the half-mass radius of the stellar component of present-day star-forming $\sim L^{\star}$ galaxies grows only from $\simeq 10^{0.5}\,$pkpc to $\simeq 10^{0.85}\,$pkpc between $z = 2$ and $z = 0$.

As noted above, it has been shown elsewhere that DM haloes, even in the absence of dissipative baryon physics, tend to become more spherical with advancing cosmic time (e.g. Bryan et al., 2013; Tenneti et al., 2014; Velliscig et al., 2015a), in marked contrast

[5] For context, we reiterate that, as noted in Section 3.3.1, present-day galaxies with a stellar component sphericity of $S \lesssim 0.6$ are broadly equivalent to star-forming disc galaxies.

to the behaviour seen for the star-forming gas. The right-hand panel of Fig. 3.5 shows that this effect is clearly seen for the host subhaloes of present-day $\sim L^{\star}$ galaxies, even when focusing primarily on the halo centre by defining the shape parameters via the use of the iterative reduced mass tensor. The resolved progenitors exhibit a median sphericity of $\tilde{S}_{\rm DM} \simeq 0.5$ at $z = 5$, and this median increases monotonically to $\tilde{S}_{\rm DM} \simeq 0.7$ at $z = 0$. A possible explanation for this evolution is prediction that mass is the primary driver of halo shape (Allgood et al., 2006), and the fact that haloes grow more massive at lower redshifts.

Besides the evolution of the median sphericity of the matter components, it is interesting to consider the evolution of their diversity. Since the PDFs can exhibit significant asymmetry, we characterise this diversity using the interquartile range. Whilst the IQR of the star-forming gas sphericity decreases markedly at later cosmic epochs (c.f 0.18 at $z = 5$ to $= 0.06$ at $z = 0$), that of the stars and the DM remain components remain largely unchanged from $z = 5$ to $z = 0$, with values of 0.13 to 0.14 for the stars and 0.14 to 0.12 for the DM.

3.3.3 Correspondence of star-forming gas and stellar structure

We noted in the Section 3.3.1 that the star-forming gas configuration in massive subhaloes is often well described by a flattened prolate spheroid, similar to the characteristic morphology of the stars and DM in such structures. Thob et al. (2019) previously demonstrated that EAGLE galaxies with flattened stellar distributions are preferentially hosted by flattened DM haloes, motivating a closer examination here of the degree to which the morphology of the star-forming gas correlates with that of the other matter components. Since the density of stars typically dominates over the density of dark matter within the region traced by the star-forming gas, we focus on the correspondence between the morphology of the star-forming gas and the stars.

The main panels of Fig. 3.6 show, as a function of subhalo mass, the sphericity (left-hand panel) and triaxiality (right-hand panel) of the star-forming gas distributions of the subhaloes comprising our sample. The distribution is shown as a 2D histogram, and black curves denote the running median of the star-forming gas shape parameters, computed via the locally weighted scatterplot smoothing method (LOWESS; e.g. Cleveland, 1979). The LOWESS curves are plotted within the interval for which there are at least 10 measurements at both lower and higher $M_{\rm sub}$. The colour of each hexbin denotes to the median value of the corresponding shape parameter of the *stellar* component: subhaloes in bins denoted by red (blue) colours typically have a stellar component with a high (low) value of the shape parameter in question.

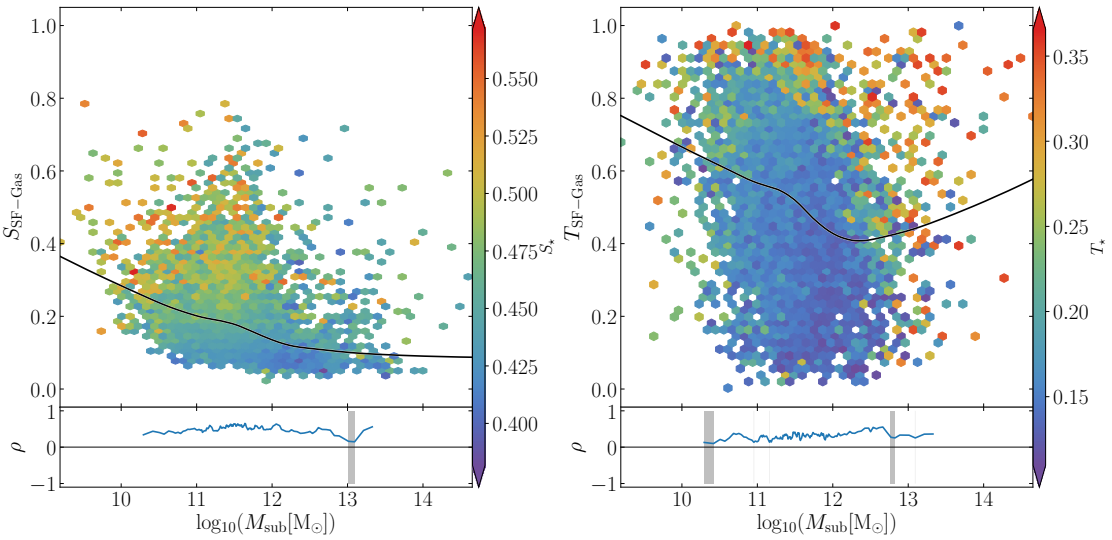

FIGURE 3.6: The sphericity (left-hand panel) and triaxiality (right-hand panel) of the star-forming gas as a function of subhalo mass. Black curves denote the running medians of the shape parameters, computed via the locally-weighted scatterplot smoothing method (LOWESS). Colours represent the median sphericity/triaxiality of the *stellar* mass distributions of the subhaloes represented by each hexbin. The lower panels display the running Spearman rank correlation coefficient, ρ, between the residual shape parameters about $M_{\rm sub}$ for the two matter distributions, i.e. $\Delta S_{\rm SF-gas} - \Delta S_\star$ and $\Delta T_{\rm SF-gas} - \Delta T_\star$, where for instance $\Delta S_{\star,i} = S_{\star,i} - \tilde{S}_\star(M_{{\rm sub},i})$. Grey shaded regions indicate mass ranges for which the correlation is recovered at low significance ($p > 0.05$). The subpanels corroborate, quantitatively, the impression given by visual inspection, that the morphology of the star-forming gas component correlates positively with that of the stellar component.

The shape parameters of the star-forming gas and stellar distributions are strongly and positively correlated at effectively all subhalo masses: flattened star-forming gas distributions are generally found in subhaloes with flattened stellar components, and more prolate star-forming gas distributions are found in subhaloes with more prolate stellar components. We quantify the strength and significance of these correlations by computing a 'running' Spearman rank correlation coefficient, $\rho(M_{\rm sub})$, for the $\Delta S_{\rm SF-gas} - \Delta S_\star$ and $\Delta T_{\rm SF-gas} - \Delta T_\star$ relations, where $\Delta X_{\rm m}$ represents the residual of shape parameter X for matter distribution m about the LOWESS median. Hence, in the case of sphericity, $\Delta S_{\star,i} = S_{\star,i} - \tilde{S}_\star(M_{{\rm sub},i})$ for the $i^{\rm th}$ subhalo. The running Spearman rank correlation coefficient is computed in subhalo mass-ordered subsamples: for bins with a median subhalo mass $M_{\rm sub} < 10^{12.5}{\rm M}_\odot$, we use samples of 200 subhaloes with starting ranks separated by 50 subhaloes (e.g. subhaloes 1-200, 51-250 and 101-300). For bins with median $M_{\rm sub} > 10^{12.5}{\rm M}_\odot$, we use samples of 50 subhaloes with starting ranks separated by 25 subhaloes, to ameliorate the effect of the relative paucity of massive subhaloes. This running $\rho(M_{\rm sub})$ is plotted in the lower subpanel. Regions shaded in grey denote a Spearman rank p-value is > 0.05, and thus indicate where the recovered correlation

cannot be considered significant. As seen in Fig. 3.4, $S_{\rm SF-gas}$ does not change significantly with mass for $M_{\rm sub} > 10^{12}{\rm M}_{\odot}$. The upturn in $T_{\rm SF-gas}$ in this region appears to be caused by a decrease in the intermediate-major axis ratio, $q_{\rm SF-gas}$, with increasing mass. At $M_{\rm sub} \sim 10^{12.5}{\rm M}_{\odot}$, $q_{\rm SF-gas} \sim 0.75$, while at $M_{\rm sub} \sim 10^{14}{\rm M}_{\odot}$, $q_{\rm SF-gas} \sim 0.5$. This indicates that the star-forming gas 'discs' at high mass are increasingly prolate. It is possible that this is driven by increased AGN activity. We leave an exploration of this to future work.

We briefly note the presence of an outlier. The blue bin at high $T_{\rm SF-gas}$ and high subhalo mass in fact contains only one galaxy, with $T_{\rm SF-gas} = 0.99$, $T_{\star} = 0.16$, and $M_{\rm sub} = 10^{13.7}{\rm M}_{\odot}$. The minor-major and intermediate-major axis ratios for the star-forming gas are similar ($\sim$0.21), while those of the stars are quite different (0.57 and 0.94, respectively). We find that such a difference in triaxiality of the two components (0.84) is found in only $\sim$0.1% of the subhaloes in our sample. This system is also fairly unusual in that its star-forming gas is not rotation supported, with $\kappa_{\rm co}^{\rm SF-gas} = 0.27$, a value which is lower than is the case for $> 99\%$ of the subhaloes in our sample. Upon inspection, the star-forming gas is highly clumpy and irregular, with many regions conventionally within the disc not being host to star-formation. In addition, the centre of the star-forming gas distribution is offset from the centre of potential. In short, this is a system which ideally would be excised by our selection criteria, however as it is highly atypical and we wish to avoid selecting galaxies by eye, we retain this galaxy in the analyses presented in the remainder of this Chapter.

The relatively high correlation coefficient ($\rho \gtrsim 0.4$) for the sphericity over a wide range in subhalo mass indicates that the degree of flattening of the two components is indeed strongly and positively correlated. The correlation is weaker ($\rho \gtrsim 0.3$) for the triaxiality parameter, but remains positive and significant over a wide range of subhalo masses. We have also examined the correlation of the shape parameters of star-forming gas with those of their host subhalo's DM, and we find that the correlation is not formally significant at any subhalo mass.

Our results suggest that examination of a large sample of galaxies with high-fidelity radio imaging is likely to reveal significant correlations between the radio continuum and optical morphologies of galaxies. There is not currently a firm consensus amongst observational studies, which are necessarily limited to comparisons of *projected* ellipticities, in regard to correlations between the morphologies of the radio continuum and optical components of galaxies. Battye & Browne (2009) report a strong, positive correlation of the two in late-type galaxies, and a weak negative correlation for early-type galaxies, whilst complementary studies using a smaller sample (Patel et al., 2010), or a sample of

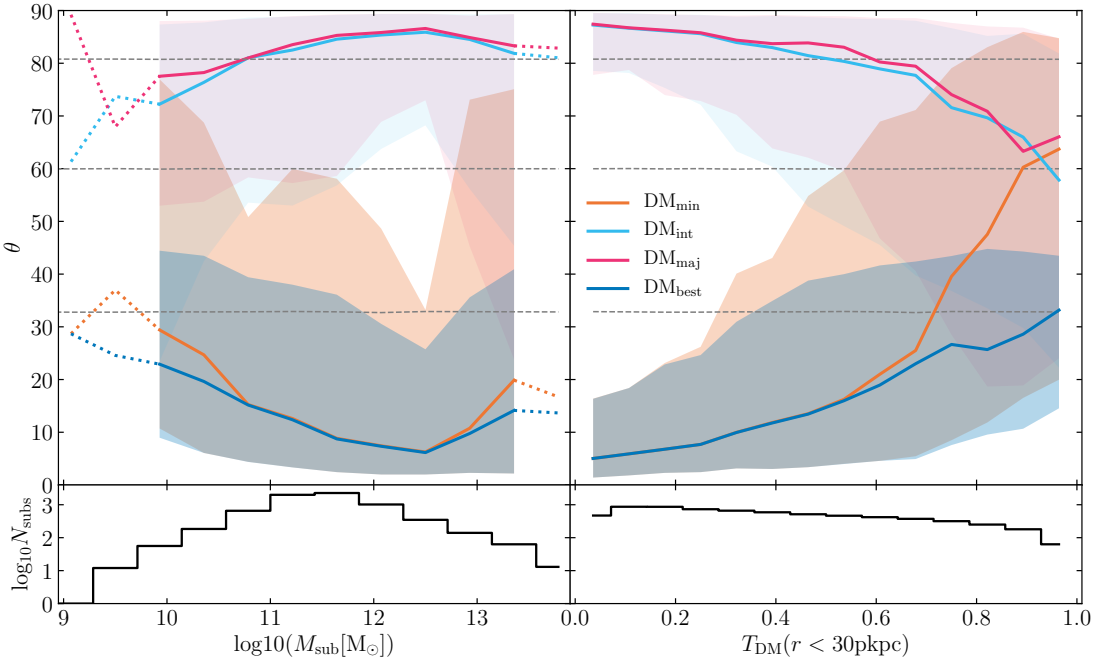

FIGURE 3.7: The misalignment angle, θ, of the minor axis of star-forming gas of our sample of subhaloes with respect to each of the principal axes of their DM distribution. The solid lines indicate the binned median values of θ, whilst the shading denotes the 10th - 90th percentiles. The values are shown as a function of subhalo mass ($M_{\rm sub}$, left-hand panel) and DM triaxiality ($T_{\rm DM}$, right-hand panel). The orange, cyan and magenta curves correspond to the alignment of the star-forming gas minor axis with respect to the minor, intermediate and major axis of the DM, respectively, whilst the blue curve is with respect to the principle DM axis with which the star-forming gas minor axis is most closely aligned. The dotted lines indicate where the sampling drops below 30 subhaloes per bin. Subpanels show the number of subhaloes per bin. The grey dashed lines denote the expected 16th, 50th and 84th percentile values of alignment angles between vectors randomly oriented in 3 dimensions. In general the minor axis of star-forming gas is well aligned with the minor axis of its corresponding DM, but in strongly triaxial subhaloes the former often aligns more closely with the intermediate or major axis of the DM distribution.

fainter, more-distant galaxies (Tunbridge et al., 2016), recovered no significant correlations. More recently, Hillier et al. (2019) examined the correlation of optical and radio continuum measurements of shape and orientation for galaxies in the COSMOS field, and recovered a significant correlation of position angles (projected orientation) between matched 3 GHz radio (VLA) and optical (HST-ACS) images (seen in their Figs. 5 and 6).

3.4 The alignment of star-forming gas with galaxies and their DM haloes

In this section we examine the orientations of the 3D distribution of star-forming gas in galaxies with respect to the stellar and DM components of their host subhaloes. We begin in Section 3.4.1 with an examination of the morphological alignment of subhalo components as a function of subhalo mass, triaxiality and cosmic epoch. In Section 3.4.2 we consider the alignment of the morphological minor axis of the star-forming gas with its kinematic axis.

3.4.1 Morphological alignment of subhalo matter components

We quantify the morphological alignment of the various components via the angle, θ, between the minor axes of the ellipsoids describing each matter distribution, such that $\theta = 0^\circ$ indicates perfect alignment and $\theta = 90^\circ$ indicates orthogonality. As noted in Section 3.2.3, we consider the minor axis to be the natural choice when focusing on discs, as the minor axis is the most distinct axis for oblate discs (though we reiterate the finding from Section 3.3.1 that many flattened star-forming structures are mildly prolate). Moreover, as seen in Section 3.3.1, the central regions of the stellar and DM distributions (to which the iterative reduced mass distribution tensor is more strongly weighted) also tend to be mildly oblate.

Fig. 3.7 shows the alignment between the star-forming gas distribution and that of the DM. In the left-hand panel the alignment is shown as a function of subhalo mass ($M_{\rm sub}$) and in the right-hand panel it is shown as a function of the triaxiality of the DM. The thick orange curve and associated shading denotes the median alignment angle, and the 10th-90th percentiles of the distribution, when considering the minor axes of the two components. In general, the alignment is strong, with the median alignment angle typically $\simeq 30^\circ$ for $M_{\rm sub} = 10^{10}\,{\rm M}_\odot$, declining to $\simeq 15^\circ$ for $M_{\rm sub} = 10^{11}\,{\rm M}_\odot$ and $\simeq 10^\circ$ for $M_{\rm sub} = 10^{12-12.5}\,{\rm M}_\odot$. In more massive subhaloes, the characteristic alignment is typically (marginally) poorer, rising to $\simeq 20^\circ$ for $M_{\rm sub} \gtrsim 10^{13}\,{\rm M}_\odot$. These alignment angles are inconsistent with random to greater than 1σ, as shown by the grey dashed lines in the figure ($\theta < 33^\circ$).

Examination of the right-hand panel shows that the alignment of the minor axes of the star-forming gas and the DM of its host subhalo is a strong function of the latter's triaxiality, with oblate subhaloes exhibiting close alignment of the two components ($\theta < 10^\circ$ for $T_{\rm DM} \lesssim 0.4$) but prolate subhaloes exhibiting much poorer alignment ($\theta > 50^\circ$ for $T_{\rm DM} \gtrsim 0.8$). As is clear from the scatter about the median relation, in prolate

systems the minor axes of the two components can become effectively orthogonal. If the shape parameters of the two components are dissimilar, as is the case for the common configuration of an oblate disc within a prolate subhalo, alignment of the minor axes might not be the most likely scenario, since in such cases the minor and intermediate DM axes are not distinct. Indeed, the axes that should be 'expected' to align are likely to be those most closely aligned with the angular momenta of the respective components (as we discuss in Section 3.4.2). We therefore examine whether this is a genuine misalignment, or is rather a consequence of the minor axis of the star-forming gas exhibiting a preference to align with one of the other principal axes of the DM.

In Fig 3.7, the intermediate and major axes are denoted by the light blue and red curves, respectively. The dark blue curve denotes the angle between the minor axis of the star-forming gas and that of the DM axis with which it best aligns. In prolate subhaloes, for which the alignment quantified by the standard measure is poor, one can often find good alignment between the star-forming gas minor axis with one of the other principle axes of the DM. However, for $T_{\rm DM}(r < 30$ pkpc$) \rightarrow 1.0$ subhaloes, the characteristic alignments of the star-forming gas minor axis with all of the DM morphological axes converge towards $\simeq 60^{\circ}$, the expectation value for the alignment angle of unit vectors randomly oriented in 3 dimensions. This implies that poor alignment between the minor axes of the two components within high-triaxiality subhaloes is not primarily due to a preference for the star-forming gas minor axis to align with a non-minor DM morphological axis. Therefore in what follows, we focus exclusively on the misalignment between the minor axes of the two matter components.

Fig. 3.8 shows the cumulative distribution function of the alignment angle θ for the three pairs of matter components, namely star-forming gas and DM (pink), star-forming gas and stars (blue), and stars and DM (green). We plot the distribution as a function of $\log_{10}(1+\theta)$ because the bulk of the misalignments (for all component pairs) are small, but there are long tails to severe misalignments. Thick lines denote our fiducial measurement, whilst the thin lines show the alignments inferred when the initial characterisation of the mass distribution considers all particles of the relevant matter component bound to the subhalo, rather than only those within 30 pkpc of the subhalo's centre. We show the latter in order to highlight the influence of the initial aperture, since an influence is to be expected: for example, Velliscig et al. (2015a) showed that the alignment of the stellar and DM components is stronger closer to the subhalo centre, i.e. that galaxies are best aligned with the local, rather than global, distribution of matter in the subhalo. For reference, the dotted black line shows the distribution function of alignment angles between randomly oriented vectors.

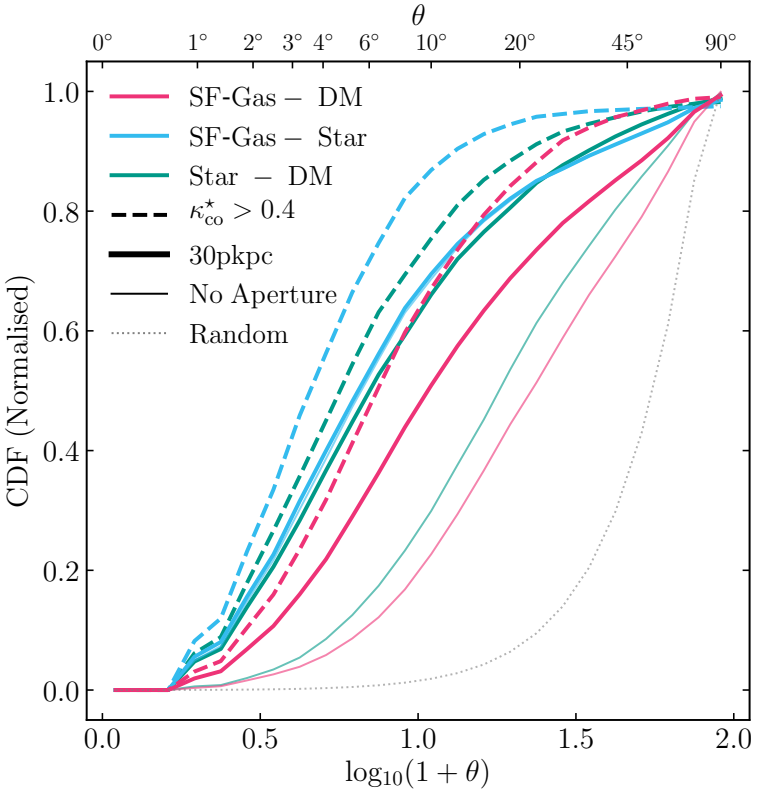

FIGURE 3.8: The misalignment of the star-forming gas, DM and stellar distributions within the subhaloes of our sample. The figure shows the cumulative distribution function of the misalignment angle, θ, between the minor axes of the matter distribution pairs in the legend. Thick curves correspond to fiducial measurements, thin curves denote alignments inferred when the initial characterisation of the mass distribution considers all particles of the relevant type bound to the subhalo, rather than only those within 30 pkpc of the subhalo centre. Thick dashed lines correspond to the subset of galaxies with $\kappa^{\star}_{\rm co}$, which broadly identifies star-forming disc galaxies. The dotted black line indicates the distribution of angles between randomly orientated vectors in 3D. Star-forming gas is a poorer tracer of the orientation of the subhalo DM distribution than are the stars.

For our fiducial measurements, half of the sampled subhaloes have star-forming gas distributions misaligned with their stellar components by more than 5°, and half have star-forming gas distributions misaligned with their DM component by more than 9.5°. Half of the subhaloes have stellar components misaligned with their DM component by more than 6°. Assessing the alignments recovered when considering all the particles of a given type associated with subhaloes, we find that half of the subhaloes have stellar-DM misalignments greater than 17°. The poorer star-forming gas - DM alignment with respect to the stars - DM alignment might be expected; since the stars and DM are collissionless components, their relevant evolutionary time-scale is the gravitational dynamical time, $t_{\rm dyn} = 1/\sqrt{G\rho} \sim 10^9\,{\rm yr}$, such that their morphologies and orientation effectively 'encode' their formation and assembly history over an appreciable fraction of a Hubble time. In contrast, the phase-space structure of the collissional, dissipative

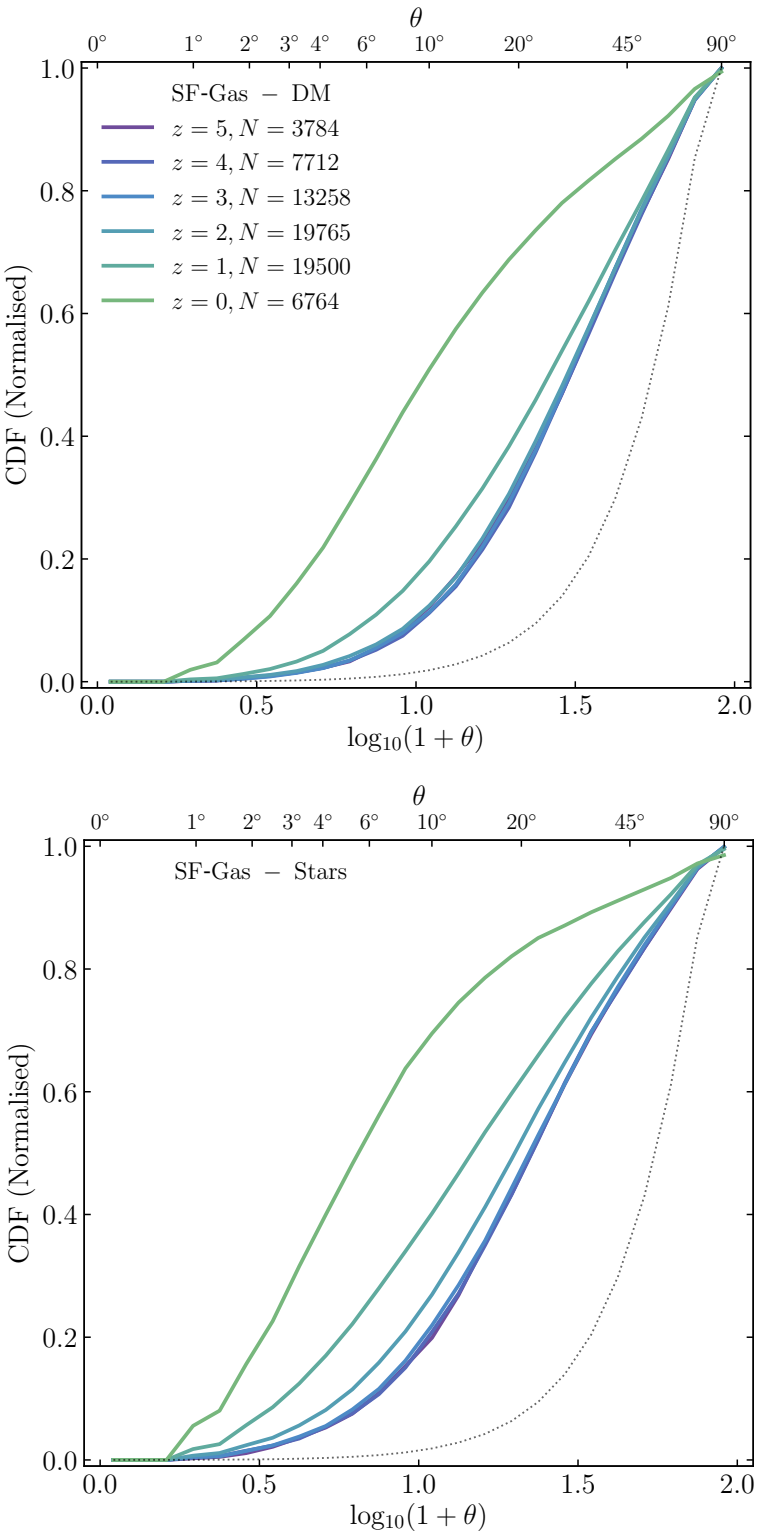

FIGURE 3.9: The temporal evolution of the misalignment of the minor axes of the star-forming gas and DM distributions (upper panel) and of the star-forming gas and stellar distributions (lower panel) comprising the subhaloes of our sample, as computed while adopting a 30 pkpc aperture. The figure shows the cumulative distribution function of the misalignment angle, θ. Colour indicates the redshift, and the thin black dotted line shows the distribution of angles between randomly orientated 3D vectors.

gas is not preserved as it accretes onto galaxies and condenses into star-forming clouds. Its morphology and orientation therefore reflects a more instantaneous snapshot of the evolution of the subhalo than is the case for the collissionless components.

We note that the stellar - DM alignment shown in Fig. 3.8 (thick green curve) is significantly better than that inferred by Velliscig et al. (2015a), who found that half of all the subhaloes they examined had misalignments worse than the 40°. This follows primarily from our use of an initial particle selection within a 30 pkpc sphere and the iterative reduced inertia tensor (which weights more strongly towards the halo centre), and also in part due to their measurement of the misalignment angle relative to the major axes of the mass distribution, and the slightly different sample selections. The influence of the initial particle selection can be assessed by comparison of the thick and thin solid curves: as expected, when one considers all matter bound to the subhalo (as opposed to only that within a 30 pkpc sphere) when initialising the iterative characterisation of the mass distribution, the misalignments with respect to the DM become significantly more pronounced. As is clear from the thinner curves of Fig. 3.8, in this case half of the sampled subhaloes have star-forming gas distributions misaligned with their DM components by more than $\simeq 20°$, and half have stellar components misaligned with their DM component by more than 15°. The misalignment of star-forming gas and the stars is however largely unaffected, since the bulk of both components is typically found within the central 30 pkpc.

Having noted that misalignments are typically most severe in massive, prolate subhaloes, which tend to host quenched elliptical galaxies (see e.g. Thob et al., 2019), it is reasonable to hypothesise that subhaloes hosting star-forming disc galaxies (i.e. those with $\kappa^{\star}_{\rm co} > 0.4$) will exhibit significantly better alignment than the broader sample. The misalignment angles for this subset of subhaloes are shown by the dashed lines in Fig. 3.8, and indeed we find that the primary consequence of restricting our focus to these systems is the exclusion of galaxies with severe misalignments. For this subsample, only 20 percent of galaxies exhibit star-forming gas distributions misaligned with their DM by more than $\simeq 10°$.

Fig. 3.9 shows the temporal evolution of the misalignment angle, θ, of the minor axes of star-forming gas and DM mass distributions (upper panel) and the star-forming gas and stars (lower panel). Here, as was the case for Fig. 3.5, we consider at all epochs subhaloes that satisfy the selection criteria specified in Section 3.2.4, however we do not here focus solely on main branch progenitors of $L_{\star}$ subhaloes. It is immediately apparent that the orientation of the star-forming gas is a much poorer tracer of the orientation of both the DM and the stars at early cosmic epochs than at the present-day (though the characteristic alignment is always much better than random). As noted above, at $z = 0$

half of the sampled subhaloes have star-forming gas distributions misaligned with their DM components by more than 10°, but at $z = 1$ half are misaligned by more than 25° and at $z = 2$ the figure is 29°. Similarly, at $z = 0$ half of the sampled subhaloes have star-forming gas distributions misaligned with their stellar components by more than 6°, but at $z = 1$ half are misaligned by more than 14° and at $z = 2$ half are misaligned by at least 19°. The deterioration of the alignment of the star-forming gas distribution with both the DM and the stars at earlier times is to be expected, since all three components tend to be more spherical (less flattened) at higher redshift. Although in principle even highly spherical distributions can exhibit perfect alignment, as $S \to 1$ the minor axis becomes less well defined.

In Section 3.7.5 we provide analytical fits to probability distribution functions of the misalignment angle, θ, of the star-forming gas distribution with those of DM and stars, enabling subhaloes in dark matter-only simulations to be populated with galaxies whose star-forming gas has a realistic misalignment distribution.

3.4.2 Alignment of the kinematic and morphological axes

A novel aspect of radio continuum lensing surveys is that complementary observations of the 21cm hyperfine transition emission line from atomic hydrogen can, in principle, be obtained simultaneously with little or no extra observing time. The Doppler shift of the 21cm line is widely used to infer the kinematics of the atomic phase of the ISM (e.g. Bosma, 1978; Swaters, 1999) and hence affords an independent means of assessing galaxy orientation. As noted by Blain (2002), Morales (2006) and de Burgh-Day et al. (2015), the kinematic axis can be used as a proxy for the unsheared morphological axis, and hence affords a means to suppress the influence of galaxy shape noise and intrinsic alignments.

Clearly, the naïve application of this method assumes perfect alignment of the kinematic and minor morphological axes. To assess the accuracy of this assumption, we define the morphokinematic misalignment angle, β, as the angle between the minor axis of the star-forming gas distribution, and the unit vector of its angular momentum. Fig. 3.10 shows the cumulative distribution function of $\log_{10}(1 + \beta)$, with solid curves denoting present-day measurements and dashed lines denoting measurements at $z = 1$. The blue curves correspond to the fiducial sample, whilst red curves correspond to the subset of galaxies with $\kappa^{\star}_{\rm co} > 0.4$. For reference, the dotted black line again shows the distribution function of alignment angles between randomly oriented vectors.

As naïvely expected, the star-forming gas minor axis and angular momentum vector of star-forming gas are well aligned for present-day subhaloes: 80 percent of systems

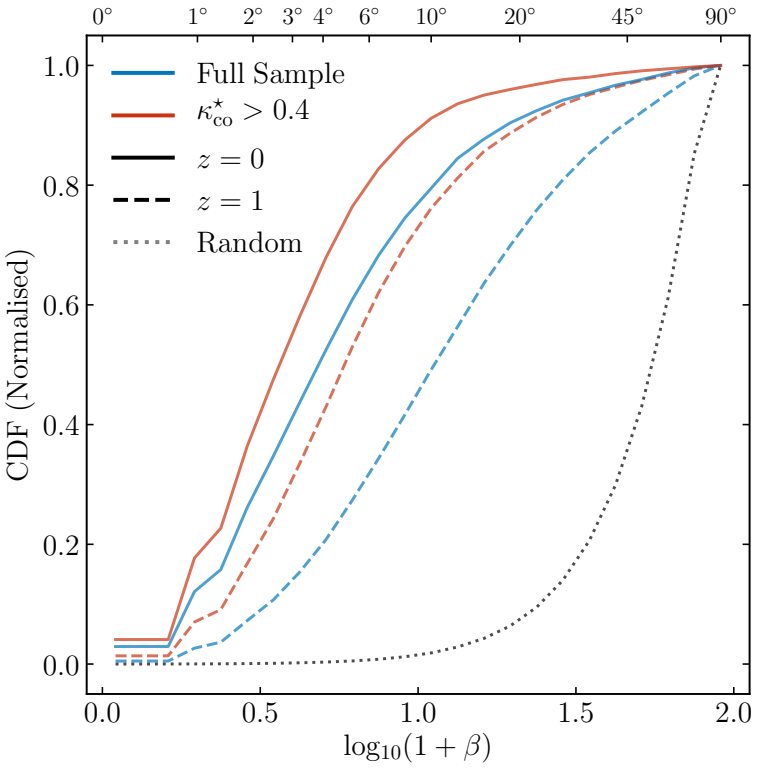

FIGURE 3.10: A histogram of the alignment between the morphological and kinematic axes of the star-forming gas within our sample. Alignment angles are given in terms of $\log_{10}(1+\beta)$, as the majority of the subhaloes have small β. The solid (dashed) lines correspond to subhaloes at redshift $z = 0(1)$. The black dotted line shows the distribution of angles between randomly orientated 3D vectors. Red lines correspond to the subset of galaxies with $\kappa^{\star}_{\rm co}$, which broadly identifies star-forming disc galaxies, while blue lines correspond to the full sample.

exhibit morphokinematic misalignments of less than 10°. However, similar to the internal component alignments, the distribution function exhibits a long tail to severe, but rare, misalignments. The morphokinematic alignment improves if one restricts the analysis to the $\kappa^{\star}_{\rm co} > 0.4$ subsample, for which eighty percent of the systems are misaligned by less than 6°, and the tail to severe misalignments is strongly diminished. At might be expected when considering the reduced prevalence of strongly flattened star-forming discs at $z = 1$, the morphokinmatic alignment is poorer at this earlier epoch, with 80 percent of subhaloes aligned to better than 30°, and 12° when restricting to the $\kappa^{\star}_{\rm co} > 0.4$ subsample.

To establish the characteristics of the subhaloes that typically suffer from poor morphokinematic alignment, we separate the primary sample of present-day subhaloes into quartiles of β, and quote in Table 3.3 the median values of key characteristics of subhaloes in each quartile, namely the star-forming gas sphericity, subhalo mass, star formation rate, stellar mass, the star-forming gas corotation parameter and the half-mass radius of the star-forming gas. This exercise illustrates that poor alignment of the minor axis

Quartile	$1^{\rm st}$	$2^{\rm nd}$	$3^{\rm rd}$	$4^{\rm th}$
$S_{\rm SF-gas}$	0.11±0.05	0.14±0.06	0.19±0.07	0.29±0.12
$M_{\rm sub}$	11.67±0.5	11.53±0.52	11.41±0.51	11.44±0.67
SFR	0.59±1.05	0.41±0.93	0.32±1.31	0.31±0.94
$M_\star$	9.97±0.54	9.75±0.56	9.6±0.52	9.56±0.61
$\kappa_{\rm co}^{\rm SF}$	0.93±0.06	0.9±0.08	0.86±0.1	0.76±0.18
$r_{\rm SF-gas}$	8.29±5.37	5.88±6.74	3.96±9.47	2.58±29.75

TABLE 3.3: The median and standard deviation in various subhalo properties for the systems binned into quartiles based on the alignment angle between the star-forming gas kinematic and morphological minor axes. In degrees, the $0^{\rm th}$, $25^{\rm th}$, $50^{\rm th}$, $75^{\rm th}$ and $100^{\rm th}$ percentile values are 0.0°, 2.14°, 4.36°, 9.15° and 89.75° respectively. The values from top to bottom are: the star-forming gas sphericity; total subhalo mass (as $\log_{10}M_{\rm sub}[{\rm M}_\odot]$); star-formation rate within 30 pkpc (in ${\rm M}_\odot{\rm yr}^{-1}$); stellar mass within 30 pkpc (as $\log_{10}M_*[{\rm M}_\odot]$); the fraction of kinetic energy in the star-forming gas invested in corotation; and the star-forming gas half-mass radius (in pkpc).

of the star-forming gas with its angular momentum vector is more typical in subhaloes hosting a spheroidal central galaxy, with a low star-formation rate and a less flattened and less extended star-forming gas distribution. In principle, such systems can be readily identified from either optical or radio continuum imaging.

3.5 The morphology and alignment of projected star-forming gas distributions

In this section we examine the morphologies, alignments and orientations of star-forming gas and DM when projected 'on the sky' in 2 dimensions, affording a direct connection with observational tests. In Section 3.5.1 we consider the ellipticity of the matter components, i.e. their projected morphology. In Section 3.5.2 we consider the projected alignments of galaxies.

3.5.1 Projected ellipticities

It is via measurement of the morphology of galaxies in projection, i.e. their ellipticity, that the weak gravitational shear is estimated. Since galaxies are intrinsically ellipsoidal (i.e. non-circular), the observed ellipticity is due to both the intrinsic ellipticity of the galaxy, and the lensing shear. The former can therefore be considered as a noise term when measuring the shear, and is often referred to as 'shape noise'. Since the variance of the observed ellipticity, $\epsilon_{\rm obs}$ is the sum of the variances of the intrinsic ellipticity and the (reduced) shear, i.e. $\sigma^2(\epsilon_{\rm obs}) = \sigma^2(\epsilon_{\rm int}) + \sigma^2(\epsilon_{\rm sh})$, the signal-to-noise ratio of

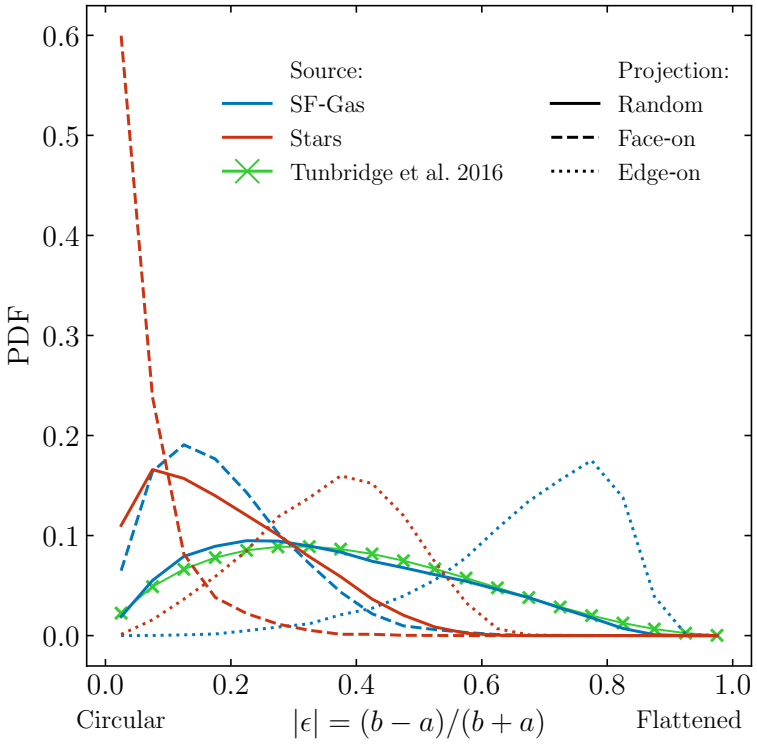

FIGURE 3.11: Probability distribution functions for the projected 2D ellipticities of the present-day mass distributions of star-forming gas (blue curves) and stars (red curves) bound to the subhaloes of our sample. The solid curves denote the aggregated ellipticities recovered from projection of the 3D mass distributions along 100 random axes of projection. For reference, the dashed and dotted curves show the distributions recovered when the galaxies are oriented face-on and edge-on, respectively, to the axis of projection. An observational comparison (green curve with crosses) is sourced from Tunbridge et al. (2016), who provide a best-fitting model to the distribution of observed ellipticities of galaxies in the radio VLA COSMOS data set.

shear measurements is markedly sensitive to the diversity of the intrinsic ellipticity of the galaxy population being surveyed.

To measure the intrinsic ellipticity of matter distributions, we adapt the iterative reduced inertia tensor algorithm presented in Section 3.2.3 to consider only two spatial coordinates and so recover the best-fitting ellipse. The intrinsic ellipticity is then $|\epsilon_{\rm int}| = (a-b)/(a+b)$, where a, b are the major and minor axis lengths of this ellipse, respectively, such that low ellipticity corresponds to near-circular morphology, and high ellipticity corresponds to a strongly flattened configuration. Hereafter we omit the subscript for brevity, such that $\epsilon \equiv \epsilon_{\rm int}$. As noted in Section 3.2.3, the first iteration of the algorithm considers all particles of the relevant type within a circular aperture of radius $r_{\rm ap} = \max(30\,{\rm pkpc}, 2r_{\rm sfg})$, where $r_{\rm sfg}$ is the 2D half-mass radius of star-forming gas within a circular aperture of 30 pkpc. The use of this additional criterion ensures a robust morphological characterisation of the image projected by the most extended

gas discs when viewed close to a face-on orientation. At each iteration, the elliptical aperture adapts to maintain a constant area.

Fig. 3.11 shows the probability distribution function of the projected ellipticity of star-forming gas (blue curves) and the stars (red curves) associated with the subhaloes of our sample. The solid curves denote the distribution of aggregated ellipticities recovered from projection of the 3D mass distributions along the line-of-sight of 100 'observers' randomly positioned on a unit sphere, thus crudely mimicking a real light cone (albeit without noise or degradation from instrumental limitations). The dashed and dotted curves show the ellipticity distributions recovered when the subhaloes are first oriented such that the projection axis is parallel to, respectively, the minor and major principal axes of the respective 3D mass distribution, in order to show the ellipticities when viewed face-on and edge-on.

The distribution of ellipticities when projected along random lines of sight is significantly broader for the star-forming gas than is the case for the stars: the IQRs of two distributions are 0.30 and 0.19, respectively. The origin of this difference is revealed by inspection of the ellipticity distributions for the face-on and edge-on reference cases: as might be inferred from the distribution of 3D shape parameters, star-forming gas is more commonly found in flattened configurations (corresponding to large values of the projected ellipticity) than is the case for the stars. The characteristic ellipticity of the flattened structures is greater for the star-forming gas, as can be quantified via the median ellipticities, $\tilde{\epsilon}^{\rm sfg}_{\rm edge} = 0.70$ and $\tilde{\epsilon}^{\rm stars}_{\rm edge} = 0.37$. Consequently, when projected along random lines of sight, there is a mild but significant paucity of low-ellipticity star-forming structures, since observing such a configuration requires that the galaxy is oriented close to face-on. Similarly, there are few high-ellipticity stellar structures, but this deficit is greater: not only does observing such a configuration require that the galaxy is oriented close to edge-on but, crucially, stellar structures that are strongly flattened (in 3D) are rare. We note that our sample selection criteria act to *minimise* these differences, since galaxies with significant star-forming gas reservoirs preferentially exhibit flattened stellar discs, i.e. elliptical and spheroidal galaxies are under represented by our sample. The solid green curve of Fig. 3.11 denotes the best-fitting functional form of the galaxy ellipticity distribution recovered from the application of the IM3SHAPE algorithm (Zuntz et al., 2013) to Very Large Array (VLA) L-band observations of galaxies in the COSMOS field (Tunbridge et al., 2016, see their equation 8). The iterative algorithm finds the best-fitting two-component Sèrsic (disc and bulge) model, yielding two-component ellipticities $\epsilon = (e_1, e_2)$, and is similar in concept, if not in detail, to the approach used here to characterise the simulated galaxies. There is a remarkable correspondence between the observed ellipticity distribution and that recovered from EAGLE. The qualitative similarity is a reassuring indication that the ellipticity distribution of star-forming gas

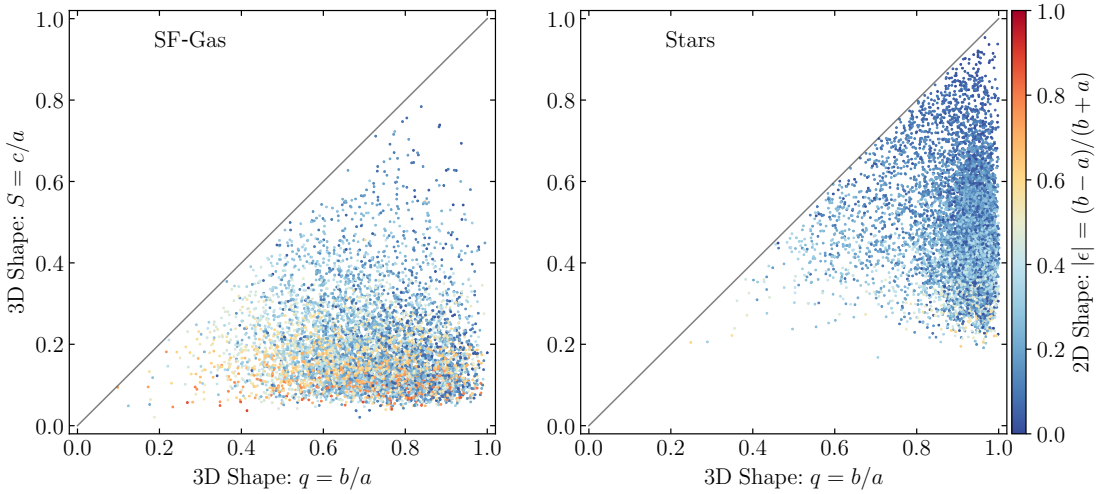

FIGURE 3.12: The relationship between 3 dimensional and projected shapes for the star-forming gas (left panel) and stars (right panel). The position of the points show the intrinsic 3 dimensional morphology in terms of the minor-major and intermediate-major axis length ratios, S and q, respectively. Points are coloured by the projected ellipticity, $|\epsilon|$, which is computed assuming an observer located infinitely distant along the x-axis of the simulation volume. Red (blue) points represent flattened (circular) ellipticities.

yielded by EAGLE is realistic, however we caution that the degree of agreement is likely to be, in part, coincidental: besides the differences in shape measurement algorithms and the absence of noise or smearing by a point spread function in the simulated shape measurements, the observed sample also spans a wide range of redshifts. Additionally, as EAGLE is unable to create discs less than ∼1pkpc in scale height, the probability distribution function of the random projection star-forming gas is likely slightly biased to more circular values than would be the case for a more resolved simulation.

In Fig. 3.12 we show the relationship between the projected and 3 dimensional morphologies of the star-forming gas and stars bound to the subhaloes of our sample. We compute the projected morphology as $|\epsilon|$, electing to collapse the simulation volume along the x-axis to obtain projected coordinates. The intrinsic 3 dimensional morphologies are computed as S and q, the minor-major and intermediate-major axis length ratios, respectively.

A number of interesting features are apparent in Fig. 3.12, however the main finding is that *the projected ellipticity depends on S, q, and the angle of inclination.* While star-forming gas distributions may reliably be expected to have a low S, a broad range of q values are possible. The converse is true for the stars, which demonstrate a range of S values but are more constrained in q. A floor in S exists for the star-forming gas, which we posit relates to the suppression of the formation of gas discs with scale heights much less than Jeans length of the gas on the temperature floor (∼1 pkpc). This then

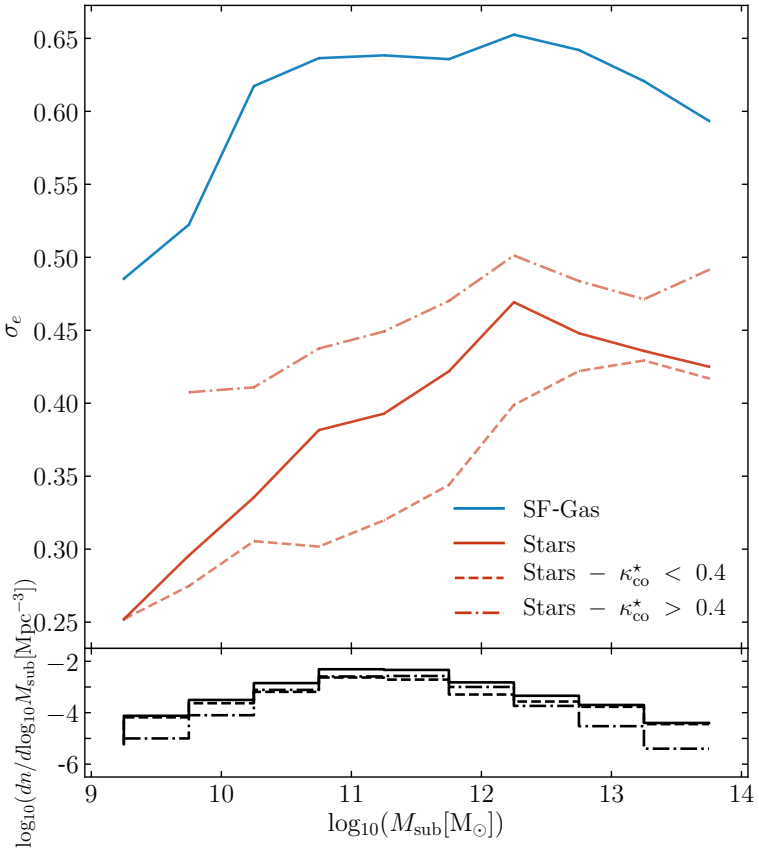

FIGURE 3.13: The scatter in the projected ellipticities of stars and star-forming gas, calculated as the standard deviation of the minor-major axis ratios within a given mass bin. Blue lines relate to the star-forming gas, and red lines to the stars. The solid lines correspond to the shape error in the projected galaxy shapes and the dotted line corresponds to the edge-on star-forming gas particle coordinate projection for the star-forming gas. The red dashed and dot-dashed lines correspond to the standard deviations for $\kappa^\star_{\rm co} < 0.4$ and $\kappa^\star_{\rm co} > 0.4$ stellar systems respectively. $\kappa^\star_{\rm co}$ is here the fraction of kinetic energy invested in corotation for the *stars*, as opposed to the star-forming gas, within 30pkpc, as outlined by Thob et al. (2019). The lower panel displays the volume density of subhaloes in a given mass bin, given as $\log_{10}({\rm dn/dlog_{10}M_{sub}[Mpc^{-3}]})$. At all masses, the shape noise is systematically greater for galaxy populations that are intrinsically flatter.

in turn prevents $|\epsilon| \to 1$. The more spherical distributions of stars (high S and high q) are uniformly circular in projection. Star-forming gas distributions characterised by low S and high q demonstrate a large spread of ϵ, as depending on the angle of inclination one may observe either the edge of a disc or a circular shape. Systems with lower S are able to be seen as high ϵ in projection. Systems with the largest differences between q and S are more triaxial, and are thus able to exhibit a wider range of possible ϵ in projection. Star-forming gas, with lower S and a broader range of q than the stars, are naturally able to present a wider variety of observed ellipticities.

Tunbridge et al. (2016) noted that the dissimilar diversity of the projected ellipticities of the star-forming gas and stellar mass distributions is of practical relevance, because it

governs the shape noise. This difference is analogous to the difference in shape noise in the optical regime expected for samples of early- and late-type galaxies: Joachimi et al. (2013) estimate that the former exhibit up to a factor of two less shape noise than the latter at fixed number. We assess the magnitude of this effect in EAGLE, by defining the shape noise of a sample of galaxies, σ_e, as

$$\sigma_e^2 = \frac{1}{N}\sum_i |e_i|^2, \tag{3.5}$$

where N is the total number subhaloes in the sample. The quantity in the summation is often referred to as the polarisation (see e.g. Blandford et al., 1991) and is defined as $|e| = (a^2 - b^2)/(a^2 + b^2)$. It is thus related to the ellipticity via $e = 2\epsilon/(1 + |\epsilon|^2)$.

We compute σ_e for the star-forming gas and stellar distributions of subhaloes as a function of subhalo mass. These measurements are shown in Fig. 3.13. The solid curves denote measurements for the star-forming gas (blue) and stars (red) considering all subhaloes comprising our sample. To place the difference in shape noise between the two matter types into context, we also show the shape noise of the stellar component when splitting the main sample into two subsamples separated about $\kappa_{\rm co}^{\star} = 0.4$, thus broadly separating the main sample into late- and early-type galaxies. The shape noise of the star-forming gas associated with subhaloes of all masses probed by our sample is systematically greater than is the case for their stars, by $\Delta\sigma_e \simeq 0.19 - 0.25$, an offset comparable to the difference between the shape noise (at fixed subhalo mass) of the stellar component of subhaloes comprising our crudely defined early- and late-type subsamples. Tunbridge et al. (2016) report a qualitatively similar offset of the shape noise of radio continuum sources relative to their optical images (see their table 3).

3.5.2 Projected alignment

In practice, it is only the misalignment angle of the various matter types *in projection* that can be measured observationally. We therefore extend the exploration of 3D misalignments presented in Section 3.4, to examine misalignments in projection. Fig. 3.14 shows the cumulative distribution function of $\theta_{\rm 2D}$, the alignment angle of the three pairs of matter components when viewed in projection. As with Fig. 3.8, we plot the distribution as a function of $\log_{10}(1 + \theta_{\rm 2D})$ since the bulk of the misalignments are small, but show long tails to severe misalignments. Thick lines denote our fiducial measurement, whilst thin lines show the alignments inferred when the initial characterisation of the projected mass distribution considers all particles of the relevant matter component bound to the subhalo. Thick dashed lines repeat the fiducial measurement for the

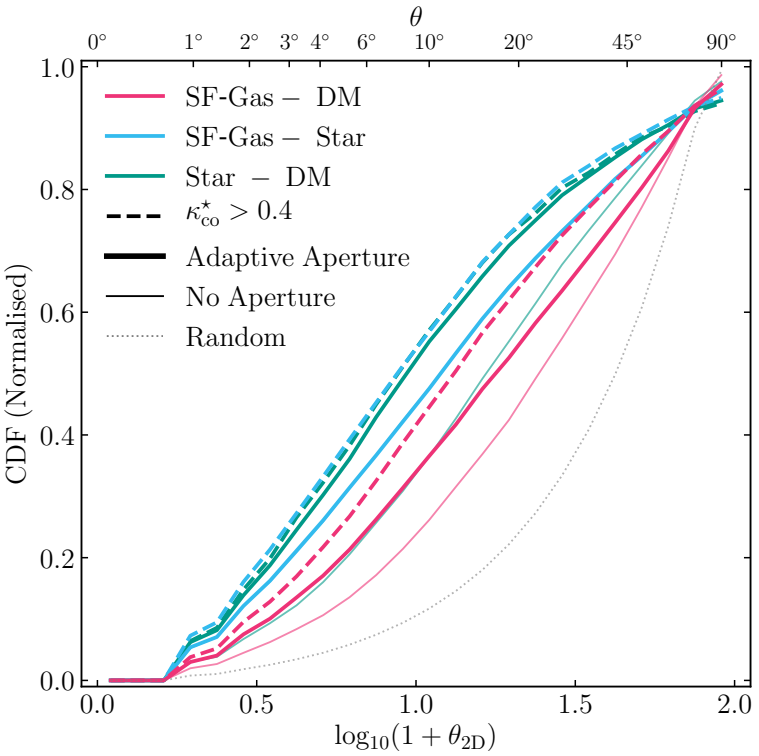

FIGURE 3.14: The projected 2D internal alignment between the stars, DM and star-forming gas within the subhaloes of our sample. The figure displays a normalised cumulative distribution function of the angle $\theta_{\rm 2D}$ between the minor axes of various matter distributions within subhaloes. The line colour indicates the two matter types assessed, thick dashed and thin solid lines correspond to the aperture used in the computation of the iterative reduced inertia tensor. The black dotted line indicates the distribution of angles between randomly orientated vectors in 2D. Star-forming gas is a poorer tracer of the underlying DM distribution than the stars in terms of orientation.

subsample of subhaloes hosting late-type galaxies, i.e. those with $\kappa^{\star}_{\rm co} > 0.4$. For reference, the dotted black line shows the distribution function of alignment angles between randomly oriented vectors.

The plot reveals that the projected alignments are qualitatively similar to those recovered in 3D, insofar that the star-forming gas and DM are most weakly aligned (half of all subhaloes are aligned to better than 16.9°), whilst the star-forming gas - stars and stars - DM alignments are aligned significantly more closely (half of all subhaloes aligned to better than 10.9° and 8.1°, respectively). Discarding the initial aperture weakens the alignment between the more centrally concentrated baryons and the DM but, in a similar fashion to the 3D case, has little impact on the alignment between star-forming gas and stars. Restricting the sample to late-type galaxies improves the alignment of all component pairs, with half of all subhaloes being aligned to better than 12.2°, 7.7° and 7.8° for, respectively, the star-forming gas - DM, star-forming gas - stars, and stars - DM pairs.

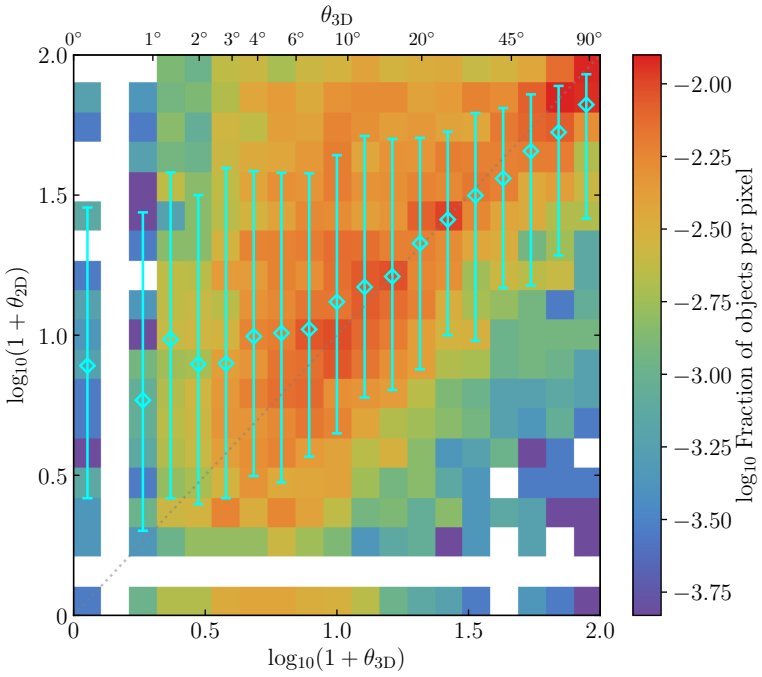

FIGURE 3.15: The relationship between 2 and 3 dimensional alignments between star-forming gas and dark matter within a given subhalo. Alignments are measured within 30 kpc, in terms of $\log_{10}(\theta+1)$. The histogram shows the fraction of subhaloes residing within a given pixel, while the cyan errorbars show the median and standard deviation of the underlying data. The grey dotted line shows a 1:1 relationship between the two quantities. While it is possible to view any θ_{2D} for a given θ_{3D}, the correlation between the two broadly follows the 1:1 relation for $\theta_{3D} > 10°$, while θ_{3D} is generally less than θ_{2D} for $\theta_{3D} < 10°$.

We note that, in contrast to Tenneti et al. (2014, their Fig 10.) and Velliscig et al. (2015a, their Fig. 13), we find that the projected alignments are in general *weaker* in projection than in 3D. For example, the median alignment angle of star-forming gas and DM using our fiducial aperture choices are 9.5° in 3D and 16.9° in projection. This is illustrated in Fig. 3.15, which shows how the star-forming gas - DM alignment in 3 dimensions relates to that in 2 dimensions, where the observer is located along the x-axis of the simulation volume. It is clear that for a given θ_{3D}, it is possible to observe any θ_{2D} due to the random angle of inclination, however in general θ_{2D}-θ_{3D} follows the 1:1 relationship closely. The notable exception to this is at $\theta_{3D} < 10°$, where it becomes more likely that the observed θ_{2D} will be greater than the intrinsic θ_{3D}. The disagreement between our results and previous studies regarding this discussion of the relationship between θ_{2D} and θ_{3D} is a consequence of our choice, motivated in Section 3.2.3, to measure misalignments relative to the minor axis rather than the major axis; whilst the projected misalignment is insensitive to this choice, the choice has a significant bearing on the alignments in 3D. We have explicitly confirmed that switching from the use of the minor axis to the major axis to define the misalignment angle results in smaller misalignments when projecting from 3D, consistent with the findings of Tenneti et al. (2014) and Velliscig et al. (2015a).

Although not shown in the figure, we have further examined the misalignment angles of all matter component pairs at $z = 1$, and find more severe misalignments at the earlier cosmic epoch. This result is largely insensitive to the use of the axisymmetry criterion.

3.6 Summary and Discussion

We have investigated the morphology of, and mutual alignments between, the star-forming gas, stars and dark matter bound to subhaloes that form in the EAGLE suite of simulations (Schaye et al., 2015; Crain et al., 2015; McAlpine et al., 2016). Our study is motivated by the complementarity of weak lensing experiments conducted using radio continuum surveys with traditional optical surveys. While recent radio weak lensing studies were limited by low source densities (see e.g. Tunbridge et al., 2016; Hillier et al., 2019; Harrison et al., 2020), the next-generation Square Kilometer Array (SKA) radio telescope will be competitive with optical surveys at a higher characteristic redshift. In simulations like EAGLE, gas that has a non-zero star formation rate is a good proxy for gas that is bright in the radio continuum. EAGLE represents a judicious test-bed for an assessment of this kind, as the simulations were calibrated to ensure a good reproduction of the galaxy stellar mass function and the size-mass relation of late-type galaxies. We focus primarily on present-day subhaloes, but also examine the simulations at earlier times to explore evolutionary trends.

A summary of our results is as follows:

1. The star-forming gas distribution of present-day subhaloes is typically flattened (i.e. low sphericity) along its minor axis. Flattening is most pronounced in subhaloes of $M_{\rm sub} \sim 10^{12.5}\,{\rm M}_{\odot}$, for which the median sphericity is $\tilde{S}_{\rm SF-gas} = 0.1$. The distribution of star-forming gas sphericities is significantly narrower than that of stars and dark matter at all subhalo masses, but particularly for those of $M_{\rm sub} = 10^{12-12.5}\,{\rm M}_{\odot}$, for which the interquartile ranges of star-forming gas, stars and DM are 0.06, 0.15 and 0.12, respectively (Fig. 3.3).

2. Star-forming gas exhibits a diverse range of triaxiality parameters. Subhaloes of mass $M_{\rm sub} \sim 10^{12-12.5}\,{\rm M}_{\odot}$ typically host oblate distributions consistent with classical gas discs, but in both low and high mass subhaloes, the distributions are more often prolate (Fig. 3.3).

3. Star-forming gas is less flattened at earlier epochs, for all subhalo masses examined, irrespective of whether one considers a sample selected in a similar fashion to the present-day sample, or considers the progenitors of the latter. Strongly flattened

star-forming gas structures ($S \lesssim 0.2$) emerge only at $z \lesssim 2$, broadly coincident with the growth of the disc's scale length (Figs. 3.4 and 3.5).

4. The shape parameters describing the morphology of star-forming gas are strongly and positively correlated with those describing the stellar morphology of the host galaxy, such that e.g. flattened gas structures are associated with flattened stellar structures (Fig. 3.6).

5. The minor axis of the star-forming distribution preferentially aligns most closely with the minor axis of the (inner) DM halo. However, in prolate subhaloes $T_{\rm DM}(r < 30{\rm pkpc}) \gtrsim 0.7$, a significant fraction of galaxies have star-forming gas distributions whose minor axis most closely aligns with one of the other principal axes of the DM (Fig. 3.7).

6. Characterised by the angle between the minor axes of the respective components of subhaloes, star-forming gas tends to align with the DM (i.e. the alignment is stronger than random), but the alignment is weaker than is the case for stars and the DM. This is the case for both the 3D matter distributions (Fig. 3.8) and their projections on the sky (Fig. 3.14). The alignments are strongest when considering the inner DM halo, and in general the alignments are stronger for late-type galaxies.

7. The alignment of the star-forming gas distribution with those of both the stars and the DM bound to its parent subhalo is typically weaker at early cosmic epochs (Fig. 3.9).

8. The kinematic axis of star-forming gas aligns closely with its minor morphological axis, with most galaxies being aligned to better than 10° at the present-day, and better than 6° if only late-type galaxies are considered. The alignment is poorer at $z = 1$, with these characteristic misalignment angles doubling (Fig. 3.10).

9. The more pronounced flattening of star-forming gas structures leads to them exhibiting a broader distribution of projected ellipticities than is the case for stellar structures, analogous to the differing ellipticity distributions of optical images of late-type and early-type galaxies. The ellipticity distribution of star-forming gas in EAGLE corresponds closely to that recovered from high-fidelity VLA radio continuum images of galaxies in the COSMOS field (Fig. 3.11). For a fixed subhalo sample, the 'shape noise' of its star-forming gas is therefore systematically greater than that of its stars 3.13).

Our analyses reveal that the morphology of star-forming gas distributions, and their orientation with respect to the DM of their parent subhalo, are more complex than

might be naïvely assumed. This complexity is particularly relevant in the context of using extended star-forming gas distributions, which can be imaged in the radio continuum, to conduct weak lensing experiments.

Forecasts for the outcomes of the next generation of the 'megasurveys' require that very large cosmic volumes are modelled. The associated expense of including the baryonic component forces the use of empirical, analytic or semi-analytic models grafted onto treatments of the evolving cosmic dark matter distribution. By construction, such techniques do not capture the full complexity of the evolution of the baryonic component resulting from the diverse range of physical processes that influence galaxies, nor do they capture the 'back reaction' of the baryons on the DM, and so can mask the importance of key systematic uncertainties.

In the specific case of modelling the radio continuum sky, the most popular approach has been to couple observed source populations with either a Press-Schechter or N-body treatment of the evolving cosmic DM distribution (see e.g. Wilman et al., 2008; Bonaldi et al., 2019). By construction, such models invoke no explicit connection between the properties of star-forming gas structures and their parent DM haloes, and often relate (or equate) the properties of the former to those of the host galaxy's stellar component. Our analyses highlight shortcomings of these approximations: the characteristic morphology of star-forming gas is a strong function of the mass of its host subhalo and, although the simulations indicate that it correlates strongly with the morphology of its associated stellar component, we find that the respective morphologies can differ significantly.

We also find that star-forming gas structures are imperfectly aligned with both the stellar and DM components of their host subhalo. While this Chapter does not focus on determining the cause of this, we comment that the physical processes setting the morphology and the timescales involved are different for the three components. Firstly, the star-forming gas is dissipative, while the stars and dark matter are collisionless. Secondly, while young star particles ($t_{\rm age} < 1$ Gyr) are highly coincident with the star-forming gas, the stellar population as a whole reflects the integrated accretion of cold gas across the galaxy's history, the rate and direction of which may vary with time. The star-forming gas disc is a more transient feature than the morphology of the stars and the dark matter halo. Environmental quenching and internal feedback processes are able to significantly disturb the morphology of the ISM, or cause the local cessation of star formation, which effectively removes particles from the calculation of morphology. Further, in intrinsic alignment models it is assumed that the tidal field can impact galaxy morphology in more than one way. In the TATT model (Blazek et al., 2019), the morphology of the stars is set by a tidal alignment term (a linear response to the tidal field), while tidal torques (a quadratic response to the tidal field) determine the

build up of angular momentum in a galaxy, and hence influence the morphology of the star-forming gas.

Although the misalignment angle is generally small (particularly with respect to the stellar component), there is a long-tail to severe misalignments, and we find that the misalignment is most pronounced in early-type galaxies. We also find that the misalignment of the star-forming gas with the DM of its host subhalo becomes more pronounced if the outer halo is considered (for instance, if disabling the use of the 30 pkpc spherical aperture). Therefore, when constructing semi-empirical radio sky models based on N-body simulations, we caution against naïvely orienting star-forming discs with the principle axes of the DM distribution.

Our analyses also highlight that the shape noise of images of a fixed sample of galaxies seen in the radio continuum should be significantly greater than when seen in the optical. This follows naturally from the lower characteristic sphericity (or, alternatively, the greater flattening) of star-forming gas structures than their stellar counterparts. A systematic offset in shape noise was previously reported by Tunbridge et al. (2016) following the examination of a relatively small sample of galaxies with high-fidelity radio and optical imaging. The corollary of this finding is that radio continuum weak lensing experiments will require a greater source density in order to obtain a signal-to-noise ratio equal to optical experiments. However, our analyses also corroborate the hypothesis that the use of the kinematic axis (revealed by ancillary 21 cm observations) affords an effective means of estimating the unsheared orientation of the minor axis, and thus mitigating the systematic uncertainty in radio weak lensing experiments.

An interesting consequence of the poorer alignment of star-forming gas structures with the DM of their host subhaloes than is the case for the stars - DM alignment, is that it implies that the intrinsic alignment signal may be less severe in radio weak lensing surveys than is the case for optical counterparts. In the following Chapter we examine the two key 'intrinsic alignment' signals recoverable from radio continuum imaging, namely the orientation of star-forming gas distributions with respect to the directions to, and orientations of, the star-forming gas structures of its neighbouring galaxies.

3.7 End of Chapter Appendix

In this section examine the influence of a series of numerical and modelling factors on the findings presented in this Chapter.

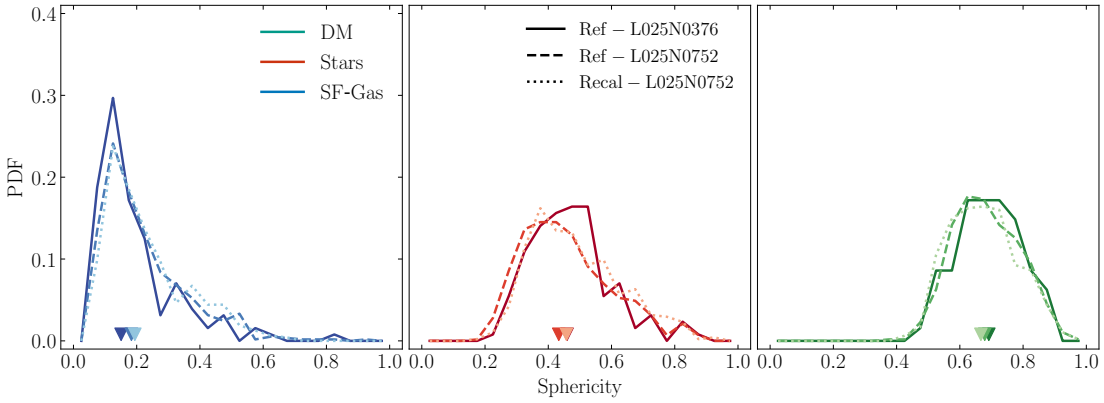

FIGURE 3.16: Probability distribution function of the sphericity parameter of the star-forming gas (left-hand panel), stars (centre) and DM (right-hand panel) of present-day subhaloes drawn from the Ref-L025N0376 (solid dark-coloured curve), Ref-L025N0752 (dashed medium), and Recal-L025N0752 (dotted light) simulations. Down arrows denote the median sphericity of the distribution of each simulation. Comparison of Ref-L025N0376 with Ref-L025N0752 and Recal-L025N0752 affords simple tests of, respectively, the strong and weak convergence behaviour of the star-forming gas sphericity.

3.7.1 Numerical Convergence

In this section we examine the influence of the numerical resolution of the EAGLE simulations on the recovered sphericity of the star-forming gas, stars and DM comprising subhaloes. We follow Schaye et al. (2015) and adopt the terms 'strong convergence' and 'weak convergence', where the former denotes a comparison at different resolutions of a fixed physical model, and the latter denotes a comparison at different resolutions of two models calibrated to recover the same observables. We use three $L = 25\,\mathrm{cMpc}$ simulations introduced by Schaye et al. (2015): Ref-L025N0376, which is identical to the flagship Ref-L100N1504 simulation with the exception of the boxsize; Ref-L025N0752, which adopts the same Reference physical model but has a factor of 8 more particles each of both baryons and DM; and Recal-L025N0752 which also adopts values for subgrid parameters governing stellar and AGN feedback that have been recalibrated to improve the match to the galaxy stellar mass function and galaxy sizes at this higher resolution. Comparison of Ref-L025N0376 with Ref-L025N0752 and Recal-L025N0752 thus affords simple tests of, respectively, the strong and weak convergence behaviour.

Fig. 3.16 shows the probability distribution functions of the sphericities of the star-forming gas (left-hand panel), stars (centre) and DM (right-hand panel) for each of the three $L = 25\,\mathrm{cMpc}$ simulations. The subhaloes shown are selected according to the standard sampling criteria outlined in the Section 3.2.4, irrespective of the resolution of the simulation. Down arrows denote the median sphericity of the distribution of each simulation. Inspection shows that the distributions are not strongly influenced by the change in resolution. The median values of the sphericity of the three matter components

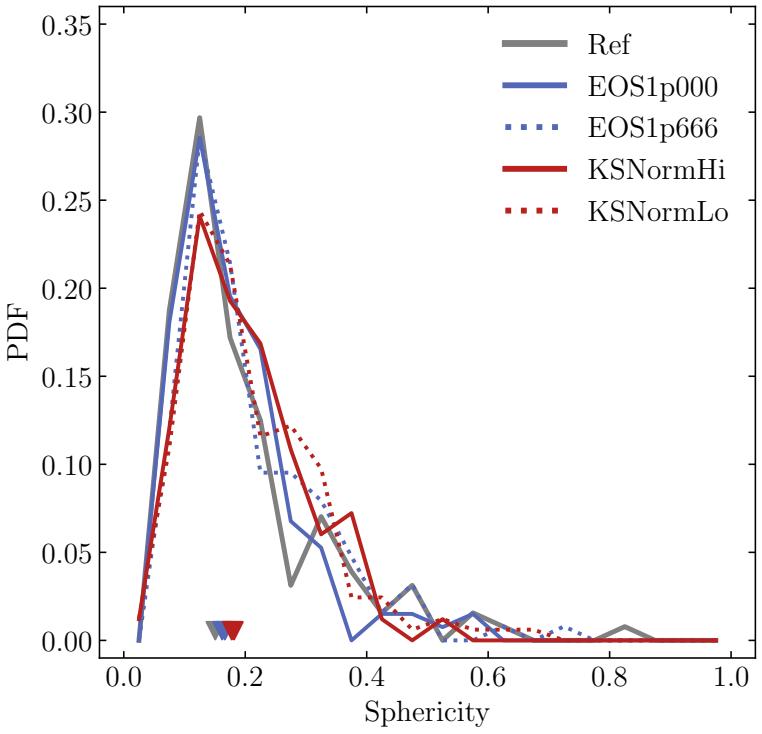

FIGURE 3.17: Probability distribution function of the sphericity parameter of the star-forming gas of present-day subhaloes drawn from the Ref-L025N0376 simulation (black curve) and two pairs of simulations that incorporate variations of the reference model: pair with alternative equation of state slopes (EOS1p00, solid blue; and EOS1p666, dotted blue) and with normalisations of the star formation law adjusted by ±0.5 dex (KSNormHi, solid red; KSNormLo, dotted red). Comparison of these runs with the reference model indicates the influence of the subgrid ISM model on the sphericity of star-forming gas distributions.

in the Ref-L025N0376 simulation are 0.15, 0.50 and 0.69 for the star-forming gas, stars and DM, respectively. As can be clearly seen from the figure, when moving to the high resolution simulations, the shift in median values is much smaller than the associated interquartile ranges of the Ref-L025N0376 simulation (IQR = 0.14, 0.15, 0.14 for the three components, respectively). Although not shown here, we recover similar behaviour when focusing on the triaxiality parameter.

3.7.2 Influence of subgrid ISM treatments

In this section we examine the sensitivity of star-forming gas morphologies to aspects of EAGLE's subgrid models that in principle influence the structure of interstellar gas directly, namely the form of the temperature floor equation of state and the star formation law. To achieve this, we compare the Ref-L025N0376 simulation with two pairs of complementary L025N0376 simulations. The first pair, introduced by Crain et al. (2015), varies the slope of the equations of state from the reference value of $\gamma_{\rm eos} = 4/3$

with different slopes, to adopt isothermal ($\gamma_{\rm eos} = 1$) and adiabatic ($\gamma_{\rm eos} = 5/3$) equations of state. Schaye & Dalla Vecchia (2008) used simulations of idealised discs to show that a stiffer equation of state generally leads to smoother star-forming gas distributions with a larger scale height. Crain et al. (2015) showed that in EAGLE, a stiffer equation of state also suppresses accretion onto the central BH in massive galaxies. The second pair, introduced by Crain et al. (2017), varies the normalisation of the Kennicutt-Schmidt law (the variable A in equation 1 of Schaye et al., 2015) from its fiducial value of $1.515 \times 10^{-4}\,{\rm M_\odot\,yr^{-1}\,kpc^{-2}}$ by ± 0.5 dex. Crain et al. (2017) showed that increasing (decreasing) this parameter tends to decrease (increase) the mass of cold gas associated with galaxies, since it governs the mass of gas that is required to maintain a balance between the gas infall rate and the outflow rate due to ejective feedback.

Fig. 3.17 shows probability distribution function of the sphericity star-forming gas for the reference model (solid black curve) and the simulations with differing equations of state ($\gamma_{\rm eos} = 1$, solid blue; $\gamma_{\rm eos} = 5/3$, dotted blue), and with higher (solid red) and lower (dotted red) normalisations of the star formation law with respect to the reference model. The subhaloes shown are selected according to the standard sampling criteria outlined in the Section 3.2.4. Down arrows denote the median sphericity of the distribution of each simulation. Inspection reveals that the distributions are not strongly influenced by changes to the subgrid modelling of the ISM. The median value of the sphericity of the star-forming gas in the Ref-L025N0376 simulation is 0.15. As can be clearly seen from the figure, the median sphericity in the three variation simulations shifts by < 0.05 with respect to the reference simulation, a value that is much smaller than the interquartile range of the reference case. Although not shown here, we recover similar behaviour when focusing on the triaxiality parameter.

3.7.3 The influence of particle sampling on shape characterisation

The morphological characterisation of structures defined by particle distributions is unavoidably influenced by sampling error. It is therefore crucial to establish the reliability of such characterisations as a function of particle number. A common methodology is to realise a mass distribution of a known analytic form with a particle distribution, and assess the deviation of the recovered shape from the input shape as the distribution is progressively subsampled (see e.g. Appendix A2 of Velliscig et al., 2015a). We adopt a similar approach here but, since star-forming gas distributions are not readily characterised by a simple analytic form, we instead draw 20 central subhaloes from the sample described in Section 3.2.4, with dynamical mass comparable to that of the Milky Way ($M_{\rm sub} \simeq 10^{12.0-12.5}{\rm M_\odot}$). We compute their 'true' shape parameters by applying the algorithm defined in Section 3.2.3 using all star-forming gas particles ($N_{\rm part} \simeq 2000$).

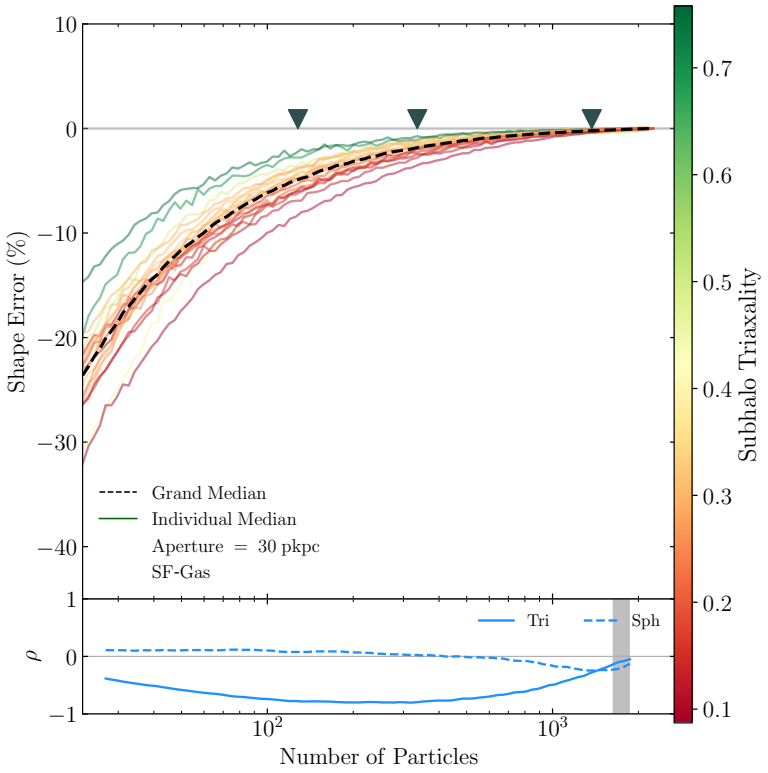

FIGURE 3.18: The sphericity shape error recovered as a function of the degree of particle subsampling for star-forming gas in 20 present-day subhaloes with dynamical mass similar to that of the Milky Way. Down arrows correspond to the 10th, 50th and 90th percentile values of the number of star-forming gas particles within the subhalo sample. Curves show the median shape error recovered from 10^5 random subsamplings of the true star-forming gas particle distribution, and are coloured by the latter's true triaxiality. The dashed curve shows the median recovered by aggregating measurements from all 20 subhaloes. The subpanel shows the running Spearman rank correlation coefficients relating the shape error to the true value of the triaxiality (solid curve) and sphericity (dashed curve) of the star-forming gas.

We then progressively subsample the particle distribution to lower $N_{\rm part}$, generating 10^5 realisations at each value of $N_{\rm part}$, and recompute the shape parameters.

Fig. 3.18 shows the median of the relative error on the sphericity of the star-forming gas distribution recovered from the 10^5 subsamplings of the particle distribution as a function of $N_{\rm part}$. The curves are coloured by the 'true' value of the triaxiality parameter of the subhalo's star-forming gas. The dashed black curve shows the 'grand median' recovered by aggregating the measurements from all 20 subhaloes. Down arrows show the 10th, 50th and 90th percentile values of the number of star-forming gas particles within the subhalo sample. Velliscig et al. (2015a) noted that poor particle sampling leads to a systematic underestimate of the sphericity parameter of the DM; we find this is also the case for the star-forming gas. A shape error of less than 10 percent typically requires at least $N_{\rm part} = 100$, hence we adopt this threshold as our lower limit for our sample selection.

Inspection of the curves for the individual subhaloes indicates that this value is sensitive to the triaxiality of the structure, with accurate recovery of the sphericity requiring fewer particles in prolate ($T > 0.5$) distributions. As shown in Fig. 3.4, the star-forming gas of low-mass subhaloes is preferentially prolate, hence a minimum of $N_{\rm part} = 100$ can be considered a conservative choice. For completeness, the subpanel shows the 'running' value of the Spearman rank coefficient recovered from $N_{\rm part}$-ordered subsamples, of the correlation between the *absolute* shape error and the true shape parameters, T (solid curve) and S (dashed curve). The solid curve highlights that a negative correlation between the shape error on sphericity and the true triaxiality persists to over 1000 particles. The dashed curve indicates that there is a very mild positive correlation of the relative shape error on sphericity with the true input sphericity.

3.7.4 The influence of particle sampling on alignment characterisation

We next assess the influence of particle sampling on our shape-finding algorithm's ability to retrieve the orientation of the star-forming gas distributions. We first compute the orientation of the 20 subhaloes detailed above in terms of the direction of their minor axes, considering all of their particles. We then randomly draw subsamples of particles and recompute their orientation, noting how the deviation from the truth varies as a function of $N_{\rm part}$. We find that at $N_{\rm part} \sim 100$, the orientation error is $< 2^{\circ}$, with the lowest sphericity subhaloes exhibiting the lowest errors ($< 1^{\circ}$).

3.7.5 Analytic fits to the misalignment angle distributions

We provide fitting functions to the distribution of internal misalignment angles between star-forming gas and DM for present-day subhaloes in three mass bins from the EAGLE Ref-L100N1504 simulation, in both 2- and 3D. The fits enable users of N-body simulations to populate subhaloes with galaxies oriented with respect to the minor axis of the subhalo in a realistic fashion. We fit to $P(\theta)$ using the following functional form:

$$\mathcal{M}(\theta) = C\exp\Big(-\frac{\theta^2}{2\sigma_1^2}\Big) + D\exp\Big(-\frac{\theta^2}{2\sigma_2^2}\Big) + E, \tag{3.6}$$

where $C, D, \sigma_1^2, \sigma_2^2, E$ are the free parameters, and θ is the misalignment angle. The same form was used by Velliscig et al. (2015a) to fit to the misalignment angle of stars and DM in projection. We calcuate the best fit parameters with the Python package SCIPY.OPTIMIZE.CURVE_FIT, using 1σ Poisson errors.

The best fit parameters are quoted in Tables 3.4. Parameters are recovered for the misalignment angles in both the cases of i) applying our fiducial aperture to the initial step

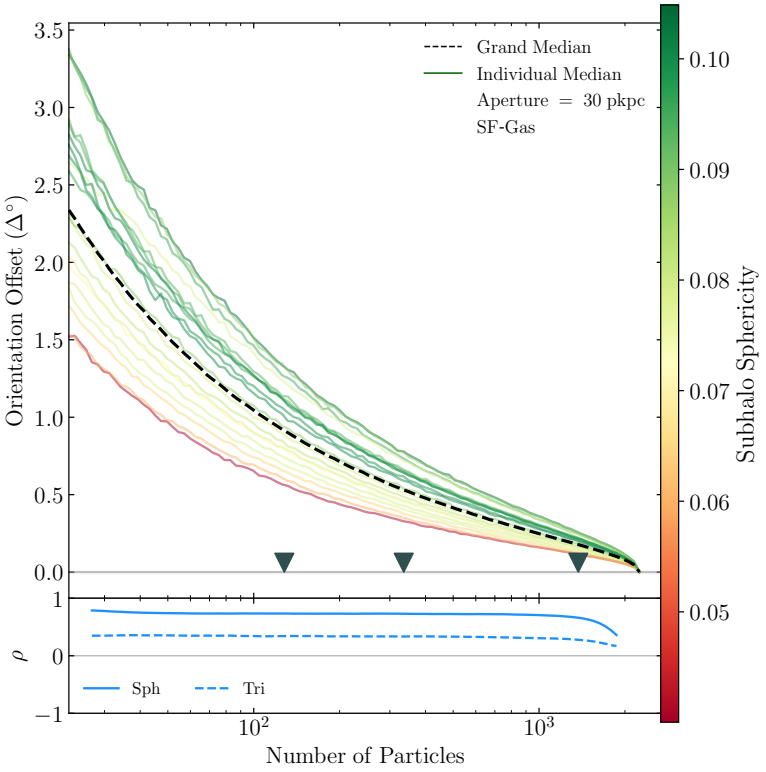

FIGURE 3.19: The orientation error recovered as a function of the degree of particle subsampling for star-forming gas in 20 present-day subhaloes with dynamical mass similar to that of the Milky Way. Down arrows correspond to the 10th, 50th and 90th percentile values of the number of star-forming gas particles within the subhalo sample. Curves show the median shape error recovered from 10^5 random subsamplings of the true star-forming gas particle distribution, and are coloured by the latter's true sphericity. The dashed curve shows the median recovered by aggregating measurements from all 20 subhaloes. The subpanel shows the running Spearman rank correlation coefficients relating the shape error to the true value of the sphericity (solid curve) and triaxiality (dashed curve) of the star-forming gas.

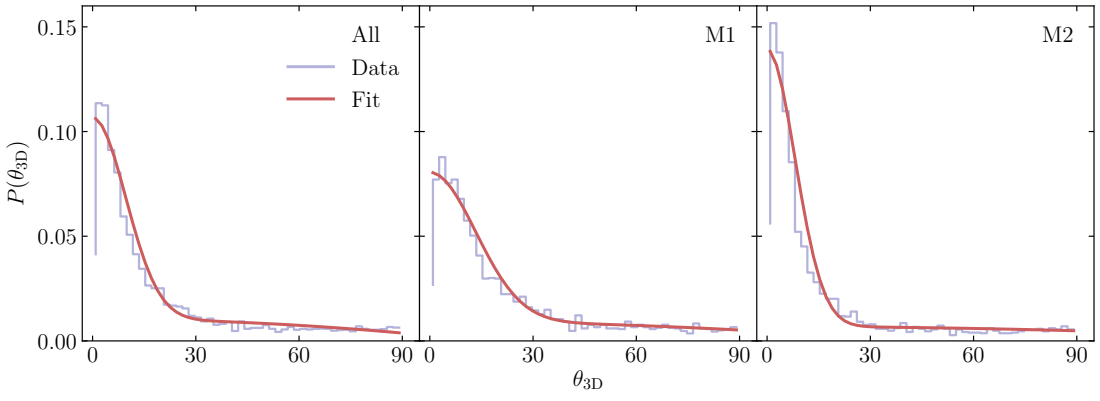

FIGURE 3.20: Probability distribution functions $P(\theta_{3D})$, where θ_{3D} is the angle between the morphological minor axes of stars and DM within the sample of subhaloes. A fiducial aperture of 30 pkpc is imposed. The faded step functions show the raw histograms, while the smooth lines are their respective analytic fits described by equation 3.6. Panels correspond to different mass bins: the full sample (left-hand panel), $M_{\rm sub} \leq 10^{11.5}\mathrm{M}_\odot$ (middle) and $10^{11.5}\mathrm{M}_\odot \leq M_{\rm sub} < 10^{13}\mathrm{M}_\odot$ (right-hand panel). During fitting, errors in the y-axis were taken to be the 1σ Poisson errors.

of the iterative algorithm, and ii) applying no initial aperture, i.e. considering all particles bound to the subhalo. In addition to presenting best fit parameters for all subhaloes in our sample ('All'), we provide fits to subsamples 'M1' and 'M2', which are subject to the additional criteria $\log_{10}M_{\rm sub}[{\rm M}_\odot] \leq 11.5$ (M1) and $11.5 < \log_{10}M_{\rm sub}[{\rm M}_\odot] \leq 13$ (M2). This is motivated by two factors. Firstly, below $M_{\rm sub} = 10^{11.5}\,{\rm M}_\odot$ our selection criteria result in significant incompleteness. Secondly, the misalignment of the minor axes of the star-forming gas and the DM components becomes large for $M_{\rm sub} > 10^{13}{\rm M}_\odot$ (see discussion in Section 3.4.1), severely degrading the value of the fits. The best fits for the 3D fiducial aperture case are shown in Fig. 3.20.

We find that the fitting is able to recover the profile of the input distribution fairly successfully. As an example we find the percentage difference in the retrieved median as compared with the input distribution to be $(1.7, 0.14, 0.51)$ percent for the three cases displayed in the panels of Fig 3.20, while for the standard deviation this becomes $(0.72, 1.04, 1.16)$ percent. For the no aperture version of these cases we find errors of $(3.1, 2.2, 2.6)$ percent for the median and $(1.6, 1.8, 1.7)$ percent for the standard deviation. When no aperture is applied, we find that the errors in the 2D fittings are comparable to the 3D case. However with the fiducial aperture the errors are noticeably larger for the 2D case, the largest being ~ 10 percent for the median and standard deviation of the M2 bin. Twelve figures comprising all variations displayed in Table 3.4 (2 dimensions $\times$ two apertures $\times$ three mass bins) in the style of Fig 3.20 may be found at the author's website[6].

[6] `www.astro.ljmu.ac.uk/~ariahill/`

	2D					3D				
Aperture & *Mass-Bin*	C	D	E	σ_1	σ_2	C	D	E	σ_1	σ_2
Fiducial										
All	24.0	8.33	0.0199	0.0507	0.00717	5130.0	9.62	43.2	0.0962	-43.2
M1	-27.0	9.21	0.0205	0.042	0.00688	-13.3	3050.0	0.0714	9.06	-9.05
M2	9.32	-9.32	-218.0	218.0	0.0107	-8.13	1440.0	0.132	1.03	-1.03
No Aperture										
All	-17.4	17.4	-87.3	87.3	0.0122	29.3	-29.3	-157.0	157.0	0.0125
M1	-17.7	17.7	-71.7	71.7	0.0124	31.2	-31.2	-181.0	181.0	0.013
M2	-17.3	17.3	-79.8	79.8	0.0124	26.9	-26.9	-114.0	114.0	0.0121

TABLE 3.4: Best fitting parameters for equation 3.6, used to fit the probability distribution functions of the intrinsic 3D and projected 2D misalignment angle between star-forming gas and DM within present-day subhaloes of three mass bins (denoted by italics). Parameters are provided for the angles recovered using our fiducial initial aperture for the iterative reduced inertia tensor, and for no aperture (denoted by font weight).

Chapter 4

Intrinsic alignments of the extended radio continuum emission of galaxies in the EAGLE simulations

We are all adventurers here, I suppose, and wild doings in wild countries appeal to us as nothing else could do. It is good to know that there remain wild corners of this dreadfully civilised world.

Scott

The content of this chapter was published in the paper Hill et al. (2022) in collaboration with Rob Crain, Ian McCarthy and Shaun Brown. Figures 4.10 and 4.11 represent subsequent unpublished work. The simulation data was created by the EAGLE collaboration.

4.1 Introduction

The morphology, spin and orientation of galaxies are influenced by the tidal field of the cosmic large scale structure (e.g. Heavens & Peacock, 1988; Bond et al., 1996; Wang & Kang, 2018). The coherence of the tidal field over large cosmic distances induces correlated orientations, a phenomenon often referred to as 'intrinsic alignment' (e.g. Heavens et al., 2000; Croft & Metzler, 2000; Lee & Pen, 2001; Brown et al., 2002; Jing, 2002; Mackey et al., 2002; Aubert et al., 2004). This alignment represents a significant source of systematic uncertainty in cosmic shear measurements from weak lensing experiments, which aim to measure the distortion of the images of distant galaxies due to the lensing effect induced by intervening matter distribution along the line of sight.

The observed correlation of the shapes of galaxies results from the *apparent* alignment of their lensed images, and the *intrinsic* alignment of their true orientations (see Troxel & Ishak, 2015, for a review). Much effort has been made to develop means of modelling intrinsic alignments in order to mitigate their impact on weak lensing surveys (for reviews see Joachimi et al., 2015; Kiessling et al., 2015; Kirk et al., 2015). Further motivation for modelling intrinsic alignment arises from its putative sensitivity to a diverse range of physical influences, such as the growth of angular momentum during galaxy formation (Lee & Pen, 2000), primordial gravitational waves (Chisari et al., 2014), modified gravity (L'Huillier et al., 2017) and self-interacting dark matter (Harvey et al., 2021).

As the depth and fidelity of observations improves, commensurate improvements in the ability of weak lensing surveys to constrain cosmological parameters are increasingly limited by an incomplete understanding of the effect of baryons on the matter power spectrum and the intrinsic alignment of galaxies. Amon et al. (2022) argue that such uncertainties cost the Dark Energy Survey Year 3 (DES Y3; Secco et al., 2022) cosmic shear measurements approximately two thirds of their constraining power. Intrinsic alignments have been estimated primarily using the analytic linear alignment model (Catelan et al., 2001; Hirata & Seljak, 2004), with the ansatz that the projected shapes of galaxies are linearly correlated with the projected tidal field. The linear alignment model accurately reproduces the inferred alignments of distantly-separated early-type galaxies ($\gtrsim 10h^{-1}$ Mpc), however recent observations have shown it to underestimate the alignments of closer pairs (Singh et al., 2015; Johnston et al., 2019). The non-linear alignment model (Bridle & King, 2007) makes use of the non-linear matter power spectrum while still assuming a linear response between galaxy shapes and the tidal field, and fares better at reproducing the observed alignments of galaxies at intermediate separations (Hirata & Seljak, 2010). It has thus enjoyed widespread adoption in the mitigation of intrinsic alignment uncertainty (e.g. Joachimi et al., 2011; Heymans et al., 2013; Abbott et al., 2016). Mitigating the uncertainty on shorter scales has motivated

the development of more complex approaches, such as the quadratic alignment model (Crittenden et al., 2001), perturbative expansions (Blazek et al., 2011, 2015, 2019), effective field theory (Vlah et al., 2020), and applications of the halo model (Schneider & Bridle, 2010; Fortuna et al., 2021).

In recent years, cosmological hydrodynamical simulations of the galaxy population, which simultaneously evolve dark matter (DM) and baryons, have achieved far better correspondence with the observed properties of the galaxy population than prior generations (see e.g. Somerville & Davé, 2015; Naab & Ostriker, 2017). These simulations include treatments of the complex baryonic physics governing the formation and evolution of galaxies, which have been shown to impact the internal structure and the spatial distribution of haloes (e.g. Duffy et al., 2010; Schaller et al., 2015a; Springel et al., 2018). Hydrodynamical simulations have been used to study the intrinsic alignment of galaxies even well within the non-linear, one-halo regime (Chisari et al., 2015, 2016; Codis et al., 2015; Tenneti et al., 2015; Velliscig et al., 2015b; Hilbert et al., 2017; Harvey et al., 2021; Shi et al., 2021). They offer a means to obtain physical insights into the origins of galaxy shape correlations, and to assess the accuracy of analytic alignment models (Samuroff et al., 2021).

Contemporary weak lensing experiments are dominated by optical/near-IR surveys, since to date only these have delivered imaging with the necessary source density required to extract a robust shear measurement. Successive data releases from the Kilo-Degree Survey (KiDS) have provided galaxy counts of $\sim$10 arcmin^{-2} over 450 deg^2 and 1350 deg^2, respectively (Hildebrandt et al., 2017; Heymans et al., 2021), while the DES Y3 dataset contains galaxy sources at 5.59 arcmin^{-2} over 4143 deg^2 (Secco et al., 2022). In principle, however, shear measurements can also be made using the extended radio continuum emission of the interstellar medium. To date, deep radio surveys such as the VLA-COSMOS (Smolčić et al., 2017) and the SuperCLuster Assisted Shear Survey (SuperCLASS; Battye et al., 2020; Harrison et al., 2020; Manning et al., 2020) have yielded insufficient source counts of galaxies ($\lesssim$1 arcmin^{-2} over a few square degrees) to enable meaningful shear measurements, but surveys conducted with the forthcoming Square Kilometer Array (SKA) have the potential to yield competitive measurements. The first phase (SKA1) is forecast to achieve galaxy source counts of 2.27 arcmin^{-2} over 5000 deg^2 (Square Kilometre Array Cosmology Science Working Group et al., 2020), while Brown et al. (2015) suggest that the most optimistic second phase (SKA2) implementation would deliver 30 galaxies arcmin^{-2} over 3π steradians. The two phases are forecast to provide cosmological constraining power on a par with Stage III and Stage IV optical surveys, respectively (Harrison et al., 2016).

Radio weak lensing surveys present numerous advantages: the characteristic redshift of sources will in general be higher than is the case for optical surveys, which due to increased mass along the line of sight will yield a stronger lensing signal, as well as enabling the analysis of the growth of structure at an earlier cosmic epoch (Brown et al., 2015; Camera et al., 2017; Square Kilometre Array Cosmology Science Working Group et al., 2020); polarisation and/or kinematic information, available at no or little extra cost to the continuum observations, affords a means of mitigating against intrinsic alignment uncertainty by indicating the unlensed orientation (Blain, 2002; Morales, 2006; de Burgh-Day et al., 2015; Whittaker et al., 2015); the point spread function (PSF) of radio measurements is deterministic, enabling its precise removal, which is not the case for the PSF of optical observations (e.g. Heymans et al., 2012); and there is the potential to measure the redshift distribution of sources directly from the radio observations via statistical detection of the (low signal-to-noise) 21-cm emission line (Harrison et al., 2017). Arguably the chief benefit in conducting radio weak lensing surveys is the potential for cross-correlation with optical measurements, providing a means of mitigating the systematic measurement uncertainties afflicting each wavelength. The extended radio continuum emission is largely associated with star-forming gas, whose morphology and orientation need not be similar that of stellar component seen in the optical (see e.g. Tunbridge et al., 2016). Realisation of the potential of radio weak lensing surveys therefore requires accurate assessments of the intrinsic alignments of the star-forming gas component of galaxies.

In this Chapter, we use the cosmological, hydrodynamical simulations of the EAGLE project (Schaye et al., 2015; Crain et al., 2015) to measure the intrinsic alignments of the star-forming gas component of galaxies. These simulations self-consistently account for the back-reaction of baryons on the DM, and by modelling galaxies numerically need not appeal to geometric approximations for their size, morphology or orientation. EAGLE represents an ideal model on which to base this study, as the properties of the interstellar gas associated with its present-day galaxy population have been shown to correspond closely with observations (see e.g. Lagos et al., 2015; Bahé et al., 2016; Crain et al., 2017; Davé et al., 2020), and it reproduces the 'fundamental plane' of star formation (Lagos et al., 2016). This work builds on the previous Chapter 3 in which we examined the morphology of star-forming gas distributions associated with EAGLE galaxies, and their internal alignment with their corresponding stellar and DM components. It also complements studies with EAGLE focussing on the alignments of the stellar component of galaxies (Velliscig et al., 2015a,b). As per Velliscig et al. (2015b), we focus on the orientation-direction and orientation-orientation intrinsic alignments in 3-dimensions and in projection.

The Chapter is structured as follows. In Section 4.2 we briefly discuss details of the EAGLE simulation and outline our numerical methodology and sample selection criteria. In Section 4.3 we examine the intrinsic alignment of star-forming gas in 3-dimensions and assess its dependence on subhalo mass, redshift and its internal alignment with the DM of its host subhalo. In Section 4.4 we examine the intrinsic alignments in projection. In Section 4.5 we discuss and summarise our findings. We then carefully assess the sensitivity of our results to the numerical resolution of the simulations, the details of the subgrid physics treatments directly governing the properties of star-forming gas, and the implementation of our shape and orientation characterisation method.

4.2 Methods

This section provides a description of the methodology utilised in this chapter, which builds on that outlined in Chapter 3. We provide a brief overview of the EAGLE simulations (Section 4.2.1), and the methods used to characterise the morphology and orientation of particle distributions (Section 4.2.2). Sample selection is discussed in Section 4.2.3, and the numerical characterisation of intrinsic alignments is discussed in Section 4.2.4.

4.2.1 Simulations

We refer the reader to Sections 3.2.1 and 3.2.2 for an overview of the EAGLE simulations and the methods used to identify haloes and galaxies. We will here only highlight aspects particular relevant to the results presented in this chapter.

We primarily make use of the flagship EAGLE simulation, Ref-L100N1504, in this chapter. The simulation has a periodic volume of side $L = 100$ cMpc[1] realised with 1504^3 DM particles and an initially equal number of SPH particles, such that the initial gas and DM particle masses are $m_{\rm g} = 1.81 \times 10^6$ M$_\odot$ and $m_{\rm DM} = 9.7 \times 10^6$ M$_\odot$, respectively. The Plummer-equivalent gravitational softening length is fixed in comoving units to be 1/25 of the mean inter-particle separation, $\epsilon_{\rm com} = 2.66$ ckpc, limited to a maximum proper length of $\epsilon_{\rm prop} = 0.7$ pkpc. In Section 4.6.1, we test the numerical convergence behaviour of our results using a pair of high-resolution $L = 25$ cMpc simulations, with particle masses and softening scales smaller than those of Ref-L100N1504 by factors of 8 and 2, respectively.

[1]Throughout this chapter we use the notation 'c' and 'p' to refer to comoving and proper units, respectively. At $z = 0$ the distinction between proper and comoving units vanishes, so here the notation is dropped.

The simulations thus marginally resolve the Jeans scales at the threshold density for star formation in the warm, diffuse phase of the ISM, but do not resolve the cold, molecular phase. The use of the aforementioned polytropic pressure law is needed to suppress the artificial fragmentation of star-forming gas, but a drawback of its use is the suppression of the formation of gas discs with a scale height less than the corresponding Jeans length (see e.g. Trayford et al., 2017). Chapter 3 examined the dependence of star-forming gas morphology on the normalisation of the pressure floor and found that reasonable variations induced systematic morphological changes that were small compared to the system-to-system scatter. We further examine the influence of the pressure floor, and that of the normalisation of the star-formation law, on the internal alignment of the various matter components of galaxies in Section 4.6.2.

Another numerical limitation that can influence galaxy morphology is two-body scattering between stellar and DM particles of unequal mass, which can also lead to artificial heating of the stellar component (Ludlow et al., 2019a). We therefore caution that discs of gas and stars are both generally thicker in EAGLE than in real galaxies. Whilst unlikely to impact galaxy orientations, these limitations may affect measures dependent upon galaxy morphology, such $\epsilon_{\mathrm{g}+}$ and ϵ_{++} (Section 4.2.4.2).

4.2.2 Characterisation of the morphology and orientation of galaxy components

As in Chapter 3, the shapes and orientations of galaxies and their subhaloes are quantitatively characterised by fitting a 3-dimensional ellipsoid to the relevant particle distribution. This ellipsoid is characterised by major, intermediate and minor axis lengths (a, b, c) and vectors $(\vec{e_1}, \vec{e_2}, \vec{e_3})$. The characteristics of the ellipsoid are computed via an algorithm which calculates an iterative form of the mass distribution tensor of the relevant particles:

$$M_{ij} = \frac{\sum_p w_p r_{p,i} r_{p,j}}{\sum_p w_p}, \tag{4.1}$$

where the sum is over all particles, p. Here $r_{p,i}$ is the i-th element of a particle p's coordinate vector relative to the galaxy centre, and w_p is a weighting factor. As the mass distribution tensor and the inertia tensor of an object share common eigenvalues and eigenvectors, it is common to use the two terms interchangeably. In this work we will refer to the inertia tensor.

To mimic the structure of radio continuum-luminous regions, whose luminosity broadly correlates linearly with the local SFR (see e.g. Condon, 1992; Schober et al., 2017), we consider gas particles but weight them by their SFR rather than their mass ($w_p = \dot{m}_{p,\star}$). The SFR of gas particles is precisely zero unless the particle is both denser than the

metallicity-dependent star formation threshold, and has a temperature within 0.5 dex of the polytropic pressure floor. We do not consider radio continuum emission due to AGN, since this is not extended. The best fit ellipsoid is therefore first computed within a spherical aperture of radius $r_{\rm ap} = 30$ pkpc, where this value is chosen for consistency with that commonly used when computing galaxy properties by aggregating particle properties (see e.g. Section 5.1.1 of Schaye et al., 2015). In 2-dimensions, a circular aperture of $r_{\rm ap} = \max(30 \text{ pkpc}, 2r_{1/2,\text{SF-Gas}})$ is used, where $2r_{1/2,\text{SF-Gas}}$ is the half-mass radius of the star-forming gas. It is then re-computed iteratively, using the particles enclosed by the best-fit ellipsoid of the previous iteration. Complete details of the algorithm are given in Section 3.2.3.

In Section 4.6.3, we assess the sensitivity of intrinsic alignments to the chosen form of the inertia tensor, and show that it has a milder influence on the intrinsic alignments inferred for the star-forming gas than is the case for the stellar and DM components of subhaloes.

4.2.3 Sample selection

Unless otherwise stated, we adopt the same sampling criteria used in Chapter 3 (outlined in Section 3.2.4), which requires that the star-forming gas exhibits an axisymmetry parameter $A_{\rm 3D} \leq 0.6$, and that at least 100 particles each of star-forming gas, stars and DM are present within the final converged ellipsoid.

At $z = 0$, both the particle sampling and axisymmetry criteria are satisfied by 6764 galaxies. The particle sampling criteria in particular introduce a strong selection bias, especially at low subhalo mass since they correspond to a minimum stellar mass of $\sim 10^8\,\mathrm{M}_\odot$ and a minimum SFR of $\simeq 6 \times 10^{-2}\ \mathrm{M}_\odot \mathrm{yr}^{-1}$. Our sample includes approximately (0.1, 10, 80) percent of all subhaloes of total mass $\log_{10}(M_{\rm sub}/\,\mathrm{M}_\odot) \sim (10, 11, 12)$, and (16, 65, 60) percent of all subhaloes of stellar mass $\log_{10}(M_\star/\,\mathrm{M}_\odot) \sim (9, 10, 11)$.

4.2.4 Intrinsic alignments

Cosmic shear, the correlation in the shapes of distant galaxies whose images have been distorted by the lensing effect of the large scale structure of the Universe, is detectable only in the correlation of the shapes of many background galaxies. In the limit of weak gravitational lensing, the observed ellipticity ($e^{\rm obs}$) of a galaxy may be expressed as the sum of its intrinsic shape ($e^{\rm int}$) and the shear distortion due to lensing (γ)

$$e^{\rm obs} = e^{\rm int} + \gamma. \tag{4.2}$$

In the absence of intrinsic alignment, $\langle e^{\rm int} \rangle = 0$. Therefore for a sufficiently large sample of galaxies in a given patch of sky, any non-zero measurement of $e^{\rm obs}$ may be interpreted as a measurement of the shear due to the influence of the integrated mass density along the line of sight.

In practice non-random galaxy alignments are a significant source of systematic bias. The projected two-point correlation function between the shapes of galaxies is defined as

$$\langle e^{\rm obs} e^{\rm obs} \rangle = \langle \gamma\gamma \rangle + \langle \gamma e^{\rm int} \rangle + \langle e^{\rm int} \gamma \rangle + \langle e^{\rm int} e^{\rm int} \rangle. \tag{4.3}$$

The right hand side of this equation may also be expressed as GG + GI + IG + II. GG is the shear-shear auto-correlation term, and it encapsulates the correlation caused by the mutual lensing of galaxy images by some common intervening matter distribution. II is the intrinsic-intrinsic auto-correlation, caused by a close pair of galaxies being mutually aligned due to their independent alignment with some common large-scale structure. The shear-intrinsic cross-correlation term GI is caused by cases where the observed shapes of two galaxies (g_i, g_j) that reside at different redshifts ($z_i < z_j$) are correlated due to a massive object at $\simeq z_i$ acting as both a lens for g_j and a source of intrinsic alignment for g_i. The mechanism causing the IG term is the similar to GI, except here the massive object resides at $\simeq z_j$. In practice IG = 0, as a background object cannot lens a foreground galaxy.

The observed intrinsic alignment of galaxies in projection is caused primarily by their true 3-dimensional orientation and morphology. In this Chapter we explore both the 2- and 3-dimensional intrinsic alignments of galaxies in order to investigate both their expected impact on radio cosmic shear measurements, and to determine their physical cause. We largely refer to 'orientation-orientation' and 'orientation-direction' alignments, where the former concerns the orientations of a pair of galaxies, and the latter compares the orientation of one galaxy with the direction vector connecting it with a neighbour. Orientation-orientation alignment is straightforwardly the II term. Orientation-direction alignment concerns the preference for a galaxy to be orientated with respect to the location of another galaxy, and hence by extension the ambient large-scale structure. Orientation-direction alignment is therefore related to the GI term. Joachimi et al. (2011) provides a derivation of the GI power spectrum from the ellipticity correlation function. In what follows, we use the term 'intrinsic alignments' to refer to both the II and GI terms.

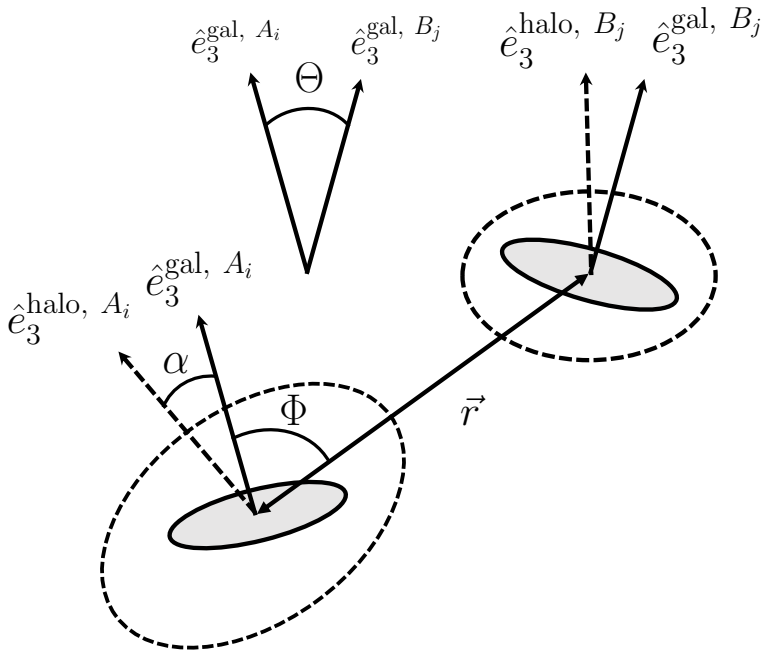

FIGURE 4.1: Schematic representation of the 3-dimensional orientation-direction and orientation-orientation intrinsic alignments. The centres of subhaloes A_i and B_j are separated by distance $|\vec{r}|$. The orientation of the galaxy (grey shaded ellipsoid) is misaligned with respect to the orientation of its dark matter subhalo (dashed ellipsoid) by the angle $\alpha = \cos^{-1}(|\hat{e}_3^{\text{gal},A_i} \cdot \hat{e}_3^{\text{halo},A_i}|)$. The orientation-direction alignment of galaxies is defined as $\Phi = \cos^{-1}(|\hat{e}_3^{\text{gal},A_i} \cdot \hat{r}|)$, while the orientation-orientation alignment is $\Theta = \cos^{-1}(|\hat{e}_3^{\text{gal},A_i} \cdot \hat{e}_3^{\text{gal},B_j}|)$.

4.2.4.1 Measuring intrinsic alignments in 3-dimensions

To measure intrinsic alignments we require the position and orientation of a pair of galaxies, necessitating two samples: $\mathcal{A} = \{A_1, A_2, ..., A_n\}$ and $\mathcal{B} = \{B_1, B_2, ..., B_m\}$. Fiducially, $\mathcal{A}$ and $\mathcal{B}$ are both the complete sample of 6764 galaxies that satisfy the criteria outlined in Section 4.2.3. To assess the sensitivity of alignments to various galaxy properties, we further sub-sample $\mathcal{A}$ and/or $\mathcal{B}$. For example, if we wish determine the orientation-direction alignment between galaxies of different subhalo masses, we sub-sample $\mathcal{A}$ and $\mathcal{B}$ accordingly and indicate this in figures with the notation $(\mathcal{A})[M^A_{\text{low}}, M^A_{\text{high}}]$ and $(\mathcal{B})[M^B_{\text{low}}, M^B_{\text{high}}]$. Sub-sampling by other properties to assess different dependencies is similarly indicated.

A graphical depiction of the 3-dimensional intrinsic and internal alignments explored in this Chapter is shown in Fig. 4.1. The 3-dimensional alignments are defined as the cosine of an angle of interest for a galaxy pair separated by some vector $\vec{r}$, $\cos(\chi)$. To assess the influence of galaxy separation, we compute the mean of $\cos(\chi)$ in bins of galaxy pair separation. A pair is comprised of one galaxy from $\mathcal{A}$ and one from $\mathcal{B}$, such that the number of galaxy pairs $N_{\text{p}} = n \times m$. In the case of the orientation-direction alignment of a galaxy pair (A_i, B_j) with positions ($\vec{x}$, $\vec{x} + \vec{r}$), respectively, we measure

the angle between A_i's morphological minor axis, $\vec{e_3}$, and the direction vector connecting the positions of the pair, $\vec{r}$, such that

$$\cos(\Phi(r)) = (|\hat{e}_3^{A_i} \cdot \hat{r}|), \tag{4.4}$$

where carets denote unit vectors. Note that taking the absolute value of the vector dot product bounds Φ between 0 and $\pi/2$, and hence $\cos(\Phi)$ between 0 and 1. The expectation value of $\cos(\Phi)$ for a random distribution of vectors in 3-dimensions is 0.5, $\cos(\Phi) = 1$ indicates perfect alignment between the two vectors, while $\cos(\Phi) = 0$ indicates perfect anti-alignment. Since we measure Φ with respect to the morphological minor axis, radial alignment (the preference for the disc plane to be aligned with the direction to a neighbour) is signified by $\cos(\Phi) < 0.5$.

In the case of the orientation-orientation alignment, we compare the orientations of both A_i and B_j as

$$\cos(\Theta(r)) = (|\hat{e}_3^{A_i} \cdot \hat{e}_3^{B_j}|). \tag{4.5}$$

The expectation value of $\cos(\Theta)$ for a random distribution of 3-vectors is again 0.5, with $\cos(\Theta) = 1$ indicating that the minor axes of two galaxies are exactly parallel, and $\cos(\Theta) = 0$ that they are exactly perpendicular.

We examine alignments as a function of both the absolute 3-dimensional distance between galaxies, and the distance normalised by the half-mass radius of the DM distribution ($r/r_{\rm DM}$) of the primary galaxy of each pair. We only consider separations less than half of the simulation boxsize.

Fig. 4.2 shows the number of galaxy pairs constructed from our fiducial sample as a function of their separation, both in terms of absolute distance (top panel) and that normalised by the half-mass radius of the primary subhalo's dark matter distribution, $r_{\rm DM}$ (bottom panel). For context, a grey vertical line is drawn at 100 times the maximum proper softening length, $\epsilon_{\rm phys} = 0.7\,$pkpc. The plot also shows the relative contribution of various combinations of central (C) and satellite (S) pairings, for example CS denotes a pairing where A_i is a central and B_j is a satellite. CC pairings are the dominant contributor to the overall pair counts, and hence the intrinsic alignments, at distant separations in both absolute ($r > 1$ Mpc) and halo-normalised terms ($r/r_{\rm DM} > 10$). At $r/r_{\rm DM} < 1$, galaxy pairings are entirely contained within one halo, with CS comprising the majority of pairings and SS making only a small contribution. Note that the CS and SC counts are identical when binned by absolute separation, but not when binned by $r/r_{\rm DM}$ since the primary halo differs in each case. Moreover, CS, SC and SS pairings do not necessarily reside in the same FoF halo, hence the non-vanishing contribution at

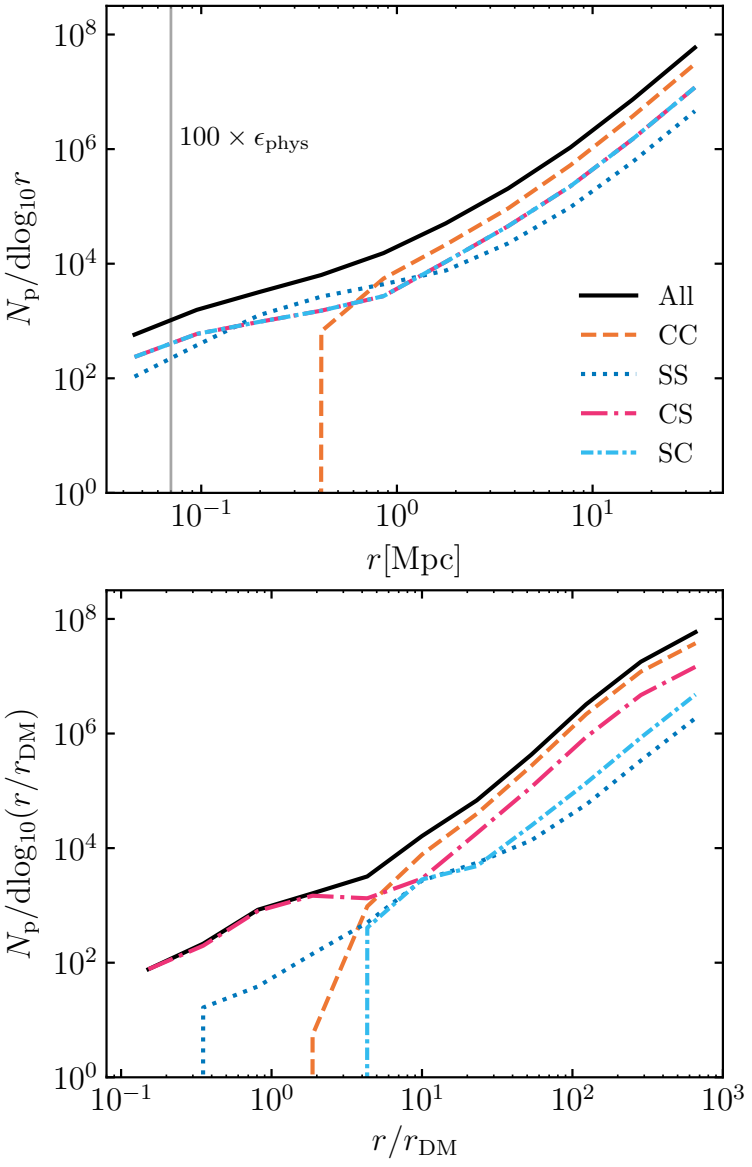

FIGURE 4.2: Galaxy pair counts, N_p, as a function of separation for our fiducial sample. Counts are shown for the entire sample (black curve) and separately for the contributions of various pairings of central (C) and satellite (S) galaxies (see legend). Pair counts are shown as a function of absolute separation in the upper panel, and as a function of separation normalised by the dark matter half-mass radius of the primary galaxy's subhalo in the lower panel. The vertical grey line in the top panel is drawn at $100\epsilon_\mathrm{phys}$, where $\epsilon_\mathrm{phys} = 0.70\,\mathrm{pkpc}$ is the maximum proper softening length of the Ref-L100N1504 simulation.

large separation. At short separations it is however generally the case that such pairings do share a FoF halo (see the bottom panels of Fig. 4.3).

We estimate the uncertainty on the alignment measurements using bootstrap re-sampling (e.g. Barrow et al., 1984). Within each radial bin containing $N_{\rm p}$ galaxy pairs, we randomly select with replacement $N_{\rm p}$ pairs and recompute $\langle \cos \chi \rangle$. This is repeated 100 times, and we show the $16^{\rm th}$ and $84^{\rm th}$ percentiles of this distribution of measurements on plots with error bars. As detailed in Section 4.6.4, we also estimate the measurement uncertainty stemming from the finite size of the simulation volume, which limits both the number of pairs we are able to sample at each separation, and the diversity of the environments from which they are drawn. We approximate the fractional uncertainty as a function of $N_{\rm p}$ using the power law function $f(N_{\rm p}) = AN_{\rm p}^{k}$, with $A = 65.7$ (-65.2) and $k = -0.524$ (-0.523) for upper and lower bounds, respectively.

In Section 4.3.4 we assess the impact that the internal alignment between a galaxy's star-forming gas and the DM distribution of its host subhalo has on the intrinsic alignments of galaxies. This internal alignment is characterised by the 'misalignment angle'

$$\alpha = \cos^{-1}(|\hat{e}_3^{\rm gal} \cdot \hat{e}_3^{\rm halo}|), \tag{4.6}$$

where $\hat{e}_3^{\rm gal}$ and $\hat{e}_3^{\rm halo}$ are the unit vectors parallel to the minor axis of the galaxy's star-forming gas and that of its DM, respectively. Since the internal alignments of components can exhibit a significant radial variation (see e.g. Velliscig et al., 2015b), we compute the misalignment angle with respect to $\hat{e}_3^{\rm halo}$ in two ways, the first applying to the DM the same initial 30 pkpc aperture that is used for the star-forming gas when computing the inertia tensor, and the second considering all DM particles bound to the subhalo. We refer to these misalignment angles as $\alpha_{\rm in}$ and $\alpha_{\rm all}$, respectively.

4.2.4.2 Measuring intrinsic alignments in 2-dimensions

The projected morphology of a galaxy depends on both its intrinsic 3-dimensional morphology and its orientation with respect to the observer. Weak lensing studies typically approximate the morphology of galaxy 'images' as a simple ellipse[2], characterised by the ratio of its axis lengths and its orientation. We therefore approximate the image morphology of simulated galaxies by fitting ellipses to their particle distributions following projection along one of the Cartesian axes of the simulation volume, using the 2-dimensional form of the reduced inertia tensor. In Chapter 3 we showed that, since the star-forming gas distribution of galaxies is typically more flattened than is the case

[2]The procedure of fitting this shape is however far from simple, see e.g. Kaiser et al. (1995) or Zuntz et al. (2013).

for its stellar component, there is greater variance in the projected ellipticity (i.e. 'shape noise') of the radio continuum image than the optical image.

The projected galaxy morphology is commonly described by the complex ellipticity (e.g. Mandelbaum et al., 2006), with components given by

$$(e_+, e_\times) = \frac{b^2 - a^2}{b^2 + a^2}[\cos(2\phi), \sin(2\phi)], \tag{4.7}$$

where ϕ is the orientation angle[3], and a and b are the minor and major axis lengths, respectively. In contrast to the 3-dimensional morphology, there is no reason to prefer the use of the minor axis to define the image orientation, so we follow convention and define ϕ as the angle subtended by the major axis of a galaxy A_i and some tracer of the density distribution, in this case a galaxy from the $\mathcal{B}$ sample[4]. e_+ is the radial component of the ellipticity, $e_\times$ is the 45°-rotated component. The 'total' (orientation-free) ellipticity is specified by $e = \sqrt{e_+^2 + e_\times^2}$.

We characterise the projected orientation-direction intrinsic alignment as a function of projected separation following

$$\epsilon_{\mathrm{g}+}(r_\mathrm{p}) = \sum_{i \neq j | r_\mathrm{p}}^{N_\mathrm{p}} \frac{e_+(i|j)}{N_\mathrm{p}}, \tag{4.8}$$

which is also known as the average intrinsic shear of galaxies (e.g. Singh et al., 2015), and the projected orientation-orientation intrinsic alignment is computed as

$$\epsilon_{++} = \sum_{i \neq j | r_p}^{N_\mathrm{p}} \frac{e_+(j|i)e_+(i|j)}{N_\mathrm{p}}. \tag{4.9}$$

We also present the average projected orientation-direction alignment angle, computed using the estimator

$$\langle \phi \rangle = \sum_{i \neq j | r_p}^{N_\mathrm{p}} \frac{\phi}{N_\mathrm{p}}, \tag{4.10}$$

This measure provides a more intuitive view of the projected alignments as a function of separation.

We consider only pairs separated along the projection axis by less than 4 pMpc in order to restrict our analyses to galaxies sharing similar large-scale structure, however we find that our results are relatively insensitive to plausible choices of this value. For the

[3]Note that Φ and ϕ correspond to the orientation-direction alignment angle in 3- and 2-dimensions, respectively.

[4]In the literature it is common that a galaxy pair is described as belonging to a shape (S) and density sample (D), particularly when relating to the construction of Landy-Szalay estimator.

avoidance of confusion, we follow Mandelbaum et al. (2006) and remark that positive values of e_+ indicate radial alignment, i.e. a tendency for the major axis of galaxies to point towards overdense regions of galaxies, which is the opposite of the often-applied convention in the weak lensing lensing literature that a positive shear signal corresponds to tangential alignment.

4.3 Intrinsic Alignments In 3-Dimensions

In this section we examine the 3-dimensional intrinsic alignments of the star-forming gas of galaxies. In Section 4.3.1 we compare the present-day orientation-direction and orientation-orientation alignments, and compare with the analogous alignments exhibited by galaxies' stars and DM. In Section 4.3.2 we assess the dependence of the alignments on subhalo mass, in Section 4.3.3 we explore their evolution with redshift, and in Section 4.3.4 we assess the sensitivity of the orientation-direction alignment to the internal alignment of star-forming gas with the DM distribution of its host subhalo.

4.3.1 Intrinsic alignments of star-forming gas, stars and dark matter

In Fig 4.3, we show the mean orientation-direction ($\langle \cos \Phi \rangle$, top row) and orientation-orientation ($\langle \cos \Theta \rangle$, middle row) alignments as a function of separation for the star-forming gas (blue curves), stars (red) and DM within the subhaloes of our sample. As noted in Section 4.2.4.1 we consider the DM bound to the entire subhalo (yellow) and that within the inner regions (green). Dotted horizontal lines correspond to the expectation value for randomly-orientated 3-vectors (i.e. no intrinsic alignment). Inset panels zoom-in to highlight the small but significant intrinsic alignments at large-separations. The bottom row shows the total number of galaxy pairs (solid curve) as a function of separation, with the dashed and dotted curves denoting the contributions of galaxies sharing the same FoF halo (one-halo term) and those in different FoF haloes (two-halo term), respectively. At $z = 0$ galaxy pairs in our sample with separations $\lesssim 0.8$ Mpc typically reside within the same FoF halo, whilst at $r > 1$ Mpc pairs typically belong to different FoF haloes. The tail of one-halo pairs towards large values of $r/r_{\rm DM}$ is due to pairs where the primary galaxy is a satellite.

The star-forming gas of galaxies exhibits a non-random orientation-direction alignment out to large separations (10s of Mpc), with $\langle \cos \Phi \rangle$ decreasing farther below 0.5 (the expectation value in the absence of intrinsic alignment) towards shorter separations. Therefore, as has been widely shown for the stellar component of simulated galaxies (e.g. Chisari et al., 2015, 2016; Tenneti et al., 2015; Velliscig et al., 2015b; Harvey et al.,

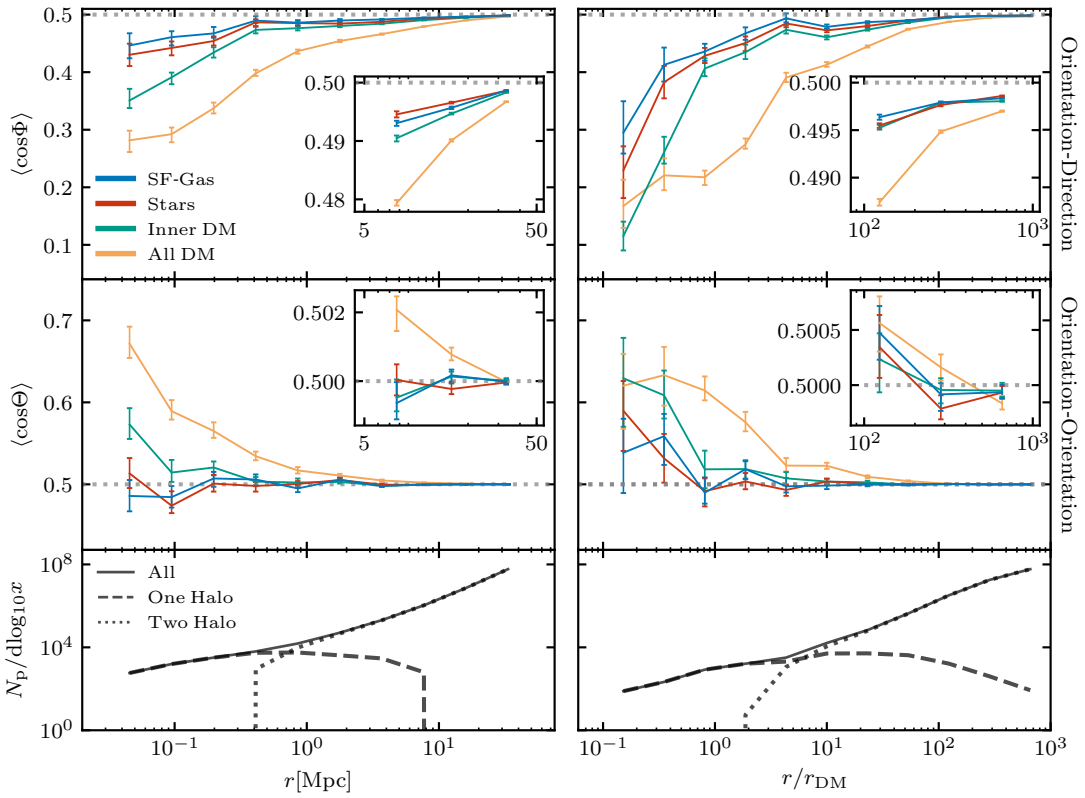

FIGURE 4.3: The present-day orientation-direction (top row) and orientation-orientation (middle row) intrinsic alignments as a function of galaxy pair separation for the star-forming gas (blue curves), stars (red) and DM (inner subhalo: green, entire subhalo: yellow) of our fiducial sample. Dotted horizontal lines correspond to the expectation value for randomly-orientated 3-vectors (i.e. no intrinsic alignment). Inset panels zoom in to highlight the small but statistically significant intrinsic alignments at large-separations. The bottom row shows the corresponding pair counts (solid curve), and the contributions of subhaloes sharing the same FoF halo (one-halo term: dashed) and those in different haloes (two-halo; dotted). The left and right columns correspond, respectively, to the separation in absolute terms and that normalised by the DM half-mass radius of the primary galaxy's subhalo (r_{DM}). Error bars denote the bootstrap-estimated uncertainty on the measurements. Curves are drawn only for bins sampled by at least 10 galaxies. The orientation-direction alignment increases at decreased separation, and is weaker for the star-forming gas than the other matter components. No significant orientation-orientation alignment is seen for the star-forming gas.

2021), the star-forming gas component exhibits a tendency to orient in a systematic fashion with respect to the ambient large-scale structure, with relatively close pairs being preferentially radially aligned. However, at all separations, the alignment is weaker than is the case for the stars, and increasingly so for the inner DM and entire DM distributions in turn. At $r = 10$ Mpc, where the two-halo term is dominant, $\langle \cos \Phi \rangle = (0.495, 0.494, 0.492, 0.482)$[5] for star-forming gas, stars, the inner DM halo and the entire DM halo, respectively. At $r = 1$ Mpc, approximately the scale of the one- to two-halo

[5]Values quoted are computed via a linear interpolation between the two closest known points.

transition, the corresponding values are $(0.487, 0.485, 0.477, 0.439)$, and at $r = 0.1$ Mpc, a scale for which the one-halo term dominates, $\langle \cos \Phi \rangle = (0.461, 0.443, 0.393, 0.295)$. At all sampled separations (the upper end of which is limited by the simulation boxsize) and for all matter components, the deviation from random is significantly larger than the estimated uncertainty on the measurement, indicating that $\langle \cos \Phi \rangle$ is inconsistent with a random distribution of alignments.

As is clear from the right-hand column, the orientation-direction alignment is particularly strong within a few $r_{\rm DM}$. Pairs in this regime generally share the same FoF halo, which dominates the local environment. Nevertheless, significant intrinsic alignment of the star-forming gas persists to $r \sim 10^2 r_{\rm DM}$. Considering entire DM haloes, strong alignments persist beyond $r \sim 10^2 r_{\rm DM}$, where central-central pairings are the largest contributors to the pair counts.

At fixed separation all matter components exhibit an orientation-orientation alignment that is much weaker than the corresponding orientation-direction alignment. Binned by absolute separation, the star-forming gas components of neighbouring galaxies exhibit no significant non-random alignment, but binning by $r/r_{\rm DM}$ reveals a small but significant intrinsic alignment at short separations ($r \lesssim r_{\rm DM}$). The alignment here is primarily due to galaxies that share a common FoF halo, and the tendency for $\langle \cos \Theta \rangle > 0.5$ indicates a preference for their minor axes to be parallel. The stellar component exhibits similar behaviour, with orientations broadly consistent with a random distribution when binned by absolute separation, but a significant intrinsic alignment is apparent at $r \lesssim r_{\rm DM}$. We note that Velliscig et al. (2015b) examined the orientation-orientation alignment of the stellar component of $\sim L^\star$ galaxies in the Ref-L100N1504 simulation, and found similarly weak (or absent) alignment when using a similar aperture to that we use here (see their Fig. 4). As per the orientation-direction case, the subhalo DM component exhibits much stronger orientation-orientation alignment at fixed separation than the baryonic components, such that a significant parallel alignment ($\langle \cos \Theta \rangle > 0.5$)) persists to separations of $\sim$10 Mpc, or $r \sim 10 r_{\rm DM}$, when one considers subhaloes in their entirety. In this case, at $r = (10, 1, 0.1)$ Mpc we find $\langle \cos \Theta \rangle = (0.502, 0.516, 0.588)$, respectively. The alignment of the inner regions of subhaloes is weaker, but still much stronger than that of the baryonic components, for example at $r = 0.1$ Mpc we find $\langle \cos \Theta \rangle = 0.515$.

While IAs have been observed for luminous red galaxies in large galaxy surveys (Singh & Mandelbaum, 2016), they have not yet been detected for blue galaxies (Johnston et al., 2019). The significance of the prediction presented here must therefore be assessed. In Fig. 4.4 we show the significance of the orientation-direction alignment measurements as a function of pair separation. The star-forming gas orientation-direction alignment

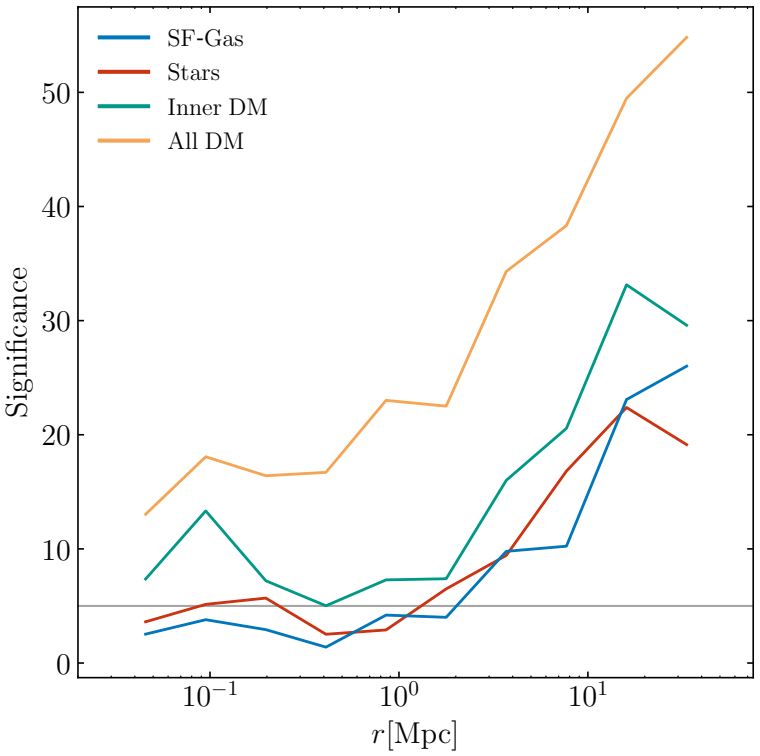

FIGURE 4.4: The significance of the measured orientation-direction alignments presented in the upper-left panel of Fig. 4.3. Significance is computed in terms of $n = |0.5 - \langle \cos\Phi \rangle|/\sigma$, where σ is the bootstrap error. The grey line indicates a significance of 5σ.

measurement becomes significant to 5σ at $\sim$2 Mpc, and further increases in significance with increased separation. Despite the weaker absolute measurement at higher separations, the lower measurement uncertainty is sufficient to drive this increase in significance. Within the largest separation bin, however, $\langle \cos\Phi \rangle = 0.499$, corresponding to a sub-percent deviation from random. It is unlikely that the sensitivity of observational measurements are sufficient to detect this subtle a signal. For the bin centred on 3.7 Mpc, there is a 1.67% deviation from random at $\sim 10\sigma$. We therefore predict that IAs between pairs of blue galaxies (characterised either by the ISM or the stellar disc) are most likely to exhibit a non-random signal at separations of a few Mpc, although this could of course change should the galaxy sample size significantly differ from the sample in this Chapter.

4.3.2 Intrinsic alignment of star-forming gas as a function of mass

We next examine the influence of subhalo mass on the intrinsic alignments of star-forming gas distributions. Since the orientation-orientation alignment is effectively consistent with random except for close central-satellite pairs, we consider only the orientation-direction alignment.

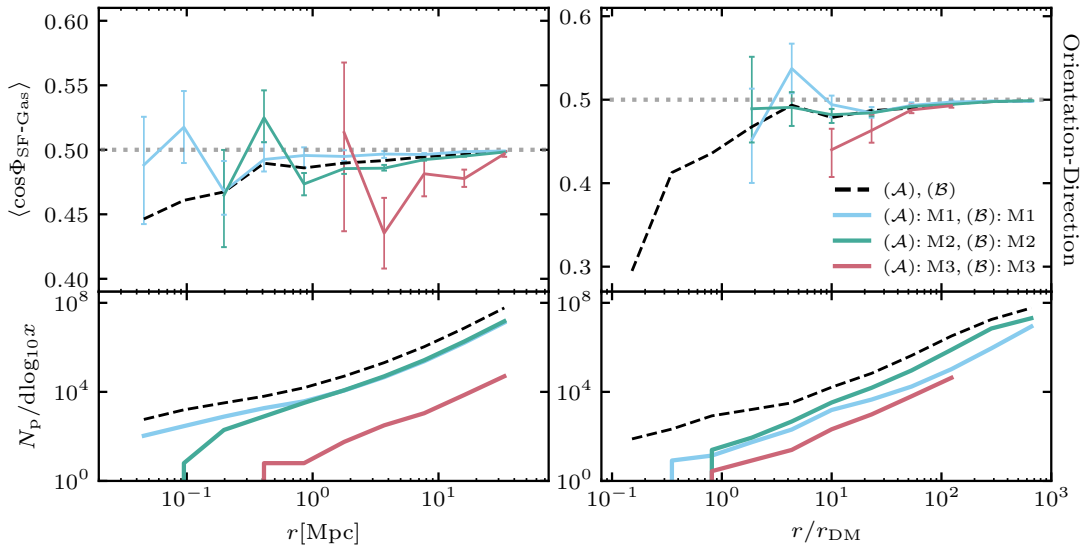

FIGURE 4.5: The present-day orientation-direction alignment of the star-forming gas component of galaxy pairs of similar subhalo mass, as a function of pair separation. The M2 bin (green curves) includes galaxies with dynamical mass broadly similar to that of the Milky Way ($\log_{10}\text{M}_{\text{sub}}/M_{\odot} \in (11.47, 12.77)$), while the M1 (blue) and M3 (red) bins include subhaloes of mass below and above this range, respectively. Dashed black curves corresponds to the $\mathcal{A}$ and $\mathcal{B}$ samples without mass binning (i.e. the blue curves from Fig. 4.3). Dotted horizontal lines correspond to the expectation value for randomly-orientated 3-dimensional vectors (i.e. no intrinsic alignment). The bottom row shows the corresponding pair counts. The left and right columns correspond, respectively, to the separation in absolute terms and that normalised by the DM half-mass radius of the primary galaxy's subhalo (r_{DM}). Error bars denote the bootstrap-estimated uncertainty on the measurements. Curves are drawn only for bins sampled by at least 10 galaxies. Orientation-direction alignment increases with subhalo mass for well-sampled separation bins. Normalising distances by r_{DM} reduces, but does not eliminates, the mass dependence.

We consider three subhalo mass bins, with the intermediate bin (M2) corresponding approximately to the dynamical mass of the Milky Way, $\log_{10}\text{M}_{\text{sub}}/M_{\odot} \in (11.47, 12.77)$. The bins M1 and M3 contain all subhaloes from the fiducial sample with mass less than and greater than the range spanned by M2, respectively. We employ this binning scheme to enable a more straightforward comparison with Velliscig et al. (2015b), who used the M2 mass bin when considering intrinsic alignments of galaxies within the Ref-L100N1504 simulation. The completeness of these mass-selected sub-samples with respect to the entire subhalo population of this simulation is complicated by the selection criteria of the fiducial sample, particularly the requirements for 100 star-forming gas particles and axisymmetry, since undisturbed gas discs are preferentially found in intermediate mass haloes. The mass bins (M1, M2, M3) comprise (47, 50, 3) percent of our fiducial sample, but correspond to (0.14, 75, 64) percent of the all subhaloes in the simulation in the corresponding mass bin. The pair counts of galaxies hosted by high-mass subhaloes declines sharply with decreasing separation distance owing to the low space density of

massive haloes.

4.3.2.1 Auto-correlation

Fig. 4.5 shows the orientation-direction alignment of the star-forming gas for subhalo pairs *of similar mass*, with the lower panels showing the corresponding pair counts. The dashed black curves correspond to the $\mathcal{A}$ and $\mathcal{B}$ samples without mass binning (i.e. the blue curves from Fig. 4.3). Note that the dynamic range of the y-axis differs in the left and right panels. Sub-sampling the fiducial sample to obtain similarly massive pairs restricts the range of separations over which the intrinsic alignments can be examined, and yields somewhat noisy results. At absolute separations of $r \lesssim 1\,\mathrm{Mpc}$ the uncertainties are sufficiently large that the measured orientations for the M1 and M2 auto-correlations are consistent with a random distribution. All three bins are well sampled for $r \gtrsim 3\,\mathrm{Mpc}$, and on these scales it is clear that at fixed separation galaxies hosted by more massive subhaloes exhibit a more pronounced radial alignment. A similar trend for the mass dependence of the stellar component has been reported widely elsewhere (e.g. Chisari et al., 2015; Tenneti et al., 2015; Velliscig et al., 2015b). As noted by Velliscig et al. (2015b) for the stars, normalising the pair separation by r_{DM} accounts for some, but not all, of the difference in star-forming gas alignment between mass bins. As is clear from the right panel of Fig. 4.5, we similarly find that using this normalisation highlights that the radial alignment of M3 pairs becomes small at separations that are large compared to the half-mass radius of the primary galaxy ($r/r_{\mathrm{DM}} \simeq 30$).

4.3.2.2 Cross-correlation

As is clear from the lower panels of Fig. 4.5, at small values of r/r_{DM} galaxy pairs of similar subhalo mass represent a small component of the total pair counts. We therefore next consider cross-correlations. Fig. 4.6 shows the orientation-direction alignment of galaxy pairs for the case in which the primary galaxy is drawn from the M2 bin, whilst the secondary galaxy is drawn from M1 (blue curves), M2 (green) or M3 (red). For brevity, we show only the case for which pair separations are normalised by r_{DM}. By construction, the cross-correlation of equal mass (i.e. the auto-correlation, M2-M2) or more massive haloes (M2-M3) is ill-defined for short r/r_{DM} separations. The regimes that are sampled by all the considered cross-correlations exhibit only a very mild radial alignment, only marginally inconsistent with a random distribution for separations of $r/r_{\mathrm{DM}} \sim 10^1$-$10^2$.

As is clear from the lower panel of Fig. 4.6, at $r/r_{\mathrm{DM}} \lesssim 3$, the fiducial sample is dominated by M2-M1 pairs, and as seen in Fig. 4.3 these pairs generally also share

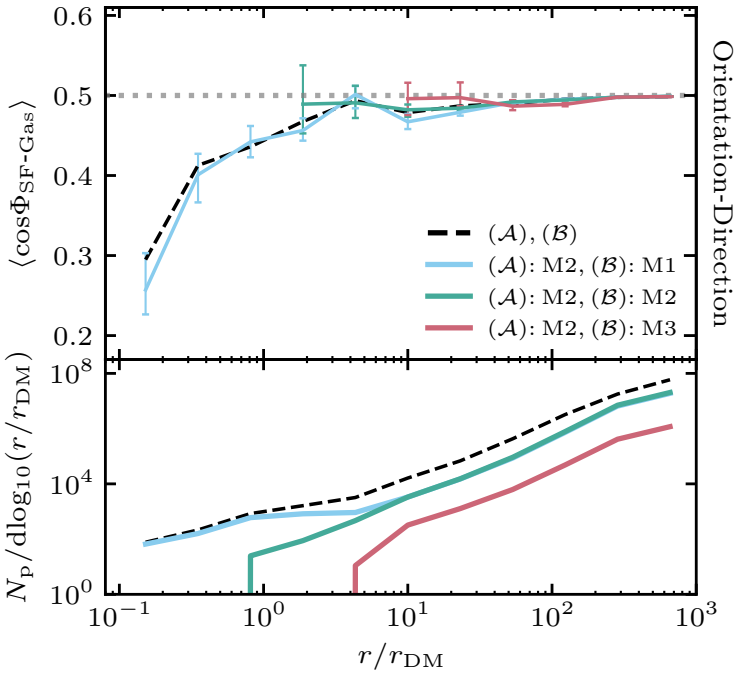

FIGURE 4.6: The present-day orientation-direction alignment of the star-forming gas component of galaxy pairs for which the primary galaxy (sample $\mathcal{A}$) is drawn from the M2 bin and the secondary (sample $\mathcal{B}$) is drawn from the M1 (blue curves), M2 (green) or M3 (red) bins. The alignment is shown as a function of pair separation normalised by the DM half-mass radius of the primary galaxy's subhalo ($r_{\rm DM}$). The bottom row shows the corresponding pair counts. Dashed black curves correspond to the $\mathcal{A}$ and $\mathcal{B}$ samples without mass binning (i.e. the blue curves from Fig. 4.3). The dotted horizontal line corresponds to the expectation value for randomly-orientated 3-vectors (i.e. no intrinsic alignment). Error bars denote the bootstrap-estimated uncertainty on the measurements. Curves are drawn only for bins sampled by at least 10 galaxies. The strong orientation-direction alignments observed at short separations are dominated by pairings of $L_\star$ galaxies and their satellites.

the same parent FoF halo. At $r/r_{\rm DM} = (1, 0.2)$, M2-M1 pairs exhibit alignments of $\langle \cos\Phi \rangle = (0.445, 0.292)$. At these separations M2-M1 pairs represent 70 percent and 85 percent of all pairs. Unsurprisingly then, the M2-M1 orientation-direction alignment therefore closely mirrors that of the overall sample in this regime (illustrated by the cyan curve closely tracking the dashed black curve). Hence the EAGLE simulation indicates that the preferential radial alignment of the star-forming gas component of close galaxy pairs is driven largely by $\sim L^\star$ galaxies and their satellites.

4.3.3 Intrinsic alignments as a function of redshift

In Chapter 3 we showed that the morphology of the star-forming gas bound to galaxies evolves with redshift, such that it exhibits increased flattening along the minor axis at later cosmic epochs. We therefore examine next whether there is a corresponding

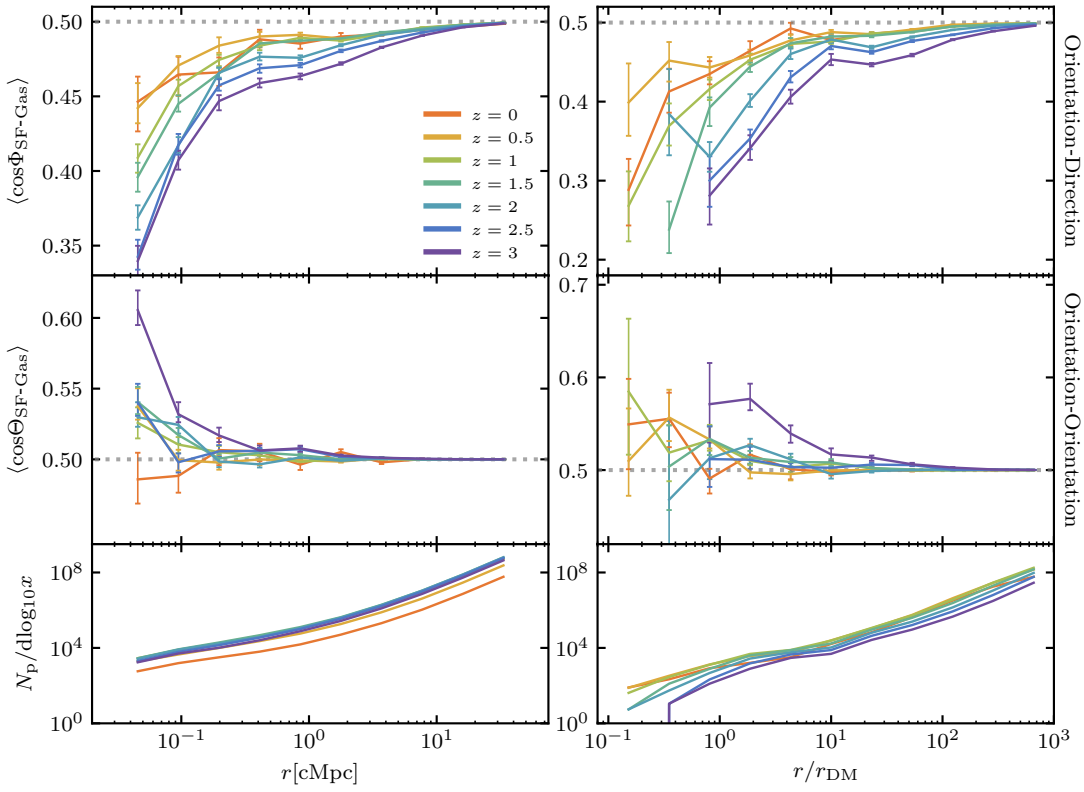

FIGURE 4.7: The orientation-direction (top row) and orientation-orientation (middle row) intrinsic alignments of star-forming gas as a function of galaxy pair separation, at seven redshifts between $z = 0$ and $z = 3$, denoted by curve colour (see legend). Dotted horizontal lines correspond to the expectation value for randomly-orientated 3-vectors (i.e. no intrinsic alignment). The bottom row shows the corresponding pair counts. The left and right columns correspond, respectively, to the separation in absolute (comoving) space, and that normalised by the DM half-mass radius of the primary galaxy's subhalo (r_{DM}). Error bars denote the bootstrap-estimated uncertainty on the measurements. Curves are drawn only for bins sampled by at least 10 galaxies. Orientation-direction alignment decreases with advancing cosmic time at fixed comoving separation. The orientation-orientation alignment is consistent with random except at high z.

evolution of the intrinsic alignments as a function of redshift. This question is pertinent in the context of radio weak lensing surveys, which will obtain shape measurements for background galaxies at higher characteristic redshifts than their optical counterparts (Brown et al., 2015; Harrison et al., 2016; Bonaldi et al., 2016; Camera et al., 2017; Square Kilometre Array Cosmology Science Working Group et al., 2020), and may therefore motivate a redshift-dependent intrinsic alignment mitigation strategy.

We assess the 3-dimensional intrinsic alignments for star-forming gas at redshifts plausibly accessible to the SKA. As we are concerned only with star-forming gas here, we relax the requirement that subhaloes exhibit at least 100 star particles. For context, we list key properties of the resulting sample at each redshift considered in Table 4.1. The typical number of particles with which we resolve the star-forming gas component is similar at all redshifts probed (∼400).

Redshift	$N_{\rm sub}$	$\log_{10} M_{\rm sub}$ [$\mathrm{M}_\odot$]	$\log_{10} M_\star$ [$\mathrm{M}_\odot$]	$\alpha_{\rm all}$	$r_{\rm DM}$ [pkpc]
$z = 0.0$	6766	$11.5^{+0.5}_{-0.4}$	$9.72^{+0.66}_{-0.53}$	$24.4^{+38.7}_{-15.6}$	$59.2^{+34.4}_{-30.0}$
$z = 0.5$	13558	$11.2^{+0.5}_{-0.5}$	$9.40^{+0.75}_{-0.55}$	$30.6^{+36.8}_{-19.3}$	$25.3^{+15.0}_{-14.0}$
$z = 1.0$	19784	$11.1^{+0.5}_{-0.5}$	$9.12^{+0.79}_{-0.54}$	$35.7^{+33.7}_{-21.7}$	$13.9^{+8.26}_{-7.71}$
$z = 1.5$	22141	$11.0^{+0.5}_{-0.5}$	$8.91^{+0.78}_{-0.53}$	$36.7^{+32.2}_{-21.8}$	$9.17^{+5.30}_{-4.90}$
$z = 2.0$	22245	$10.9^{+0.5}_{-0.5}$	$8.71^{+0.76}_{-0.51}$	$36.8^{+32.6}_{-21.2}$	$6.37^{+3.52}_{-3.21}$
$z = 2.5$	21173	$10.8^{+0.5}_{-0.5}$	$8.56^{+0.75}_{-0.52}$	$36.8^{+32.1}_{-20.8}$	$4.82^{+2.55}_{-2.19}$
$z = 3.0$	18421	$10.8^{+0.5}_{-0.5}$	$8.43^{+0.72}_{-0.52}$	$36.9^{+31.3}_{-21.1}$	$3.68^{+1.82}_{-1.57}$

TABLE 4.1: Key properties of the galaxy sample, recovered using the less restrictive criteria described in Section 4.3.3, as a function of redshift. The table presents median values and the intervals to the $16^{\rm th}$ and $84^{\rm th}$ percentiles. Columns are as follows: the snapshot redshift, the sample size ($N_{\rm sub}$), the typical subhalo mass ($M_{\rm sub}$); the stellar mass ($M_\star$); the misalignment angle in degrees between the star-forming gas and the (entire) dark matter subhalo ($\alpha_{\rm all}$); and the half-mass radius of the dark matter ($r_{\rm DM}$).

Fig. 4.7 shows the 3-dimensional intrinsic alignments, as a function of comoving galaxy pair separation, at seven redshifts spanning the range $z = 0 - 3$. The orientation-direction alignment evolves markedly and in a largely monotonic fashion, such that at fixed separation the radial alignment is stronger at earlier times: at $r = 10$ cMpc, $\langle \cos\Phi \rangle (z = 0,\ 1.5,\ 3) = (0.495,\ 0.496,\ 0.492)$; at $r = 1$ cMpc, $\langle \cos\Phi \rangle (z = 0,\ 1.5,\ 3) = (0.486,\ 0.487,\ 0.465)$; and at $r = 0.1$ cMpc, $\langle \cos\Phi \rangle (z = 0,\ 1.5,\ 3) = (0.465,\ 0.446,\ 0.409)$. The orientation-orientation alignment is weaker than the orientation-direction alignment at fixed separation, at all redshifts, being broadly consistent with random for pairs separated by $r > 0.3$ cMpc or $r/r_{\rm DM} \gtrsim 10$. At early epochs, closely separated pairs exhibit a preference for parallel alignment of their minor axes.

We generally recover greater alignment amplitudes for close pairs when normalising their separations by $r_{\rm DM}$, highlighting the important role of one-halo pairs in determining the overall alignment. At $r/r_{\rm DM} = 100$, $\langle \cos\Phi \rangle (z = 0,\ 1.5,\ 3) = (0.493, 0.493, 0.472)$; at $r/r_{\rm DM} = 10$, $\langle \cos\Phi \rangle (z = 0,\ 1.5,\ 3) = (0.478,\ 0.482,\ 0.453)$; and at $r/r_{\rm DM} = 1$, $\langle \cos\Phi \rangle (z = 0,\ 1.5,\ 3) = (0.440,\ 0.402,\ 0.283)$. We note that the horizontal shift of the $r_{\rm DM}$-normalised curves is driven in part by the growth of subhaloes.

Since strong radial alignments at short separations are dominated by one-halo central-satellite pairs, we interpret the strong evolution in the orientation-direction alignment primarily as a horizontal shift of the curves, driven by the decreasing characteristic separation of galaxy pairs, both in terms of absolute comoving distance and with respect to the (growing) half-mass radius of the primarily galaxy's subhalo half-mass radius (see

Table 4.1). The evolutionary behaviour of the two alignments is qualitatively similar to that exhibited by DM haloes (e.g. Lee et al., 2008; Chen et al., 2016), but does not perfectly mimic the evolution of the DM component's alignments because, as shown in Chapter 3, star-forming gas is a relatively poor tracer of the DM structure. As shown in Table 4.1, the misalignment of the two components, characterised by $\alpha_{\rm all}$, is generally stronger at earlier epochs and likely leads to the intrinsic alignments of star-forming gas evolving less markedly than those of the DM over the same redshift range. We explore the impact of the alignment of the baryons and the DM of subhaloes on intrinsic alignments in greater detail in the next sub-section.

4.3.4 Impact of internal galaxy-halo alignment on intrinsic alignments

The markedly different intrinsic alignments exhibited by the star-forming gas, stars and DM shown in Fig. 4.3 imply that the different matter components within subhaloes can be poorly aligned. In Chapter 3, we showed that the distribution of present-day misalignment angles connecting the star-forming gas with the subhalo DM (see equation 4.6) peaks at low values ($< 10°$, i.e. good alignment) but exhibits a long tail to severe misalignments. That we find the star-forming gas to exhibit weaker intrinsic alignments than the stars is likely therefore a consequence of the former being a poorer tracer of the overall matter distribution, which is dominated by the DM. Such misalignment is clearly of consequence for weak lensing experiments: early studies of the auto-correlation of the intrinsic (stellar) ellipticities of galaxies found a lower amplitude than expected from theoretical predictions based on the assumption of perfect galaxy-halo alignment (Heymans et al., 2004; Mandelbaum et al., 2006; Heymans et al., 2006). Okumura et al. (2009) explored the impact of luminous red galaxy-host halo misalignment on the intrinsic ellipticity auto-correlation using N-body simulations, and concluded that the assumption of perfect galaxy-halo alignment results in predicted auto-correlation amplitudes four times higher than observed.

We therefore assess the sensitivity of the orientation-direction alignment of galaxy pairs to the internal alignment of the baryonic components of the *primary* galaxy and its subhalo DM, by constructing the $\mathcal{A}$ sample from sub-samples of galaxies that exhibit particularly good and particular poor internal alignment, characterised by the misalignment angle. We consider the misalignment of the star-forming gas and the stars with respect to the DM, and define well- and poorly-aligned systems, respectively, as those with misalignment angles below the $25^{\rm th}$ and above the $75^{\rm th}$ percentile values. To assess the influence of subhalo DM structure, we consider misalignment angles measured with respect to both the inner subhalo ($\alpha_{\rm in}$) and the subhalo in its entirety ($\alpha_{\rm all}$). For context, the sample boundaries for the misalignment of star-forming gas and the DM are

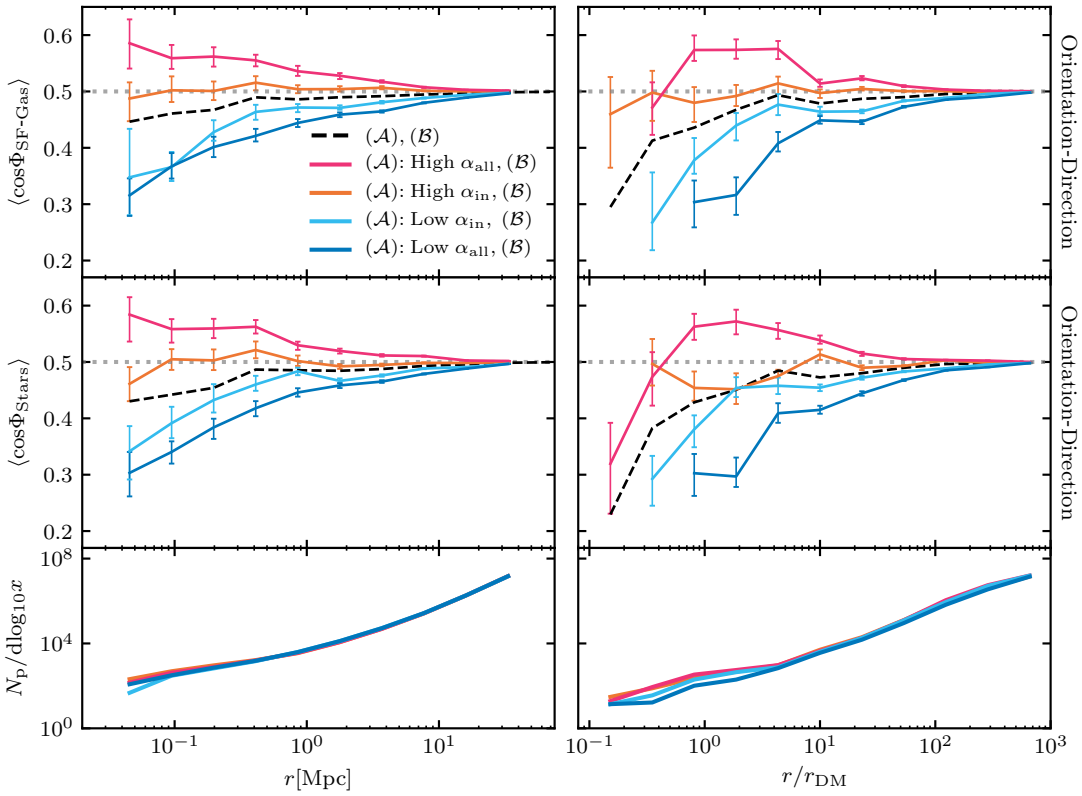

FIGURE 4.8: The present-day orientation-direction intrinsic alignments of the baryonic components of galaxies (top row: star-forming gas, middle row: stars) as a function of galaxy pair separation. The bottom row shows the pair counts corresponding to the top row. Dashed black curves correspond to the fiducial galaxy sample, whilst coloured curves correspond to sub-samples with misalignment angles (defined by equation 4.6) between the relevant baryonic component and the subhalo DM that are either below the $25^{\rm th}$ percentile value ('Low α', blue curves) or above the $75^{\rm th}$ percentile value ('High α', red/orange shades). The misalignment angles are measured with respect to both the inner subhalo DM ($\alpha_{\rm in}$) and that of the entire subhalo ($\alpha_{\rm all}$). The left and right columns correspond, respectively, to the separation in absolute space, and that normalised by the DM half-mass radius of the primary galaxy's subhalo ($r_{\rm DM}$). Error bars denote the bootstrap-estimated uncertainty on the measurements. Curves are drawn only for bins sampled by at least 10 galaxies. Intrinsic alignments are strongly dependent on the internal alignment between baryons and the host dark matter halo.

12° and 49° for $\alpha_{\rm all}$ and 5° and 26° for $\alpha_{\rm in}$. Note that the $\mathcal{B}$ sample remains comprised of the entire fiducial sample.

The resulting orientation-direction alignments at $z = 0$, as a function of pair separation, are shown in Fig. 4.8. The top row shows the effect on the orientation-direction alignment when sub-sampling based on the misalignment of the primary galaxy's star-forming gas and DM, whilst the middle row sub-samples based on the misalignment of the primary galaxy's stars and DM. The bottom row shows the pair counts corresponding to the top panel: these deviate from a simple one-quarter scaling of the pair counts for the fiducial sample only at short separations ($r \lesssim 100\,{\rm kpc}$ or $r \lesssim 3r_{\rm DM}$).

Whether one considers the star-forming gas or the stars, the orientation-direction alignment of galaxy pairs is clearly sensitive to the misalignment of the baryons with respect to the DM. Well-aligned galaxies ('Low α', blue and cyan curves) exhibit a systematically stronger radial orientation-direction alignment (lower values of $\langle\cos\Phi\rangle$) than the fiducial sample (dashed black curves) at all separations. Conversely, galaxies with strong internal misalignment ('High α', red and orange curves) exhibit systematically larger values of $\langle\cos\Phi\rangle$ than the fiducial sample at all pair separations. When binned by absolute separation, the 'High $\alpha_{\rm in}$' sub-samples (defined using the misalignment of the DM with either the star-forming gas or the stars) are consistent with no intrinsic alignment at all separations, whilst the 'High $\alpha_{\rm all}$' sub-samples exhibit *tangential* alignment ($\langle\cos\Phi\rangle > 0.5$). Recalling that the orientation-direction alignment exhibited by subhaloes is stronger when one considers the entire subhalo rather than only its inner structure (see Fig. 4.3), it is unsurprising that the well- and poorly-aligned galaxies exhibit greater differences in their intrinsic alignment when defined using $\alpha_{\rm all}$ (red and blue curves) rather than $\alpha_{\rm in}$ (orange and cyan curves).

The appearance of tangential orientation-direction alignment, i.e. the preference for the disc plane to be orthogonal to the direction to a neighbour, in galaxies with large misalignment angles is likely due to the minor axis of the baryonic component of these galaxies being well aligned with a different principal axis of the subhalo DM, rather than exhibiting poor alignment with any of the subhalo axes (see Fig. 3.7). It is interesting that, when binning by $r/r_{\rm DM}$, the 'High $\alpha_{\rm all}$' sub-sample reverts to random orientation, or even radial alignment (as is the case when classifying misalignment based on the stars), at the short separations dominated by central-satellite pairs. However, we caution that for such close pairs, the DM structure of either or both of the subhaloes may deviate from axisymmetry as a result of tidal forces, and/or may be ill-defined as a consequence of the inability of purely 3-dimensional halo finding algorithms to identify sub-structures against the high background density of a parent halo (Muldrew et al., 2011). In either case the inferred subhalo orientation(s), and the corresponding misalignment angle, is compromised.

4.4 Projected alignment measurements

In this section we examine the projected orientation-direction and orientation-orientation alignments, mimicking the intrinsic alignments that act as sources of systematic uncertainty for observational weak lensing experiments. These quantities depend not only on the relative orientations of galaxies, but also on their projected morphology: more circular projected morphologies at fixed orientation result in lower ellipticity, e_+, and

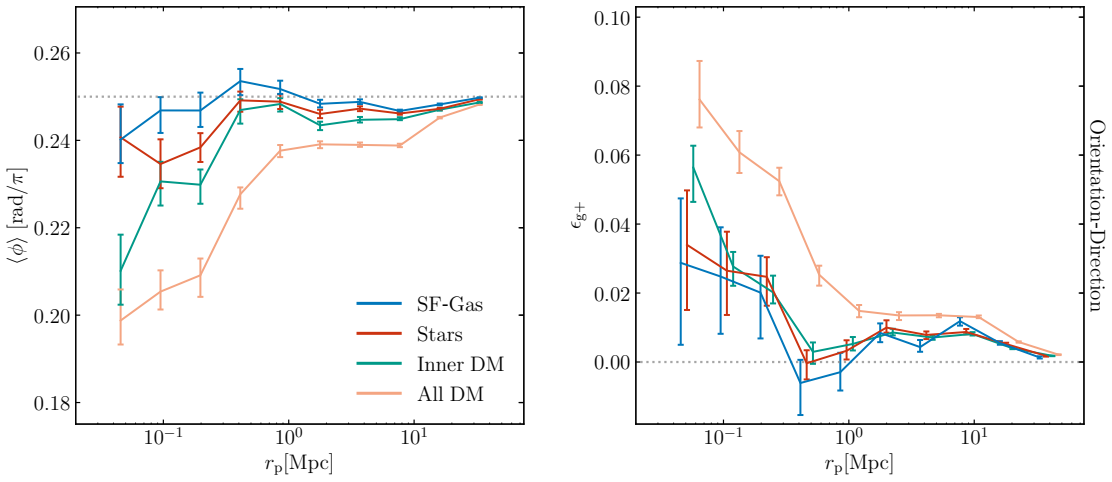

FIGURE 4.9: The present-day 2-dimensional orientation-direction intrinsic alignments as a function of projected galaxy pair separation, for the star-forming gas (blue curves), stars (red) and DM (inner subhalo: green, entire subhalo: yellow) of our fiducial sample. The alignment is presented as the mean of the 2-dimensional alignment angle, ϕ (equation 4.10), in the left panel, and as the mean intrinsic shear, $\epsilon_{g,+}$ (equation 4.8), in the right column. Dotted horizontal lines correspond to the expectation values for randomly-orientated 2-vectors (i.e. no intrinsic alignment). Error bars denote the bootstrap-estimated uncertainty on the measurements. Curves are drawn only for bins sampled by at least 10 galaxies. For clarity, curves in the right panel are artificially offset along the x-axis by multiples of 0.05 dex. The projected orientation-direction alignment generally increases at decreased separation, and is weaker for the star-forming gas than the other matter components.

therefore reduced correlation function amplitudes. Authoritative prediction of the complex ellipticity therefore requires models with realistic galaxy morphologies. We showed in Fig. 3.11 that the projected star-forming gas morphologies of the galaxies comprising our sample are in good agreement those inferred by Tunbridge et al. (2016) from Very Large Array (VLA) $L-$band observations of galaxies in the COSMOS field. For context, we remark that the 'shear responsivity' values of our fiducial sample, defined as $\mathcal{R} = 1 - \langle e^2 \rangle$ (Kaiser et al., 1995; Bernstein & Jarvis, 2002), are $\mathcal{R}_{\text{SF-Gas}} = 0.59$ and $\mathcal{R}_{\text{stars}} = 0.83$, where the latter is comparable to the values obtained from analyses of SDSS data (e.g. Sheldon et al., 2004; Singh et al., 2015).

Fig. 4.9 shows the projected orientation-direction alignment of the various matter components of galaxies. The left panel shows $\langle \phi \rangle$ (equation 4.10), the mean angle subtended by the major axis of the primary galaxy's image and the direction vector to neighbouring galaxies (i.e. the 2-dimensional analogue of $\langle \Phi \rangle$). The expectation value for a random distribution of 2-vectors, $\pi/4$ radians, is denoted by a dotted horizontal line. Values of $\langle \Phi \rangle$ below $\pi/4$ indicate a preference for radial alignment, i.e for the major axis of the image ellipse to point towards (projected) galaxy overdensities. We include this panel for ease of interpretation and to enable a more direct comparison with the 3-dimensional results presented in Fig. 4.3. The right panel shows the mean intrinsic

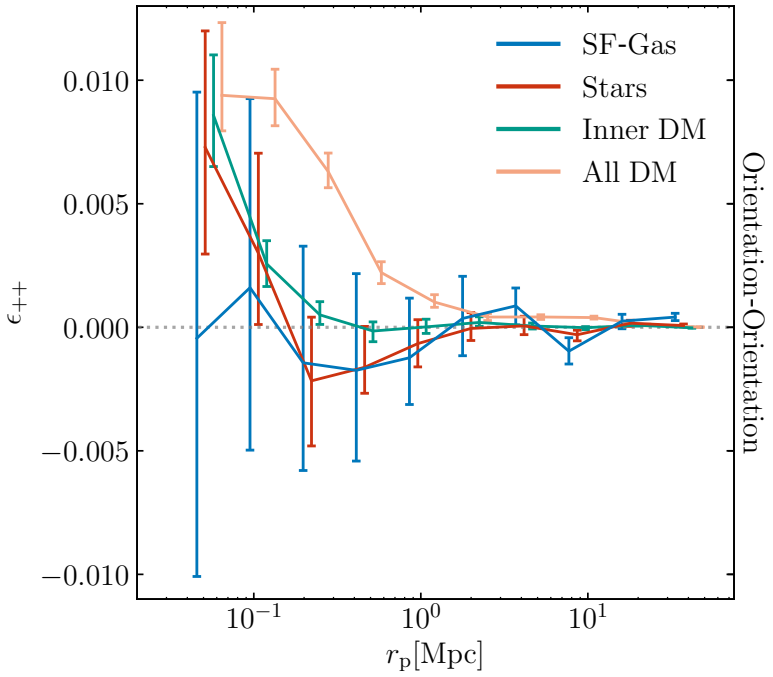

FIGURE 4.10: The present-day 2-dimensional orientation-orientation alignment as a function of projected galaxy pair separation, for the star-forming gas (blue curves), stars (red) and DM (inner subhalo: green, entire subhalo: yellow) of our fiducial sample. The dotted horizontal line corresponds to the expectation values for randomly-orientated 2-vectors (i.e. no intrinsic alignment). Error bars denote the bootstrap-estimated uncertainty on the measurements. Curves are drawn only for bins sampled by at least 10 galaxies. For clarity, the curves are artificially offset along the separation axis by multiples of 0.05 dex. The orientation-orientation alignment of the star-forming gas is consistent with random at all separations.

shear for galaxy pairs ($\epsilon_{\rm g+}$, equation 4.8), for which the expectation value in the absence of intrinsic alignment is zero. Here, positive non-zero values indicate a preference for radial alignment.

In a similar fashion to the 3-dimensional case, all components exhibit an increasingly strong preferential radial alignment with decreasing separation. At fixed separation, the intrinsic alignment is strongest for the DM of the entire subhalo, followed in order by the DM of the inner subhalo, the stars and finally the star-forming gas. For the latter, $\langle\phi\rangle$ exhibits a significant deviation from $\pi/4$ only for pairs separated by $r \lesssim 100\,\mathrm{kpc}$, a markedly shorter scale than is the case for the stars ($r \lesssim 400\,\mathrm{kpc}$). The alignment we recover for the stars is broadly consistent with that inferred by Velliscig et al. (2015b, their Fig. 8). Besides the difference in sample selection (since our fiducial sample is weighted towards star-forming galaxies), we note that Velliscig et al. (2015b) highlighted the particular sensitivity of $\epsilon_{\rm g+}$ (for the stars) to the choice of aperture used, which is in effect analogous to the application of a surface brightness limit.

The slightly greater statistical uncertainty on $\epsilon_{\rm g+}$ than $\langle\phi\rangle$ stems from the convolution

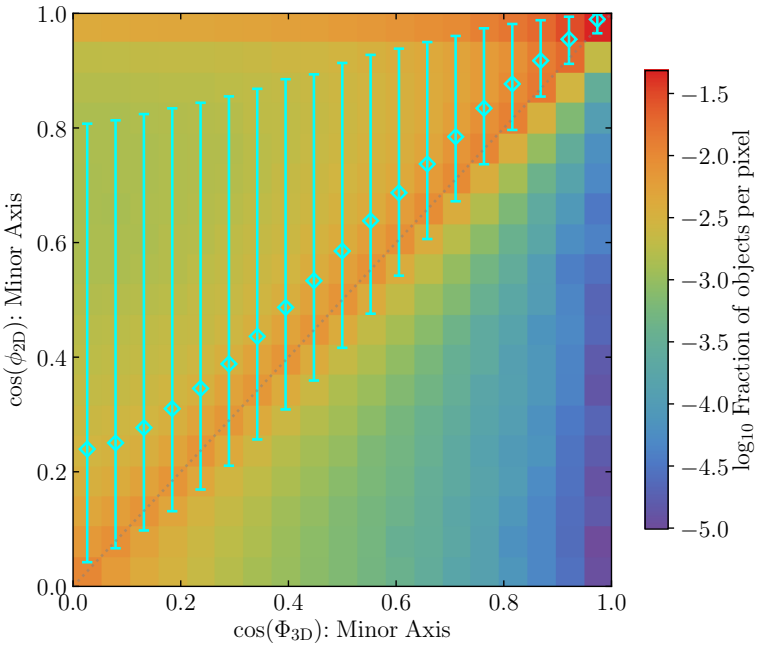

FIGURE 4.11: The orientation-direction alignments for pairs of galaxies as characterised by the star-forming gas in 2 and 3 dimensions. We consider pairs that in 3 dimensions are separated by less than 50 Mpc, and in projection are separated by less than 4 Mpc along the line of sight. The fraction of objects per pixel are indicated by the colour. The cyan curve shows the median $\cos(\phi_{2D})$ in each $\cos(\Phi_{3D})$ bin. The error bars indicate the 16^{th} and 84^{th} percentiles. Orientation is measured in terms of the minor axis.

of the projected morphology in the former. Although the 3-dimensional star-forming gas morphology exhibits a lower variance than the stars and DM, the converse is true for the projected morphology (Fig. 3.11). Despite these greater uncertainties and the generally poorer internal alignment of star-forming gas with the DM structure of subhaloes, the simulations indicate that a significant projected orientation-direction alignment of the star-forming gas component of galaxies is present for relatively close pairs. In contrast, the projected orientation-orientation alignment of the star-forming gas component (ϵ_{++}, equation 4.9), shown in Fig. 4.10, is consistent with random at all separations. This finding is perhaps unsurprising when one considers that the statistically significant orientation-orientation alignment of the entire subhalo DM at short separations, $\epsilon_{++,\mathrm{DM}}(r = 0.1\,\mathrm{Mpc}) \simeq 0.01$, is a factor of several weaker than the corresponding orientation-direction alignment, $\epsilon_{g+,\mathrm{DM}}(r = 0.1\,\mathrm{Mpc}) \simeq 0.75$. As such, it is unlikely that cosmic shear measurements in the radio continuum will be afflicted by a significant systematic error contributed by the II term.

4.4.1 Relationship between 3 dimensional and projected intrinsic alignments

In this subsection, we investigate the link between 3 dimensional intrinsic alignments and the projected alignments. In Fig. 4.11 we show the 3 dimensional and projected orientation-direction alignment for star-forming gas. For ease of comparison, we measure the orientation using the minor axis, and present the alignments in terms of the cosine of the alignment angle. We consider galaxy pairs with any separation less than 50 Mpc, and in projection are separated by less than 4 Mpc along the line of sight. This results in a sample of 3,055,648 galaxy pairs, which exhibit a broad range of values of $\cos(\Phi_{3D})$. We find that alignments characteristically appear stronger in projection than they intrinsically are in 3 dimensions. Furthermore, the standard deviation of $\cos(\phi_{2D})$ decreases with increasing $\cos(\Phi_{3D})$.

4.4.2 Projected intrinsic alignments and morphology as a function of redshift

We next explore how the projected star-forming gas intrinsic alignments and morphology change as a function of redshift. These factors have particular relevance for forecasts of the SKA's ability to constrain cosmological parameters via weak lensing (Harrison et al., 2016). For the figures in this section, we employ no aperture in our computation of the iterative reduced inertia tensors, and follow the sampling criteria outline in 4.3.3.

In Fig. 4.12 we display redshift dependence of the observed projected ellipticity, calculated as $|\epsilon| = (a - b)/(a + b)$, where a and b are the lengths of the major and minor axes of the best-fitting ellipse, respectively. Galaxies are observed along 100 random lines of sight to increase the sampling. We find at all redshifts a preference for $|\epsilon| < 0.5$. While we find little evolution $z = 3$ and $z = 2$, the tail to high $|\epsilon|$ increases with advancing cosmic time. Galaxies as characterised by their star-forming gas exhibit the largest spread in observed ellipticities at $z = 0$. This is in agreement with Figs. 3.4 and 3.5, where we found that the 3D morphologies are increasingly flattened at later times. This then allows the 2D ellipticities to attain values which are impossible at higher redshift. Consequently, the 'shape noise' in the measured galaxy ellipticities peaks decreases with increasing redshift: at $z = 3$ the standard deviation in $|\epsilon|$ is 0.15, while at $z = 0$ it is 0.19.

Fig. 4.13 displays the projected intrinsic alignments as a function of redshift. Projected separations are given in comoving units, and galaxy pairs are restricted to be separated by no more than 4cMpc along the line of sight. The results largely follow those seen in

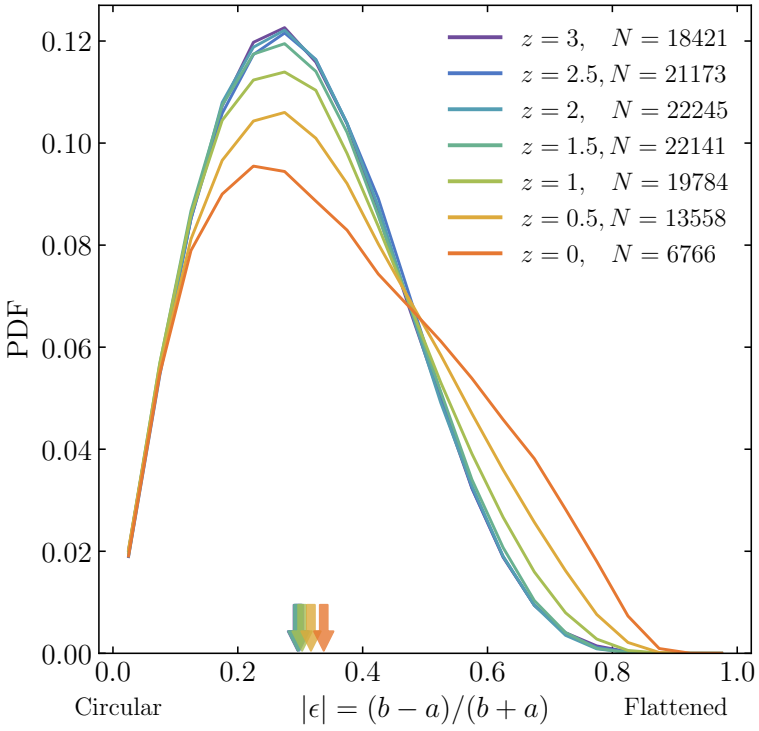

FIGURE 4.12: PDFs of the projected ellipticity of star-forming gas, split into bins of redshift. The number of galaxies included as part of the sample at each redshift is indicated in the legend. The projected morphologies are computed for each galaxy 100 times along random lines of sight. The spread in observed ellipticities are found to increase at lower redshift. Down arrows denote the median values of each distribution.

Section 4.3.3: the projected orientation-direction alignment is largely inconsistent with random at all redshifts, increasing with decreased separation and increased redshift. The largest orientation-direction alignments are found for closely neighbouring pairs at $z = 3$. Conversely the projected orientation-orientation alignment is largely consistent with random, with the exception of pairs of close separation at high redshift.

4.5 Summary and discussion

We have investigated the intrinsic alignments of the star-forming gas component of galaxies in the EAGLE suite of simulations (Schaye et al., 2015; Crain et al., 2015; McAlpine et al., 2016). Our work is motivated by the need for authoritative theoretical predictions of the systematic uncertainties inherent to cosmic shear measurements conducted using radio continuum surveys which, with the forthcoming commissioning of the Square Kilometer Array (SKA; Square Kilometre Array Cosmology Science Working Group et al., 2020), are poised to become competitive with, and complementary to, traditional optical weak lensing surveys.

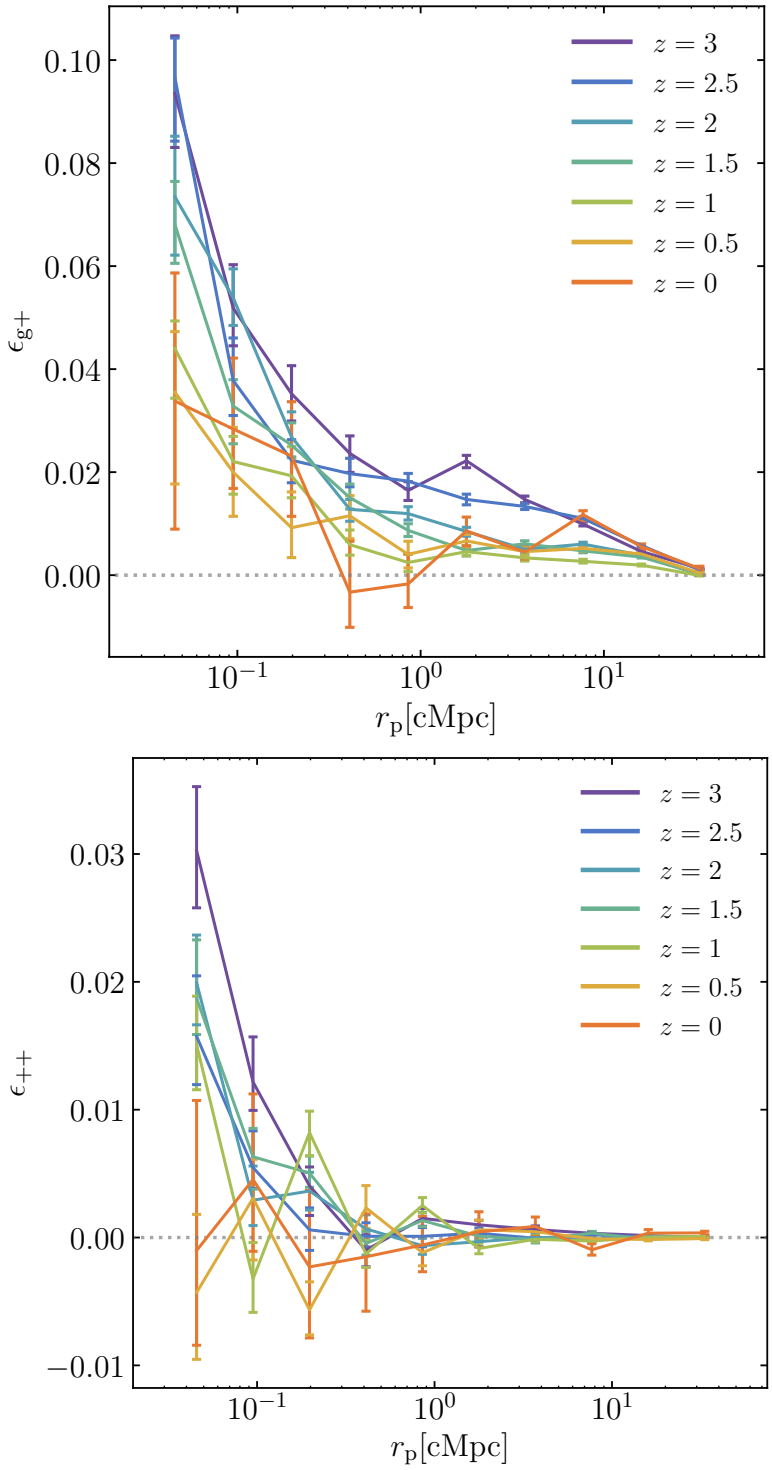

FIGURE 4.13: Projected intrinsic alignments as a function of redshift. The upper panel displays the projected orientation-direction alignment, while the lower panel displays the projected orientation-orientation alignment. Galaxy pairs are separated by no more than 4cMpc along the line of sight. The projected orientation-direction alignment is larger at higher redshift, while the projected orientation-direction alignment is consistent with random except for pairs at close separation at high redshift.

The realisation of these predictions requires state-of-the-art cosmological hydrodynamical simulations, which self-consistently follow the evolution of galaxies, their dark matter haloes and the cosmic large-scale structure, with spatial resolution on the order of 1 kpc. They hence do not need to appeal to several of the most important assumptions and approximations inherent to the analytic and semi-analytic treatments of baryon physics used by galaxy alignment models, such as those relating the morphology and orientation of galaxies' baryonic components with respect to the dark matter of their host subhaloes. In the current state-of-the-art generation of hydrodynamical simulations of the galaxy population, fluid elements (i.e. gas particles or cells) with a non-zero star formation rate represent a good proxy for the interstellar gas that emits radio continuum radiation. EAGLE therefore represents an advantageous test-bed for this study, as many of the gaseous properties of its present-day galaxy population are broadly consistent with observations (see e.g. Lagos et al., 2015; Bahé et al., 2016; Lagos et al., 2016; Crain et al., 2017; Davé et al., 2020).

We focus primarily on the present-day galaxy population, but also examine the evolution of intrinsic alignments over cosmic time. We examine the 3-dimensional orientation-direction, $\langle \cos \Phi \rangle$, and orientation-orientation, $\langle \cos \Theta \rangle$, alignments of galaxy pairs as a function of their separation, where the former is defined as the cosine of the angle between the minor axis of a galaxy and the direction vector to a neighbouring galaxy, and the latter is the cosine of the angle between the minor axes of neighbouring galaxies. To mimic the intrinsic alignments that potentially influence cosmic shear experiments, we also examine the corresponding alignments in 2-dimensions: the projected orientation-direction ($\epsilon_{\mathrm{g}+}$) and projected orientation-orientation (ϵ_{++}) alignments.

Our results are summarised as follows:

1. At fixed galaxy separation, the star-forming gas component of $z = 0$ galaxies exhibits weaker intrinsic alignments in 3-dimensions than is the case for the stellar and dark matter (DM) components. Galaxy pairs, traced by any of these three matter components, exhibit an increasingly strong radial orientation-direction alignment at shorter separations. Radial orientation-direction alignment of the star-forming gas component persists even for pairs separated by 10s of Mpc, however the corresponding alignments for the stars and DM persist to greater separations still (Fig. 4.3).

2. In contrast, the star-forming gas component of galaxy pairs exhibits no significant orientation-orientation alignment at any separation, despite a significant preference for parallel alignment of the minor axes of DM subhaloes that persists out to separations of $r \sim 10\,\mathrm{Mpc}$ (Fig. 4.3).

3. We assess the mass dependence of the orientation-direction alignment by auto- and cross-correlating sub-samples of the fiducial sample defined by subhalo mass. The auto-correlation (Fig. 4.5) reveals that, at absolute separations adequately sampled by galaxy pairs hosted by subhaloes with diverse masses, pairs of more massive subhaloes exhibit a more pronounced preference for radial alignment (at fixed separation), and this preference persists to greater separations. Normalising the pair separations by the half mass radius of the primary subhalo reduces, but does not eliminate, the mass dependence. Cross-correlating galaxy pairs when the primary galaxy is drawn from the intermediate subhalo mass bin reveals that the radial alignment of the fiducial sample is driven primarily by pairs comprising an $\sim L^{\star}$ galaxy and one of their satellites (Fig. 4.6) .

4. At fixed comoving separation, the orientation-direction alignment of galaxies' star-forming gas is greater at higher redshift, in a fashion qualitatively similar to that exhibited by the DM of subhaloes. We posit that this evolution is primarily a 'horizontal' shift, i.e. the evolution of the characteristic separation of galaxy pairs dominates over the evolution of pairwise alignments. The orientation-orientation alignment is consistent with random for most redshifts and separations, however close pairs exhibit mildly preferential parallel alignment at early epochs (Fig. 4.7).

5. The orientation-direction alignment of star-forming gas is strongly influenced by the degree of misalignment between the star-forming gas and the DM structure of the galaxy's host subhalo. Galaxies whose star-forming gas is poorly aligned with the subhalo DM do not exhibit the radial orientation-direction alignment characteristic of the broader population. The most poorly-aligned galaxies (i.e. those with the largest internal misalignment angles) exhibit a preferential tangential alignment that increases with decreasing pair separation, likely as a consequence of the star-forming gas aligning more closely with either the intermediate or major, rather than the minor, axis of the subhalo's DM (Fig. 4.8).

6. The 2-dimensional orientation-direction alignments behave in a similar fashion to the 3-dimensional case, exhibiting increasingly preferential radial alignment at decreasing pair separations. The star-forming gas exhibits a weaker alignment at fixed separation that then stars and the DM, in turn (Fig 4.9). The projected orientation-orientation alignment of star-forming gas is consistent with random at all separations, despite their host DM subhalo exhibiting a preference for parallel alignment of the minor axes (Fig. 4.10).

In Chapter 3 we showed that the characteristic morphology of the star-forming gas component of galaxies is a strong function of the mass of their host (sub)halo, and

that the structure of the gas preferentially aligns with that of the subhalo's DM, albeit to a lesser degree than is the case for the stellar component. Here, we have shown that this internal alignment leads to the star-forming gas component of galaxy pairs exhibiting significant 3-dimensional orientation-direction alignment: the minor axis of a star-forming gas disc is preferentially perpendicular with respect to the direction vector connecting it with neighbouring galaxies, which can also be viewed as the plane of the disc pointing towards neighbouring galaxies. Viewed in projection, the 2-dimensional images of the discs, potentially visible as extended radio continuum emission, also exhibit an orientation-direction alignment that is strongest for close galaxy pairs.

However, we find that the intrinsic alignments of the star-forming gas component of galaxies are weaker (at fixed pair-separation) than the corresponding alignments of the galaxies' stars. This difference stems from the star-forming gas generally being a poorer tracer than the stars of the orientation and shape of the galaxies' DM structure. As such, we expect that the systematic uncertainty due to the intrinsic alignment of galaxies will have a milder influence on cosmic shear measurements conducted in the radio continuum regime than would be the case for an optical weak lensing survey over a similar redshift range.

To our knowledge, the intrinsic alignments of star-forming gas have yet to be examined with traditional alignment models, in part owing to the complexity of realistically populating haloes with radio continuum sources. A promising avenue by which to estimate the intrinsic alignment uncertainty in radio continuum surveys may therefore be to adapt state-of-the-art simulations of the radio continuum sky (see e.g. Wilman et al., 2008; Bonaldi et al., 2019). These simulations graft empirical or (semi-)analytic treatments of baryons onto N-body simulations of the large cosmic volumes needed to construct weak lensing survey lightcones, but cannot yet be used to model intrinsic alignments because, amongst other approximations, they assume that the radio continuum images of galaxies are oriented on the sky randomly. We caution against remedying this shortcoming by simply aligning the images with the projected structure of DM (sub)haloes, since we have shown that this leads to an overestimate of the star-forming gas intrinsic alignments. However, by relating the morphology and orientation of star-forming gas distributions to the properties of their host subhaloes, with careful reference to the corresponding relationships that emerge in state-of-the-art hydrodynamical simulations of the galaxy population, we envisage that it will be possible to use radio continuum sky simulations to predict the impact of intrinsic alignments on specific survey geometries. To this end, we note that analytic fits to the distribution functions star-forming gas misalignment angles, as a function of subhalo mass, are provided in Chapter 3.

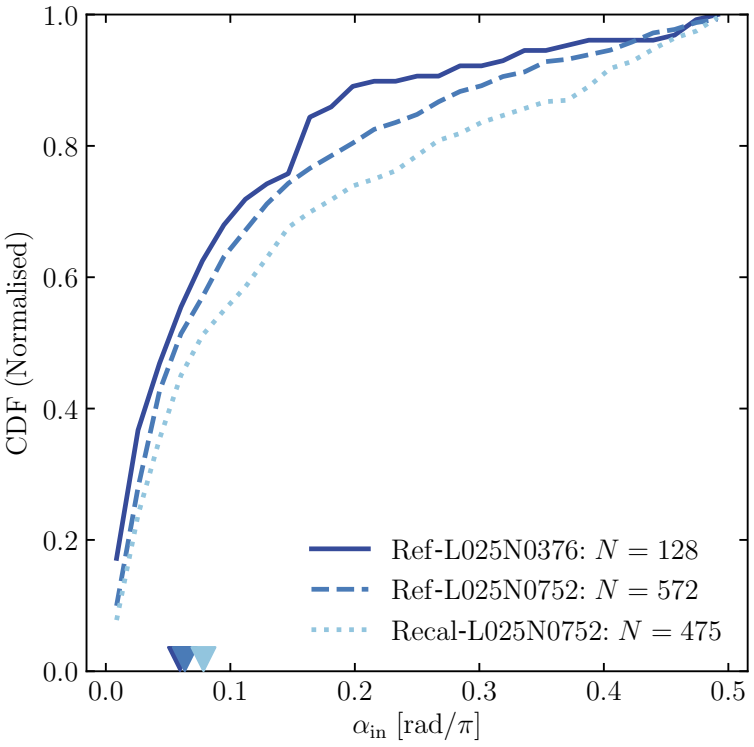

FIGURE 4.14: Cumulative probability distribution functions of the present-day misalignment angle, $\alpha_{\rm in}$, between the minor axes of the star-forming gas of galaxies and the inner DM structure of their host subhaloes. These are drawn from the Ref-L025N0376 (solid dark blue curve), Ref-L025N0752 (dashed medium blue), and Recal-L025N0752 (dotted light blue) simulations. The number of galaxies satisfying the fiducial selection criteria is quoted in the legend. Down arrows denote the median values of each distribution. The similarity of the medians of each distribution compared to their interquartile ranges indicates that the misalignment angles are well converged in both the strong and weak senses.

4.6 End of Chapter Appendix

In this section examine the influence of a series of numerical and modelling factors on the findings presented in this Chapter.

4.6.1 Numerical convergence

To assess the sensitivity of our findings to the numerical resolution of the Ref-L100N1504 simulation we examine three simulations from the EAGLE suite of a smaller $L = 25\,$cMpc cosmological volume, also introduced by Schaye et al. (2015). This enables direct comparison of the Reference model at EAGLE's fiducial resolution, Ref-L025N0376, with two higher-resolution simulations using particle masses a factor of eight lower. The first of these, Ref-L025N0752, again adopts the Reference model, enabling a test of what Schaye et al. (2015, see their Section 2) terms 'strong convergence' (i.e. for a fixed

model with changing resolution). The second, Recal-L025N0752, adopts a model recalibrated to achieve a better match to the calibration diagnostics at higher resolution, enabling a 'weak convergence' test.

The number of galaxies satisfying the fiducial selection criteria (Section 4.2.3) in an $L = 25\,\mathrm{cMpc}$ volume is too small to yield instructive measurements of orientation-direction alignment as a function of separation, so we focus here on the internal misalignment angle, $\alpha_{\rm in}$, subtended by the minor axes of the star-forming gas and the inner DM. As shown in Section 4.3.4, it is primarily this quantity that drives the difference in the intrinsic alignment of star-forming gas with respect to that of the subhalo DM. Fig. 4.14 shows the cumulative probability distribution function of $\alpha_{\rm in}$ for the subhaloes satisfying the fiducial selection criteria in the Ref-L025N0376 (solid curve), Ref-L025N0752 (dashed) and Recal-L025N0752 (dotted) simulations. Down arrows denote the median values of each distribution, which are (0.19, 0.2, 0.25) radians, respectively. The differences between these median values are much smaller than the interquartile range of $\alpha_{\rm in}$ from any of the three simulations, e.g. for Ref-L025N0376 this range is 0.36. A similar trend is seen if one instead considers the misalignment angle between the minor axis of the star-forming gas, and that of the entire DM halo, $\alpha_{\rm all}$. The internal alignment angle α is therefore well-converged in both the strong and weak senses at the resolution of Ref-L100N1504, from which we infer that the star-forming gas intrinsic alignments are similarly well-converged.

4.6.2 Influence of the subgrid ISM treatment

We turn next to the sensitivity of alignments to the subgrid physics treatments in EAGLE that directly govern the properties of interstellar gas. We therefore compare results from Ref-L025N376 with those from two pairs of simulations of the same volume, and again consider the cumulative distribution function of $\alpha_{\rm in}$. The first pair, introduced by Crain et al. (2015), varies the slope of the equations of state (EoS) from the reference value of $\gamma_{\rm eos} = 4/3$ to $\gamma_{\rm eos} = 1$ (corresponding to an isothermal EoS) and $\gamma_{\rm eos} = 5/3$ (an adiabatic EoS). Schaye & Dalla Vecchia (2008) demonstrated that a stiffer EoS creates a smoother ISM with an increased scale height, and Crain et al. (2015) showed that a stiffer EoS also suppresses gas accretion onto central supermassive black holes in massive galaxies. The second pair, introduced by Crain et al. (2017), varies the normalisation of the Kennicutt-Schmidt law (the variable A in equation 1 of Schaye et al., 2015) from the reference value of $1.515 \times 10^{-4}\,\mathrm{M_\odot\,yr^{-1}\,kpc^{-2}}$ by ± 0.5 dex. Crain et al. (2017) demonstrated that this parameter is inversely correlated with the mass of cold gas within galaxies, as it governs the gas mass needed to maintain an equilibrium between

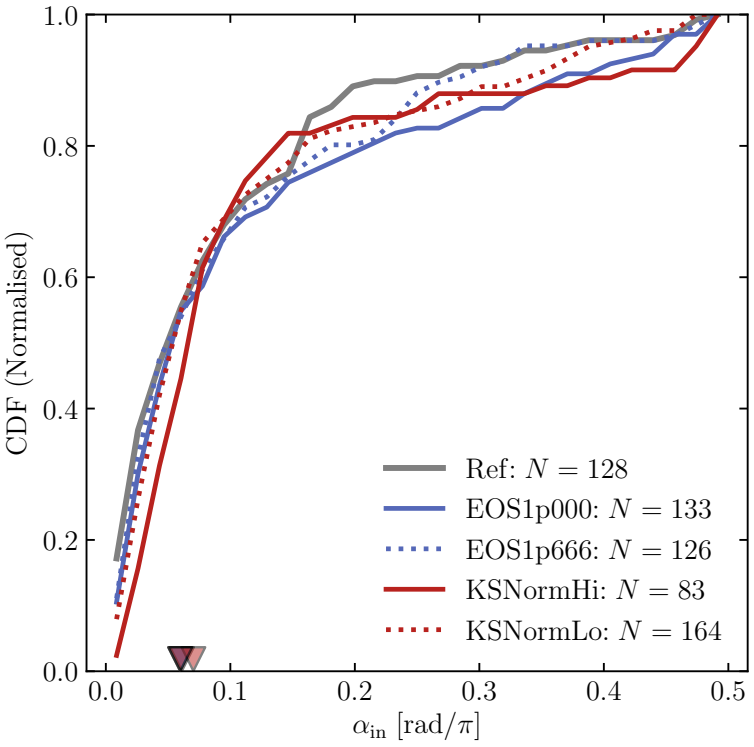

FIGURE 4.15: Cumulative probability distribution functions of the present-day misalignment angle, $\alpha_{\rm in}$, between the minor axes of the star-forming gas of galaxies and the inner DM structure of their host subhaloes. These are drawn from the Ref-L025N0376 simulations (grey curve), and two pairs of simulations that incorporate variations of the reference model, with different slopes of the ISM equation of state (EOS1p00, solid blue; and EOS1p666, dotted blue) or normalisations of the relationship between the gas pressure and the star formation rate that differ from the reference value by ± 0.5 dex (KSNormHi, solid red; KSNormLo, dotted red). The number of galaxies satisfying the fiducial selection criteria is quoted in the legend. Down arrows denote the median values of each distribution. The similarity of the medians of each distribution compared to their interquartile ranges indicates that the misalignment angles are robust to plausible changes to the subgrid physics of interstellar gas.

the rate of gas infall on one hand, and the rates of star formation and gas outflow due to ejective feedback on the other.

Fig. 4.15 shows the cumulative probability distribution function of $\alpha_{\rm in}$ for Ref-L025N0376 (grey curve), the simulations with a differing EoS ($\gamma_{\rm eos} = 1$, solid blue; $\gamma_{\rm eos} = 5/3$, dotted blue); and those with higher (solid red) and lower (dotted red) normalisations of the star formation law. As with the convergence test presented in Fig. 4.14, the distributions are not strongly affected by these significant changes to the subgrid physics: the median values of $\alpha_{\rm in}$ for each of the four variation simulations differ from that of Ref-L025N0376 by a maximum of 0.03 radians, which is small compared to the interquartile range of the latter (0.36). Intrinsic alignments are therefore robust to plausible changes to the subgrid physics of interstellar gas.

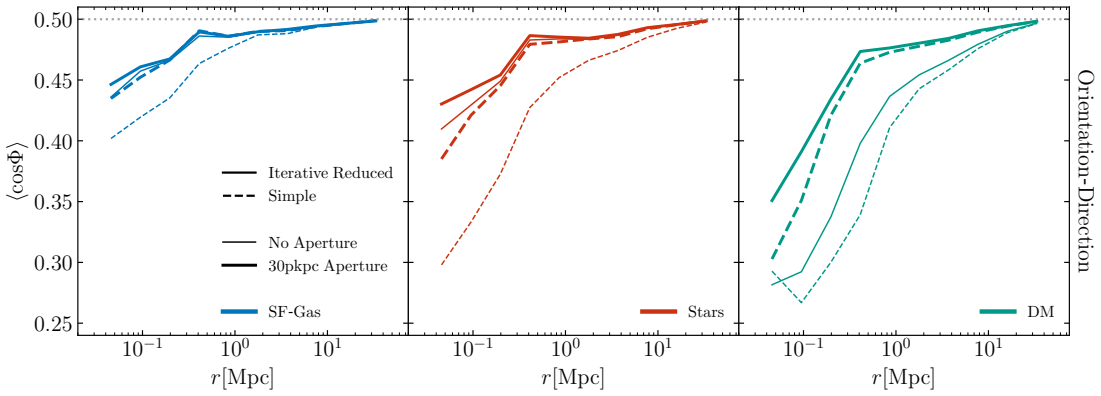

FIGURE 4.16: The present-day 3-dimensional orientation-direction alignment as a function of galaxy pair separation. Displayed are the star-forming gas (left), stars (centre) and dark matter (right) components of galaxies in the Ref-L100N1504 simulation satisfying our fiducial selection criteria. Different curve styles and thicknesses correspond to different forms of inertia tensor (solid: iterative reduced, dashed: simple) and aperture (30 pkpc: thick, no aperture: thin). The retrieved orientation-direction alignment of the star-forming gas is largely robust to the choice of shape-measurement algorithm, with the caveat that the simple inertia tensor with no aperture predicts larger alignments than the others at $r < 1$ Mpc.

4.6.3 The influence of the adopted inertia tensor and aperture on inferred intrinsic alignments

The adopted form of the inertia tensor can significantly influence the inferred morphology and orientation of the ellipsoid that best fits a particle distribution (see e.g. Bett, 2012). Similarly, the choice of the aperture used to select the particles to be fitted has also been shown to markedly influence the inferred morphology and orientation of cosmic structures (see e.g. Schneider et al., 2012; Velliscig et al., 2015b). We therefore assess the sensitivity of the inferred 3-dimensional orientation-direction alignment to our use of an iterative form of the reduced inertia tensor, with an initially spherical aperture of radius 30 kpc. Fig. 4.16 shows the alignment as a function of separation, recovered using both the reduced iterative inertia tensor (solid curves) and the simple inertia tensor (dashed curves), using both our standard aperture (thick curves) and no aperture (thin curves). From left to right, the three panels correspond to the star-forming gas, stars and dark matter, respectively.

This exercise reveals that that the qualitative trend inferred is the same in all cases, with the orientation-direction alignment of the star-forming gas being a decreasing function of pair separation. It is encouraging that, in a qualitative sense, the alignments of star-forming gas are much less sensitive to the choice of tensor and initial aperture than is the case for stars and the dark matter. We infer that this lower sensitivity stems from the more compact structure of the star-forming gas, which tends to be concentrated in subhalo centres. The deviation of the no aperture, simple tensor case from the other

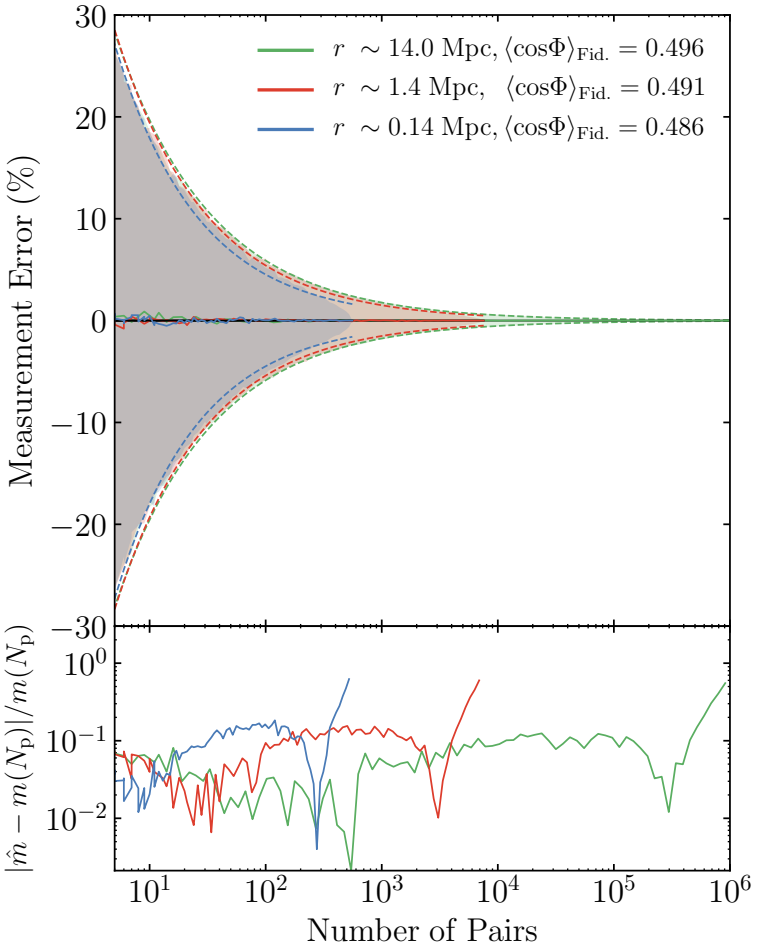

FIGURE 4.17: The estimated fractional measurement error on the 3-dimensional orientation-direction alignment of star-forming gas, as a function of the number of galaxy pairs sampled. The estimates are obtained via 5000 measurements of $N_{\rm p}$ galaxies randomly drawn from the population of three well-sampled separation bins (r∼0.14, 1.4, 14 Mpc, denoted by blue, red and green curves, respectively). Solid curves correspond to the median sampling error at fixed $N_{\rm p}$, and the shaded regions denote the interval bound by the 16$^{\rm th}$ and 84$^{\rm th}$ percentiles. The best-fit power laws are shown as dashed curves, whose residuals are shown in the lower panel.

cases likely stems from the influence of isolated clouds of star-forming gas embedded in the circumgalactic medium of galaxies, some of which may be spurious (see e.g. Schaller et al., 2015b).

4.6.4 The influence of galaxy pair sampling on inferred intrinsic alignments

Measurement of the intrinsic alignments of simulated galaxies is unavoidably influenced by the finite sampling of galaxy pairs, particularly for short separations. We therefore obtain a basic estimate of the fractional uncertainty on inferred alignments as a function

r [Mpc]	0.14	1.4	14
$N_{\rm tot}$	558	7562	1047806
$\langle\cos\Phi\rangle_{\rm fid}$	0.486	0.491	0.496
A_{84}	70.9	69.7	65.7
k_{84}	-0.598	-0.555	-0.524
A_{16}	-72.0	-69.0	-65.2
k_{16}	-0.603	-0.553	-0.523

TABLE 4.2: Best-fitting parameters of equation 4.11, describing the the $16^{\rm th}$ and $84^{\rm th}$ percentiles of fractional measurement error estimated for the three separation bins ($r = 0.14, 1.4, 14\,$Mpc) as a function of the number of galaxies sampled, $N_{\rm p}$. $\langle\cos\Phi\rangle_{\rm fid}$ is the fiducial measurement calculated using all $N_{\rm tot}$ galaxy pairs in each separation bin. The subscripts 16 and 84 on (A, k), the free parameters associated with equation 4.11, denote the corresponding percentile being described.

of the number of galaxy pairs used for the measurement, by recomputing the alignment of a well-sampled separation bin for sub-samples of the galaxy pairs. Fig. 4.17 shows the fractional sampling error in $\langle\cos\Phi\rangle$ for the star-forming gas within three pair separation bins centred on ∼0.14, 1.4 and 14 Mpc. For each bin, we first compute a fiducial alignment measurement using all pairs, and then re-compute the measurement for 5000 randomly-drawn samples of $N_{\rm p}$ pairs. The dashed curves are functional fits to these bounds, calculated according to the power law

$$m(N) = AN_{\rm p}^{k}, \tag{4.11}$$

where A and k are free parameters, and $N_{\rm p}$ is the number of galaxy pairs. We calculate the best-fitting parameters with the Python package SCIPY.OPTIMIZE.CURVE_FIT, and quote these in Table 4.2.

The sampling error is roughly proportional to $1/\sqrt{N_{\rm p}}$, and is largely insensitive to the fiducial value of $\langle\cos\Phi\rangle$. Based on the best-fit associated with the $r = 14.0$ Mpc separation bin, we find that the sampling error may be expected to fall below 1% for $N_{\rm p} > 3000$, 5% for $N_{\rm p} > 140$ and 10% for $N_{\rm p} > 35$. We find similar results when repeating this test for the stars and the dark matter.

Chapter 5

The influence of clustering on galaxy properties at fixed halo mass

The struggle itself towards the heights is enough to fill a man's heart.

One must imagine Sisyphus happy.

Camus

The content of this chapter is as yet unpublished. It reflects ongoing work in collaboration with Rob Crain and Ivan Baldry. The simulation data was created by the EAGLE, Illustris, and BAHAMAS collaborations.

5.1 Introduction

The greatest predictor of galaxy clustering is halo mass, with those residing in more massive haloes clustering the most strongly (e.g. Kaiser, 1984; Sheth & Tormen, 1999), however halo clustering is more complex than can be described by this primary linear halo bias. Assembly bias, the secondary dependence of galaxy/halo clustering on the assembly time of the halo, has been predicted by simulations but is yet to be conclusively observed (e.g. Sheth & Tormen, 2004; Gao et al., 2005; Angulo et al., 2008). Observational confirmation of these predictions remain challenging due to the need to first control for the dominating effect of halo mass, a quantity which is difficult to measure. Should a robust detection of assembly bias in observations be made, it would provide an additional means of testing the ΛCDM concordance model of cosmology. It is therefore important to determine the degree of agreement between simulations in their predictions of assembly bias. Simulations may also be used to predict the influence that cosmology and baryonic physics has on the observed signal, and identify the most robust means of detecting such a signal.

Previous studies utilising the EAGLE suite of simulations have found that the assembly time of a halo influences the properties of the galaxy it hosts at fixed halo mass (e.g. Faltenbacher et al., 2005; Matthee et al., 2017; Davies et al., 2019b, 2020), with earlier forming haloes demonstrating properties such as larger stellar mass and lower CGM mass fractions. As assembly time is correlated with clustering, one might assume that properties that vary with assembly time will also demonstrate differences in their clustering. This is *galaxy* assembly bias, or secondary bias: the secondary dependence of clustering on some (potentially observable) galaxy property.

In this chapter, we assess the galaxy assembly bias prediction of EAGLE and determine the dependence of clustering on properties other than mass, which we will refer to as secondary biases. We then compare the stellar mass secondary bias prediction of a range of simulations. Finally, we will explore the use of environmental measures as an alternative to the conventional two-point correlation function. The research presented in this final science chapter represents ongoing work between the author and collaborators.

5.2 Assembly bias in EAGLE

We first confirm the presence of the assembly bias effect in the full hydrodynamic (Ref) EAGLE simulation. We measure assembly time as the estimated time taken for the main branch progenitor of the $z = 0$ halo to acquire 50% of its final mass. As we make use of the EAGLE snapshot data, the known temporal evolution of M_{200} is coarse. For the two

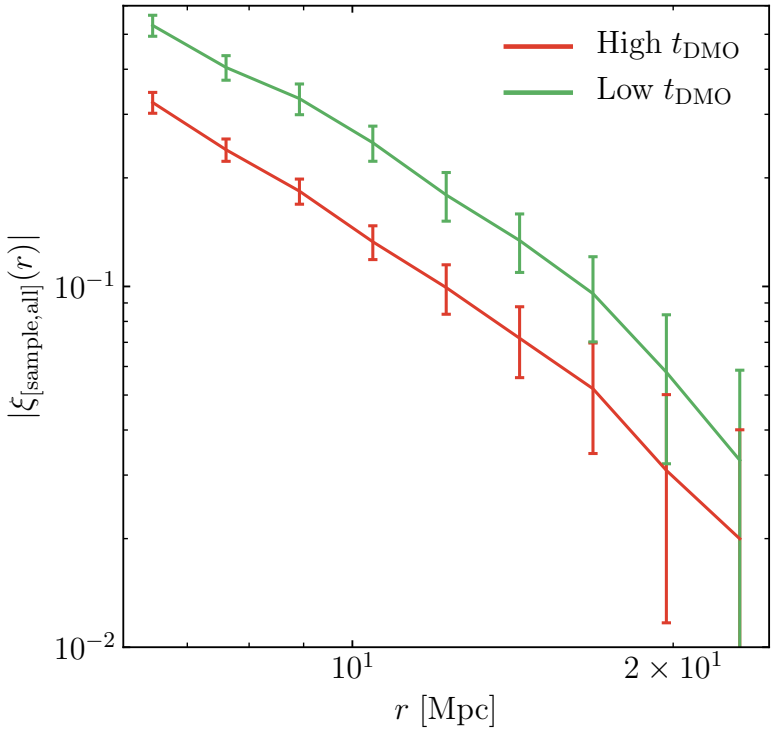

FIGURE 5.1: The assembly bias of galaxies in the Ref-L100N1504 EAGLE simulation. Galaxies are binned by $t_{\rm DMO}$, the assembly time of matched haloes in DMO-L100N1504. $|\xi_{[\rm sample,all]}(r)|$ is the cross-correlation between binned galaxies and the master sample of central galaxies with $M_{200} > 10^{10.5}/h$. Errorbars are the standard deviation computed via jackknife re-sampling.

snapshots either side of when this 50% threshold is first achieved, we perform a simple linear interpolation to estimate the assembly redshift, and then compute a conversion to assembly time assuming EAGLE's quoted cosmological parameters. In this analysis we measure assembly time via the dark matter only (DMO) EAGLE simulation, using the bijective particle matching algorithm described by Schaller et al. (2015a) to identify the same halo in both Ref and DMO simulations. In this method the IDs of dark matter particles are tracked, and a pair are confirmed as matched when a halo in each shares at least 50% of their particles. We measure the assembly time, $t_{\rm DMO}$, and other halo features using the DMO simulation in order to obtain the 'pure' halo properties, lacking any dissipative effects from baryonic physics which can enhance or dampen the intrinsic properties of haloes.

Fig. 5.1 shows the differences in clustering for galaxies based on their assembly time in the 100 cMpc EAGLE simulation. From a master sample of 17,594 central galaxies with $M_{200} > 10^{10.5}/h$, we create two sub-samples based on $t_{\rm DMO}$ and compute the two-point correlation function between each of these samples and the master [1]. 'High $t_{\rm DMO}$' represents the 20% of galaxies with the latest assembly times ($t_{\rm DMO} > 5.69$ Gyr), and

[1]The two-point correlation function is measured using the CORRFUNC code, presented by Sinha & Garrison (2017).

'Low $t_{\rm DMO}$' represents the 20% of galaxies with the earliest ($t_{\rm DMO} < 3.19$Gyr). The errorbars are computed via jackknife resampling.

We find the trend that has been reported in other studies making use of other simulations: galaxies residing in haloes that formed earlier are typically more clustered than those in haloes that formed later. An average offset of 0.26 dex is found between the curves across the 3-dimensional separation range probed, 6 to 25 Mpc. This figure is not computed at fixed halo mass, which is the primary cause of differences in clustering. We note, however, that more massive haloes tend to be younger (have larger $t_{\rm DMO}$, see Fig. 5.3), so not controlling for halo mass here likely underestimates the degree of assembly bias in EAGLE.

5.3 Secondary biases in EAGLE

We next explore the dependence of galaxy clustering on galaxy/halo properties once the primary halo mass dependence has been controlled for. Galaxy properties are obtained from haloes in the Ref simulation, while halo properties denoted with the subscript 'DMO' indicates that the quoted value has been extracted from the DMO simulation.

The properties considered are as follows:

- Assembly time ($t_{\rm DMO}$ [Gyr]): the estimated time taken for the main branch progenitor of the $z = 0$ halo to acquire 50% of the final mass.
- Halo concentration ($V^{\rm max}_{\rm DMO}/V^{200}_{\rm DMO}$): the ratio between the maximum circular velocity of dark matter and that at the virial radius. This provides an approximation of halo concentration, and is commonly used as a proxy for assembly time.
- Binding energy ($E^{2500}_{\rm DMO}$): The sum of the binding energies of dark matter particles within r_{2500}. Binding energies are inherently negative, however the sign of the quoted binding energies in subsequent figures are flipped to enable plotting on a log scale.
- Black hole mass ($M_{\rm BH}$ [M$_\odot$]): the mass of the supermassive black hole (SMBH) residing at the galaxy's centre.
- Stellar mass ($M_\star$ [M$_\odot$]): the sum of the mass of star particles residing within 30 kpc of the halo's centre of potential.
- Star formation rate ($\dot{M}_\star$ [M$_\odot$yr^{-1}]): the sum of the star formation rate (SFR) of gas particles residing within 30 kpc of the halo's centre of potential. Galaxies with no ongoing star-formation are assigning a SFR floor of 10^{-6} M$_\odot$yr^{-1}.

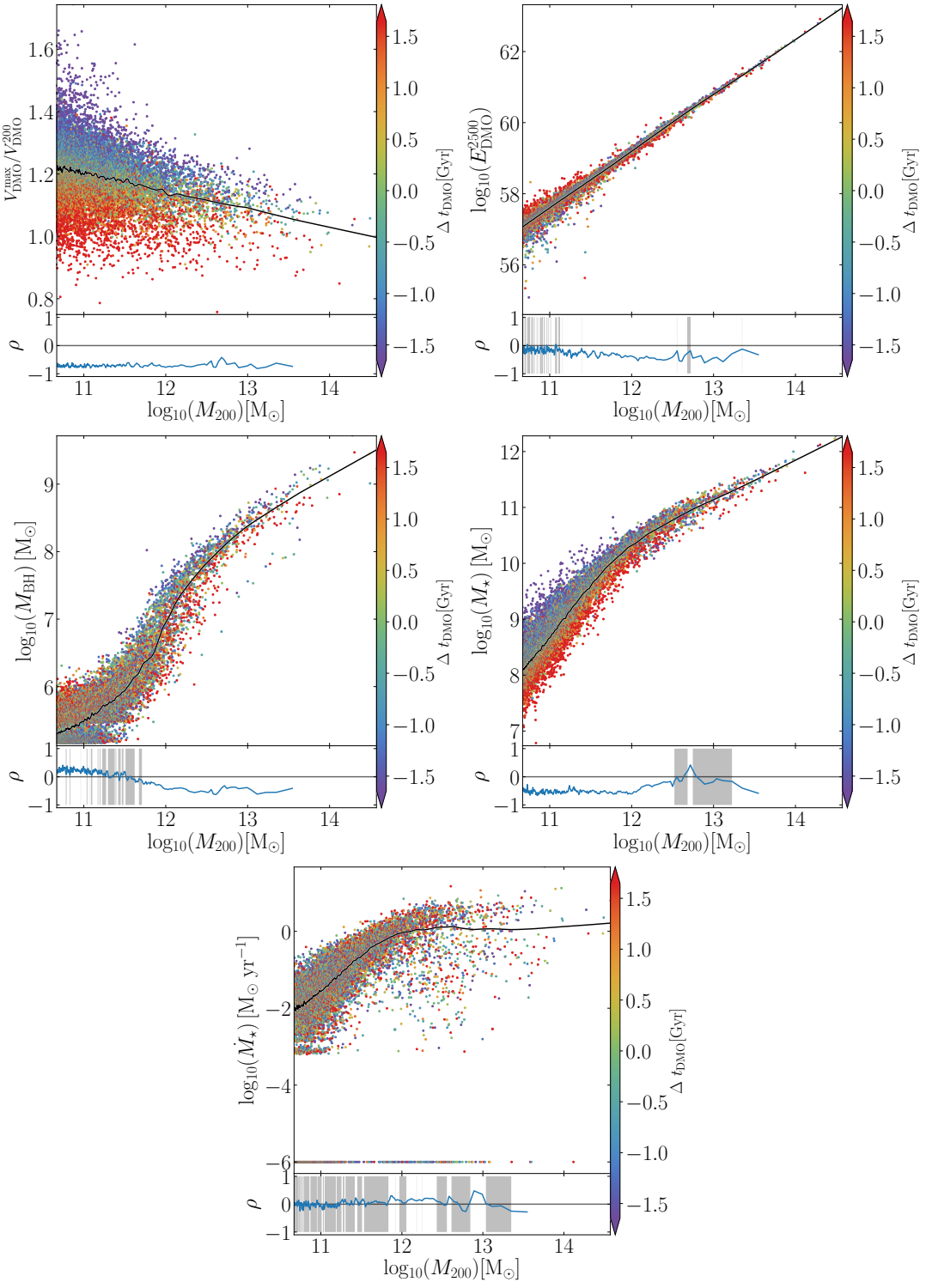

FIGURE 5.2: The correlation between numerous galaxy/halo properties and the assembly time of the halo as measured in the DMO simulation. Black curves represent the locally weighted smoothed medians of the scatter points, which are coloured by the difference between the object's assembly time and the local median assembly time. Subpanels denote the running Spearman rank coefficient for the correlation between ΔY, for some y-axis variable Y, and $\Delta t_{\rm DMO}$. Regions shaded in grey denote a Spearman rank p-value is > 0.05, and thus indicate where the recovered correlation cannot be considered significant.

5.3.1 Correlation of galaxy and halo properties with assembly time

We first calculate the extent to which the above properties correlate with halo assembly time at fixed halo mass. Properties which correlate strongly with $t_{\rm DMO}$ are likely to exhibit some form of secondary bias in their clustering. The results are displayed in Fig. 5.2. We employ the LOWESS algorithm (Cleveland, 1979) and a running Spearman rank coefficient to quantify the correlation. The means by which this is computed is the same as outlined in Section 3.3.3. Regions shaded in grey denote a Spearman rank p-value is > 0.05, and thus indicate where the recovered correlation cannot be considered significant. Subpanels quantify the visual implication of correlation at fixed halo mass. Our findings are as follows:

- Halo concentration correlates strongly with assembly time at all halo masses, with earlier forming haloes exhibiting higher concentrations. This validates the use of halo concentration as a close proxy of assembly time.
- Haloes with high binding energy are generally found to have earlier assembly times for $\log_{10}M_{200}/[\mathrm{M}_\odot] > 11$.
- The sign of the correlation between black hole mass and assembly time flips around $\log_{10}M_{200}/[\mathrm{M}_\odot] = 11.5$, below this more massive black holes are found in late assembling haloes, above this more massive black holes are found in early forming haloes.
- Higher stellar mass is strongly correlated with early assembly times for haloes with $\log_{10}M_{200}/[\mathrm{M}_\odot] < 12.5$.
- The SFR of a galaxy is not found to correlate strongly with assembly time at $z = 0$.

5.3.2 Measurement of secondary biases

We measure assembly bias and other secondary biases in the clustering of galaxies through the 'relative bias' measure (Xu & Zheng, 2020; Montero-Dorta et al., 2020). We aim to measure the differences in clustering for galaxies based on the value of some secondary property at fixed halo mass. The relative bias, $b(r)$, is measured between a sample based on a secondary property (S) with respect to primary property (P). In all cases explored in this chapter, P is the halo mass, M_{200}. We define two samples based on S and P, $\mathcal{A}_\mathcal{S}$ and $\mathcal{A}_\mathcal{P}$, which in turn are subsets of the master sample of galaxies with $M_{200} > 10^{11.5}\mathrm{M}_\odot$ ('all'). $\mathcal{A}_\mathcal{P}$ is first defined as all galaxies residing within a narrow

M_{200} bin. $\mathcal{A}_\mathcal{S}$ is subsequently defined as a subset of $\mathcal{A}_\mathcal{P}$, selected based on values of S. We define two $\mathcal{A}_\mathcal{S}$ samples each containing $\sim$50% of the objects in $\mathcal{A}_\mathcal{P}$, one with all objects with a higher S than average, and the other containing all objects with a lower S than average. The relative bias is computed as

$$b(r) = \frac{\xi_{[\mathcal{A}_\mathcal{S},\mathrm{all}]}(r,S)}{\xi_{[\mathcal{A}_\mathcal{P},\mathrm{all}]}(r,P)}, \tag{5.1}$$

where $\xi_{[\mathcal{A}_\mathcal{S},\mathrm{all}]}$ is the cross-correlation between galaxies within $\mathcal{A}_\mathcal{S}$ and the entire master sample, while $\xi_{[\mathcal{A}_\mathcal{P},\mathrm{all}]}$ is the cross-correlation between the galaxies within the larger $\mathcal{A}_\mathcal{P}$ and the entire master sample.

The strength of the correlation between galaxy clustering and halo mass is such that even within narrow halo mass bins, care needs to be taken to remove any remaining dependencies when assessing secondary biases. For example, $M_\star$ is closely correlated with M_{200}, such that within even a narrow M_{200} bin the $M_\star - M_{200}$ correlation remains significant with respect to the scatter. Such issues would be removed with sufficiently small bin widths, however in practice the challenges of sampling high-mass haloes are such that bins are required to be broad in order to achieve sufficient statistics. Simply splitting the M_{200}-selected sample about the median value of $M_\star$ is therefore insufficient, as selected galaxies with higher than the median $M_\star$ will preferentially select more massive haloes, which will introduce a spurious secondary bias signal.

In order to ameliorate this challenge, we split galaxies into $\sim$50% subsamples at fixed halo mass by determining whether or not they lie above or below the running median computed via the LOWESS algorithm (i.e. is ΔS_i greater or less than zero). We employ a small smoothing kernel in order to capture the occasionally complex $S - M_{200}$ relationships and maintain an approximately equal sample sizes for both $\mathcal{A}_\mathcal{S}$ at all halo masses. Depictions of this method in action for the examined properties are shown in Fig. 5.3. The main panels of these figures depict the relationship between S and M_{200} for the objects of our sample. Black curves denote the running median, and points are coloured based on whether they reside above (red: 'High') or below (blue: 'Low') this line. We note that this method is preferable to using linear fits within halo mass bins to determine whether a galaxy has a high or low S, as it captures the occasional expected non-linearity of some aspects of the measured parameter space, such as the knee in the $M_\star - M_{200}$ relation. There is evidence of over-fitting at low halo masses, however any biasing of samples that this engenders is small due to the high sampling within this regime. The lower subpanels show the number of objects which are deemed to have a higher or lower than average value of S at a given halo mass. Our methodology is successful in maintaining approximately equal-sized subsamples within well-sampled

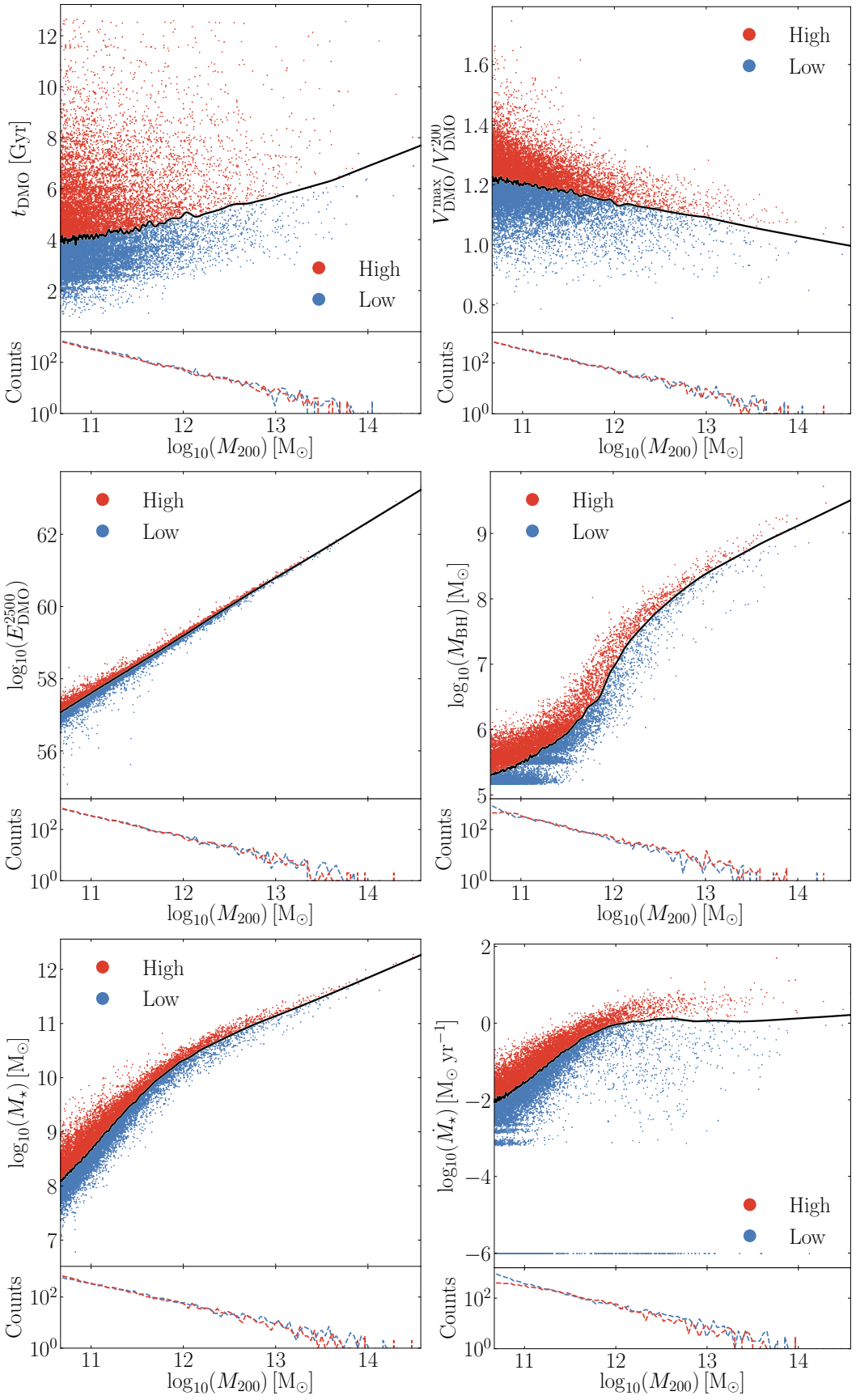

FIGURE 5.3: A depiction of the method used to separate objects into two samples, based on whether they have a higher value than average at fixed halo mass. The black curves are locally weighted smoothed medians. Points above this ($\Delta S_i > 0$)) are deemed to have a 'High' value, points below this ($\Delta S_i < 0$)) are deemed 'Low'. The subpanels denote the number of such objects at a given halo mass.

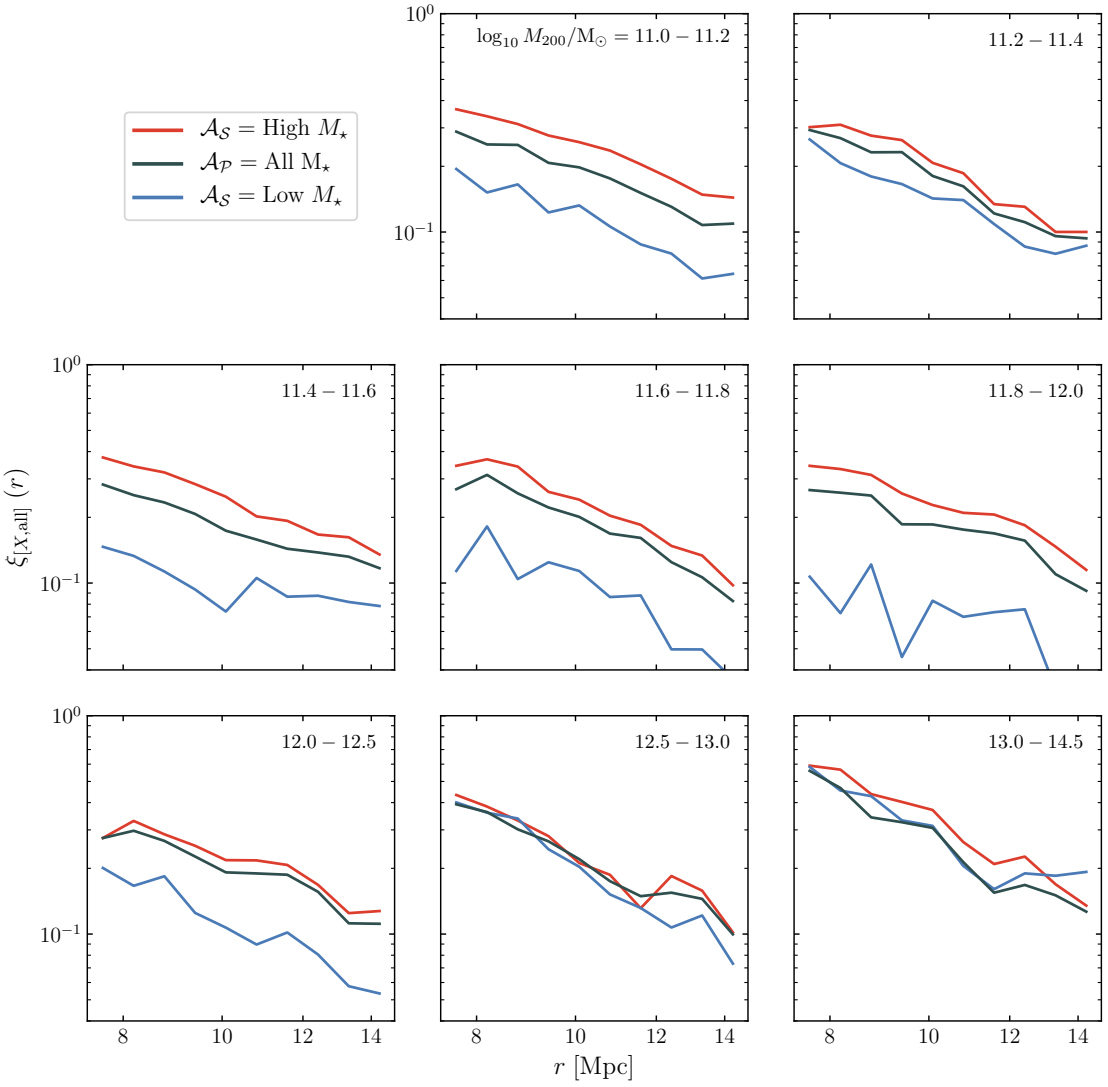

FIGURE 5.4: Differences in clustering based on $M_\star$ at fixed M_{200}. Displayed are the cross-correlations between a galaxy sample, X, and the full master sample. X is either all galaxies within an M_{200} bin ($\mathcal{A}_\mathcal{P}$: All $M_\star$), those in the same bin with $\Delta M_{\star,i} > 0$ ($\mathcal{A}_\mathcal{S}$: High $M_\star$), or those in the same bin with $\Delta M_{\star,i} < 0$ ($\mathcal{A}_\mathcal{S}$: Low $M_\star$).

regions. Challenges in obtaining equal sample sizes at low halo mass arise when the data is discretised, such as is the case with M_{BH} and the masses with which they are seeded.

The bias factor is computed within M_{200} bins for the range $r/[\mathrm{Mpc}] = 5/h - 10/h$. The cross-correlations involved for the case of $S = M_\star$ are displayed in Fig. 5.4. Galaxies with higher stellar mass than average are generally more strongly clustered than those with lower stellar mass, even after the effect of halo mass has been ameliorated. This trend becomes weaker for group mass haloes. We collapse these functions into a single measure by calculating the mean $b(r)$ within each M_{200} bin. This provides a means of determining how secondary biases vary as a function of halo mass.

In Fig. 5.5 we display how bias factor varies with halo mass for the various galaxy/halo

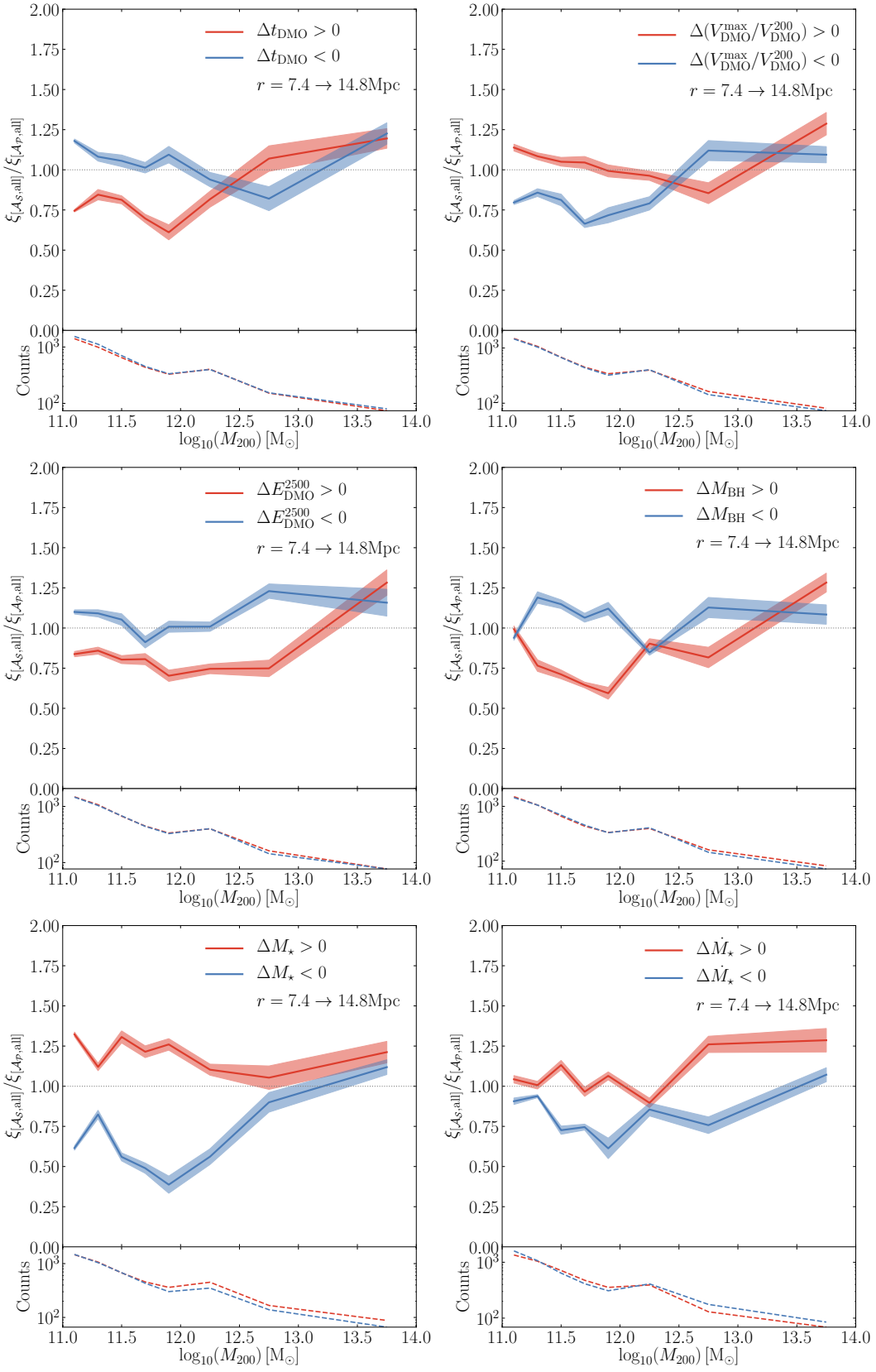

FIGURE 5.5: The secondary bias in the clustering of galaxies based on various galaxy/halo properties, as a function of halo mass. The bias factor is averaged over the range $7.4 \rightarrow 14.8$ Mpc. Red curves denote the bias factor for galaxies with a higher S value than average, blue curves denote the bias factor for galaxies with a lower S value than average. Lower panels denote the number of galaxies within A_S within each M_{200} bin. Errorbars are the standard deviation computed via jackknife re-sampling.

properties we consider in this chapter. The main panels depict $b(r)$ for each of the $\mathcal{A}_{\mathcal{S}}$ samples, which contain galaxies with ΔS_i greater or less than zero. Values above one indicate that galaxies within the $\mathcal{A}_{\mathcal{S}}$ sample clusters more strongly than in for case for all galaxies within the larger $\mathcal{A}_{\mathcal{P}}$ sample, values below one indicate the reverse.

While we recover the expected result that earlier assembly time and higher halo concentration predict greater clustering for $\log_{10} M_{200} < 12$ M$_\odot$, the greatest predictor of clustering appears to be stellar mass. This is in contrast to other studies, which suggest that all other properties are only as predictive of clustering as their ability to correlate with assembly time. Montero-Dorta et al. (2020) finds that for the IllustrisTNG300 simulation, $b(r)$ is approximately the same for stellar mass and assembly time. Curiously, we find that the halo binding energy does not follow the expected trend: lower binding energies are associated with greater clustering, despite the fact that assembly time is inversely correlated with binding energy. Another surprising result is the secondary bias in $\dot{M}_\star$ at all halo masses and $M_{\rm BH}$ for $\log_{10} M_{200} < 12$ M$_\odot$, regimes which show little to no correlation with $t_{\rm DMO}$. This indicates that at least part of the secondary biases in EAGLE are unrelated to halo assembly bias. A further exploration of these effects will be addressed in future work.

5.3.3 Differences in clustering based on stellar mass in various hydrodynamical simulations

We next compare the secondary bias in the clustering of galaxies based on stellar mass between different hydrodynamical simulations, which employ different subgrid schemes and are of different resolution and volume. The findings are shown in Fig. 5.6. The simulations we consider are the 100 Mpc EAGLE simulation, the 300 Mpc IllustrisTNG300 simulation (Springel et al., 2018), and the 400 Mpc BAHAMAS simulation (McCarthy et al., 2017). For the BAHAMAS simulation we consider separate versions with slightly different implementations of AGN feedback, which vary in the temperature that SPH neighbours to the AGN are heated by: $\Delta T_{\rm AGN}$.

All simulations predict a positive correlation between stellar mass and galaxy clustering at fixed halo mass. However we find considerable differences in the amplitudes and profiles of the measured signal between the three simulations considered. Only very slight differences are found between the two BAHAMAS simulations. EAGLE and BAHAMAS share a similar tuning fork feature at $M_{200} < 10^{12}$ M$_\odot$, which is not seen in IllustrisTNG300. Between $M_{200} = 10^{12}$ and 10^{13} M$_\odot$, BAHAMAS exhibits a flat profile which is not seen in IllustrisTNG300, and the increase in offset between the two $\Delta M_\star$

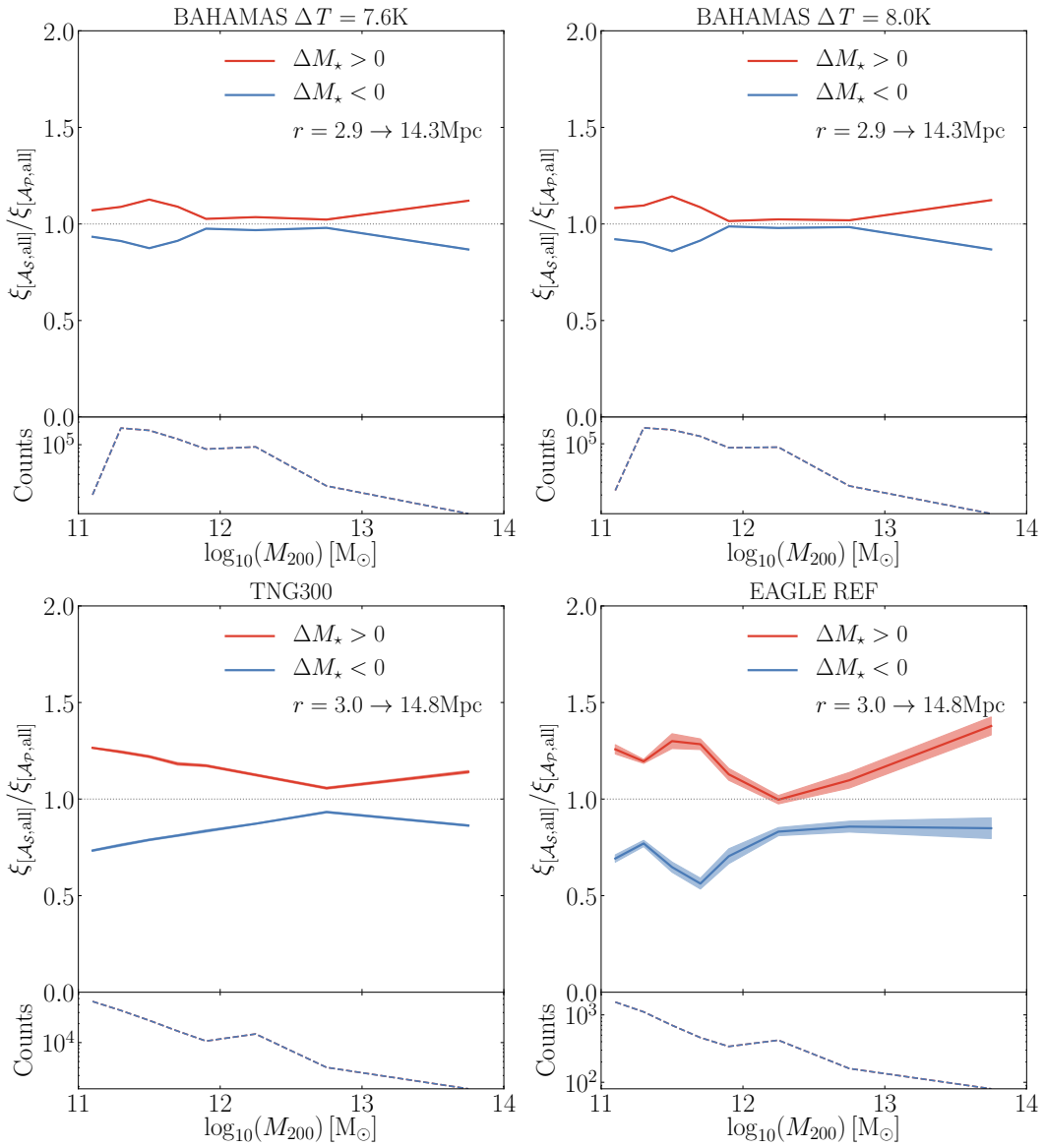

FIGURE 5.6: Bias factors based on stellar mass, computed for four cosmological simulations. The scales probed in each case is $r = 5/h - 12/h$.

curves at higher halo mass occurs at different transition points in all three main simulations. The errors and asymmetry associated with the EAGLE curves appear to be caused by its low sampling. The different predictions of these simulations highlights the need to further explore the impact that baryonic physics have on observable proxies of the expected assembly bias signal. This will be the topic of future work.

5.4 Environment as a probe of bias

In this section, we explore the possibility of exploring the assembly bias phenomenon through measurements of environmental density, rather than the conventional two-point

correlation function. The motivation for this is to provide observers with alternative and complementary methodology. For this to be successful, an environmental measure is required which is uncorrelated with halo mass, yet is correlated with clustering strength.

5.4.1 3-dimensional environmental measures

There is no universal definition of galactic environment (e.g. Muldrew et al., 2012, and references therein). Many studies attempt to compare the various definitions of this fundamental property (e.g. Cooper et al., 2005; Gallazzi et al., 2009; Wilman et al., 2010; Haas et al., 2012; Shattow et al., 2013; Fossati et al., 2017). Parameterisations used to characterise the environment include the local number density (e.g. Dressler, 1980; Lewis et al., 2002; Cooper et al., 2005; Shattow et al., 2013), measurements of galaxy clustering (e.g. Skibba et al., 2013, 2015; Gunawardhana et al., 2018), and placement within cosmic structures (e.g. Zhang et al., 2009; Darvish et al., 2014; Kuutma et al., 2017; Liao & Gao, 2019).

In this work, we primarily quantify environmental density of a galaxy using the measure $\rho_{\rm N}$, defined as

$$\rho_N = \frac{N}{4/3\ \pi\ d_N^3}, \tag{5.2}$$

where d_N is the distance to the Nth nearest neighbour that is a member of the 'density defining population' (DDP). Locations of individual galaxies are taken to be the centre of potential of their associated subhalo. We fiducially measure ρ_N for both centrals and satellites $M_\star > 10^{8.5}{\rm M}_\odot$ with respect to a DDP containing both central and satellite galaxies with $M_\star > 10^{9.5}{\rm M}_\odot$.

In Fig. 5.7 we display the environmental densities of central and satellite galaxies. We elect to measure densities with respect to the sixth nearest neighbour, however similar qualitative results are found for $N = 3, 4$ and 5. Densities are normalised by $\bar{\rho} = N_{\rm DDP}/V = 0.0072{\rm Mpc}^{-3}$, where $V = (100\ {\rm Mpc})^3$ is the simulation volume. The left panel displays the volume density function separated into one- and two-halo contributions, where these reflect when the sixth nearest neighbour resides in the same or a different FOF halo as the galaxy being considered. The centre and right panels show 30 Mpc slices of the simulation volume along the line of sight. In both cases the DDP galaxies are shown as black points, while red points show the locations of galaxies in the bottom $20^{\rm th}$ and top $80^{\rm th}$ percentile in terms of their environmental density, respectively.

For galaxies residing within regions 100 times more dense than the average, the sixth nearest neighbour is overwhelmingly likely to reside within the same FOF halo. By

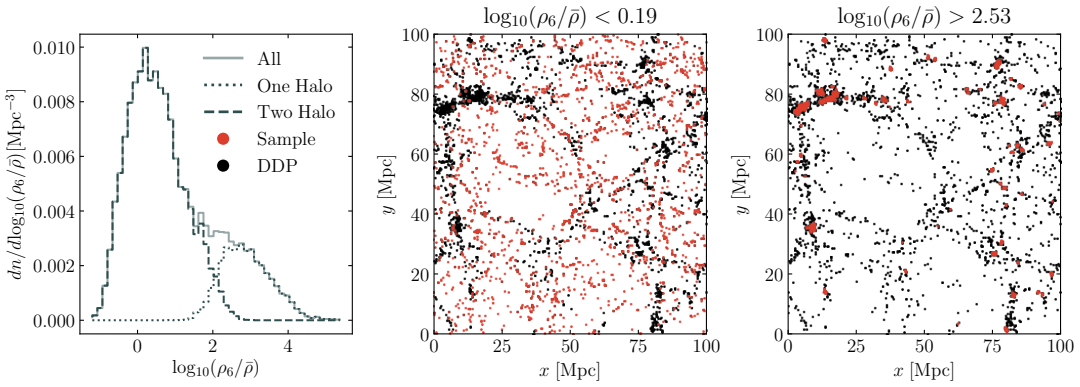

FIGURE 5.7: 3-dimensional environmental density values, ρ_6, for galaxies with respect to a density defining population (DDP) with $M_\star > 10^{9.5}\mathrm{M}_\odot$. Densities are normalised by $\bar{\rho}$, the number of DDP galaxies divided by the simulation volume. Galaxies here are extracted from the $z = 0$ snapshot of the flagship EAGLE 100 Mpc simulation. Left panel: volume density function of ρ_6, separated into one- and two-halo contributions. Centre panel: the location of galaxies residing in low density environments (red points), as defined by the DDP (black points). Right panel: the location of galaxies residing in high density environments (red points), as defined by the DDP (black points). Both the centre and left panels represent a 30 Mpc slice of the simulation volume along the line of sight.

eye these galaxies also appear to cluster more strongly than those of low-density, preferentially residing in knots and filaments rather than voids. Similar results are found when we restrict our analysis to centrals only, however here the 20$^{\mathrm{th}}$ and 80$^{\mathrm{th}}$ percentiles become $\rho/\bar{\rho} = 0.08$ and 0.96, respectively.

In Fig. 5.8 we show the relation between subhalo mass and environmental density. As we consider both central and satellite galaxies, we describe subhalo mass as the total mass of all particles bound to the central or satellite subhalo, M_{sub}. Very similar results are found for the 'Centrals Only' panel when one uses M_{200} instead. As above, focus on galaxies with $M_\star > 10^{8.5}\mathrm{M}_\odot$, and compute their environmental density with respect to galaxies with $M_\star > 10^{9.5}\mathrm{M}_\odot$. The colour-scale in the histograms represent the fraction of objects found per pixel. The magenta crosses indicate the median subhalo mass in bins of ρ_6, while the errorbars represent range spanned by the 16$^{\mathrm{th}}$ and 84$^{\mathrm{th}}$ percentiles.

As noted by Haas et al. (2012), differentiating between (sub)halo mass and environmental density measures is often challenging. When considering centrals and satellites, we find a slight anti-correlation between M_{sub} and ρ_6, the slope of which is driven primarily by the numerous massive satellites residing in high-density environments. This correlation is largely erased for centrals only, with the expectation of a high-mass, high-density tail for $\rho_6 > 10$. There is therefore cause for optimism in the hope that ρ_6 is sufficiently unrelated to M_{sub} (and M_{200}, as seen below in Fig. 5.10) as to enable the extraction of an assembly bias signal through its measurement, which would provide an alternative

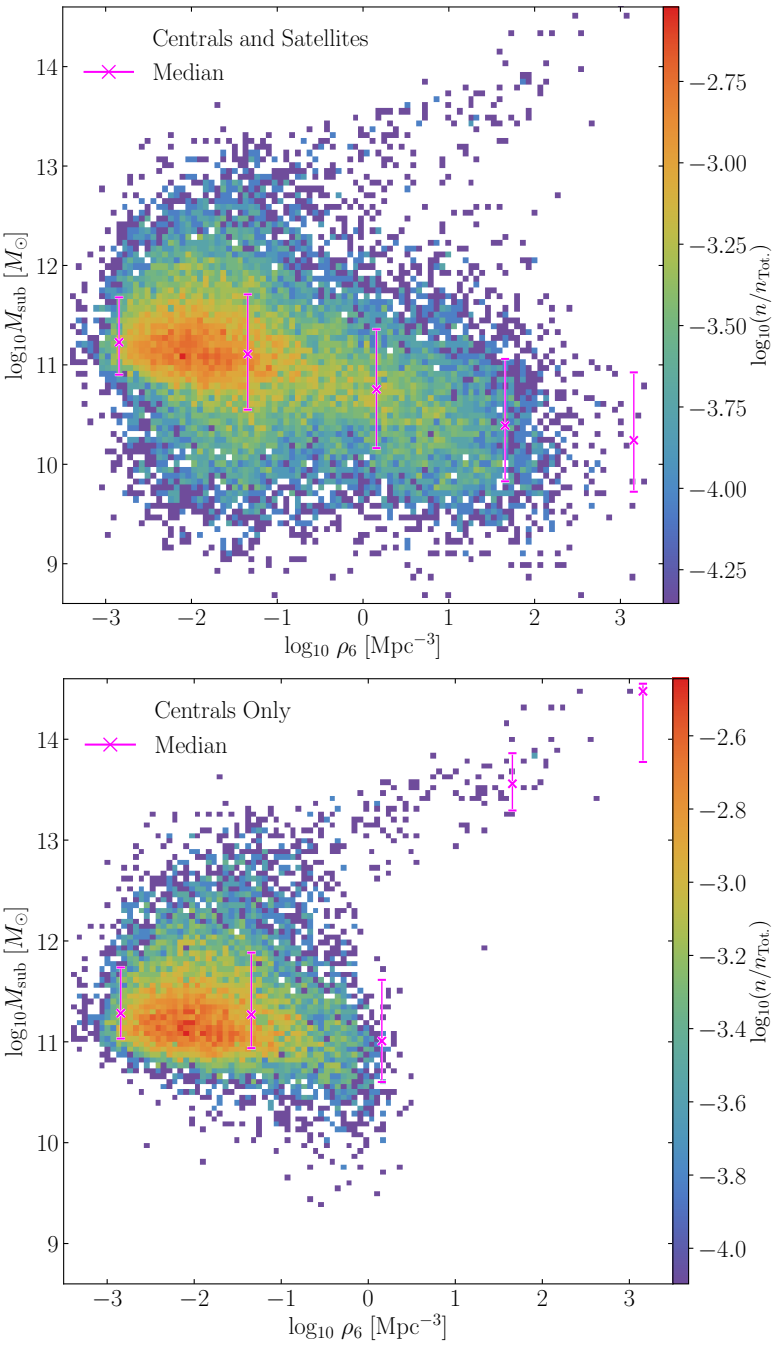

FIGURE 5.8: The correlation between subhalo mass and the environmental density parameter ρ_6. Centrals and satellites are displayed in the top panel, while the lower panel shows only central galaxies. Galaxies are selected to have $M_\star > 10^{8.5}{\rm M}_\odot$, and ρ_6 is computed with respect to a DDP comprising both centrals and satellites with $M_\star > 10^{9.5}{\rm M}_\odot$.

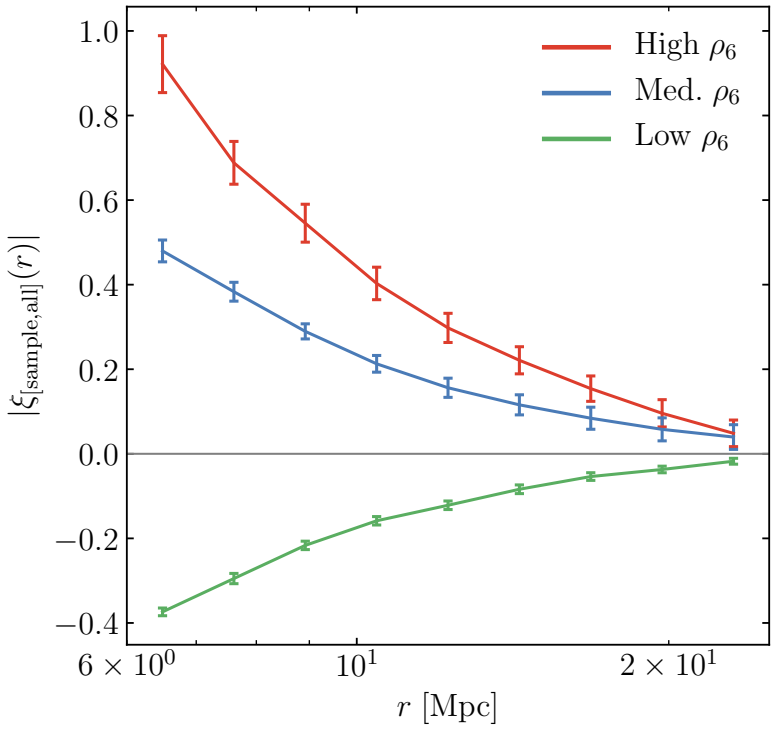

FIGURE 5.9: The clustering of galaxies in different environmental bins. $|\xi_{[\mathrm{sample,all}]}(r)|$ is the cross-correlation between binned galaxies and the master sample of central galaxies with $M_{200} > 10^{10.5}/h$. Errorbars are the standard deviation computed via jackknife re-sampling.

to two-point statistics. We must therefore first determine whether ρ_6 is itself predictive of clustering.

Fig. 5.9 shows the differences in clustering observed for galaxies residing in different environments. Low, medium and high density environments are quantified as $\rho_6 < 10^{-2.42}$, $10^{-2.08} < \rho_6 < 10^{-1.75}$, and $\rho_6 > 10^{-1.30}$ Mpc^{-3}, respectively. These subsamples each contain 20% of the master sample of 17,594 central galaxies with $M_{200} > 10^{10.5}/h$. Fig. 5.9 displays cross-correlations between a density-selected sample ('sample') and the master sample ('all'). The two-point correlation function is measured using the CORRFUNC code, presented by Sinha & Garrison (2017).

We find that central galaxies residing in high density environments indeed are more strongly clustered than those in low density environments, as indicated in Fig. 5.7. There is an offset of ∼0.4 dex between the correlation functions of high and low density galaxies. We highlight that the sign of the low density correlation function is *negative*, indicative of anti-correlation, or regularity (e.g. Martinez & Saar, 2002). This suggests that environmental density measures which are independent of halo mass can be used in place of clustering statistics to measure secondary biases in the clustering of galaxies.

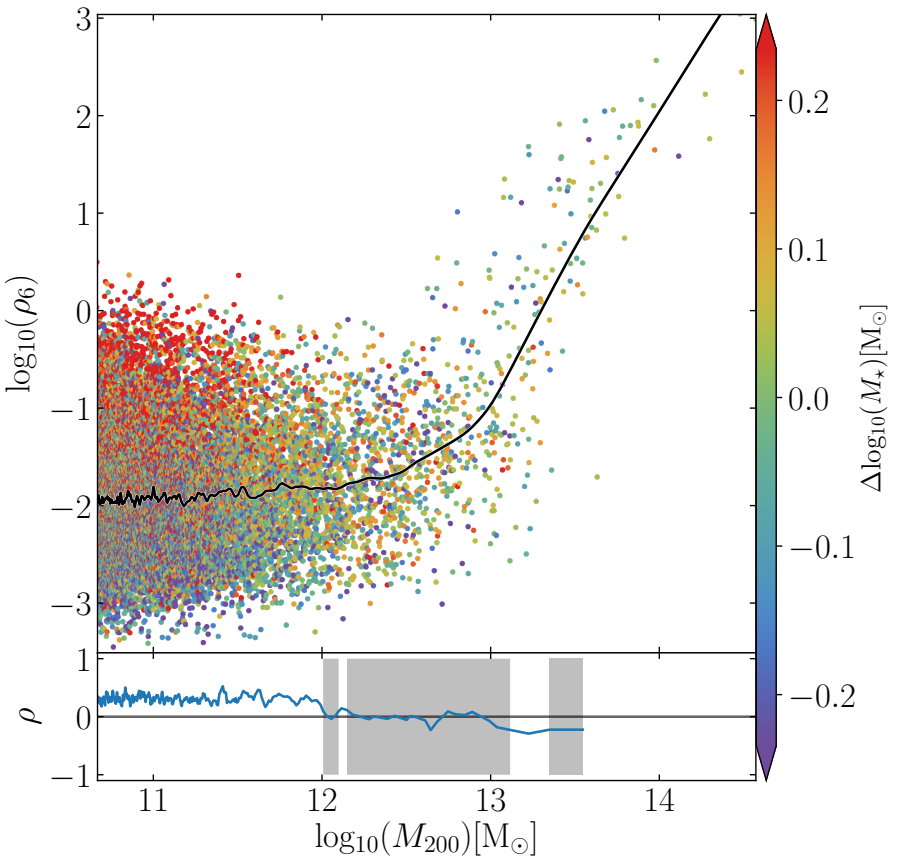

FIGURE 5.10: The correlation between galaxy environmental density and stellar mass at fixed halo mass. The black curve denotes the running median of $M_\star$, computed via the locally weighted scatterplot smoothing method (LOWESS; e.g. Cleveland, 1979). The colour of each point denotes the stellar mass of a galaxy in excess of the running median at fixed halo mass: galaxies denoted by red (blue) colours typically have higher (lower) values of $M_\star$. The lower panel denotes the running Spearman rank correlation coefficient between $\Delta\rho_6$ and $\Delta M_\star$

Fig. 5.10 shows the relationship between environmental density and stellar mass at fixed halo mass. Here we focus only on centrals. We choose $M_\star$ as our z-axis parameter as it has been found to correlate with assembly time in simulations, and is therefore a target as an observational proxy for assembly bias measurements (e.g. Montero-Dorta et al., 2020). The figure is similar to Fig. 5.8, except here individual galaxies are represented as points rather than binned in pixels. The black curve denotes the running median of the ρ_6, computed via the locally weighted scatterplot smoothing method LOWESS (Cleveland, 1979). This alternate method of quantifying the relationship between ρ_6 and M_{200} agrees with the more conventional median measurements shown in Fig. 5.8: only a marginal correlation between environment and halo mass is seen for $M_{200} < 10^{12}$, with a strong positive correlation seen at higher halo masses.

Points in Fig. 5.10 are coloured by $\Delta M_{\star,i}$, the residual stellar mass at fixed M_{200} with respect to the smoothed median of $M_\star$ vs M_{200}, hence $\Delta M_{\star,i} = M_{\star,i} - \tilde{M}_\star(M_{200,i})$ for the

$i^{\rm th}$ subhalo. The running Spearman rank correlation coefficient between $\Delta\rho_6$ and $\Delta M_\star$ is shown in the lower subpanel. The subpanels corroborate, quantitatively, the impression given by visual inspection, that the stellar mass of galaxies correlates positively with their environmental density at fixed halo mass for $M_{200} < 10^{12}$. Improved statistics are required to determine whether this trend should be expected to continue to higher halo masses. Following the link between ρ_6 and clustering, this seems to support the hypothesis that environmental density measures can be used to highlight secondary biases in the clustering of galaxies.

5.4.2 2-dimensional environmental measures

We next consider environmental density in projection, given as

$$\Sigma_N = \frac{N}{\pi\ d_{p,N}^2}, \tag{5.3}$$

where $d_{p,N}$ is the projected distance to the Nth nearest neighbour. We collapse the simulation volume along one axis to crudely mimic a lightcone for an observer at large distance.

When constructing the DDP sample, observational measurements remove distant galaxies which appear close in projection by imposing a cut in recessional velocity, via redshift measurements, with respect to the galaxy whose density is being measured. For example Baldry et al. (2006) employs a maximum offset of $\pm\Delta zc = 1000$ kms^{-1} (which is not strictly a velocity) to remove spuriously close galaxies.

Assuming that the measures ρ_N and Σ_N are linearly correlated in the absence of significant projection effects, we can use simulations to identify the optimal choice of recessional velocity cut. We compute the recessional velocity of galaxies as the sum of their peculiar velocity along the line of sight and their Hubble flow, $v_{\rm rec} = v_{\rm los} + v_{\rm Hub}$, where $v_{\rm Hub}$ is the product of the Hubble constant and the distance along the line of sight.

In selecting the optimal value of $\pm\Delta v_{\rm rec}$, we fit ρ_N vs Σ_N with a simple linear function and attempt to minimise the RMSE between the model and the data. We demonstrate this process in Fig. 5.11; the top left panel shows ρ_6 vs Σ_6 with a linear fit, and the top right panel shows the measured RMSE for varied $\pm\Delta v_{\rm rec}$. We find that the RMSE is minimised for $\pm\Delta v_{\rm rec} = 500 - 700$ kms^{-1}, with lower (higher) values of N displaying minimal RMSE for lower (higher) values of $\pm\Delta v_{\rm rec}$. In the remainder of this work we set $N = 6$ and compute Σ_6 with a value of $\pm\Delta v_{\rm rec} = 600$ kms^{-1}.

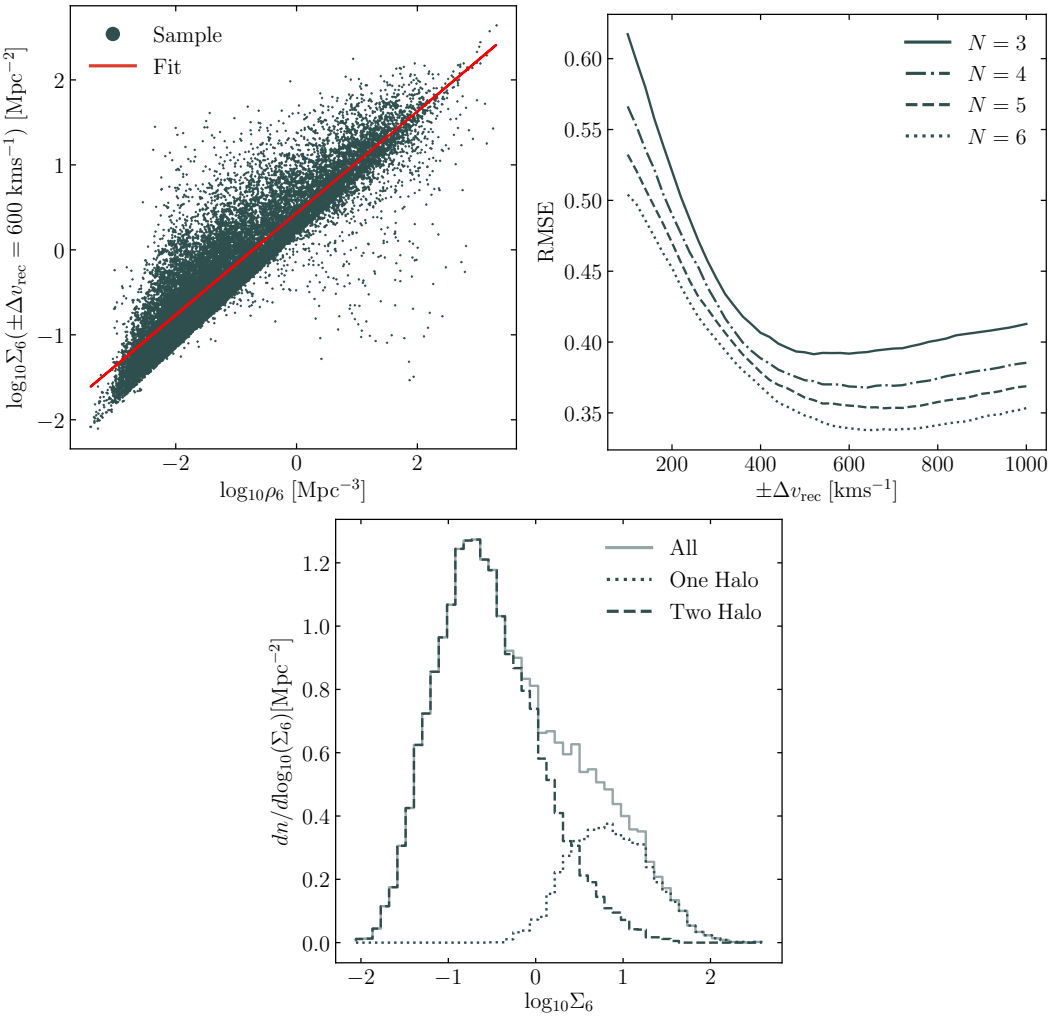

FIGURE 5.11: Projected environmental density and the optimisation of $\pm\Delta v_{\rm rec}$. The top left panel shows Σ_6 compared with ρ_6, where the former is computed with a recessional velocity cut of $\pm\Delta v_{\rm rec} = 600$ kms^{-1}. Densities are displayed for galaxies with $M_\star > 10^{8.5}{\rm M}_\odot$, with respect to a DDP of $M_\star > 10^{9.5}{\rm M}_\odot$. The red line is a best-fitting linear function to the data. The top right panel displays the RMSE between the linear model and the data for varying $\pm\Delta v_{\rm rec}$. Different line styles correspond to a different Nth nearest neighbour. The RMSE is minimised for $\pm\Delta v_{\rm rec} = 500 - 700$ kms^{-1}. The lower panel shows a PDF of the projected environmental density, Σ_6, for simulated galaxies with a recessional velocity cut of $\pm\Delta v_{\rm rec} = 600$ kms^{-1} employed. The PDF is decomposed into one- and two-halo contributions, where the former is when the sixth nearest neighbour resides in the same FOF halo as the galaxy in questions, and the latter is where it does not.

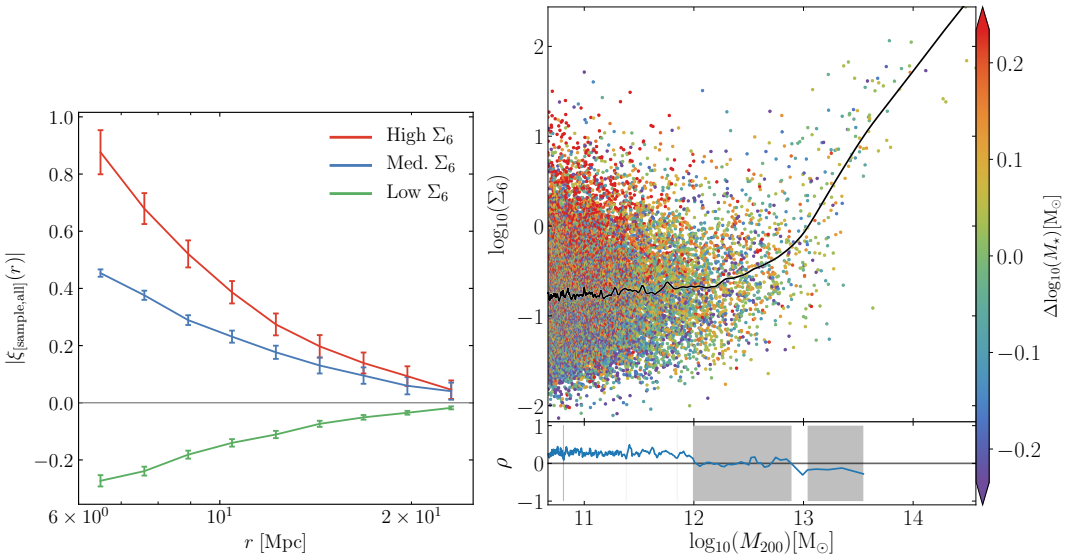

FIGURE 5.12: The same as Figs. 5.9 and 5.10, with the exception that Σ_6 is used in place of ρ_6.

The lower panel of Fig. 5.11 shows a probability distribution function of Σ_6 values. The distribution of Σ_6 is similar to that seen for ρ_6: a double histogram comprising dominant contributions from one- and two-halo terms at low and high densities respectively.

In Fig. 5.12 we reproduce the analyses of Figs. 5.9 and 5.10 with Σ_6 is used in place of ρ_6 (note that clustering is still measured here in 3-dimensions), and we find very similar results. This indicates that projected density measurements are sufficiently unbiased by projection effects as to enable an extraction of an assembly bias signal.

5.5 Summary

We have explored the use of environmental density measures and two-point statistics in extracting signals of assembly bias in cosmological simulations, primarily focusing on the Ref-L100N1054 EAGLE simulation. Our main findings are as follows:

- Simulations can be used to infer which observationally accessible properties correlate strongly enough with assembly time to open the prospect of assembly bias detection in the real Universe (Fig. 5.2).
- The LOWESS algorithm (Cleveland, 1979) can be used to separate galaxies into separate samples based on some property at fixed halo mass, in a manner which erases the dependence that this property has on halo mass (Fig. 5.3).
- Galaxies are found to cluster more strongly if they reside in earlier forming haloes, and largely properties which correlate with assembly time also impart secondary

biases in the observed clustering (Fig. 5.5). The amplitude and profile of observed secondary biases in different hydrodynamical simulations are found to vary substantially.

- Environmental density measures such as ρ_N can be calculated in such a way that they are correlated with galaxy clustering (Figs. 5.7 and 5.9) but, crucially, not halo mass (Fig. 5.8). This opens the possibility for constructing measurements of assembly bias in a manner that does not rely on two-point clustering statistics. Fig. 5.10 shows that ρ_6 correlates with stellar mass at fixed halo mass, a result which can be interpreted as a secondary bias signal.

- Simulations can be used to inform an optimised selection for recessional velocity cuts in measurements of projected environmental density (Fig. 5.11). Projected environmental measures are sufficiently closely linked to 3-dimensional measures that they can be used to perform the same analyses with minimal bias imposed through projection effects (Fig. 5.12).

Our preliminary findings highlight the need for continued work to consolidate the expected prediction of the assembly bias signal in simulations. Conversely, should such a detection be made in observations, it would provide a means of further constraining the appropriate implementation of baryonic processes in simulations, further improving their validity. Through our analysis of projected environmental density measures, we have demonstrated the possibility of exploring this effect in a manner that complements the usual two-point statistics employed. The key to this is constructing density measures in such a way that they are not correlated with halo mass. Future work will explore the robustness of our proposed Σ_6 measure to different simulations, samples, DDPs. We will also explore the use of observational proxies of halo mass, perhaps again using environmental measures but with a smaller N in order to properly separate halo-environment and large scale-environment.

We finally propose to explore the differences in assembly bias predictions between simulations with fixed baryonic physics and varied cosmology, in a way that mirrors the typical use of the power spectrum in exploring extensions to ΛCDM. As a colliery to this, the intrinsic alignment of galaxies also encodes information of cosmology and galaxy evolution, and has been proposed as a means of constraining models of dark matter (Harvey et al., 2021). We propose to study the impact that galaxy evolution, cosmology, and the chosen dark matter model have on the morphology and alignments of galaxies within a halo in zoom simulations, as well as the number and distribution of satellite galaxies within a halo. We will then extend this study to cosmological simulations, where will explore the impact that these factors have on clustering, assembly bias, and intrinsic

alignments. Such measures could provide a novel means of probing the nature of our Universe. Future work in this area will explore the relative importance of galaxy clustering, environment and assembly time in determining galaxy properties, with the hypothesis that at least some of the dependence of properties on clustering can be explained by the typical differences in their assembly time.

Chapter 6

Summary and Conclusions

I know simply that the sky will last longer than I.

Camus

The three main science questions outlined at the end of **Chapter 1** were as follows:

1. What is the expected morphology of the radio continuum-emitting regions of galaxies, and how does it relate to the stellar and dark matter components?
2. What is the expected intrinsic alignment of the radio continuum regions, and how will it affect future radio weak lensing surveys?
3. What is the connection between galaxy properties and their clustering, and how does this manifest for different properties and different simulations?

These are have been the subject of **Chapters** 3, 4 and 5, respectively. **Chapter 1** introduces these topics in the context of the contemporary understanding of galaxy evolution and cosmology. I then went on to highlight the usefulness of contemporary hydrodynamical cosmological simulations of galaxy formation in addressing challenges facing the interpretation of extant and future galaxy surveys, as well as in measuring predictions of ΛCDM which are yet to be conclusively detected in observations. The history and details of these simulations are outlined in Chapter 2, with a particular focus on the EAGLE suite which provides the foundation of the work presented in this thesis.

Chapter 3 uses the EAGLE suite of simulations to measure the 3- and 2-dimensional morphology of the star-forming gas, and compared to those of the stars and the dark matter. The star-forming gas, which I use as a proxy for the radio continuum emission which will be the target of radio weak lensing surveys conducted with the Square Kilometer Array (SKA: Brown et al., 2015; Camera et al., 2017; Square Kilometre Array Cosmology Science Working Group et al., 2020), is found to be distinct from the optical-emitting stars in terms of both morphology and orientation, despite the presence of a clear correlation in their shapes. Star-forming gas is characteristically flat along its minor axis at present times, however it shows significant evolution with redshift, with more spheroidal shapes characterising later times. This introduces the possible need for a redshift-dependent shape fitting algorithm in future SKA radio weak lensing surveys, which are forecast to observe significant numbers of galaxies out to $z \sim 3$.

The characteristically flattened and discy morphology of star-forming gas at $z = 0$ has an interesting consequence for projected morphologies. The ellipticity distribution is found to be significantly broader than is the case for the stars, owing to the fact that a randomly oriented observer may see a star-forming gas disc as a circle when face-on, a thin line when edge-on, and everything in between. One cannot obtain an ellipticity measurement which is flatter than the 3-dimensional minor-major axis length ratio, resulting in a larger ellipticity distribution for the star-forming gas than is seen for the stars. A consequence of this is that the expected shape noise for radio galaxies may be

higher than is the case for stars, which may then necessitate a larger sample of source galaxies to achieve similar precision in cosmological constraining power.

I then demonstrate that the orientation angle between a star-forming gas disc and its host dark matter halo is characteristically larger than is the case between the stars and dark matter. I go on to provide fitting functions to the distribution of star-forming gas-dark matter alignment angles, which may be applied to semi-analytic models to more realistically model the intrinsic alignment effect in far larger volumes than can be followed by the current generation of state of the art hydrodynamical simulations. I find that the results presented are robust in the context of resolution, box-size, and subgrid implementation.

The poorer alignment between the star-forming gas disc and its host dark matter halo likely has consequences for the expected intrinsic alignment of galaxies as seen in radio continuum emission. This is the subject of **Chapter** 4, where I measure the 3- and 2-dimensional intrinsic alignments of galaxies in EAGLE in terms of their star-forming gas, stars, and dark matter. I demonstrate that the intrinsic alignment measure known as 'orientation-direction alignment' is characteristically weaker for the star-forming gas than is the case for the stars, however it follows the same general trend of increased alignment at reduced galaxy pair separations. This holds true in both 3-dimensions and in projection. The 'orientation-orientation alignment' is found to be largely negligible for the star-forming gas, as might be expected when considering the lack of an observational detection of intrinsic alignment in blue, star-forming galaxies. Exploring the mass dependence of the orientation-direction alignment, I find that a stronger signal at low separations is largely driven by the one-halo term associated with Milky Way mass haloes. Considering the redshift evolution of orientation-direction alignment, at fixed comoving separation I find that the alignment signal increases at higher redshift. This may at least in part be caused by the comoving separation of fixed pairs decreasing at low redshift.

Connecting the intrinsic alignment of galaxies to the galaxy-halo internal alignment, I bin galaxies by α, the angle between star-forming gas and dark matter minor axes. I find that systems characterised by low values of α demonstrate much stronger intrinsic alignments. Large misalignments (high α) likewise demonstrate poor (or even anti-) intrinsic alignments. This appears to corroborate the hypothesis that radio weak lensing surveys will be less affected by the intrinsic alignment effect than is the case for the conventional optical weak lensing surveys, and that this is caused by the poorer alignment between star-forming gas and the dark matter halo.

I next turn to a prediction of ΛCDM which has been 'observed' in simulations but has yet to be detected conclusively in observations: galaxy assembly bias. This is the topic

of **Chapter 5**. Galaxy assembly bias is the connection between galaxy clustering and the assembly time of the host halo, once the dominant effect of halo mass has been controlled for. Secondary biases more generally are the dependence of clustering on a given galaxy/halo property. I use EAGLE to assess the strength of secondary biases for various properties, and measure the correlation of these properties with halo assembly time in an attempt to see if all of these secondary biases can be explained by halo assembly time. I first show galaxy assembly bias in EAGLE. Next, I demonstrate that some properties which correlate strongly with assembly time at fixed halo mass (e.g. halo concentration and stellar mass) do produce secondary biases in the clustering, however other properties which do not correlate with assembly time (e.g. star formation rate, black hole mass) also produce secondary biases.

I next compare predictions of the secondary biases in galaxies as determined by their stellar mass in various simulations: EAGLE, BAHAMAS (McCarthy et al., 2017), and IllustrisTNG (Springel et al., 2018). In the case of BAHAMAS, I present results for two variations with slightly different AGN implementations. I find that while all simulations broadly predict a secondary bias signal for the stellar mass, the strength and profile of such a detection varies significantly between each. This highlights the need to make use of various simulations to determine the full range of galaxy assembly bias predictions which are compatible with ΛCDM.

Finally, I explore the use of alternative environment measures in probing galaxy assembly bias. Such measures are required to be uncorrelated with halo mass in order to facilitate accurate measurements of assembly bias, which I demonstrate is the case with ρ_N for centrals with $M_{200} < 10^{12}$ $\mathrm{M}_\odot$. After showing the clear link between ρ_N and clustering, I demonstrate a clear correlation between ρ_N and stellar mass at fixed halo mass. As ρ_N is a 3-dimensional measure, I explore the feasibility of 2-dimensional density measures in conducting a similar study. Σ_N, the 2-dimensional equivalent of ρ_N, naturally suffers from projection effects, i.e. galaxies which appear close are in fact separated by large distances along the line of sight. I calculate that a recessional velocity cut of $\pm\Delta v_{\mathrm{rec.}} \simeq 600$ kms^{-1} is optimal in minimising the bias induced by projection effects. I then demonstrate that Σ_N thus calculated is similarly correlated with clustering as is seen for ρ_N, and demonstrates a similar correlation with stellar mass at fixed halo mass.

6.1 Future work in the field of radio weak lensing

As outlined in Chapter 1, cosmic shear is measured through the correlation of observed galaxy shapes. Galaxy shapes themselves are treated as simple ellipses with an axis ratio and orientation, which may be computed using a variety of methods (e.g. Trujillo et al.,

2001; Refregier, 2003; Refregier & Bacon, 2003; Miller et al., 2007; Zuntz et al., 2013). Mapping the cosmic shear across an extended area of sky requires the observation of many background galaxies. Once measured, the correlation in the shapes are linked to the convergence and shear terms, κ and γ, which are direct probes of the fluctuations in the Universe's density (i.e. the matter power spectrum). As the matter power spectrum is sensitive to variations in the assumed cosmological model, weak lensing measurements may be used to constrain parameters of ΛCDM and explore possible extensions.

The intrinsic alignment of galaxies is a source of systematic uncertainty in cosmic shear measurements. Optical surveys typically employ alignment models (e.g. NLA Bridle & King (2007); TATT Blazek et al. (2019)) which parameterise intrinsic alignments assuming that they arise from tidal fields induced by the distribution of matter. These parameters are treated as nuisances, and are marginalised over in the calculation of the cosmic shear. While this approach has proven successful, astrophysical uncertainties such as intrinsic alignments and the impact of baryons on the matter power spectrum are the current limiting factor in cosmic shear surveys (Amon et al., 2022). The results presented in Chapter 4 suggest that the while the amplitude of intrinsic alignments are lower for galaxies observed in the radio continuum than the optical, they follow the same general profile. This suggests that alignment models commonly used in optical weak lensing surveys are appropriate for use in radio weak lensing surveys, with the expectation that they will have a lesser effect on the constraining power.

In optical surveys, the intrinsic alignment of galaxies is subdominant to the cosmic shear. While cosmic shear remains undetected in precursor radio weak lensing continuum surveys (Harrison et al., 2020), the intrinsic alignment effect is therefore of secondary interest to issues such as shape extraction. However, with the results I have presented here and recent advances in the measurement of shape in radio surveys (POLISH Connor et al., 2021), the radio weak lensing community is in a position to update their cosmological forecasts. The finding in Chapter 3 that the shape noise is stronger for the star-forming gas than stars and shows a strong redshift dependence, is something that is directly implementable to cosmological forecasts (e.g. Harrison et al., 2016), and as far as I know has yet to be considered. I am engaged in collaborations with observers in updating the predicted constraining power of radio weak lensing measurements conducted with the SKA. The hope is that these new insights from simulations, as well as the inclusion of the POLISH shape extraction method, radio weak lensing will prove to be competitive with the next generation of optical surveys.

Possible future avenues of study exist in the theoretical regime. As an extension to the results presented in this thesis, I am interested in studying the impact that baryonic physics implementations and cosmology have on the alignment between a galaxy and

its host halo, and thence the intrinsic alignment signal for both stars and star-forming gas. Previous studies have shown that intrinsic alignments are theoretically capable of distinguishing different models of dark matter (Harvey et al., 2021).

6.2 Future work in the field of galaxy assembly bias

With the next generation of galaxy surveys soon to deliver data, the topic of galaxy assembly bias is an active one and many avenues of future study are available. As mentioned, work remains to be done in consolidating the prediction of assembly bias in simulations. As shown in this thesis, simulations such as EAGLE and IllustrisTNG both predict the existence of assembly bias, however due to differences in their implementation of baryonic processes they disagree in the specifics. For instance the mass scale at which the bias becomes significant differs between the two, providing a possible means of improving simulation subgrid implementation through observations. I propose using a suite of cosmological hydrodynamical simulations (such as BAHAMAS(-XL), EAGLE-XL) which vary in their application of subgrid routines and cosmology to (i) set realistic limits on the significance of the assembly bias signal and (ii) identify which factors in simulations have the greatest effect on the prediction. I envisage identifying a bias parameter which can be plotted against various factors, such as van Daalen et al. (2020) achieved with the suppression of the power spectrum and its dependence on the baryon fraction of haloes. Additionally, the exact definition of assembly time appears to affect the retrieved assembly bias signal at high mass (Li et al., 2008; Chue et al., 2018). As the EAGLE galaxy assembly bias prediction appears low in comparison to the stellar mass-based secondary bias, I aim to identify whether alternative definitions of assembly time corroborate this finding.

Following on from this, I aim to identify the most promising means of detecting assembly bias in observations. Galaxy assembly bias is a secondary effect detectable only once the much larger primary dependence of clustering on halo mass has been controlled for. Its detection in observations therefore requires knowledge of proxies which vary with halo mass or assembly time, but not both at the same time. Simulations are well-placed to enable an exploration of galaxy/halo parameter space, which I propose to achieve through the use of zoom and cosmological simulations. I will also explore alternatives to the commonly used two-point correlation function, such as environmental density measures (e.g. ρ_N, Σ_N) and cosmic web extractors (e.g. DISPERSE, NEXUS), in detecting a correlation between assembly time and environment. Regarding environmental densities, the results presented in this thesis indicate that disentangling clustering from halo mass is possible.

Finally, I envisage conducting a study that jointly assesses the impact that environment and assembly time have on galaxy properties. Assembly time influences the properties of galaxies through impact on evolutionary pathways such as the growth rate of the supermassive black hole (Davies et al., 2021). If assembly time correlates strongly with environment, it is possible that galaxy properties seemingly affected by environment are in fact driven by assembly time. I propose to address this using simulations, observations, and machine learning methods. For example, using Bayesian inference to predict the assembly history of local galaxies (e.g. McAlpine et al., 2022) and using this to train machine learning algorithms to assign assembly times to distant galaxies.

Bibliography

Abbott T., et al., 2016, Phys. Rev. D, 94, 022001

Abbott T. M. C., et al., 2018, Phys. Rev. D, 98, 043526

Adams C., Blake C., 2017, Monthly Notices of the Royal Astronomical Society, 471, 839

Agertz O., et al., 2007, Monthly Notices of the Royal Astronomical Society, 380, 963

Agustsson I., Brainerd T. G., 2006a, ApJ, 644, L25

Agustsson I., Brainerd T. G., 2006b, The Astrophysical Journal, 650, 550

Aihara H., et al., 2018a, PASJ, 70, S4

Aihara H., et al., 2018b, PASJ, 70, S8

Albrecht A., et al., 2006, arXiv e-prints, pp astro–ph/0609591

Allen S. W., Evrard A. E., Mantz A. B., 2011, ARA&A, 49, 409

Allgood B., Flores R. A., Primack J. R., Kravtsov A. V., Wechsler R. H., Faltenbacher A., Bullock J. S., 2006, Monthly Notices of the Royal Astronomical Society, 367, 1781

Alpher R. A., Bethe H., Gamow G., 1948, Physical Review, 73, 803

Amon A., et al., 2022, Phys. Rev. D, 105, 023514

Anders F., et al., 2014, Astronomy & Astrophysics, 564, A115

Angulo R. E., Baugh C. M., Lacey C. G., 2008, Monthly Notices of the Royal Astronomical Society, 387, 921

Aprile E., et al., 2017, European Physical Journal C, 77, 881

Arcadi G., Dutra M., Ghosh P., Lindner M., Mambrini Y., Pierre M., Profumo S., Queiroz F. S., 2018, European Physical Journal C, 78, 203

Artale M. C., Zehavi I., Contreras S., Norberg P., 2018, Monthly Notices of the Royal Astronomical Society, 480, 3978

Asgari M., et al., 2021, Astronomy & Astrophysics, 645, A104

Aubert D., Pichon C., Colombi S., 2004, Monthly Notices of the Royal Astronomical Society, 352, 376

Bacon D. J., Refregier A. R., Ellis R. S., 2000, Monthly Notices of the Royal Astronomical Society, 318, 625

Bahé Y. M., et al., 2016, Monthly Notices of the Royal Astronomical Society, 456, 1115

Bahé Y. M., et al., 2017, Monthly Notices of the Royal Astronomical Society, 470, 4186

Baldry I. K., Glazebrook K., Brinkmann J., Ivezić Ž., Lupton R. H., Nichol R. C., Szalay A. S., 2004, The Astrophysical Journal, 600, 681

Baldry I. K., Balogh M. L., Bower R. G., Glazebrook K., Nichol R. C., Bamford S. P., Budavari T., 2006, Monthly Notices of the Royal Astronomical Society, 373, 469

Baldry I. K., et al., 2012, Monthly Notices of the Royal Astronomical Society, 421, 621

Balogh M. L., Pearce F. R., Bower R. G., Kay S. T., 2001, Monthly Notices of the Royal Astronomical Society, 326, 1228

Barnes J., Hut P., 1986, Nature, 324, 446

Barnes D. J., et al., 2017, Monthly Notices of the Royal Astronomical Society, 471, 1088

Barrow J. D., Bhavsar S. P., Sonoda D. H., 1984, Monthly Notices of the Royal Astronomical Society, 210, 19

Bartelmann M., Schneider P., 2001, Phys. Rep., 340, 291

Battye R. A., Browne I. W. A., 2009, Monthly Notices of the Royal Astronomical Society, 399, 1888

Battye R. A., et al., 2020, Monthly Notices of the Royal Astronomical Society, 495, 1706

Baugh C. M., Gaztanaga E., Efstathiou G., 1995, Monthly Notices of the Royal Astronomical Society, 274, 1049

Beers T. C., et al., 2012, The Astrophysical Journal, 746, 34

Behroozi P. S., Conroy C., Wechsler R. H., 2010, The Astrophysical Journal, 717, 379

Behroozi P. S., Wechsler R. H., Wu H.-Y., 2013, The Astrophysical Journal, 762, 109

Behroozi P., et al., 2019, BAAS, 51, 125

Belokurov V., et al., 2006, ApJ, 642, L137

Belokurov V., Erkal D., Evans N. W., Koposov S. E., Deason A. J., 2018, Monthly Notices of the Royal Astronomical Society, 478, 611

Benitez-Llambay A., 2015, py-sphviewer: Py-SPHViewer v1.0.0, doi:10.5281/zenodo.21703, `http://dx.doi.org/10.5281/zenodo.21703`

Benítez-Llambay A., Navarro J. F., Abadi M. G., Gottlöber S., Yepes G., Hoffman Y., Steinmetz M., 2013, ApJ, 763, L41

Benítez-Llambay A., Navarro J. F., Frenk C. S., Ludlow A. D., 2018, Monthly Notices of the Royal Astronomical Society, 473, 1019

Benjamin J., et al., 2013, Monthly Notices of the Royal Astronomical Society, 431, 1547

Bensby T., Feltzing S., Lundström I., 2003, Astronomy & Astrophysics, 410, 527

Benson A. J., Lacey C. G., Baugh C. M., Cole S., Frenk C. S., 2002a, Monthly Notices of the Royal Astronomical Society, 333, 156

Benson A. J., Frenk C. S., Lacey C. G., Baugh C. M., Cole S., 2002b, Monthly Notices of the Royal Astronomical Society, 333, 177

Benson A. J., Bower R. G., Frenk C. S., Lacey C. G., Baugh C. M., Cole S., 2003, The Astrophysical Journal, 599, 38

Berlind A. A., Weinberg D. H., 2002, The Astrophysical Journal, 575, 587

Bernabei R., et al., 2013, European Physical Journal C, 73, 2648

Bernstein G. M., Jarvis M., 2002, AJ, 123, 583

Bernstein G. M., Norberg P., 2002, AJ, 124, 733

Bernstein J. P., et al., 2012, The Astrophysical Journal, 753, 152

Bett P., 2012, Monthly Notices of the Royal Astronomical Society, 420, 3303

Bett P., Eke V., Frenk C. S., Jenkins A., Okamoto T., 2010, Monthly Notices of the Royal Astronomical Society, 404, 1137

Beutler F., et al., 2014, Monthly Notices of the Royal Astronomical Society, 443, 1065

Binney J., 1977, The Astrophysical Journal, 215, 483

Birnboim Y., Dekel A., 2003, Monthly Notices of the Royal Astronomical Society, 345, 349

Blain A. W., 2002, ApJ, 570, L51

Blandford R. D., Saust A. B., Brainerd T. G., Villumsen J. V., 1991, Monthly Notices of the Royal Astronomical Society, 251, 600

Blanton M. R., et al., 2003, The Astrophysical Journal, 594, 186

Blazek J., McQuinn M., Seljak U., 2011, J. Cosmology Astropart. Phys., 5, 010

Blazek J., Vlah Z., Seljak U., 2015, J. Cosmology Astropart. Phys., 2015, 015

Blazek J. A., MacCrann N., Troxel M. A., Fang X., 2019, Phys. Rev. D, 100, 103506

Blumenthal G. R., Pagels H., Primack J. R., 1982, Nature, 299, 37

Blumenthal G. R., Faber S. M., Primack J. R., Rees M. J., 1984, Nature, 311, 517

Blumenthal G. R., Faber S. M., Flores R., Primack J. R., 1986, The Astrophysical Journal, 301, 27

Bocquet S., Saro A., Dolag K., Mohr J. J., 2016, Monthly Notices of the Royal Astronomical Society, 456, 2361

Bonaldi A., Harrison I., Camera S., Brown M. L., 2016, Monthly Notices of the Royal Astronomical Society, 463, 3686

Bonaldi A., Bonato M., Galluzzi V., Harrison I., Massardi M., Kay S., De Zotti G., Brown M. L., 2019, Monthly Notices of the Royal Astronomical Society, 482, 2

Bond J. R., Szalay A. S., 1983, The Astrophysical Journal, 274, 443

Bond J. R., Szalay A. S., Turner M. S., 1982, Phys. Rev. Lett., 48, 1636

Bond J. R., Kofman L., Pogosyan D., 1996, Nature, 380, 603

Bondi H., Gold T., 1948, Monthly Notices of the Royal Astronomical Society, 108, 252

Bondi H., Hoyle F., 1944, Monthly Notices of the Royal Astronomical Society, 104, 273

Booth C. M., Schaye J., 2009, Monthly Notices of the Royal Astronomical Society, 398, 53

Booth C. M., Schaye J., 2010, Monthly Notices of the Royal Astronomical Society, 405, L1

Bose S., Eisenstein D. J., Hernquist L., Pillepich A., Nelson D., Marinacci F., Springel V., Vogelsberger M., 2019, Monthly Notices of the Royal Astronomical Society, 490, 5693

Bosma A., 1978, PhD thesis, -

Bovill M. S., Ricotti M., 2009, The Astrophysical Journal, 693, 1859

Bower R. G., Benson A. J., Malbon R., Helly J. C., Frenk C. S., Baugh C. M., Cole S., Lacey C. G., 2006, Monthly Notices of the Royal Astronomical Society, 370, 645

Bower R. G., Schaye J., Frenk C. S., Theuns T., Schaller M., Crain R. A., McAlpine S., 2017, Monthly Notices of the Royal Astronomical Society, 465, 32

Boylan-Kolchin M., Ma C.-P., Quataert E., 2006, Monthly Notices of the Royal Astronomical Society, 369, 1081

Boylan-Kolchin M., Bullock J. S., Kaplinghat M., 2012, Monthly Notices of the Royal Astronomical Society, 422, 1203

Bozorgnia N., et al., 2016, J. Cosmology Astropart. Phys., 2016, 024

Brainerd T. G., 2005, ApJ, 628, L101

Bridle S., King L., 2007, New Journal of Physics, 9, 444

Brook C. B., Kawata D., Gibson B. K., Flynn C., 2004, Monthly Notices of the Royal Astronomical Society, 349, 52

Brown M. L., Battye R. A., 2011, Monthly Notices of the Royal Astronomical Society, 410, 2057

Brown M. L., Taylor A. N., Hambly N. C., Dye S., 2002, Monthly Notices of the Royal Astronomical Society, 333, 501

Brown M., et al., 2015, Advancing Astrophysics with the Square Kilometre Array (AASKA14), p. 23

Bryan G. L., Norman M. L., 1998, The Astrophysical Journal, 495, 80

Bryan S. E., Kay S. T., Duffy A. R., Schaye J., Dalla Vecchia C., Booth C. M., 2013, Monthly Notices of the Royal Astronomical Society, 429, 3316

Bullock J. S., Boylan-Kolchin M., 2017, ARA&A, 55, 343

Bullock J. S., Kravtsov A. V., Weinberg D. H., 2000, The Astrophysical Journal, 539, 517

Burton C. S., et al., 2013, Monthly Notices of the Royal Astronomical Society, 433, 771

CDMS Collaboration et al., 2013, arXiv e-prints, p. arXiv:1304.4279

Calore F., et al., 2016, in Journal of Physics Conference Series. p. 042010, doi:10.1088/1742-6596/718/4/042010

Camera S., Harrison I., Bonaldi A., Brown M. L., 2017, Monthly Notices of the Royal Astronomical Society, 464, 4747

Catelan P., Kamionkowski M., Blandford R. D., 2001, Monthly Notices of the Royal Astronomical Society, 320, L7

Chabrier G., 2003, PASP, 115, 763

Chang T.-C., Refregier A., Helfand D. J., 2004, The Astrophysical Journal, 617, 794

Chaves-Montero J., Angulo R. E., Schaye J., Schaller M., Crain R. A., Furlong M., Theuns T., 2016, Monthly Notices of the Royal Astronomical Society, 460, 3100

Chen D. N., Jing Y. P., Yoshikaw K., 2003, The Astrophysical Journal, 597, 35

Chen S., Wang H., Mo H. J., Shi J., 2016, The Astrophysical Journal, 825, 49

Chevallier M., Polarski D., 2001, International Journal of Modern Physics D, 10, 213

Chisari N. E., Dvorkin C., Schmidt F., 2014, Phys. Rev. D, 90, 043527

Chisari N., et al., 2015, Monthly Notices of the Royal Astronomical Society, 454, 2736

Chisari N., et al., 2016, Monthly Notices of the Royal Astronomical Society, 461, 2702

Chisari N. E., et al., 2017, Monthly Notices of the Royal Astronomical Society, 472, 1163

Chue C. Y. R., Dalal N., White M., 2018, J. Cosmology Astropart. Phys., 2018, 012

Cicone C., et al., 2015, Astronomy & Astrophysics, 574, A14

Cicone C., Maiolino R., Marconi A., 2016, Astronomy & Astrophysics, 588, A41

Cleveland W. S., 1979, Journal of the American Statistical Association, 74, 829

Clowe D., Bradač M., Gonzalez A. H., Markevitch M., Randall S. W., Jones C., Zaritsky D., 2006, ApJ, 648, L109

Codis S., et al., 2015, Monthly Notices of the Royal Astronomical Society, 448, 3391

Codis S., Jindal A., Chisari N. E., Vibert D., Dubois Y., Pichon C., Devriendt J., 2018, Monthly Notices of the Royal Astronomical Society, 481, 4753

Cole S., Lacey C., 1996, Monthly Notices of the Royal Astronomical Society, 281, 716

Colless M., et al., 2003, arXiv e-prints, pp astro–ph/0306581

Condon J. J., 1992, ARA&A, 30, 575

Connor L., Bouman K. L., Ravi V., Hallinan G., 2021, arXiv e-prints, p. arXiv:2111.03249

Conroy C., Wechsler R. H., Kravtsov A. V., 2006, The Astrophysical Journal, 647, 201

Cooper M. C., Newman J. A., Madgwick D. S., Gerke B. F., Yan R., Davis M., 2005, The Astrophysical Journal, 634, 833

Correa C. A., Schaye J., Clauwens B., Bower R. G., Crain R. A., Schaller M., Theuns T., Thob A. C. R., 2017, Monthly Notices of the Royal Astronomical Society, 472, L45

Cowie L. L., Songaila A., Hu E. M., Cohen J. G., 1996, AJ, 112, 839

Crain R. A., et al., 2009, Monthly Notices of the Royal Astronomical Society, 399, 1773

Crain R. A., et al., 2015, Monthly Notices of the Royal Astronomical Society, 450, 1937

Crain R. A., et al., 2017, Monthly Notices of the Royal Astronomical Society, 464, 4204

Crittenden R. G., Natarajan P., Pen U.-L., Theuns T., 2001, The Astrophysical Journal, 559, 552

Croft R. A. C., Metzler C. A., 2000, The Astrophysical Journal, 545, 561

Croft R. A. C., Di Matteo T., Springel V., Hernquist L., 2009, Monthly Notices of the Royal Astronomical Society, 400, 43

Croton D. J., et al., 2006, Monthly Notices of the Royal Astronomical Society, 365, 11

Cuesta A. J., Betancort-Rijo J. E., Gottlöber S., Patiri S. G., Yepes G., Prada F., 2008, Monthly Notices of the Royal Astronomical Society, 385, 867

Cullen L., Dehnen W., 2010, Monthly Notices of the Royal Astronomical Society, 408, 669

Curtis H. D., 1917, PASP, 29, 206

DES Collaboration et al., 2021, arXiv e-prints, p. arXiv:2105.13549

Dalla Vecchia C., Schaye J., 2008, Monthly Notices of the Royal Astronomical Society, 387, 1431

Dalla Vecchia C., Schaye J., 2012, Monthly Notices of the Royal Astronomical Society, 426, 140

Darling J., 2011, ApJ, 732, L2

Darvish B., Sobral D., Mobasher B., Scoville N. Z., Best P., Sales L. V., Smail I., 2014, The Astrophysical Journal, 796, 51

Davé R., Thompson R., Hopkins P. F., 2016, Monthly Notices of the Royal Astronomical Society, 462, 3265

Davé R., Anglés-Alcázar D., Narayanan D., Li Q., Rafieferantsoa M. H., Appleby S., 2019, Monthly Notices of the Royal Astronomical Society, 486, 2827

Davé R., Crain R. A., Stevens A. R. H., Narayanan D., Saintonge A., Catinella B., Cortese L., 2020, Monthly Notices of the Royal Astronomical Society, 497, 146

Davies L. J. M., et al., 2019a, Monthly Notices of the Royal Astronomical Society, 483, 5444

Davies J. J., Crain R. A., McCarthy I. G., Oppenheimer B. D., Schaye J., Schaller M., McAlpine S., 2019b, Monthly Notices of the Royal Astronomical Society, 485, 3783

Davies J. J., Crain R. A., Oppenheimer B. D., Schaye J., 2020, Monthly Notices of the Royal Astronomical Society, 491, 4462

Davies J. J., Crain R. A., Pontzen A., 2021, MNRAS, 501, 236

Davis M., Efstathiou G., Frenk C. S., White S. D. M., 1985, The Astrophysical Journal, 292, 371

De Lucia G., Blaizot J., 2007, Monthly Notices of the Royal Astronomical Society, 375, 2

Debattista V. P., Moore B., Quinn T., Kazantzidis S., Maas R., Mayer L., Read J., Stadel J., 2008, The Astrophysical Journal, 681, 1076

Dehnen W., 2000, ApJ, 536, L39

Dekel A., Silk J., 1986, The Astrophysical Journal, 303, 39

Desjacques V., Jeong D., Schmidt F., 2018, Phys. Rep., 733, 1

Di Matteo T., Springel V., Hernquist L., 2005, Nature, 433, 604

Diemand J., Kuhlen M., Madau P., Zemp M., Moore B., Potter D., Stadel J., 2008, Nature, 454, 735

Dolag K., Borgani S., Murante G., Springel V., 2009, Monthly Notices of the Royal Astronomical Society, 399, 497

Doroshkevich A. G., Zel'dovich Y. B., Syunyaev R. A., 1978, Soviet Ast., 22, 523

Doroshkevich A. G., Khlopov M. I., Sunyaev R. A., Szalay A. S., Zeldovich I. B., 1981, Annals of the New York Academy of Sciences, 375, 32

Dressler A., 1980, The Astrophysical Journal, 236, 351

Drlica-Wagner A., et al., 2015, The Astrophysical Journal, 813, 109

Dubinski J., 1994, The Astrophysical Journal, 431, 617

Dubinski J., 1998, The Astrophysical Journal, 502, 141

Dubinski J., Carlberg R. G., 1991, The Astrophysical Journal, 378, 496

Dubois Y., Teyssier R., 2008, Astronomy & Astrophysics, 477, 79

Dubois Y., Gavazzi R., Peirani S., Silk J., 2013, Monthly Notices of the Royal Astronomical Society, 433, 3297

Dubois Y., et al., 2014, Monthly Notices of the Royal Astronomical Society, 444, 1453

Duffy A. R., Schaye J., Kay S. T., Dalla Vecchia C., Battye R. A., Booth C. M., 2010, Monthly Notices of the Royal Astronomical Society, 405, 2161

Durier F., Dalla Vecchia C., 2012, Monthly Notices of the Royal Astronomical Society, 419, 465

Dyer C. C., Shaver E. G., 1992, ApJ, 390, L5

Dyson F. W., Eddington A. S., Davidson C., 1920, Philosophical Transactions of the Royal Society of London Series A, 220, 291

Efstathiou G., Davis M., White S. D. M., Frenk C. S., 1985, ApJS, 57, 241

Efstathiou G., Sutherland W. J., Maddox S. J., 1990, Nature, 348, 705

Efstathiou G., Bond J. R., White S. D. M., 1992, Monthly Notices of the Royal Astronomical Society, 258, 1P

Eifler T., Krause E., Dodelson S., Zentner A. R., Hearin A. P., Gnedin N. Y., 2015, Monthly Notices of the Royal Astronomical Society, 454, 2451

Einasto J., Kaasik A., Saar E., 1974, Nature, 250, 309

Einstein A., 1916, Annalen der Physik, 354, 769

Eisenstein D. J., Hu W., 1998, The Astrophysical Journal, 496, 605

Eisenstein D. J., Hu W., 1999, The Astrophysical Journal, 511, 5

Eisenstein D. J., et al., 2005, The Astrophysical Journal, 633, 560

Elbert O. D., Bullock J. S., Garrison-Kimmel S., Rocha M., Oñorbe J., Peter A. H. G., 2015, Monthly Notices of the Royal Astronomical Society, 453, 29

Erben T., et al., 2013, Monthly Notices of the Royal Astronomical Society, 433, 2545

Event Horizon Telescope Collaboration et al., 2019, ApJ, 875, L1

Faber S. M., Gallagher J. S., 1979, ARA&A, 17, 135

Fakhouri O., Ma C.-P., 2008, Monthly Notices of the Royal Astronomical Society, 386, 577

Fakhouri O., Ma C.-P., Boylan-Kolchin M., 2010, Monthly Notices of the Royal Astronomical Society, 406, 2267

Faltenbacher A., Allgood B., Gottlöber S., Yepes G., Hoffman Y., 2005, Monthly Notices of the Royal Astronomical Society, 362, 1099

Faltenbacher A., Li C., Mao S., van den Bosch F. C., Yang X., Jing Y. P., Pasquali A., Mo H. J., 2007, ApJ, 662, L71

Fattahi A., et al., 2016, Monthly Notices of the Royal Astronomical Society, 457, 844

Faucher-Giguère C.-A., Lidz A., Hernquist L., 2008, Science, 319, 52

Feng J. L., 2010, ARA&A, 48, 495

Ferland G. J., Korista K. T., Verner D. A., Ferguson J. W., Kingdon J. B., Verner E. M., 1998, Publications of the Astronomical Society of the Pacific, 110, 761

Flores R. A., Primack J. R., 1994, ApJ, 427, L1

Fortuna M. C., Hoekstra H., Joachimi B., Johnston H., Chisari N. E., Georgiou C., Mahony C., 2021, Monthly Notices of the Royal Astronomical Society, 501, 2983

Fossati M., et al., 2017, The Astrophysical Journal, 835, 153

Frenk C. S., White S. D. M., Efstathiou G., Davis M., 1990, The Astrophysical Journal, 351, 10

Friedmann A., 1922, Zeitschrift fur Physik, 10, 377

Fuhrmann K., 1998, Astronomy & Astrophysics, 338, 161

Furlong M., et al., 2017, Monthly Notices of the Royal Astronomical Society, 465, 722

Gallazzi A., et al., 2009, The Astrophysical Journal, 690, 1883

Gao L., Springel V., White S. D. M., 2005, Monthly Notices of the Royal Astronomical Society, 363, L66

Gehren T., Fried J., Wehinger P. A., Wyckoff S., 1984, The Astrophysical Journal, 278, 11

Geller M. J., Huchra J. P., 1989, Science, 246, 897

Genel S., Genzel R., Bouché N., Naab T., Sternberg A., 2009, The Astrophysical Journal, 701, 2002

Genzel R., Eckart A., Ott T., Eisenhauer F., 1997, Monthly Notices of the Royal Astronomical Society, 291, 219

Gerritsen J. P. E., 1997, PhD thesis, -

Ghigna S., Moore B., Governato F., Lake G., Quinn T., Stadel J., 1998, Monthly Notices of the Royal Astronomical Society, 300, 146

Górski K. M., Hivon E., Banday A. J., Wand elt B. D., Hansen F. K., Reinecke M., Bartelmann M., 2005, The Astrophysical Journal, 622, 759

Gunawardhana M. L. P., et al., 2018, Monthly Notices of the Royal Astronomical Society, 479, 1433

Gunn J. E., Gott J. Richard I., 1972, The Astrophysical Journal, 176, 1

Guo Q., et al., 2011, Monthly Notices of the Royal Astronomical Society, 413, 101

Guo Q., et al., 2016, Monthly Notices of the Royal Astronomical Society, 461, 3457

Haardt F., Madau P., 2001, in Neumann D. M., Tran J. T. V., eds, Clusters of Galaxies and the High Redshift Universe Observed in X-rays. p. 64 (`arXiv:astro-ph/0106018`)

Haas M. R., Schaye J., Jeeson-Daniel A., 2012, Monthly Notices of the Royal Astronomical Society, 419, 2133

Hahn O., Abel T., 2011, Monthly Notices of the Royal Astronomical Society, 415, 2101

Hahn O., Teyssier R., Carollo C. M., 2010, Monthly Notices of the Royal Astronomical Society, 405, 274

Hamana T., et al., 2020, PASJ, 72, 16

Hargis J. R., Willman B., Peter A. H. G., 2014, ApJ, 795, L13

Häring N., Rix H.-W., 2004, ApJ, 604, L89

Harrison C. M., Alexander D. M., Mullaney J. R., Swinbank A. M., 2014, Monthly Notices of the Royal Astronomical Society, 441, 3306

Harrison I., Camera S., Zuntz J., Brown M. L., 2016, Monthly Notices of the Royal Astronomical Society, 463, 3674

Harrison I., Lochner M., Brown M. L., 2017, arXiv e-prints, p. arXiv:1704.08278

Harrison I., et al., 2020, Monthly Notices of the Royal Astronomical Society, 495, 1737

Harvey D., Chisari N. E., Robertson A., McCarthy I. G., 2021, Monthly Notices of the Royal Astronomical Society, 506, 441

Hashimoto Y., Oemler Augustus J., Lin H., Tucker D. L., 1998, The Astrophysical Journal, 499, 589

Hawkins E., et al., 2003, Monthly Notices of the Royal Astronomical Society, 346, 78

Haywood M., Di Matteo P., Lehnert M. D., Snaith O., Khoperskov S., Gómez A., 2018, The Astrophysical Journal, 863, 113

Heavens A., Peacock J., 1988, Monthly Notices of the Royal Astronomical Society, 232, 339

Heavens A., Refregier A., Heymans C., 2000, Monthly Notices of the Royal Astronomical Society, 319, 649

Helmi A., Babusiaux C., Koppelman H. H., Massari D., Veljanoski J., Brown A. G. A., 2018, Nature, 563, 85

Hernquist L., Katz N., Weinberg D. H., Miralda-Escudé J., 1996, ApJ, 457, L51

Hewitt J. N., Turner E. L., Schneider D. P., Burke B. F., Langston G. I., 1988, Nature, 333, 537

Heymans C., Heavens A., 2003, Monthly Notices of the Royal Astronomical Society, 339, 711

Heymans C., Brown M., Heavens A., Meisenheimer K., Taylor A., Wolf C., 2004, Monthly Notices of the Royal Astronomical Society, 347, 895

Heymans C., White M., Heavens A., Vale C., van Waerbeke L., 2006, Monthly Notices of the Royal Astronomical Society, 371, 750

Heymans C., Rowe B., Hoekstra H., Miller L., Erben T., Kitching T., van Waerbeke L., 2012, Monthly Notices of the Royal Astronomical Society, 421, 381

Heymans C., et al., 2013, Monthly Notices of the Royal Astronomical Society, 432, 2433

Heymans C., et al., 2021, Astronomy & Astrophysics, 646, A140

Hezaveh Y., Dalal N., Holder G., Kisner T., Kuhlen M., Perreault Levasseur L., 2016, J. Cosmology Astropart. Phys., 2016, 048

Hikage C., et al., 2019, PASJ, 71, 43

Hilbert S., Xu D., Schneider P., Springel V., Vogelsberger M., Hernquist L., 2017, Monthly Notices of the Royal Astronomical Society, 468, 790

Hildebrandt H., et al., 2017, Monthly Notices of the Royal Astronomical Society, 465, 1454

Hildebrandt H., et al., 2020, Astronomy & Astrophysics, 633, A69

Hillier T. J. M., 2020, PhD thesis, University of Manchester

Hillier T., Brown M. L., Harrison I., Whittaker L., 2019, Monthly Notices of the Royal Astronomical Society, 488, 5420

Hinshaw G., et al., 2013, ApJS, 208, 19

Hirata C. M., Seljak U., 2004, Phys. Rev. D, 70, 063526

Hirata C. M., Seljak U., 2010, Phys. Rev. D, 82, 049901

Hirata C. M., et al., 2004, Monthly Notices of the Royal Astronomical Society, 353, 529

Hirata C. M., Mandelbaum R., Ishak M., Seljak U., Nichol R., Pimbblet K. A., Ross N. P., Wake D., 2007, Monthly Notices of the Royal Astronomical Society, 381, 1197

Hockney R. W., Eastwood J. W., 1981, Computer Simulation Using Particles. Routledge

Hoekstra H., Jain B., 2008, Annual Review of Nuclear and Particle Science, 58, 99

Hopkins P. F., 2013, Monthly Notices of the Royal Astronomical Society, 428, 2840

Hopkins P. F., Quataert E., 2011, Monthly Notices of the Royal Astronomical Society, 415, 1027

Hopkins P. F., Hernquist L., Cox T. J., Di Matteo T., Martini P., Robertson B., Springel V., 2005, The Astrophysical Journal, 630, 705

Hopkins P. F., Kereš D., Oñorbe J., Faucher-Giguère C.-A., Quataert E., Murray N., Bullock J. S., 2014, Monthly Notices of the Royal Astronomical Society, 445, 581

Hopkins P. F., et al., 2018, Monthly Notices of the Royal Astronomical Society, 480, 800

Horta D., et al., 2021, Monthly Notices of the Royal Astronomical Society, 500, 1385

Hoyle F., 1948, Monthly Notices of the Royal Astronomical Society, 108, 372

Hu W., 2002, Phys. Rev. D, 65, 023003

Hubble E. P., 1926, The Astrophysical Journal, 64, 321

Hubble E., 1929a, Proceedings of the National Academy of Science, 15, 168

Hubble E. P., 1929b, The Astrophysical Journal, 69, 103

Huff E. M., Krause E., Eifler T., Fang X., George M. R., Schlegel D., 2013, arXiv e-prints, p. arXiv:1311.1489

Hui L., Zhang J., 2008, The Astrophysical Journal, 688, 742

Hummels C. B., et al., 2019, The Astrophysical Journal, 882, 156

Huterer D., 2002, Phys. Rev. D, 65, 063001

Huterer D., Takada M., 2005, Astroparticle Physics, 23, 369

Jahnke K., Macciò A. V., 2011, The Astrophysical Journal, 734, 92

Jain B., Jarvis M., Bernstein G., 2006, J. Cosmology Astropart. Phys., 2006, 001

Jeans J. H., 1902, Philosophical Transactions of the Royal Society of London Series A, 199, 1

Jenkins A., 2010, Monthly Notices of the Royal Astronomical Society, 403, 1859

Jenkins A., 2013, Monthly Notices of the Royal Astronomical Society, 434, 2094

Jenkins A., Booth S., 2013, arXiv e-prints, p. arXiv:1306.5771

Jiang L., Helly J. C., Cole S., Frenk C. S., 2014, Monthly Notices of the Royal Astronomical Society, 440, 2115

Jing Y. P., 2002, Monthly Notices of the Royal Astronomical Society, 335, L89

Joachimi B., Schneider P., 2008, Astronomy & Astrophysics, 488, 829

Joachimi B., Mandelbaum R., Abdalla F. B., Bridle S. L., 2011, Astronomy & Astrophysics, 527, A26

Joachimi B., Semboloni E., Bett P. E., Hartlap J., Hilbert S., Hoekstra H., Schneider P., Schrabback T., 2013, Monthly Notices of the Royal Astronomical Society, 431, 477

Joachimi B., et al., 2015, Space Sci. Rev., 193, 1

Johansson P. H., Burkert A., Naab T., 2009, The Astrophysical Journal, 707, L184

Johnson J. W., Maller A. H., Berlind A. A., Sinha M., Holley-Bockelmann J. K., 2019, Monthly Notices of the Royal Astronomical Society, 486, 1156

Johnston H., et al., 2019, Astronomy & Astrophysics, 624, A30

Joudaki S., et al., 2018, Monthly Notices of the Royal Astronomical Society, 474, 4894

Kaiser N., 1984, ApJ, 284, L9

Kaiser N., Squires G., Broadhurst T., 1995, The Astrophysical Journal, 449, 460

Kaiser N., Wilson G., Luppino G. A., 2000, arXiv e-prints, pp astro–ph/0003338

Kang X., Wang P., 2015, The Astrophysical Journal, 813, 6

Kang X., Mao S., Gao L., Jing Y. P., 2005, Astronomy & Astrophysics, 437, 383

Kang X., van den Bosch F. C., Yang X., Mao S., Mo H. J., Li C., Jing Y. P., 2007, Monthly Notices of the Royal Astronomical Society, 378, 1531

Kant I., 1755, Allgemeine Naturgeschichte und Theorie des Himmels

Kapteyn J. C., 1922, The Astrophysical Journal, 55, 302

Kardashev N., 1967, ApJ, 150, L135

Katz N., Gunn J. E., 1991, The Astrophysical Journal, 377, 365

Katz N., Quinn T., Bertschinger E., Gelb J. M., 1994, Monthly Notices of the Royal Astronomical Society, 270, L71

Katz N., Weinberg D. H., Hernquist L., 1996, ApJS, 105, 19

Katz N., Keres D., Dave R., Weinberg D. H., 2003, How Do Galaxies Get Their Gas?. Monthly Notices of the Royal Astronomical Society, p. 185, doi:10.1007/978-94-010-0115-1_34

Kauffmann G., Haehnelt M., 2000, Monthly Notices of the Royal Astronomical Society, 311, 576

Kauffmann G., White S. D. M., Guiderdoni B., 1993, Monthly Notices of the Royal Astronomical Society, 264, 201

Kauffmann G., Colberg J. M., Diaferio A., White S. D. M., 1999, Monthly Notices of the Royal Astronomical Society, 303, 188

Kay S. T., Pearce F. R., Frenk C. S., Jenkins A., 2002, Monthly Notices of the Royal Astronomical Society, 330, 113

Kazantzidis S., Kravtsov A. V., Zentner A. R., Allgood B., Nagai D., Moore B., 2004, ApJ, 611, L73

Kelvin W. T., 1904, Baltimore Lectures on Molecular Dynamics and the Wave Theory of Light, London, England: C.J. Clay and Sons, 274

Kennicutt Jr. R. C., 1998, ARA&A, 36, 189

Kennicutt R. C., Evans N. J., 2012, ARA&A, 50, 531

Kereš D., Katz N., Weinberg D. H., Davé R., 2005, Monthly Notices of the Royal Astronomical Society, 363, 2

Kereš D., Katz N., Fardal M., Davé R., Weinberg D. H., 2009, Monthly Notices of the Royal Astronomical Society, 395, 160

Khandai N., Di Matteo T., Croft R., Wilkins S., Feng Y., Tucker E., DeGraf C., Liu M.-S., 2015, Monthly Notices of the Royal Astronomical Society, 450, 1349

Kiessling A., et al., 2015, Space Sci. Rev., 193, 67

Kilbinger M., 2015, Reports on Progress in Physics, 78, 086901

Kilbinger M., et al., 2013, Monthly Notices of the Royal Astronomical Society, 430, 2200

King L., Schneider P., 2002, Astronomy & Astrophysics, 396, 411

King L. J., et al., 1998, Monthly Notices of the Royal Astronomical Society, 295, L41

Kirk D., et al., 2015, Space Sci. Rev., 193, 139

Kitching T. D., et al., 2014, Monthly Notices of the Royal Astronomical Society, 442, 1326

Klypin A. A., Shandarin S. F., 1983, Monthly Notices of the Royal Astronomical Society, 204, 891

Klypin A., Gottlöber S., Kravtsov A. V., Khokhlov A. M., 1999, The Astrophysical Journal, 516, 530

Klypin A. A., Trujillo-Gomez S., Primack J., 2011, The Astrophysical Journal, 740, 102

Knebe A., et al., 2011, Monthly Notices of the Royal Astronomical Society, 415, 2293

Kofman L. A., Gnedin N. Y., Bahcall N. A., 1993, The Astrophysical Journal, 413, 1

Koopmans L. V. E., 2005, Monthly Notices of the Royal Astronomical Society, 363, 1136

Koppelman H. H., Helmi A., Massari D., Price-Whelan A. M., Starkenburg T. K., 2019, Astronomy & Astrophysics, 631, L9

Kormendy J., Ho L. C., 2013, Annual Review of Astronomy and Astrophysics, 51, 511

Kormendy J., Richstone D., 1995, ARA&A, 33, 581

Krause E., Eifler T., Blazek J., 2016, Monthly Notices of the Royal Astronomical Society, 456, 207

Kravtsov A. V., Borgani S., 2012, ARA&A, 50, 353

Kruijssen J. M. D., Pfeffer J. L., Reina-Campos M., Crain R. A., Bastian N., 2019, Monthly Notices of the Royal Astronomical Society, 486, 3180

Kuijken K., et al., 2015, Monthly Notices of the Royal Astronomical Society, 454, 3500

Kuutma T., Tamm A., Tempel E., 2017, Astronomy & Astrophysics, 600, L6

L'Huillier B., Winther H. A., Mota D. F., Park C., Kim J., 2017, Monthly Notices of the Royal Astronomical Society, 468, 3174

LSST Dark Energy Science Collaboration 2012, arXiv e-prints, p. arXiv:1211.0310

LSST Science Collaboration et al., 2009, arXiv e-prints, p. arXiv:0912.0201

Lacey C., Cole S., 1993, Monthly Notices of the Royal Astronomical Society, 262, 627

Lagos C. d. P., et al., 2015, Monthly Notices of the Royal Astronomical Society, 452, 3815

Lagos C. d. P., et al., 2016, Monthly Notices of the Royal Astronomical Society, 459, 2632

Larson R. B., Tinsley B. M., Caldwell C. N., 1980, The Astrophysical Journal, 237, 692

Laureijs R., et al., 2011, arXiv e-prints, p. arXiv:1110.3193

Laureijs R., et al., 2012, in Proc. SPIE. p. 84420T, doi:10.1117/12.926496

Lazeyras T., Musso M., Schmidt F., 2017, J. Cosmology Astropart. Phys., 2017, 059

Lee J., Pen U.-L., 2000, ApJ, 532, L5

Lee J., Pen U.-L., 2001, The Astrophysical Journal, 555, 106

Lee J., Springel V., Pen U.-L., Lemson G., 2008, Monthly Notices of the Royal Astronomical Society, 389, 1266

Lemaître G., 1927, Annales de la Société Scientifique de Bruxelles, 47, 49

Lemaître G., 1931, Monthly Notices of the Royal Astronomical Society, 91, 483

Lewis A., Challinor A., Lasenby A., 2000, The Astrophysical Journal, 538, 473

Lewis I., et al., 2002, Monthly Notices of the Royal Astronomical Society, 334, 673

Li Y., Mo H. J., Gao L., 2008, Monthly Notices of the Royal Astronomical Society, 389, 1419

Liao S., Gao L., 2019, Monthly Notices of the Royal Astronomical Society, 485, 464

Libeskind N. I., Frenk C. S., Cole S., Helly J. C., Jenkins A., Navarro J. F., Power C., 2005, Monthly Notices of the Royal Astronomical Society, 363, 146

Libeskind N. I., Knebe A., Hoffman Y., Gottlöber S., Yepes G., Steinmetz M., 2011, Monthly Notices of the Royal Astronomical Society, 411, 1525

Linder E. V., 2003, Phys. Rev. Lett., 90, 091301

Loeb A., Cox T. J., 2008, Astronomy, 36, 28

Lovell M. R., et al., 2012, Monthly Notices of the Royal Astronomical Society, 420, 2318

Ludlow A. D., Schaye J., Schaller M., Richings J., 2019a, Monthly Notices of the Royal Astronomical Society, 488, L123

Ludlow A. D., Schaye J., Bower R., 2019b, Monthly Notices of the Royal Astronomical Society, 488, 3663

Lynden-Bell D., Lynden-Bell R. M., 1995, Monthly Notices of the Royal Astronomical Society, 275, 429

Ma C.-P., Bertschinger E., 1995, The Astrophysical Journal, 455, 7

Mackereth J. T., Crain R. A., Schiavon R. P., Schaye J., Theuns T., Schaller M., 2018, Monthly Notices of the Royal Astronomical Society, 477, 5072

Mackereth J. T., et al., 2019, Monthly Notices of the Royal Astronomical Society, 482, 3426

Mackey J., White M., Kamionkowski M., 2002, Monthly Notices of the Royal Astronomical Society, 332, 788

Madau P., Pozzetti L., Dickinson M., 1998, The Astrophysical Journal, 498, 106

Madau P., Shen S., Governato F., 2014, ApJ, 789, L17

Magorrian J., et al., 1998, AJ, 115, 2285

Maiolino R., et al., 2012, Monthly Notices of the Royal Astronomical Society, 425, L66

Majewski S. R., Skrutskie M. F., Weinberg M. D., Ostheimer J. C., 2003, The Astrophysical Journal, 599, 1082

Mandelbaum R., 2018, ARA&A, 56, 393

Mandelbaum R., Hirata C. M., Ishak M., Seljak U., Brinkmann J., 2006, Monthly Notices of the Royal Astronomical Society, 367, 611

Manning S. M., et al., 2020, Monthly Notices of the Royal Astronomical Society, 495, 1724

Mao Y.-Y., Zentner A. R., Wechsler R. H., 2018, Monthly Notices of the Royal Astronomical Society, 474, 5143

Marigo P., 2001, Astronomy & Astrophysics, 370, 194

Marinacci F., et al., 2018, Monthly Notices of the Royal Astronomical Society, 480, 5113

Martin C. L., Shapley A. E., Coil A. L., Kornei K. A., Bundy K., Weiner B. J., Noeske K. G., Schiminovich D., 2012, The Astrophysical Journal, 760, 127

Martinez V., Saar E., 2002, in Starck J.-L., Murtagh F. D., eds, Society of Photo-Optical Instrumentation Engineers (SPIE) Conference Series Vol. 4847, Astronomical Data Analysis II. pp 86–100 (`arXiv:astro-ph/0209208`), doi:10.1117/12.461972

Mashchenko S., Wadsley J., Couchman H. M. P., 2008, Science, 319, 174

Massey R., et al., 2015, Monthly Notices of the Royal Astronomical Society, 449, 3393

Mathews W. G., 1978, The Astrophysical Journal, 219, 413

Matthee J., Schaye J., Crain R. A., Schaller M., Bower R., Theuns T., 2017, Monthly Notices of the Royal Astronomical Society, 465, 2381

McAlpine S., et al., 2016, Astronomy and Computing, 15, 72

McAlpine S., et al., 2022, MNRAS,

McCarthy I. G., Font A. S., Crain R. A., Deason A. J., Schaye J., Theuns T., 2012, Monthly Notices of the Royal Astronomical Society, 420, 2245

McCarthy I. G., Schaye J., Bird S., Le Brun A. M. C., 2017, Monthly Notices of the Royal Astronomical Society, 465, 2936

McCarthy K. S., Zheng Z., Guo H., Luo W., Lin Y.-T., 2022, Monthly Notices of the Royal Astronomical Society, 509, 380

McKee C. F., Ostriker J. P., 1977, The Astrophysical Journal, 218, 148

McKee C. F., Ostriker E. C., 2007, ARA&A, 45, 565

Mead A. J., Peacock J. A., Heymans C., Joudaki S., Heavens A. F., 2015, Monthly Notices of the Royal Astronomical Society, 454, 1958

Mihos J. C., Hernquist L., 1996, The Astrophysical Journal, 464, 641

Milgrom M., 1983, The Astrophysical Journal, 270, 365

Miller L., Kitching T. D., Heymans C., Heavens A. F., van Waerbeke L., 2007, Monthly Notices of the Royal Astronomical Society, 382, 315

Miller L., et al., 2013, Monthly Notices of the Royal Astronomical Society, 429, 2858

Mitchell P. D., Schaye J., Bower R. G., Crain R. A., 2020, Monthly Notices of the Royal Astronomical Society, 494, 3971

Miyatake H., More S., Takada M., Spergel D. N., Mandelbaum R., Rykoff E. S., Rozo E., 2016, Phys. Rev. Lett., 116, 041301

Mo H., van den Bosch F. C., White S., 2010, Galaxy Formation and Evolution. Cambridge University Press

Montero-Dorta A. D., et al., 2020, Monthly Notices of the Royal Astronomical Society, 496, 1182

Moore B., 1994, Nature, 370, 629

Morales M. F., 2006, ApJ, 650, L21

Moran E. C., Shahinyan K., Sugarman H. R., Vélez D. O., Eracleous M., 2014, AJ, 148, 136

More S., et al., 2016, The Astrophysical Journal, 825, 39

Mori M., Yoshii Y., Tsujimoto T., Nomoto K., 1997, ApJ, 478, L21

Moster B. P., Somerville R. S., Maulbetsch C., van den Bosch F. C., Macciò A. V., Naab T., Oser L., 2010, The Astrophysical Journal, 710, 903

Muldrew S. I., Pearce F. R., Power C., 2011, Monthly Notices of the Royal Astronomical Society, 410, 2617

Muldrew S. I., et al., 2012, Monthly Notices of the Royal Astronomical Society, 419, 2670

Myeong G. C., Vasiliev E., Iorio G., Evans N. W., Belokurov V., 2019, Monthly Notices of the Royal Astronomical Society, 488, 1235

Naab T., Ostriker J. P., 2017, ARA&A, 55, 59

Naab T., Khochfar S., Burkert A., 2006, ApJ, 636, L81

Nagamine K., Loeb A., 2003, New Astron., 8, 439

Naiman J. P., et al., 2018, Monthly Notices of the Royal Astronomical Society, 477, 1206

Narayan R., Bartelmann M., 1996, arXiv e-prints, pp astro–ph/9606001

Navarro J. F., Benz W., 1991, The Astrophysical Journal, 380, 320

Navarro J. F., White S. D. M., 1994, Monthly Notices of the Royal Astronomical Society, 267, 401

Navarro J. F., Frenk C. S., White S. D. M., 1997, The Astrophysical Journal, 490, 493

Neistein E., van den Bosch F. C., Dekel A., 2006, Monthly Notices of the Royal Astronomical Society, 372, 933

Nelson D., et al., 2018, Monthly Notices of the Royal Astronomical Society, 475, 624

Newberg H. J., et al., 2002, The Astrophysical Journal, 569, 245

Nielsen N. M., Kacprzak G. G., Pointon S. K., Murphy M. T., Churchill C. W., Davé R., 2020, arXiv e-prints, p. arXiv:2002.08516

Nuza S. E., Kitaura F.-S., Heß S., Libeskind N. I., Müller V., 2014, Monthly Notices of the Royal Astronomical Society, 445, 988

Oñorbe J., Boylan-Kolchin M., Bullock J. S., Hopkins P. F., Kereš D., Faucher-Giguère C.-A., Quataert E., Murray N., 2015, Monthly Notices of the Royal Astronomical Society, 454, 2092

Okumura T., Jing Y. P., Li C., 2009, The Astrophysical Journal, 694, 214

Oman K. A., et al., 2015, Monthly Notices of the Royal Astronomical Society, 452, 3650

Oort J. H., 1932, Bull. Astron. Inst. Netherlands, 6, 249

Oppenheimer B. D., Davé R., 2008, Monthly Notices of the Royal Astronomical Society, 387, 577

Oppenheimer B. D., Schaye J., 2013, Monthly Notices of the Royal Astronomical Society, 434, 1043

Oppenheimer B. D., Davé R., Kereš D., Fardal M., Katz N., Kollmeier J. A., Weinberg D. H., 2010, Monthly Notices of the Royal Astronomical Society, 406, 2325

Oppenheimer B. D., et al., 2016, Monthly Notices of the Royal Astronomical Society, 460, 2157

Oppenheimer B. D., et al., 2020, Monthly Notices of the Royal Astronomical Society, 491, 2939

Ostriker J. P., Peebles P. J. E., 1973, The Astrophysical Journal, 186, 467

Ostriker J. P., Steinhardt P. J., 1995, Nature, 377, 600

Ostriker J. P., Peebles P. J. E., Yahil A., 1974, ApJ, 193, L1

Paranjape A., Hahn O., Sheth R. K., 2018, Monthly Notices of the Royal Astronomical Society, 476, 3631

Parkinson H., Cole S., Helly J., 2008, Monthly Notices of the Royal Astronomical Society, 383, 557

Patel P., Bacon D. J., Beswick R. J., Muxlow T. W. B., Hoyle B., 2010, Monthly Notices of the Royal Astronomical Society, 401, 2572

Peacock J. A., 1997, Monthly Notices of the Royal Astronomical Society, 284, 885

Peacock J. A., et al., 2001, Nature, 410, 169

Peacock J. A., Schneider P., Efstathiou G., Ellis J. R., Leibundgut B., Lilly S. J., Mellier Y., 2006, ESA-ESO Working Group on "Fundamental Cosmology", ESA-ESO Working Group on "Fundamental Cosmology (`arXiv:astro-ph/0610906`)

Peebles P. J. E., 1980, The large-scale structure of the universe. Princeton University Press

Peebles P. J. E., 1982, ApJ, 263, L1

Peebles P. J. E., Yu J. T., 1970, The Astrophysical Journal, 162, 815

Peebles P. J. E., Schramm D. N., Turner E. L., Kron R. G., 1991, Nature, 352, 769

Peeples M. S., et al., 2019, The Astrophysical Journal, 873, 129

Pen U.-L., Lee J., Seljak U., 2000, ApJ, 543, L107

Peng Y., Maiolino R., Cochrane R., 2015, Nature, 521, 192

Penzias A. A., Wilson R. W., 1965, The Astrophysical Journal, 142, 419

Percival W. J., Cole S., Eisenstein D. J., Nichol R. C., Peacock J. A., Pope A. C., Szalay A. S., 2007, Monthly Notices of the Royal Astronomical Society, 381, 1053

Perlmutter S., et al., 1999, The Astrophysical Journal, 517, 565

Petrosian V., Salpeter E., Szekeres P., 1967, The Astrophysical Journal, 147, 1222

Pfeffer J., Kruijssen J. M. D., Crain R. A., Bastian N., 2018, Monthly Notices of the Royal Astronomical Society, 475, 4309

Pichon C., Codis S., Pogosyan D., Dubois Y., Desjacques V., Devriendt J., 2016, in van de Weygaert R., Shandarin S., Saar E., Einasto J., eds, Vol. 308, The Zeldovich Universe: Genesis and Growth of the Cosmic Web. pp 421–432 (arXiv:1409.2608), doi:10.1017/S1743921316010309

Pillepich A., et al., 2018a, Monthly Notices of the Royal Astronomical Society, 473, 4077

Pillepich A., et al., 2018b, Monthly Notices of the Royal Astronomical Society, 475, 648

Pillepich A., et al., 2019, Monthly Notices of the Royal Astronomical Society, 490, 3196

Planck Collaboration et al., 2014a, Astronomy & Astrophysics, 571, A1

Planck Collaboration et al., 2014b, Astronomy & Astrophysics, 571, A16

Planck Collaboration et al., 2016, Astronomy & Astrophysics, 594, A23

Planck Collaboration et al., 2020, Astronomy & Astrophysics, 641, A6

Poggianti B. M., et al., 2017, The Astrophysical Journal, 844, 48

Poincare H., 1906, Popular Astronomy, 14, 475

Pontzen A., Governato F., 2012, Monthly Notices of the Royal Astronomical Society, 421, 3464

Poole-McKenzie R., Font A. S., Boxer B., McCarthy I. G., Burdin S., Stafford S. G., Brown S. T., 2020, J. Cosmology Astropart. Phys., 2020, 016

Portinari L., Chiosi C., Bressan A., 1998, Astronomy & Astrophysics, 334, 505

Potter D., Stadel J., Teyssier R., 2017, Computational Astrophysics and Cosmology, 4, 2

Press W. H., Schechter P., 1974, The Astrophysical Journal, 187, 425

Price D. J., 2008, Journal of Computational Physics, 227, 10040

Qu Y., et al., 2017, Monthly Notices of the Royal Astronomical Society, 464, 1659

Read J. I., Agertz O., Collins M. L. M., 2016, Monthly Notices of the Royal Astronomical Society, 459, 2573

Rees M. J., Ostriker J. P., 1977, Monthly Notices of the Royal Astronomical Society, 179, 541

Refregier A., 2003, Monthly Notices of the Royal Astronomical Society, 338, 35

Refregier A., Bacon D., 2003, Monthly Notices of the Royal Astronomical Society, 338, 48

Reid B. A., et al., 2012, Monthly Notices of the Royal Astronomical Society, 426, 2719

Reines A. E., Sivakoff G. R., Johnson K. E., Brogan C. L., 2011, Nature, 470, 66

Riess A. G., et al., 1998a, AJ, 116, 1009

Riess A. G., et al., 1998b, AJ, 116, 1009

Robertson B. E., Kravtsov A. V., 2008, The Astrophysical Journal, 680, 1083

Robertson B., Bullock J. S., Cox T. J., Di Matteo T., Hernquist L., Springel V., Yoshida N., 2006, The Astrophysical Journal, 645, 986

Roos M., Harun-or-Rashid S. M., 2002, arXiv e-prints, pp astro–ph/0209611

Rosas-Guevara Y. M., et al., 2015, Monthly Notices of the Royal Astronomical Society, 454, 1038

Rubin V. C., Ford W. Kent J., 1970, The Astrophysical Journal, 159, 379

Rubin V. C., Ford W. K. J., Thonnard N., 1980, The Astrophysical Journal, 238, 471

Rubin K. H. R., Prochaska J. X., Koo D. C., Phillips A. C., Martin C. L., Winstrom L. O., 2014, The Astrophysical Journal, 794, 156

Rupke D. S. N., Veilleux S., 2011, The Astrophysical Journal, 729, L27

Sachs R. K., Wolfe A. M., 1967, The Astrophysical Journal, 147, 73

Saitoh T. R., Makino J., 2013, The Astrophysical Journal, 768, 44

Salcedo A. N., Maller A. H., Berlind A. A., Sinha M., McBride C. K., Behroozi P. S., Wechsler R. H., Weinberg D. H., 2018, Monthly Notices of the Royal Astronomical Society, 475, 4411

Sales L. V., Navarro J. F., Schaye J., Dalla Vecchia C., Springel V., Booth C. M., 2010, Monthly Notices of the Royal Astronomical Society, 409, 1541

Sales L. V., Navarro J. F., Theuns T., Schaye J., White S. D. M., Frenk C. S., Crain R. A., Dalla Vecchia C., 2012, Monthly Notices of the Royal Astronomical Society, 423, 1544

Salpeter E. E., 1955, The Astrophysical Journal, 121, 161

Samuroff S., Mandelbaum R., Blazek J., 2021, Monthly Notices of the Royal Astronomical Society, 508, 637

Sancisi R., Fraternali F., Oosterloo T., van der Hulst T., 2008, A&ARv, 15, 189

Sato-Polito G., Montero-Dorta A. D., Abramo L. R., Prada F., Klypin A., 2019, Monthly Notices of the Royal Astronomical Society, 487, 1570

Sawala T., et al., 2015, Monthly Notices of the Royal Astronomical Society, 448, 2941

Sawala T., et al., 2016, Monthly Notices of the Royal Astronomical Society, 457, 1931

Schaller M., et al., 2015a, Monthly Notices of the Royal Astronomical Society, 451, 1247

Schaller M., Dalla Vecchia C., Schaye J., Bower R. G., Theuns T., Crain R. A., Furlong M., McCarthy I. G., 2015b, Monthly Notices of the Royal Astronomical Society, 454, 2277

Schawinski K., et al., 2014, Monthly Notices of the Royal Astronomical Society, 440, 889

Schaye J., 2004, The Astrophysical Journal, 609, 667

Schaye J., Dalla Vecchia C., 2008, Monthly Notices of the Royal Astronomical Society, 383, 1210

Schaye J., et al., 2010, Monthly Notices of the Royal Astronomical Society, 402, 1536

Schaye J., et al., 2015, Monthly Notices of the Royal Astronomical Society, 446, 521

Schneider M. D., Bridle S., 2010, Monthly Notices of the Royal Astronomical Society, 402, 2127

Schneider M. D., Frenk C. S., Cole S., 2012, J. Cosmology Astropart. Phys., 5, 030

Schober J., Schleicher D. R. G., Klessen R. S., 2017, Monthly Notices of the Royal Astronomical Society, 468, 946

Schönrich R., Asplund M., Casagrande L., 2014, The Astrophysical Journal, 786, 7

Secco L. F., et al., 2022, Phys. Rev. D, 105, 023515

Seljak U., Zaldarriaga M., 1996, The Astrophysical Journal, 469, 437

Semboloni E., Hoekstra H., Schaye J., van Daalen M. P., McCarthy I. G., 2011, Monthly Notices of the Royal Astronomical Society, 417, 2020

Shandarin S., Habib S., Heitmann K., 2010, Phys. Rev. D, 81, 103006

Shao S., Cautun M., Frenk C. S., Gao L., Crain R. A., Schaller M., Schaye J., Theuns T., 2016, Monthly Notices of the Royal Astronomical Society, 460, 3772

Shapley H., 1919, J. R. Astron. Soc. Canada, 13, 438

Shapley H., Curtis H. D., 1921, Bulletin of the National Research Council, 2, 171

Sharma S., Steinmetz M., 2005, The Astrophysical Journal, 628, 21

Shattow G. M., Croton D. J., Skibba R. A., Muldrew S. I., Pearce F. R., Abbas U., 2013, Monthly Notices of the Royal Astronomical Society, 433, 3314

Sheldon E. S., et al., 2004, AJ, 127, 2544

Sheth R. K., Tormen G., 1999, Monthly Notices of the Royal Astronomical Society, 308, 119

Sheth R. K., Tormen G., 2004, Monthly Notices of the Royal Astronomical Society, 350, 1385

Shi J., Kurita T., Takada M., Osato K., Kobayashi Y., Nishimichi T., 2021, J. Cosmology Astropart. Phys., 2021, 030

Shirasaki M., Yoshida N., 2014, The Astrophysical Journal, 786, 43

Shklovsky J., 1967, ApJ, 150, L1

Shlosman I., Frank J., Begelman M. C., 1989, Nature, 338, 45

Sijacki D., Springel V., Di Matteo T., Hernquist L., 2007, Monthly Notices of the Royal Astronomical Society, 380, 877

Silk J., 1967, Nature, 215, 1155

Silk J., 1968, The Astrophysical Journal, 151, 459

Silk J., 1977, The Astrophysical Journal, 211, 638

Silk J., Rees M. J., 1998, Astronomy & Astrophysics, 331, L1

Singh S., Mandelbaum R., 2016, Monthly Notices of the Royal Astronomical Society, 457, 2301

Singh S., Mandelbaum R., More S., 2015, Monthly Notices of the Royal Astronomical Society, 450, 2195

Sinha M., Garrison L., 2017, Corrfunc: Blazing fast correlation functions on the CPU (ascl:1703.003)

Skibba R. A., Sheth R. K., Croton D. J., Muldrew S. I., Abbas U., Pearce F. R., Shattow G. M., 2013, Monthly Notices of the Royal Astronomical Society, 429, 458

Skibba R. A., et al., 2015, The Astrophysical Journal, 807, 152

Slipher V. M., 1913, Lowell Observatory Bulletin, 1, 56

Slipher V. M., 1915, Popular Astronomy, 23, 21

Slipher V. M., 1917, Proceedings of the American Philosophical Society, 56, 403

Sluse D., et al., 2003, Astronomy & Astrophysics, 406, L43

Smargon A., Mandelbaum R., Bahcall N., Niederste-Ostholt M., 2012, Monthly Notices of the Royal Astronomical Society, 423, 856

Smolčić V., et al., 2017, Astronomy & Astrophysics, 602, A1

Smoot G. F., et al., 1992, ApJ, 396, L1

Sohn S. T., Anderson J., van der Marel R. P., 2012, The Astrophysical Journal, 753, 7

Somerville R. S., Davé R., 2015, ARA&A, 53, 51

Somerville R. S., Primack J. R., 1999, Monthly Notices of the Royal Astronomical Society, 310, 1087

Sommer-Larsen J., Götz M., Portinari L., 2003, The Astrophysical Journal, 596, 47

Spergel D., et al., 2015, arXiv e-prints, p. arXiv:1503.03757

Springel V., 2005, Monthly Notices of the Royal Astronomical Society, 364, 1105

Springel V., 2010a, ARA&A, 48, 391

Springel V., 2010b, Monthly Notices of the Royal Astronomical Society, 401, 791

Springel V., Hernquist L., 2003, Monthly Notices of the Royal Astronomical Society, 339, 289

Springel V., White S. D. M., Tormen G., Kauffmann G., 2001, Monthly Notices of the Royal Astronomical Society, 328, 726

Springel V., White S. D. M., Hernquist L., 2004, in Ryder S., Pisano D., Walker M., Freeman K., eds, Vol. Proc. IAU Symp. 220, Dark Matter in Galaxies. Astronom. Soc. Pac., San Francisco, CA. p. 421

Springel V., Di Matteo T., Hernquist L., 2005a, Monthly Notices of the Royal Astronomical Society, 361, 776

Springel V., et al., 2005b, Nature, 435, 629

Springel V., Frenk C. S., White S. D. M., 2006, Nature, 440, 1137

Springel V., et al., 2008, Monthly Notices of the Royal Astronomical Society, 391, 1685

Springel V., et al., 2018, Monthly Notices of the Royal Astronomical Society, 475, 676

Square Kilometre Array Cosmology Science Working Group et al., 2020, Publ. Astron. Soc. Australia, 37, e007

Stinson G., Seth A., Katz N., Wadsley J., Governato F., Quinn T., 2006, Monthly Notices of the Royal Astronomical Society, 373, 1074

Sunayama T., More S., 2019, Monthly Notices of the Royal Astronomical Society, 490, 4945

Suresh J., Nelson D., Genel S., Rubin K. H. R., Hernquist L., 2019, Monthly Notices of the Royal Astronomical Society, 483, 4040

Swaters R. A., 1999, PhD thesis, -

Tanabashi M., et al., 2018, Phys. Rev. D, 98, 030001

Tanaka M., Goto T., Okamura S., Shimasaku K., Brinkmann J., 2004, AJ, 128, 2677

Tasitsiomi A., Kravtsov A. V., Wechsler R. H., Primack J. R., 2004, The Astrophysical Journal, 614, 533

Tegmark M., et al., 2004, The Astrophysical Journal, 606, 702

Tegmark M., et al., 2006, Phys. Rev. D, 74, 123507

Tenneti A., Mandelbaum R., Di Matteo T., Feng Y., Khandai N., 2014, Monthly Notices of the Royal Astronomical Society, 441, 470

Tenneti A., Singh S., Mandelbaum R., di Matteo T., Feng Y., Khandai N., 2015, Monthly Notices of the Royal Astronomical Society, 448, 3522

Tenneti A., Mandelbaum R., Di Matteo T., 2016, Monthly Notices of the Royal Astronomical Society, 462, 2668

Thacker R. J., Couchman H. M. P., 2000, The Astrophysical Journal, 545, 728

The Dark Energy Survey Collaboration 2005, arXiv e-prints, pp astro–ph/0510346

Thob A. C. R., et al., 2019, Monthly Notices of the Royal Astronomical Society, 485, 972

Tollerud E. J., Bullock J. S., Strigari L. E., Willman B., 2008, The Astrophysical Journal, 688, 277

Tollerud E. J., Boylan-Kolchin M., Bullock J. S., 2014, Monthly Notices of the Royal Astronomical Society, 440, 3511

Trayford J. W., Theuns T., Bower R. G., Crain R. A., Lagos C. d. P., Schaller M., Schaye J., 2016, Monthly Notices of the Royal Astronomical Society, 460, 3925

Trayford J. W., et al., 2017, Monthly Notices of the Royal Astronomical Society, 470, 771

Trayford J. W., Frenk C. S., Theuns T., Schaye J., Correa C., 2019, Monthly Notices of the Royal Astronomical Society, 483, 744

Trenti M., Hut P., 2008, arXiv e-prints, p. arXiv:0806.3950

Troxel M. A., Ishak M., 2015, Phys. Rep., 558, 1

Troxel M. A., et al., 2018, Phys. Rev. D, 98, 043528

Trujillo I., Aguerri J. A. L., Cepa J., Gutiérrez C. M., 2001, Monthly Notices of the Royal Astronomical Society, 321, 269

Tunbridge B. J., 2018, PhD thesis, University of Manchester

Tunbridge B., Harrison I., Brown M. L., 2016, Monthly Notices of the Royal Astronomical Society, 463, 3339

Tyson J. A., Valdes F., Wenk R. A., 1990, ApJ, 349, L1

Uson J. M., Wilkinson D. T., 1984, Nature, 312, 427

Van Waerbeke L., et al., 2000, Astronomy & Astrophysics, 358, 30

Van Waerbeke L., et al., 2013, Monthly Notices of the Royal Astronomical Society, 433, 3373

Vegetti S., Koopmans L. V. E., Bolton A., Treu T., Gavazzi R., 2010, Monthly Notices of the Royal Astronomical Society, 408, 1969

Vegetti S., Lagattuta D. J., McKean J. P., Auger M. W., Fassnacht C. D., Koopmans L. V. E., 2012, Nature, 481, 341

Veilleux S., Cecil G., Bland-Hawthorn J., 2005, ARA&A, 43, 769

Velliscig M., et al., 2015a, Monthly Notices of the Royal Astronomical Society, 453, 721

Velliscig M., et al., 2015b, Monthly Notices of the Royal Astronomical Society, 454, 3328

Vlah Z., Chisari N. E., Schmidt F., 2020, J. Cosmology Astropart. Phys., 2020, 025

Vogelsberger M., et al., 2014, Nature, 509, 177

Vogelsberger M., Marinacci F., Torrey P., Puchwein E., 2020, Nature Reviews Physics, 2, 42

Walsh D., Carswell R. F., Weymann R. J., 1979, Nature, 279, 381

Wang P., Kang X., 2018, Monthly Notices of the Royal Astronomical Society, 473, 1562

Wang Y. O., Lin W. P., Kang X., Dutton A., Yu Y., Macciò A. V., 2014, The Astrophysical Journal, 786, 8

Wang L., Dutton A. A., Stinson G. S., Macciò A. V., Penzo C., Kang X., Keller B. W., Wadsley J., 2015, Monthly Notices of the Royal Astronomical Society, 454, 83

Wang Y., et al., 2018, The Astrophysical Journal, 868, 130

Wang P., Libeskind N. I., Tempel E., Pawlowski M. S., Kang X., Guo Q., 2020, The Astrophysical Journal, 900, 129

Wechsler R. H., Zentner A. R., Bullock J. S., Kravtsov A. V., Allgood B., 2006, The Astrophysical Journal, 652, 71

Weinmann S. M., van den Bosch F. C., Yang X., Mo H. J., 2006, Monthly Notices of the Royal Astronomical Society, 366, 2

Wendland H., 1995, Advances in Computational Mathematics, 04, 389

Wetzel A. R., Tinker J. L., Conroy C., 2012, Monthly Notices of the Royal Astronomical Society, 424, 232

Wetzel A. R., Tinker J. L., Conroy C., van den Bosch F. C., 2013, Monthly Notices of the Royal Astronomical Society, 432, 336

White S. D. M., 1994, arXiv e-prints, pp astro–ph/9410043

White S. D. M., Frenk C. S., 1991, The Astrophysical Journal, 379, 52

White S. D. M., Rees M. J., 1978, Monthly Notices of the Royal Astronomical Society, 183, 341

White S. D. M., Frenk C. S., Davis M., 1983, ApJ, 274, L1

White S. D. M., Davis M., Efstathiou G., Frenk C. S., 1987, Nature, 330, 451

White S. D. M., Navarro J. F., Evrard A. E., Frenk C. S., 1993, Nature, 366, 429

Whittaker L., Brown M. L., Battye R. A., 2015, Monthly Notices of the Royal Astronomical Society, 451, 383

Wiersma R. P. C., Schaye J., Smith B. D., 2009a, Monthly Notices of the Royal Astronomical Society, 393, 99

Wiersma R. P. C., Schaye J., Theuns T., Dalla Vecchia C., Tornatore L., 2009b, Monthly Notices of the Royal Astronomical Society, 399, 574

Williams J. P., Blitz L., McKee C. F., 2000, in Mannings V., Boss A. P., Russell S. S., eds, Protostars and Planets IV. p. 97 (`arXiv:astro-ph/9902246`)

Wilman R. J., et al., 2008, Monthly Notices of the Royal Astronomical Society, 388, 1335

Wilman D. J., Zibetti S., Budavári T., 2010, Monthly Notices of the Royal Astronomical Society, 406, 1701

Wilson M. L., Silk J., 1981, The Astrophysical Journal, 243, 14

Winkel N., Pasquali A., Kraljic K., Smith R., Gallazzi A. R., Jackson T. M., 2021, arXiv e-prints, p. arXiv:2105.13368

Wittman D. M., Tyson J. A., Kirkman D., Dell'Antonio I., Bernstein G., 2000, Nature, 405, 143

Wright T., 1750, An original theory or new hypothesis of the universe : founded upon general phaenomena of the visible creation; and particularly the Via the laws of nature, and solving by mathematical principles : the Lactea ...compris'd in nine familiar letters from the author to his friendand : illustrated with upward of thirty graven and mezzotinto plates .... H. Chapelle, doi:10.3931/e-rara-28672

Wright E. L., et al., 1992, ApJ, 396, L13

Xia Q., Kang X., Wang P., Luo Y., Yang X., Jing Y., Wang H., Mo H., 2017, The Astrophysical Journal, 848, 22

Xu G., 1995, ApJS, 98, 355

Xu X., Zheng Z., 2020, Monthly Notices of the Royal Astronomical Society, 492, 2739

Yang X., Mo H. J., van den Bosch F. C., 2003, Monthly Notices of the Royal Astronomical Society, 339, 1057

Yang X., van den Bosch F. C., Mo H. J., Mao S., Kang X., Weinmann S. M., Guo Y., Jing Y. P., 2006, Monthly Notices of the Royal Astronomical Society, 369, 1293

Yao J., Ishak M., Lin W., Troxel M., 2017, J. Cosmology Astropart. Phys., 2017, 056

Young P., Gunn J. E., Kristian J., Oke J. B., Westphal J. A., 1980, The Astrophysical Journal, 241, 507

Zehavi I., Contreras S., Padilla N., Smith N. J., Baugh C. M., Norberg P., 2018, The Astrophysical Journal, 853, 84

Zel'Dovich Y. B., 1970, Astronomy & Astrophysics, 500, 13

Zel'dovich Y. B., 1968, Soviet Physics Uspekhi, 11, 381

Zeldovich I. B., Einasto J., Shandarin S. F., 1982, Nature, 300, 407

Zemp M., Gnedin O. Y., Gnedin N. Y., Kravtsov A. V., 2012, The Astrophysical Journal, 748, 54

Zentner A. R., Hearin A. P., van den Bosch F. C., 2014, Monthly Notices of the Royal Astronomical Society, 443, 3044

Zhang Y., Yang X., Faltenbacher A., Springel V., Lin W., Wang H., 2009, The Astrophysical Journal, 706, 747

Zhang Y., Yang X., Wang H., Wang L., Luo W., Mo H. J., van den Bosch F. C., 2015, The Astrophysical Journal, 798, 17

Zheng Z., et al., 2005, The Astrophysical Journal, 633, 791

Zhu G., Zheng Z., Lin W. P., Jing Y. P., Kang X., Gao L., 2006, ApJ, 639, L5

Zolotov A., et al., 2012, The Astrophysical Journal, 761, 71

Zu Y., Mandelbaum R., Simet M., Rozo E., Rykoff E. S., 2017, Monthly Notices of the Royal Astronomical Society, 470, 551

Zuntz J., Kacprzak T., Voigt L., Hirsch M., Rowe B., Bridle S., 2013, Monthly Notices of the Royal Astronomical Society, 434, 1604

Zwicky F., 1933, Helvetica Physica Acta, 6, 110

Zwicky F., 1937, The Astrophysical Journal, 86, 217

de Burgh-Day C. O., Taylor E. N., Webster R. L., Hopkins A. M., 2015, Monthly Notices of the Royal Astronomical Society, 451, 2161

de Jong J. T. A., et al., 2015, Astronomy & Astrophysics, 582, A62

de Lapparent V., Geller M. J., Huchra J. P., 1986, ApJ, 302, L1

de Vaucouleurs G., 1959, Handbuch der Physik, 53, 275

van Daalen M. P., Schaye J., Booth C. M., Dalla Vecchia C., 2011, Monthly Notices of the Royal Astronomical Society, 415, 3649

van Daalen M. P., McCarthy I. G., Schaye J., 2020, Monthly Notices of the Royal Astronomical Society, 491, 2424

van Dokkum P., et al., 2018, Nature, 555, 629

van Uitert E., Joachimi B., 2017, Monthly Notices of the Royal Astronomical Society, 468, 4502

van de Voort F., Schaye J., Booth C. M., Haas M. R., Dalla Vecchia C., 2011, Monthly Notices of the Royal Astronomical Society, 414, 2458

van de Voort F., Springel V., Mandelker N., van den Bosch F. C., Pakmor R., 2019, Monthly Notices of the Royal Astronomical Society, 482, L85

van den Bosch F. C., et al., 2007, Monthly Notices of the Royal Astronomical Society, 376, 841

van der Marel R. P., Besla G., Cox T. J., Sohn S. T., Anderson J., 2012, The Astrophysical Journal, 753, 9